# THE
# SHOCK AND ViBRATION
# BULLETIN

### Part 1
### Invited Papers, Vibration and Acoustics,
### Blast and Shock

## SEPTEMBER 1979

A Publication of
## THE SHOCK AND VIBRATION
## INFORMATION CENTER
Naval Research Laboratory, Washington, D.C.

Office of
The Director of Defense
Research and Engineering

# THE
# SHOCK AND VIBRATION
# BULLETIN

## SEPTEMBER 1979

The 49th Symposium on Shock and Vibration was held at the International Inn, Washington, DC on October 17-19, 1978. The NASA Goddard Space Flight Center, Greenbelt, Maryland, was the host.

# FOREWORD

The 49th Shock and Vibration Symposium was, from all reports, well received by those in attendance. The opening session was inspirational in a number of ways. Unfortunately, some invited papers for the opening session are not included in this proceedings. For the benefit of the reader, a review of that session, written by Dr. R.L. Eshleman, is offered below.

### The Opening Session

The opening session was chaired by W Brian Keegan Symposium participants were welcomed on behalf of the NASA, Goddard Space Flight Center by Dr Robert S Cooper, Director of the Center Dr Cooper stressed the importance of the Symposium to Goddard and NASA in its role of helping to solve shock and vibration problems in space systems Andrew J Stofan, Deputy Associate Administrator for Space Sciences, NASA, presented the keynote address Mr Stofan noted the fact that he never received good news from shock and vibration engineers in his fifteen years of experience with launch vehicles Shock and vibration problems were always present but were solved He reviewed some past problems and NASA's future program plans Mr Stofan described some of the pogo problems encountered in the early Titan-Centour vehicles In the process of solving these problems he observed the fact that analytical tools lag hardware in development and shock and vibration people are typically brought in too late Analytical tools have to be improved for large structures in space Among the programs described by Mr Stofan were

- GALILEO SPACECRAFT · fly by Mars and Juniper in 1985 (dynamics and control problems)
- SPACE TELESCOPE · 1983 (problems in absolute pointing accuracy)
- LARGE AREA MODULAR ARRAY · look for x-ray sources
- UV OPTICAL INTERFEROMETER · measure sources near edge of solar system
- GEOSTATIONARY PLATFORM · remote area communications
- X-RAY PINHOLE TELESCOPE · determine x-ray sources in Sun
- GRAVITY WAVE INTERFEROMETER

Mr. Stofan observed that the technology does not exist for some of the projects and that analysts will have to work closely with designers

The first invited paper was "The Role of Dynamics in DoD Science and Technology Programs" by Dr George P Millburn of the Office of the Deputy Director of Research and Engineering Dr Millburn noted that the SVIC services form a central role in DoD RT&DE programs He observed that we must use the latest technology to combat the lack of people and numbers of hardware in our defense He reviewed the DoD research and development and noted the difficult problem of distributing the R&D effort to government laboratories, contract research firms, and Universities The key thrusts in DoD research include artificial intelligence, smart weapons, directed beams, microelectronics, and composite materials Dr Millburn observed the need for technology transfer groups such as SVIC in an effort to eliminate costly duplication

Dr Michael Card of NASA, Langley Research Center presented the second invited paper on "Dynamic Problems in Large Space Structures" Dr Card showed previous large vehicles (EXPLORER ('49), ECHO II ('64), SKYLAB ('73)) launched by NASA All had reliability problems New large space structures have a lot of open truss work Dr. Card described the three main areas with dynamics problems ·· structural analysis, dynamic loads, and controls Problems have begun to arise with saturated computer programs and with scaling Dr. Card reviewed the common dynamic modeling and computation techniques and discussed his progress in continuum analyses for repetitive structures He also reviewed load sources for large space structures including ground handling, boosting, deployment, assembly, control, thrusting, docking, operations, and environments Low frequencies (to .1 Hz) of large space structures are a problem -- for instance low earth orbit forcing frequency is .002 Hz Dr. Card talked about means for control of large space structures including counter rotating rings and adaptive control. He summarized with a discussion on methods for structural analysis, dynamic loads, and controls.

Dr. John F. Wilby of Bolt Beranek and Newman gave the third invited paper, "Analytical Model for Predictions of Noise Levels in Space Shuttle Payload Bay." Their work on acoustic noise environment includes efforts on mathematical analysis and experimental validation. The problems involve structural response and acoustic radiation. He showed program development, analytical models, and scale test models. Statistical energy analysis was used for high frequency vibration and modal analysis for low fre-

iii

quency The analysis was conducted in one-third octave bandwidths Testing of the OV 101 model will be conducted at the Palmdale, California test facility followed by a second test at Edwards Air Force Base using F 104 aircraft as the noise source Dr Wilby showed the microphone and accelerometer test locations The payload modeling was particularly interesting for this test program. Current and future work on this program was discussed by Dr Wilby

We regret in this case that full text of all invited papers is not included. We pledge, for all future symposia, to make every effort to include these timely and useful presentations.

Henry C. Pusey
Director, SVIC

# CONTENTS

## PAPERS APPEARING IN PART 1

## PAPERS APPEARING IN PART 2

### MODAL AND IMPEDANCE ANALYSIS

### HUMAN RESPONSE TO VIBRATION AND SHOCK

### ISOLATION AND DAMPING

COMBINED VIBRATION/TEMPERATURE/SIDI LOAD ENVIRONMENTAL TESTING OF
UHF BLADE ANTENNAS
R. Volker, McDonnell Douglas Corporation, St. Louis, MO

SHOCK ISOLATION PLATFORM FOR SEASPARROW LAUNCHER
P.V. Roberts, Raytheon Company, Bedford, MA


TITLES AND AUTHORS OF PAPERS
PRESENTED IN THE
SHORT DISCUSSION TOPICS SESSION

NOTE: These papers were only presented at the Symposium. They are
not published in the Bulletin and are only listed here as a convenience.


RESEARCH IN COLLISION DYNAMICS OF SURFACE SHIPS
M.P. Pakstys, General Dynamics, Croton, CT

FORCED VIBRATION RESONATORS AND VIBRATIONS OF THE SHIP
G. Volcy, Bureau Veritas, Paris, France

RINGING PLATE SIMULATION OF PYROTECHNIC SHOCKS
S.H. Neff, Sandia Laboratories, Albuquerque, NM

QUARTZ CRYSTAL RESONATORS FOR HIGH G ENVIRONMENTS
R.L. Filler, ET&D Laboratory, Fort Monmouth, NJ

THE BENCHLESS LASER
J. Pearson, Air Force Flight Dynamics Laboratory, Wright-Patterson AFB, OH

PULSED HOLOGRAPHIC ANALYSIS OF LARGE VEHICLE COMPONENTS
G. Arutunian and G.R. Gerhart, U.S. Army Tank Automotive Research and Development Command, Warren, MI

CALIBRATION OF SHOCK AND VIBRATION MEASURING TRANSDUCERS
R.R. Bouche, Bouche Laboratories, Sun Valley, CA

CRITICAL SPEEDS OF MULTITHROW NONUNIFORM CRANKSHAFTS USING SPATIAL FINITE LINE
ELEMENT TECHNIQUE
C. Bagci, Tennessee Tech. University, Cookeville, TN

VIBRATION OF INPLANE LOADED ISOTROPIC AND ORTHOTROPIC RECTANGULAR PLATES
S.M. Dickinson, The University of Western Ontario, London, Ontario, Canada

ATTENUATION OF VIBRATIONS IN VISCOELASTIC SOLIDS CONTAINING MULTIPLE DEFECTS
M.P. Wnuk, South Dakota University, Brookings, SD

SOLVING PC-CARD VIBRATION PROBLEMS WITH UNIQUE DAMPING APPLICATIONS
W.J. Vitaliano, Harris GISD, Melbourne, FL

MINI COMPUTER SWEPT SINUSOIDAL DATA PROCESSING TECHNIQUES
F.E. Anderson, U.S. Army Missile R&D Command, Redstone Arsenal, AL

SHUTTLE PAYLOADS TEST FACILITIES
E.J. Kirchman, NASA Goddard Space Flight Center, Greenbelt, MD

AERODYNAMIC COUPLING BETWEEN CLOSELY SPACED PANELS
C.V. Stahel, Jr., General Electric Company, Philadelphia, PA

UPDATE ON COMBINED ENVIRONMENT GROWTH TESTING OF A BLACK BOX
J. Hutchinson, Vought Corporation, Dallas, TX

Session Chairmen and Cochairmen
49th Shock and Vibration Symposium
October 17-19, 1978, Washington, DC

| Date | Session Title | Chairmen | Cochairmen |
|------|---------------|----------|------------|
| Tuesday, 17 Oct.<br>A.M. | Opening Session | Mr. Brian Keegan, NASA, Goddard Space Flight Center, Greenbelt, MD | Mr. Henry C. Pusey, Director, Shock and Vibration Inf. Ctr., Naval Research Lab., Washington, DC |
| Tuesday, 17 Oct.<br>P.M. | Vibration and Acoustics | :. E. Ken Stewart, U.S. Army Armament R&D Command, Dover, NJ | Mr. Larry Cook, NASA, Goddard Space Flight Center, Greenbelt, MD |
| Tuesday, 17 Oct.<br>P.M. | Blast and Shock | Dr. Jimmie P. Balsara, U.S. Army Engineer Waterways Experiment Station, Vicksburg, MS | Mr. Edwin Rzepka, Naval Surface Weapons Center, Silver Spring, MD |
| Wednesday, 18 Oct.<br>A.M. | Modal and Impedance Analysis | Dr. Ben Wada, Jet Propulsion Laboratory, Pasadena, CA | Dr. George Morosow, Martin Marietta Corp., Denver, CO |
| Wednesday, 18 Oct.<br>A.M. | Human Response to Vibration and Shock | Dr. John C. Guignard, Naval Aerospace Medical Research Laboratory Detachment, New Orleans, LA | Mr. Donald Wasserman, National Institute for Occupational Safety and Health, Cincinnati, OH |
| Wednesday, 18 Oct.<br>P.M. | Isolation and Damping | Professor Frederick Nelson, Tufts University, Medford, MA | Dr. John Henderson, Air Force Materials Laboratory, Wright-Patterson AFB, OH |
| Wednesday, 18 Oct.<br>P.M. | Dynamic Analysis | Mr. Summer A. Leadbetter, NASA Langley Research Center, Hampton, VA | Mr. Jess Jones, NASA, Marshall Space Flight Center, Huntsville, AL |
| Thursday, 19 Oct.<br>A.M. | Structure Medium Interaction | Lt.Col. John Galloway, Defense Nuclear Agency, Washington, DC | Dr. Jack Kalinowski, Naval Underwater Systems Center, New London, CT |
| Thursday, 19 Oct.<br>A.M. | Case Studies in Dynamics | Dr. Anthony Amos, NASA Headquarters Washington, DC | Mr. Don McCutchen, NASA LBJ Space Center, Houston, TX |
| Thursday, 19 Oct.<br>P.M. | Short Discussion Topics | Mr. Roland Seely, Naval Weapons Handling Evaluation Facility Earle, NJ | Mr. Charles Fridinger, Naval Surface Weapons Center, Silver Spring, MD |
| Thursday, 19 Oct.<br>P.M. | Classified Session | Mr. Anthony Paladino, Naval Sea Systems Command, Washington, DC | Mr. Kenneth Cornelius, Naval Ship R&D Center, Bethesda, MD |

# INVITED PAPERS

## THE DYNAMICS OF THE DOD SCIENCE AND TECHNOLOGY PROGRAM

Dr George P. Millburn
Office of the Deputy Under Secretary of Defense for Research and Engineering
Research and Advanced Technology
Washington, D.C.

I am delighted to be here to have the opportunity to address the 49th Shock and Vibration Symposium on the Science and Technology Program of the Department of Defense. It is especially pleasant to acknowledge our host, the NASA Goddard Space Flight Center.

My congratulations go to the program committee for the excellent program it has developed for the symposium. I have read through the agenda with better understanding of the depth and breadth of the subjects that have been chosen and the quality of the speakers who will illuminate them. The three days of the symposium should be a splendid experience for all of you. Let me also express appreciation to Henry Pusey and his staff for their unsung contributions over the years in operating the Shock and Vibration Information Center. It is unfortunate that activities such as information analysis centers do not get the attention that they merit, but we will try to do better in the future.

When I was approached to give this talk, I must confess that my first reaction was: "I don't know anything about shock or vibration that could be of interest to experts in the field." Then I remembered all the scars — the reworks, the slipped schedules, the cost overruns — which shock and vibration have given me and my doubts increased. However, Mr. Pusey assured me that the audience would like to hear more details of the DOD Science and Technology Program, particularly the major thrusts that impact the dynamics area.

The subject of this symposium — shock and vibration — is a technical area involving loads and stresses which, potentially, can alter reliability or affect survivability of any of our major defense systems. It is therefore a technology that is an essential part of all RDT&E Programs aimed at maintaining a strong national defense capability.

By their nature, military organizations everywhere strive to use the latest technology available to them in order to maximize their effectiveness. History is full of examples where the use of high technology has made a significant and occasionally a dramatic difference in the outcome of a battle or a war. There are, of course, occasional examples, too, where the attempts to use high technology have not only failed to be productive but have even been disastrous — witness the defeat of their enemies by Israel when rain and mud mired the advanced, highly mobile enemy chariots and permitted the inferior forces of Israel to prevail. Perhaps if

the chariot performance in mud had been adequately tested prior to battle, the whole outcome might have been changed. Certainly the scars I alluded to from shock and vibration testing are minor compared with those that would have resulted from equipment malfunction in the action arena.

It is important for all of us but particularly those of us who promote high technology with the greatest zeal to be aware of such lessons and to insist that proper precautions be taken to avoid premature use of technological advances. But where would the United States be today without the widespread use of high technology in its military forces? Certainly we cannot match our potential adversaries in manpower, and we have chosen not to attempt to match them in equipment numbers. Thus, our tanks, aircraft, carriers, command and control, and missiles must use the latest technology if we are to be strong enough to deter any possible aggression either against us or against areas vital to our national concern. It is the intent of the DOD Science and Technology Program to provide the proper foundation for military use of the high technology we have developed.

I have heard that there has been, on occasion, some quarrel with the severe design requirements for military systems. Let us take a lesson from history and understand that such systems are designed to operate in environments which, it is hoped, they will never have to face. The greater assurance we have that our systems will operate reliably in combat, the greater are our chances we will never have to use them. In terms used today, this is called deterrent capability.

It is the science and technology portion of the Defense R&D Program that gives us the options and opportunities to provide technological solutions to complex and difficult national security problems. It is the Science and Technology Program that provides new ideas, components, materials and techniques upon which technological advances in strategic, tactical, intelligence and support systems emerge. And not forgetting the human element, the Science and Technology Program seeks to improve our capability in recruiting, training and protecting our soldiers, sailors and airmen in both a peacetime and wartime environment. And now some details on the science and technology aspects of DOD R&D.

The science and technology budget for 1979 is $2.7 billion, about 20 percent of the total DOD R&D budget. It is divided into four major categories: Research, Exploratory

Development or Applied Research, Advanced Technology Demonstrations and Manufacturing Technology. The Air Force spends about 23 percent, the Navy, 29 percent; the Army, 29 percent; and the Defense Agencies, 19 percent. The program content is heavily weighted towards the physical sciences but there is a significant effort in terms of the life sciences and training. Our office is also heavily involved in technology export, an area whose importance is growing rapidly.

The Secretary of Defense and the Under Secretary of Defense for Research and Engineering recognize the importance of the Science and Technology Program in the achievement of our goals. We have had the support of the Administration and Congress in emphasizing the Science and Technology Program. This is reflected in our current budget and planned programs. There is about a 7 percent increase between FY 77 and FY 78. In FY 79, the forthcoming budget period, an increase of 13 percent over FY 78 is anticipated. Our longer range goals are to increase the research category by 10 percent per year in real terms and 5 percent, again in real terms, in Exploratory Development Programs.

The advanced technology demonstrations, the ATD's in acronym language, have also increased over the past two years. However, the ATD demonstrations have a "supply and demand" characteristic. The ATD program typically picks up the "winners" from the exploratory development and carries them through real life demonstrations to prove their military worth or general utility. It is the output of the ATDs that usually provide us with options for system prototype developments. It is my view that the need for ATDs will increase as we increase our output from the Exploratory Development Program. I will say more about ATDs later.

Dr. Davis, the Deputy Under Secretary of Defense for Research and Advanced Technology, has set up a number of management goals which are essential to successful formulation and execution of the Science and Technology Program. Among these goals are:

1. To interact with the scientific community so that it adequately understands DOD's scientifically-based problems and can respond to them.

2. To provide the structured mechanisms between R&D groups and operational military organizations that will allow the needed two-way flow of information and results on mission needs and R&D capabilities.

3. To prevent any crippling dependency by DOD on a specific segment of the scientific community that could harm DOD's ability to be properly responsive to its mission needs

4. To keep to a minimum the time period between relevant invention or creative idea, and its first developmental application in an operational environment.

5. To smoothly transition the substance of our R&D Programs so that it always mirrors the best of the old and the best of the new from our rapidly changing scientific environment.

One of our most difficult problems is the distribution of the R&D workload between the various performers — the DOD in-house laboratories, industry and universities. There are some 78 DOD in-house R&D installations in the Department but they by no means perform all of the R&D program About three out of every four DOD R&D dollars go to the private sector. However, the science and technology portion of the DGD R&D program has been more in-house oriented. In 1974 it was estimated that about 43 percent of the science and technology program was performed in-house. In 1975 a concerted effort was made to reduce this percentage in order to broaden the source of innovative ideas and capabilities. The result has been a reduction in the percentage of the science and technology program performed in-house from about 43 percent in FY 1974 to about 37 percent at the end of FY 77. The change results primarily from a larger portion of the science and technology program increases going to universities and industry.

In FY 77, in the DOD Research Program (about 18 percent of the Science and Technology Program) some 40 percent of the work was carried out by DOD in-house laboratories, 40 percent by universities and 20 percent by industry and non-profit organizations. As would be expected, this program balance shifts increasingly from universities through the DOD laboratories to industry during the progression from research through exploratory development to the advanced technology demonstration component of the Science and Technology Program. In the latter program, the effort is about 70 percent in industry and 30 percent in DOD laboratories. We do not see any major perturbations in these ratios for FY 78 or the out-years.

There are differing views within the Executive Branch, Congress and Industry as to the proper balance between the performers of Science and Technology work for DOD. The House Armed Services Committee placed temporary limits on the amount of the FY 78 Research and Exploratory Development that could be performed by private contractors. The Senate's view as was expressed in the Armed Services Committee report was that "the strength of this country will continue to be the initiative and motivation provided by our free enterprise system. Current trends preventing more participation by non-Department of Defense laboratories must be reversed and done so quickly and dramatically."

The second management initiative I would like to discuss is our effort in the area of advanced technology demonstrations — our 6.3A Program. The role of ATDs is not generally understood. One way to describe ATDs would be as "Technology Push" Projects maturing successfully from ideas and components in exploratory development which need to be demonstrated prior to gaining the confidence and acceptance of designers as potentially viable options for application to systems. ATD projects are generally functional bread-board items built as inexpensively as possible in very small quantities so that an engineering principle can be demonstrated as feasible. ATD projects generally are more expensive than exploratory development projects because they involve working models and testing. An example of a successful ATD is the Advanced Low Volume Ram Jet Technology Project which reached fruition through flight demonstrations in 1976 and 1977. This technology is being applied toward high speed air-to-air and air-to-ground tactical missiles. It promises significant advantages in time required to destroy hostile targets and in decreased vulnerability while attacking defended targets. Other ATD programs include efforts in

2

Fighter Aircraft Aerodynamics, Jet Engines and High Energy Lasers.

ATDs are an important component of our Science and Technology Program. They provide the finishing touches in demonstrating feasibility of the products of the Science and Technology Program. Successful ATD programs provide options and, essentially, the bridge to application to mission element needs across the spectrum of strategic, tactical and support systems.

Candidate ATD Projects compete for resources on their merits. Factors considered in selecting projects include the engineering need to do the demonstration, the probability of application to an existing or perceived need, and the probability of success in completing the demonstration. The ATD Program has not been as successful over the past two years in competing for resources with other portions of the RDT&E Program as some of their proponents had hoped. The growth within the ATD Program has exceeded inflation, however, the "supply and demand" of candidate ATD projects indicates that we need to put more resources into this area.

Key thrusts can be described as those technical areas or projects which are receiving increased resources, sometimes at the expense of "not-so-key" areas or projects. Key thrusts are usually found in areas where the technology is changing rapidly and technological breakthroughs might be expected. Consequently, technological surprises could be anticipated by the Soviets, others or ourselves. Some of the technologies in which scientific breakthroughs or surprises may well occur include those of:

- controlled thermonuclear reaction
- directed energy
- highly energetic munitions
- quiet underwater vehicles
- "smart" weapons
- adaptive optics
- composite materials
- very high speed microelectronics, and
- artificial intelligence.

I should point out that this same list has been separately generated almost in toto by several different groups on different occasions over the last year. It must, therefore, possess considerable credibility both within the military and intelligence communities.

Generally, the U.S. holds an assertable technological lead in these and other areas of high interest to national defense. However, based on recent assessments and group judgments, some important areas in which the U.S. does not necessarily lead appear to be in the technologies of:

- nuclear and chemical warfare
- land vehicle mobility, and
- composite materials.

We must watch closely in the expectation of seeing new advances in the level of such technologies incorporated in future Soviet weapons systems. We should also pursue with vigor in our defense program the areas we have just identified as rapidly changing technologies.

As I view the technologies which are highly pervasive and which seem to form the framework for so many of our current and predictable advances, I am compelled to conjecture a technological infrastructure, i.e., the technical basis for our military future. The kingpins in this infrastructure are:

- computer and software technology
- microelectronics
- distributed systems technology (for information, sensor, control, etc. networks)
- materials technology
- automated or unmanned operation technology
- sensor technology using both the electromagnetic and acoustic spectra
- human engineering, and
- manufacturing technology.

A good example of how some of these technologies fit together to form a new advance occurs in precision guided weapons application — cited by Dr. Perry, the Under Secretary of Defense for Research and Engineering, as our technology with the single greatest potential for force multiplication. He has predicted that precision guided weapons have the potential of revolutionizing warfare.

With the advent of microelectronics and advanced computer technology, we are now on the verge of developing unique terminal guidance signal processing techniques which will permit a munition delivered into the target area to scan the cluttered battlefield background. Using new imaging and, in some cases, non-imaging infrared seekers the target can be acquired and hit day or night. What remains, however, to provide a fully effective capability is the development of seekers that can see through bad weather, smoke and dust. We have therefore highlighted precision guidance technology programs directed toward the demonstration of an effective fair weather capability and development of all-weather sensors. Specific demonstration programs involving terminally guided submissiles are directed toward destruction of enemy armor which has not yet reached the range of our direct fire weapons. Longer term technology development in the area of millimeter wave (mmw) sensors is directed toward the destruction of enemy armor in adverse weather.

Our FY 79 Science and Technology budget contains specific thrusts in precision guided munitions, directed energy weapons, chemical warfare defense, materials and electronic warfare.

I have described the Science and Technology Program and discussed some of our management technical initiatives. I would like to now describe some of our activities in technology export.

The DOD role in technology export stems from the Export Administration Act of 1969, as amended. It states that "It is the policy of the U.S. . . . to restrict the export of goods and technology which would make a significant contribution to the military potential of any other nation or nations which would prove detrimental to the national security of the United States."

The same act authorizes the "Secretary of Defense to review any proposed export of goods or technology to any

country to which exports are restricted for national security purposes and whenever he determines that the export of such goods or technology will make a significant contribution, which would prove detrimental to the national security of the United States, to the military potential of any such country, to recommend to the President that such export be disapproved."

Interim DOD policy regarding technology export was published by the Secretary of Defense on 26 August 1977. Subsequently, the responsibility within DOD for the technical aspects of technology export matters was assigned to the Under Secretary of Defense for Research and Engineering. Our objectives are to control only those critical technologies which, if exported, would prove detrimental to our national security and to do this with minimal interruption to international commerce.

Several interrelated activities are underway to meet these objectives. We have participated extensively in U.S. preparations for the COCOM List Review which is now underway. DOD provided the Chairman of 7 of 13 Technology Transfer Groups (TTGs) and senior representatives to the remaining 6. These TTGs prepared the U.S. proposed technical positions on the various items and have prepared U.S. counterproposals to the other COCOM nations' proposals.

Finally, with the rapid advancements in technology and the ever expanding technical literature that follows, we need more than ever to concentrate on methods and resources for managing and disseminating this information, if only for the purpose of eliminating costly duplication of research and development efforts. Symposia such as this one are a means to that end. Specialized information analysis centers, such as the Shock and Vibration Information Center, fill a special need in this area. Their task is analyzing, reviewing and filtering information to get to the heart of a problem. Part of the problem as to why this capability is not more widely recognized may be that the broad research and development spectrum is not covered by such centers. We may wish to take a new look, to establish an information management system that includes document archives and information analysis centers to cover our wide technological base. The mechanics of such an effort may be difficult, but the results could be rewarding.

In conclusion, we are faced with requirements for higher performance systems under more adverse requirements. We are offered less money to do a greater job. The challenge is yours and mine. I think we can meet that challenge. History tends to support this prediction.

I hope this short overview gives you a better appreciation of the DOD Science and Technology Program and its dynamics — it is indeed a changing program which we strive to make responsive to future needs of our military strength.

To this point, I have successfully avoided saying anything about shock and vibration, and it probably would be wise for me to quit now. But I must repeat and reinforce the comment I made earlier. The United States depends on and utilizes high technology military hardware to a greater extent than any of our possible major adversaries. This is a deliberate decision but one which carries some hidden responsibilities. Not the least of these is making certain these new gadgets perform as advertised and as needed. The work of groups such as yours is an essential element in providing that assurance.

# THE DEVELOPMENT OF A METHOD FOR PREDICTING THE
# NOISE EXPOSURE OF PAYLOADS IN THE SPACE SHUTTLE
# ORBITER VEHICLE

John F. Wilby, Larry D. Pope
Bolt Beranek and Newman Inc.
Canoga Park, California 91303

## 1.0 INTRODUCTION

The advent of the space shuttle as a means of placing payloads into orbit introduced a series of new problem areas in vehicle and payload design. One such problem was the exposure of the payload to high acoustic levels at lift-off. When it was recognized, from studies such as that by On [1], that the sound levels surrounding a payload could be higher than those to which the payload has been designed, a program was initiated by NASA Headquarters with the objectives of obtaining reliable estimates of the sound levels and designing noise control approaches. NASA Goddard Space Flight Center served as contracting center and technical monitor for the program. The purpose of this paper is to review the tasks undertaken by Bolt Beranek and Newman Inc. (BBN) during the program and to outline future efforts required to complete the construction of an analytical model for the prediction of sound levels in the payload bay of the space shuttle orbiter vehicle at lift-off. The program is of interest because it provides an excellent example of the development of an analytical acoustic model, through the various stages of formulation and validation.

Results of the work accomplished to date have been presented in a series of BBN reports and technical papers. These are listed, at the end of this paper [2-11] so that an interested reader can obtain further details. The reports document the development of the analytical model, including modifications made as a result of comparisons with data obtained from a series of four tests on model and full-scale orbiter vehicles, with and without payload. These tests were conducted in conjunction with NASA Goddard Space Flight, Dryden Flight Research and Johnson Space Centers, and Rockwell International Space Division. In making the comparison between analytical and experimental results, three factors have to be kept in mind. First, although every effort is made to reproduce the acoustic environment of lift-off, the experimental external pressure fields are not necessarily good representations of the lift-off condition. Secondly, in no case has the payload bay been completely representative of the lift-off condition. There have been differences, for example, in the bay door, thermal control system material, and door radiators. Finally, at the present time, the analytical model has certain limitations which are currently being removed. These three factors have introduced some uncertainty into the interpretation of the comparisons of experimental and analytical results.

The development of the analytical model is shown in chronological order in Fig. 1. The initial formulation of the model was performed in 1976 with subsequent validation tests from 1976 to 1978. In addition, tasks to extend the low frequency range of the model are also identified.

## 2.0 SPACE SHUTTLE ORBITER VEHICLE

At lift-off the space shuttle system consists of the orbiter vehicle, a large fuel tank and two solid rocket boosters (SRB) in the familiar configuration shown in Fig. 2. The propulsive thrust, prior to the separation of the boosters later in the ascent, is provided by the Space Shuttle main engines (SSME) on the orbiter vehicle and the two SRB's. The configuration is different from preceding launch vehicles in that the rocket engine nozzles are separated by relatively large distances, and the engines provide an asymmetric thrust force which causes the space shuttle to drift sideways during launch.

A further difference between the space shuttle and earlier launch vehicles is the location of the payload bay relative to the rocket exhaust nozzles. In previous vehicles the payload was on the upper portion of the vehicle, well away from the rocket exhaust. The space shuttle, in contrast, has the payload bay located relatively close to the exhaust nozzles.

At lift-off the exhausts from the rocket engines pass through holes in the launch pad and are deflected by the turning ramps (Fig. 3). The high noise levels generated by the exhaust are reduced to some extent by the introduction of large quantities of water into the gas streams. This noise suppression system is the result of extensive tests undertaken by personnel at NASA Marshall Space Flight Center [13].

As the lift-off distance increases, the rocket exhausts impinge on the launch platform structure. This impingement increases the noise generation of the exhaust flow and also reduces the effectiveness of the water injection noise suppression system. Consequently, the maximum noise levels on the orbiter vehicle occur several seconds after lift-off.

The structural region of interest to the present discussion is the mid-fuselage region which is defined longitudinally by the fore and aft bulkheads of the payload bay at stations 582 and 1307 respectively (Fig. 4). The other bounding
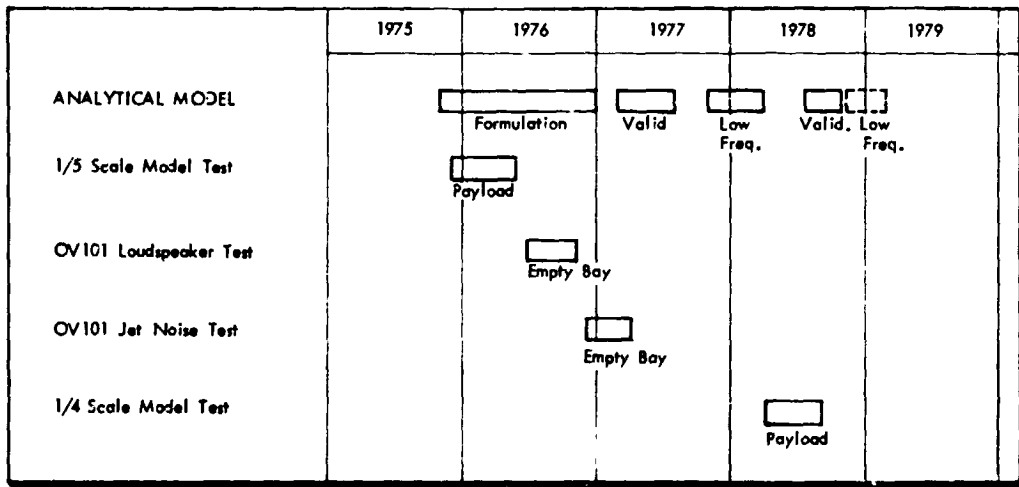
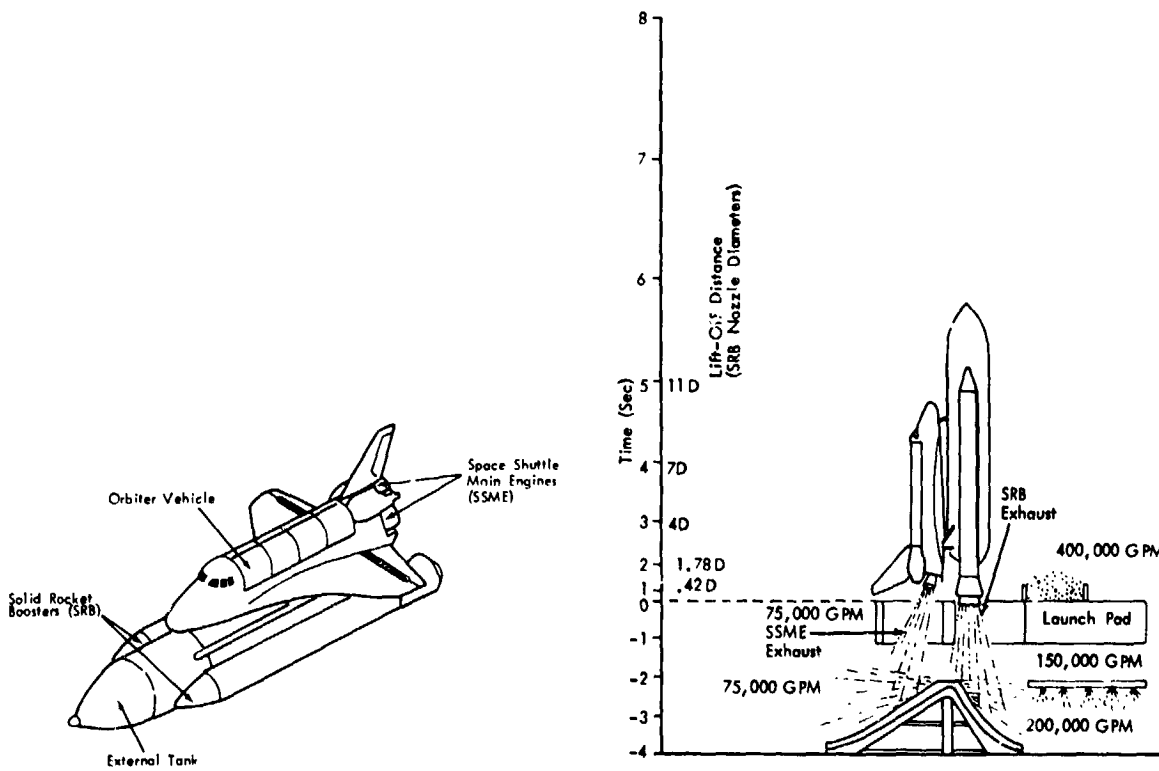Fig. 1 — Chronological development of the analytical model



Fig. 2 — Space Shuttle configuration at lift-off



Fig. 3 — Space Shuttle Vehicle at lift-off
(showing noise suppression water flow rates)

6

structures are the fuselage sidewall and bottom panels and the payload by doors. The sidewall panels are flat, the lower part being covered by the wing structure. The bottom panels and payload bay doors are curved, although the radius of curvature for the bottom is large. The payload bay defined by the mid-fuselage structure is approximately 18.4 m long, 5.3 m wide and 6.1 m high.
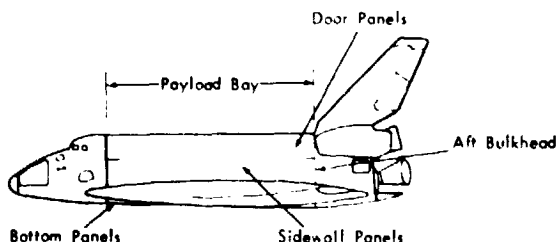


Fig. 4 — Space Shuttle Orbiter Vehicle showing mid-fuselage structure

Most of the mid-fuselage structure is of the aluminum skin-stringer-frame construction. The main exceptions are the payload bay doors which are honeycomb structures with a Nomex core and graphite epoxy face sheets and ring stiffeners. The exterior surfaces of the mid-fuselage structure are protected from heat loads during reentry by a Thermal Protection System (TPS) which varies in composition from the bottom of the fuselage to the top, according to the variation in predicted temperatures. A description of the TPS can be found, for example, in [12]. Additional thermal protection is provided for the payload by placing Thermal Control System (TCS) material on the inside of the payload bay.

## 3.0 ANALYTICAL ACOUSTIC MODEL FOR PAYLOAD BAY

The analytical model has been developed to allow the prediction of space-averaged sound pressure levels in the pay-load bay of the Space Shuttle Orbiter Vehicle. The model provides a physical basis for estimating the interior sound field when the payload bay is empty and when a payload is present. In the latter case, the region around the payload is divided into a series of subvolumes.

Structural characteristics of the shuttle mid-fuselage are described in a relatively simple manner as is described in the following section, so that acoustic power flow through the structure can be estimated. Acoustic absorption prop-erties of the interior walls of the bay and the exterior sur-faces of the payload are included in the determination of the payload bay sound levels.

In the present stage of development, the output of the analytical model consists of space-averaged, one-third octave band sound pressure levels or the frequency range 31.5 Hz to 4,000 Hz. One spectrum is associated with the empty bay, and one spectrum with each of the subvolumes surrounding a given payload.

The basic concept of the analytical model is that of acoustic power balance. This concept is formulated as a series of power balance equations which relate acoustic power transmitted into and out of a volume with power dissipated within that volume. The analysis considers first the case of a single rectangular cavity which accepts acoustic power from the exterior space. The cavity can be allowed some modifica-tion to the boundaries to represent curvature of the structure or payload. Furthermore, the single cavity can be broken down into a series of interconnecting subvolumes which surround a given payload.

The various steps which constitute the analytical model are shown in the flow diagram in Fig. 5. The first steps involve the response of the structure to the external pressure field. These are followed by several steps which calculate the acoustic power radiating into the cavities.

At this stage, the frequency range is divided into low and high frequency segments, which are determined by the acoustic modal content of the cavity. Finally, net power flow is equated to the dissipation provided by the acoustic absorp-tion in the cavity.

The development of the acoustic power flow relation-ships for the empty bay and the bay with payload, formed the central core of the analytical modeling effort for the Space Shuttle. This application of the power flow concept to noise transmission into an aerospace vehicle constitutes a new approach to the problem of predicting vehicle interior noise levels, and the results show that the concept provides a very useful tool.

Various assumptions and approximations are incorpo-rated in the development and application of the analytical model. These simplifications are introduced in order to make the model into an engineering tool which can be used with an available digital computer. Some of the more important assumptions are identified in the following discussion.

### 3.1 Structural Response

In order to calculate structural response to the external acoustic field, the mid-fuselage is first divided into six struc-tural regions which are determined on the basis of structural similarity and acoustic pressure level. The payload bay door, sidewall, bottom panels and aft bulkhead are each considered separately. The forward bulkhead is omitted since there is negligible acoustic power inflow through this structure, the noise levels in the crew compartment being relatively low. The doors and aft bulkhead are each considered as single units, whereas the sidewall and bulkhead are each divided into fore and aft regions on the basis of different structural make-up. The regions are shown in Fig. 6, which also shows the region on the sidewall which is "masked" by the wing structure. The acoustic power transmission through this masked area is assumed, in the analytical model, to be negli-gible.

The analytical model contains two alternative ap-proaches to the calculation of the dynamic characteristics (resonance frequency, mode shape and modal density) of the payload bay structure. For most modes it is assumed that the

**OPERATION**

**INPUTS**

Select Structural Representation

Structural Properties and Dimensions → Calculate Resonance Frequencies and Classify Modes

Calculate Modal Densities and Radiation Efficiencies

Excitation SPL and Correlation → Calculate Joint Acceptances

Payload Configuration → Select Subvolumes

Determine Dimensions and Interconnecting Areas

Determine High and Low Frequency Ranges

LOW FREQUENCY     HIGH FREQUENCY

Calculate Internal Coupling Factors

Calculate Power Into Cavities     Calculate Power Into Cavities

Formulate Power Balance Equation → Absorption → Formulate Power Balance Equation
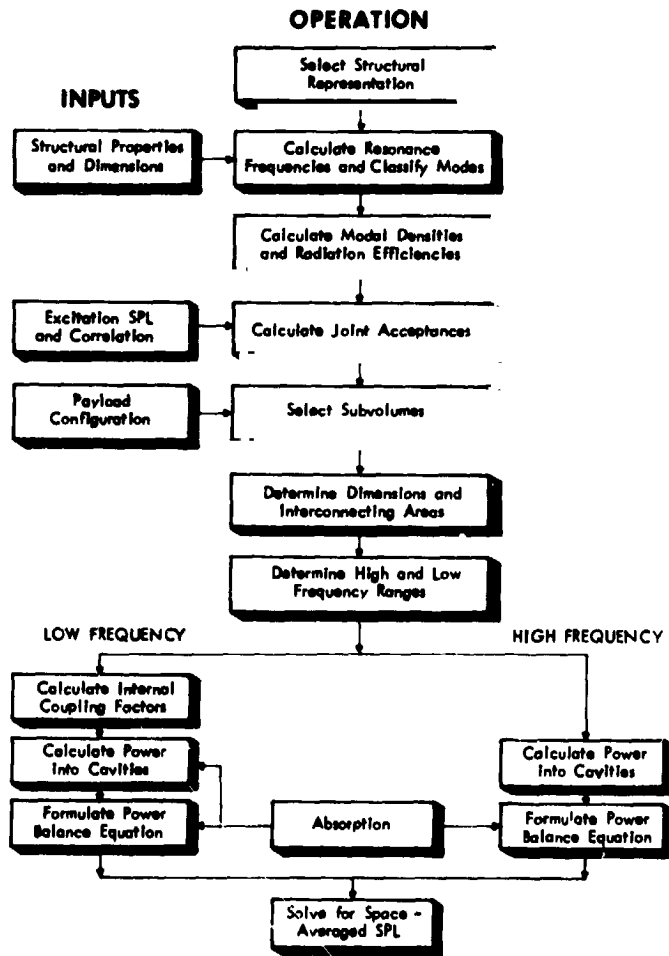
Solve for Space - Averaged SPL

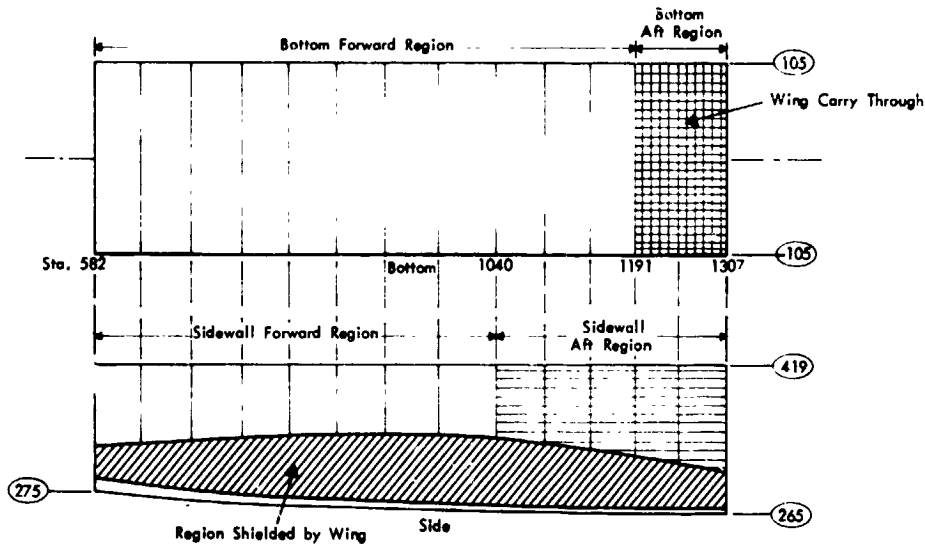Fig. 5 — Flow diagram for prediction method

8

Fig. 6 — Panel arrangement on bottom and sidewall of payload bay
showing separate regions used in analytical model

structure, including ring frames and other stiffeners, can be
represented by equivalent single orthotropic plates, with
simply-supported boundary conditions. Resonance fre-
quencies are then calculated using the usual closed-form
equations. Unfortunately the accuracy of this approach
decreases as mode order decreases, since the boundary condi-
tions become more critical. Thus, where possible, an alterna-
tive approach is followed at low frequencies whereby the
analytical model utilizes resonance frequencies and mode
shapes which were calculated using finite element analysis
of the orbiter mid-fuselage structure. Data from the finite
element analyses were supplied by Rockwell International,
and are based on calculations associated with ground vibra-
tion tests. The upper frequency limits of the finite element
analyses are restricted by the large computational require-
ments required for higher order modes.

The mode shapes from the finite element analyses are
simplified in shape into sinusoidal forms for use in the pay-
load bay acoustic model, the sine wave being assumed to
exist over only that part of the structure for which the mode
is active. Examples of two modes calculated by finite element
analysis for the bottom structure are shown in Fig. 7. The
same approach was used for the aft bulkhead and a similar
method is proposed for the sidewall. At the present time,
there is no low frequency representation of the sidewall in
the analytical model — the model assumes that there is no
acoustic power flow through that structure at low fre-
quencies.

Structural responses to the exterior acoustic pressures is
expressed in terms of panel joint acceptance functions which
quantify the coupling between the predicted structural mode
shapes and the spatial correlation characteristics of the
random excitation field [3]. In calculating the structural
joint acceptances, it is assumed that the correlation proper-
ties of the exterior acoustic field can be represented analyt-
ically as exponentially — decaying cosines. This representa-
tion is discussed in more detail in Section 4.1.

## 3.2 Structure Cavity Coupling

Having calculated the structural response, it is necessary
to couple it to the cavity in order to calculate the acoustic
power flow. Thus, some analytical representation of the
cavity is required. Since the cross-section of the payload
bay is essentially rectangular in shape, with some curvature
of the bottom and doors, the basic representation for a
receiving cavity is taken as a rectangular parallelepiped. Then,
the model has the capability of allowing each surface of the
cavity to be displaced to represent concave or convex curva-
ture, such as is illustrated in Fig. 8. The resonance freq-
uencies and mode shapes for the "deformed" cavity are
then calculated using a perturbation-type analysis. The final
step is the coupling of these modes to the structural modes
of the surrounding structure. A diagrammatic representation
for the case of a subvolume exposed to a structural mode
which exists over a distance greater than the length of the
cavity is shown in Fig. 9. Other combinations of structural
and cavity modal coupling are discussed in [3].

The present analytical model calculates acoustic power
flow in one-third octave bandwidths, and, within such a
bandwidth, calculations are performed for resonant and non-
resonant response of the structure and resonant response of
the subvolume. The resonant response refers to conditions
where the modes have their resonance frequencies in the
bandwidth of interest. Nonresonant structural response is
linked to the case where the structural mode has its reso-
nance frequency below the band of interest, i.e. the response
is mass-controlled. These limitations are adequate for the
frequency range above 31.5 Hz, but additional nonresonant
response (for structure and cavity) will have to be considered
for any low frequency extension to the analytical model.

The analytical model assumes that the structural and
cavity modes are weakly coupled. Under this assumption the
coupling can be calculated using the *in vacuo* panel
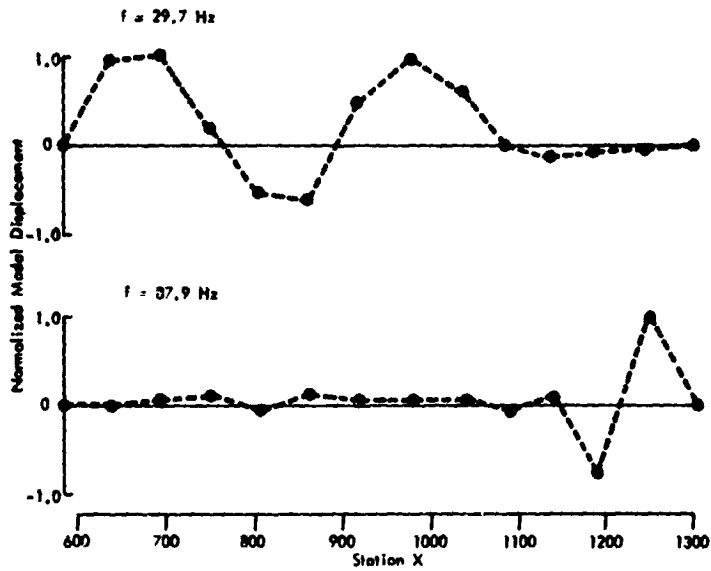resonance frequencies and the rigid wall resonant response of

9

Fig. 7 — Typical low frequency mode shapes for bottom structure,
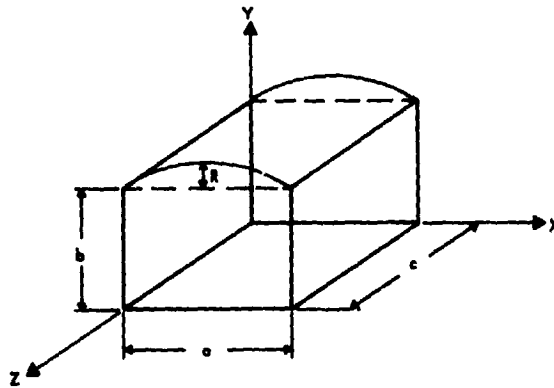predicted by Rockwell International (Y = 0)



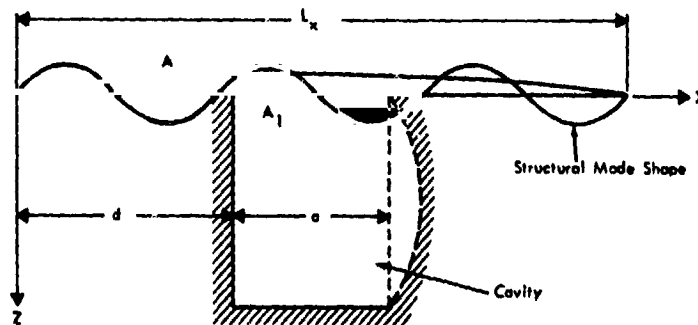Fig. 8 — Deformed parallelepiped representation for
payload bay volumes



Fig. 9 — Coupling between structure and subvolume when structure
mode extends beyond subvolume

10

the cavity. Mathematically, this means that the acoustic power flow between a structural mode and a cavity mode can be calculated without including the interaction with any other mode. It should be emphasized, however, that the assumption of weak coupling in no way excludes "well-coupled" modes i.e., structural and cavity modes with resonance frequencies closely-spaced relative to the modal bandwidth.

It is indicated in Fig. 5 that the coupling of the structural and cavity modes is performed in either low or high frequency regimes. In the low frequency regime, which contains frequency bands with few cavity modes, the coupling calculations are performed mode-by-mode. At higher frequencies where there are a large number of cavity modes in a given bay, the coupling is performed using methods similar to those of statistical energy analysis.

### 3.3 Acoustical Absorption

The final step in the calculation of the space-average sound levels is the equating of the net inflowing acoustic power to the dissipation within the cavity. This dissipation occurs because of absorption of the sound by the thermal control material, the payload, and the mid-fuselage structure.

The absorbing surfaces are assumed to be locally — reacting, so that the acoustic impedance at any point on a surface is not affected by the response at any other point on the surface.

### 3.4 Payload Effects

When a payload is placed in the bay, the single volume of the empty bay becomes a series of small subvolumes interconnected by openings of various shapes. Thus, the analyst is faced with the task of constructing a set of subvolumes which represent the regions around the payload and which have fairly well defined boundaries that can be assumed to be capable of supporting standing wave systems. The analytical model then considers each subvolume in the same manner as for the empty bay. This means that the subvolume is assumed to be basically rectangular in shape, with curvature of one or more bounding surfaces. In addition it is assumed that from an acoustical standpoint, the interconnecting openings can be represented to sufficient accuracy, by impedance functions for rectangular or circular pistons, when these functions are weighted to account for average mode excitation. In its present form the analytical model assumes that acoustic energy from subvolume modes resonant in a given frequency band is accepted in a connected subvolume only by modes resonant in the same frequency band.

An example of the breakdown of the payload bay into subvolumes is shown in Figure 10 where the payload is an approximation to the Spacelab Configuration 2. Other examples can be found in [3] and [7]. Several types of subvolume can be identified in Fig. 10. Subvolume 1 extends the full height of the bay from door to bottom, and contains

a relatively small volume of payload. Subvolumes 4 and 5 have no payload except for the empty pallets which form the lower surfaces of the subvolumes and shield the subvolumes from the bottom panels of the mid-fuselage. In contrast, subvolume 3 is shielded from the door by the pallets. Subvolume 2 is also shielded from the door, but, this time the intervening body is the large-diameter section of the payload. Subvolume 6 is a region above a payload on a pallet and, finally, subvolume 7 is an annular-type region around the upper part of the Spacelab. All the subvolumes are connected by openings around the payloads and pallets.
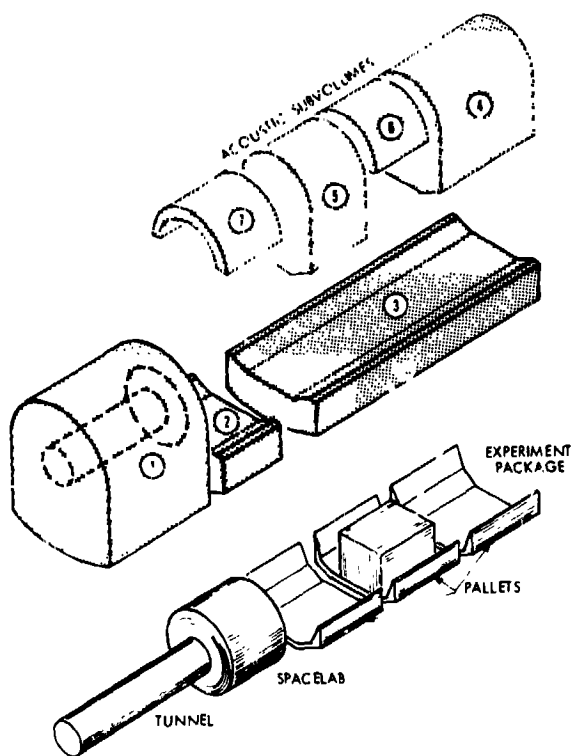


Fig. 10 — Spacelab Configuration 2 payload showing idealization of subvolumes for analytical model

Subvolumes 1, 4 and 5 have well-defined modal characteristics as they have reflecting surfaces at all boundaries. Subvolumes 2 and 3 are less well-defined because of the absence of reflecting surfaces at some of the fore and aft boundaries. Finally, subvolumes 6 and 7 are the most difficult to model acoustically because there are no reflective surfaces at some of the boundaries and also, the cavities have small dimensions in one or more directions. As a result of the latter property, subvolumes 6 and 7 have very few modes at low frequencies. In an attempt to overcome this problem the analytical model allows subvolumes such as 6 and 7 to be represented as "coupling nodes" which do not accept acoustic power from the exterior of the payload bay. These "nodes" act solely as transmitters of acoustic power from one subvolume to another.

## 4.0 EMPIRICAL INPUTS

The analytical model requires certain information which has to be acquired from experimental investigation since the data cannot be determined from purely analytical reasoning. This information includes spectral and correlation data for the external acoustic field, damping coefficients or loss factors for the mid-fuselage structure, and acoustic absorption coefficients for the payload and payload bay surfaces. These data were obtained from various sources, as is described in the following sections.

### 4.1 External Pressure Field

In order to calculate the response of the mid-fuselage structure to the external acoustic pressure field it is necessary to know the pressure spectrum level and the associate correlation characteristics. Calculation of these parameters from first principles is not a feasible task, and use has to be made of the limited amount of applicable experimental data. One important source of such information for the space shuttle vehicle is the test series performed at NASA Marshall Space Flight Center to explore exhaust noise control methods [13].

The NASA tests were performed on a 6.4% scale model during simulated lift-off conditions. Measurements of the surface pressure fluctuations were made at a number of microphone locations on the payload bay door, and

sidewall and bottom panels. Measurements were made for several noise control approaches and the data taken for use in the analytical model are associated with the water — injection noise control method selected for full-scale lift-off operations.

One-third octave band spectra from the model scale tests were scaled to full-scale conditions, and the levels were space-averaged for each of the six structural regions used in the analytical model. The resulting spectra, and their associated structural regions, are given in Fig. 11. It is seen that the spectra are similar in shape and level for the doors, sidewall (fore and aft) and forward bottom regions. The aft bottom region presents an acoustic "hot-spot" region, while the sound field on the aft bulkhead has a signficiantly different spectrum shape.

Correlation properties of the acoustic field could be obtained from the 6.4% tests onlt for the longitudinal direction, since microphone pairings did not provide circumferential correlation data. For use in the analytical model, the correlation characteristics were determined in terms of coherence and phase velocity. The coherence function was represented as an inverse exponential function in order to simplify the formulation of the model. This requirement was rather difficult to satisfy in the test data, as can be seen in Fig. 12, which shows a typical measured coherence spectrum, with an inverse exponential curve superimposed.



Fig. 11 — External acoustic field used in analytical model for different structural regions

12

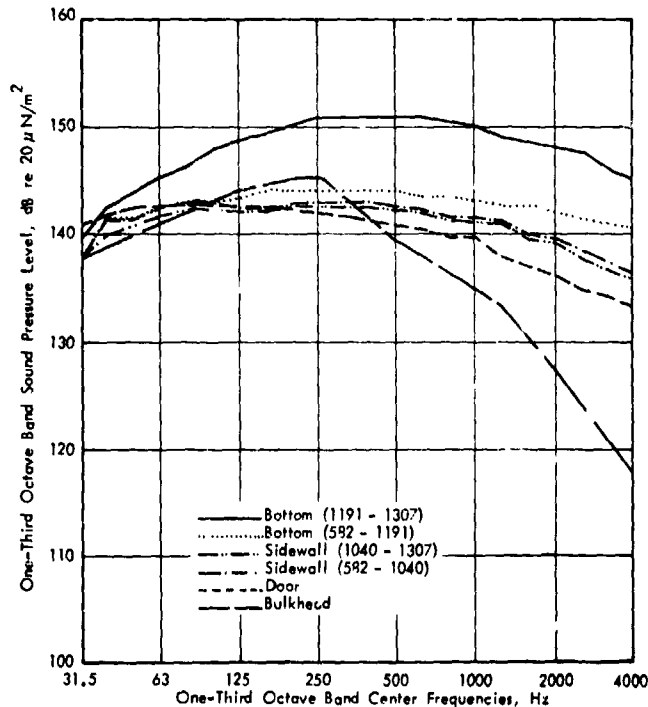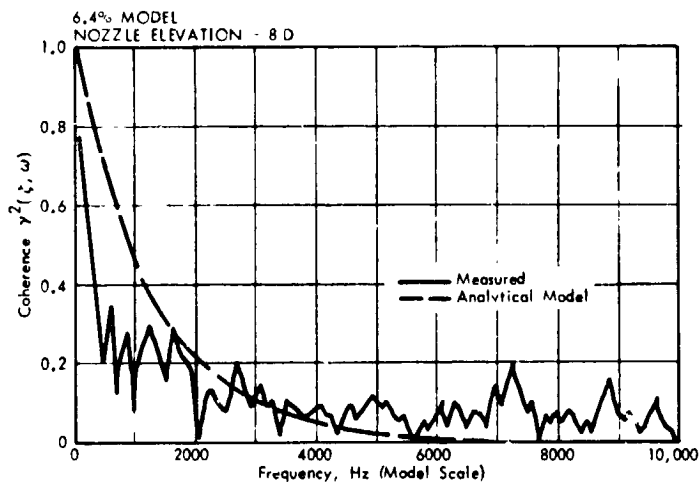6.4% MODEL
NOZZLE ELEVATION - 8 D

Fig. 12 — Comparison of measured and analytical representation of
external pressure coherence function, based on 6.4% model tests

The phase velocity was obtained from the phase angle
spectrum of the pressure cross-power spectral density func-
tion. It was found that, to a first approximation, the phase
velocity was independent of frequency and was supersonic
(indicative of acoustic waves at some non-zero angle of
incidence). Data were averaged for door, sidewall and bottom
microphone locations and the resulting average phase, or
trace, velocity in the longitudinal direction was calculated
to be $U_x = 1.12c$ where $r$ is the speed of sound. Then the
coherence function can be written in the form

$$\gamma^2(\xi,\omega) = \exp\left[-\frac{2k_x|\xi|}{31}\right]$$

where $\xi$ is the separation distance in the longitudinal direc-
tion and wavenumber $k_x = \omega/U_x$.

The corresponding relationship for the circumferen-
tial direction was more difficult to determine because of the
very small amount of appropriate data. After a review of the
available information, the circumferential coherence func-
tion was constructed from data presented by Cockburn and
Jolly [14], such that

$$\gamma^2(\zeta,\omega) = \exp\left[-\frac{2k_y|\zeta|}{3.2}\right]$$

with $k_y = \omega/U_y$ and $U_y = 2.62c$.

As these representations for the correlation characteris-
tics of the excitation field are based on a limited amount of
data, a more comprehensive set of data would be desirable
to remove some of the uncertainties, particularly for the
circumferential direction.

4.2 Structural Damping

Structural damping, expressed in terms of the loss
factor, $\eta$, by means of the complex Young's modulus
$E(1+i\eta)$, has an important role in the analytical model in
determining the acoustic power transmitted by structural

modes which are resonant in the frequency band of interest.
Unfortunately, as is often the case in the prediction of
structural response, values of the loss factor are either
not known, or, if they are known, the values are not known
very accurately.

The damping of different types of aerospace structures
has been measured by several investigators and some of the
results are summarized in [15-17]. In many cases the data
were obtained from test specimen rather than complete
vehicles. Thus care has to be taken in interpreting the
results. Measurements by Hay [15] on riveted structures
with machined skins and viscoelastic sealants show loss
factors in the range 0.004 to 0.029, with a mean value of
0.012. Data from measurements on complete airplane fuse-
lage structures give loss factors in the range of 0.008 to 0.110
with a mean of 0.038. Measurements on spacecraft structures
[17] show loss factors of 0.040 to 0.130 with a mean of
0.083. However these latter data probably refer to low-
order overall modes of the spacecraft so that the damping
provided by various attachments becomes significant.

In the case of the Space Shuttle mid-fuselage, the
structure has TPS tiles attached to the external surfaces,
and the door is graphite-epoxy construction rather than
aluminum. The influence of the TPS tiles has been measured
on small structural samples Rucker and Mixon [18] and by
Rockwell International. The data are summarized in Fig. 13.
Rucker and Mixson bonded 5.8 cm-thick selica tiles to a
0.4 cm-thick Nomex felt strain-isolator pad, which in turn
was bonded to an aluminum panel with stiffeners. The tiles
increased the damping from an average of 0.006 to 0.015.
Unpublished data from Rockwell International tests show
higher loss factors for the structure and tiles, with values in
the range of 0.03 to 0.18. The average value is 0.06.

Turning to the case of graphite-epoxy honeycomb door
panels, there is a much smaller amount of data. Measure-
ments for fiber-reinforced plates show a wide scatter of
results, as shown in [3] with an average value of about 0.012.
The trend with frequency is by no means clear. Loss factors

13

Loss Factor, $\eta$

$10^{-1}$

Average

$\eta \propto 1/f$

$10^{-2}$

O    Without Tile
●    With Tile      } [18]
▧    With Tile  }  Rockwell
                    (Unpub-
                    lished)

$10^{-3}$

10    50    100    500    1000

Frequency, Hz
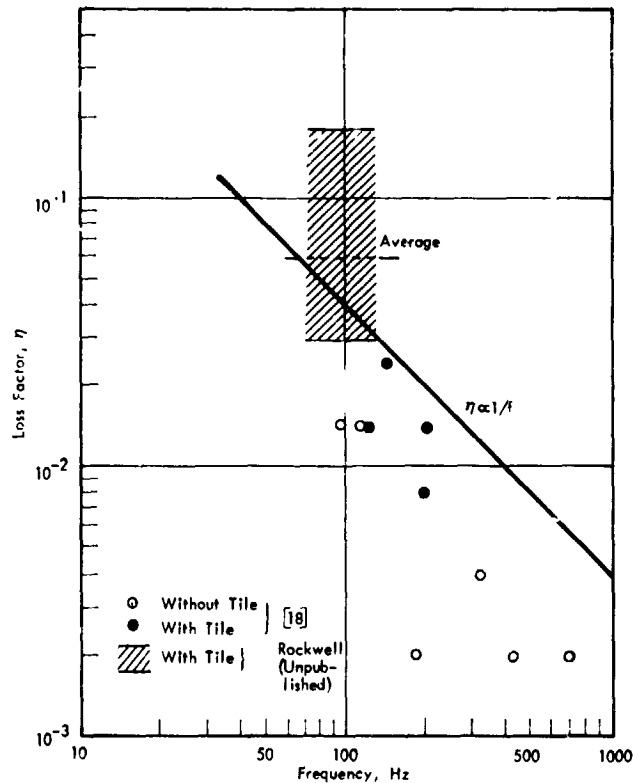
Fig. 13 — Damping of shuttle fuselage structure
with and without TPS tiles

for honeycomb panels with fiber reinforcement have been measured by Soovere [19] and Bert et al [20] and the results are plotted in Fig. 14. The mean loss factor is 0.031 but the value is heavily weighted by the high loss factors at low mode orders.

These wide ranges of values make it very difficult to pick representative values for the analytical model. Furthermore, it is even more difficult to determine a suitable frequency dependency. Initial forms for the analytical model assumed that the damping was independent of frequency but later validation tests on OV 101 suggested that a more appropriate damping representation would be a loss factor which was inversely proportional to frequency. This representation was anchored to loss factors at 100 Hz of 0.04 for the aluminum sidewall and bottom panels and 0.02 for the payload bay door. These frequency — dependent representations are shown in Figs. 13 and 14. Although the current representation does appear to be adequate for the frequency range of 31.5 to 4000 Hz associated with the present analytical model, it has the disadvantage that it implies that the loss factors are high at lower frequencies. As this is unlikely to occur, some modification will be necessary when the analytical model is extended to lower frequencies.

4.3  Acoustic Absorption Coefficients

All the surfaces in the payload bay provide some absorption of the acoustic field, even if the values of the absorption coefficient are small for surfaces such as the bare aluminum panels. Several different types of surface are present in the payload bay and estimates of the appropriate acoustic absorption coefficients were obtained from the small amount of available experimental data.

Unpublished measurements by the Lockheed Missiles and Space Company on various shrouded and unshrouded spacecraft give absorption coefficients of 0.05 to 0.30 with a mean of 0.175. As the data appeared to be essentially independent of frequency, it was assumed in the analytical model that the value of 0.175 was valid for all frequencies.

The door itself is not exposed directly to the payload bay, because of the presence of the radiator panels, which are somewhat similar in construction to a spacecraft. Thus an absorption coefficient of 0.1, which is at the low end of the range of the Lockheed test data, was assigned to the radiator/door combination. An absorption coefficient of 0.05 was assumed for the bare aluminum structure of the aft bulkhead, but higher values were assigned to the sidewall and bottom panels to account for the TCS material. On the basis of tests on TCS samples, absorption coefficient spectra were determined with values ranging from a minimum of 0.05 at low frequencies to a maximum of 0.62 at frequencies in the neighborhood of 500 Hz. Due allowance was made for cases where the TCS material was placed directly adjacent to the structural panels, and where there was a gap between the material and the structure. Detailed values of the absorption coefficient are listed in [3].

14
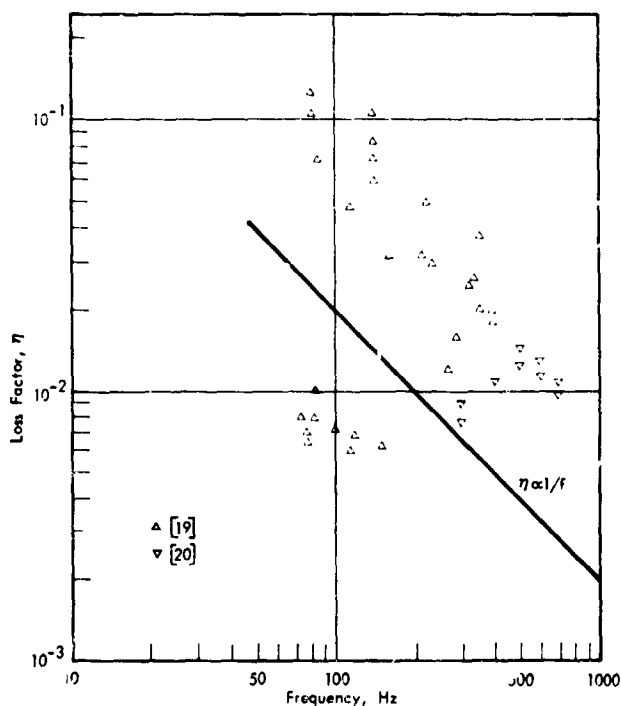
Fig. 14 — Damping of honeycomb structures with
fiber-reinforced face sheets

## 5.0 VALIDATION TESTS: EMTPY BAY

Two test series have been performed in order to obtain
empty bay acoustic data which could be used to validate the
analytical model, or to provide empirical data which could be
used in the model data input. Both tests involved the use
of Orbiter Vehicle, OV 101, the first test being performed
while the vehicle was still in the assembly area at the
Rockwell International facility in Palmdale, California
[8,11], and the second at NASA Dryden Flight Research
Center at Edwards Air Force Base, California [8,9,11].
Loudspeakers were used as noise sources in the first test
and the jet exhaust from two F-104 aircraft formed the
noise sources in the second test.

The OV 101 vehicle used in the tests was similar to
Orbiter OV 102 which will be used in the first launches,
except that there was no TCS material in the payload bay,
and the TPS material on the exterior was only a simulation.
Furthermore, there were no radiator panels attached to the
payload bay door.

### 5.1 Speaker Experiments

The test set-up for the speaker tests is shown in Fig. 15
Four microphones mounted on movable booms were used
to survey the sound levels in the bay. Other microphones
measured the external sound levels. Two types of excita-
tion field were used. A propagating field, generated by
placing five speakers aft of the orbiter and located symmet-
rically around its circumference, was used as a simulation of

the launch condition. Then a diffuse field, achieved by
mounting speakers in the corners of the assembly room, was
used for diagnostic purposes. Speakers were also placed
inside the payload bay for supplementary tests on noise
transmission through the structure, and absorption in the
bay.

### 5.2 Jet Noise Experiments

During the jet noise tests the OV 101 was mounted on
the transporter used to carry it by road from the Rockwell
International facility in Palmdale, California to Edwards
Air Force Base. Two F-104 aircraft used as noise sources
were positioned to the rear of the OV 101 as shown diagram-
matically in Fig. 16 and in the photograph of Fig. 17. Tests
were performed with the engine nozzles of the F-104 air-
craft at either 30.5 m or 76 m aft of the orbiter vehicle,
and all the tests were performed during the night of 31
January - 1 February 1977.

Microphones were located on the exterior of the OV
101 (Fig. 18) to measure the sound level and correlaton
characteristics of the acoustic field from the jet exhausts.
Other microphones were located in the payload bay, and
six accelerometers were attached to the midfuselage struc-
ture. Speakers were placed in the bay for acoustics absorp-
tion measurements.

Noise levels were measured outside the payload bay,
and the values used as data input for the analytical model.
The interior noise levels predicted by the model were then

Fig. 15 — Microphone and internal speaker locations for OV101 speaker experiments

Fig. 16 — Positions of OV101 and F-104 aircraft for jet noise tests



Fig. 17 — Orbiter vehicle OV101 and F-104 aircraft for jet noise tests
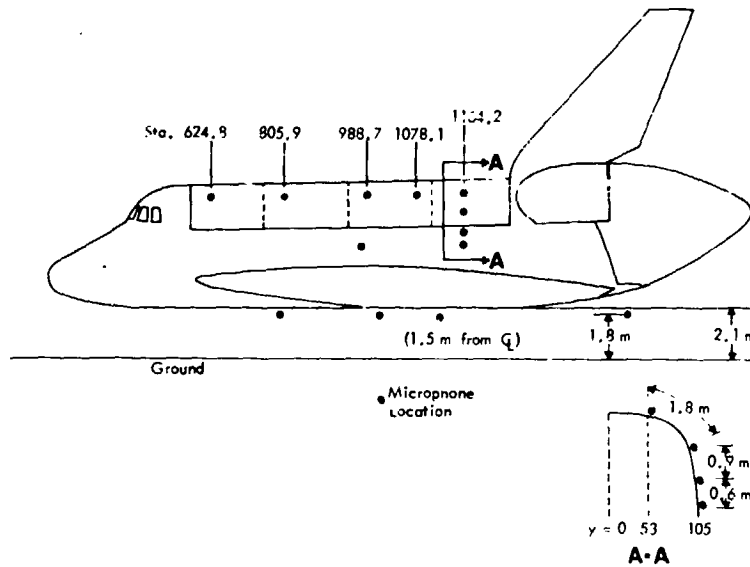
Fig. 18 — Exterior microphone locations on OV101 for jet noise tests

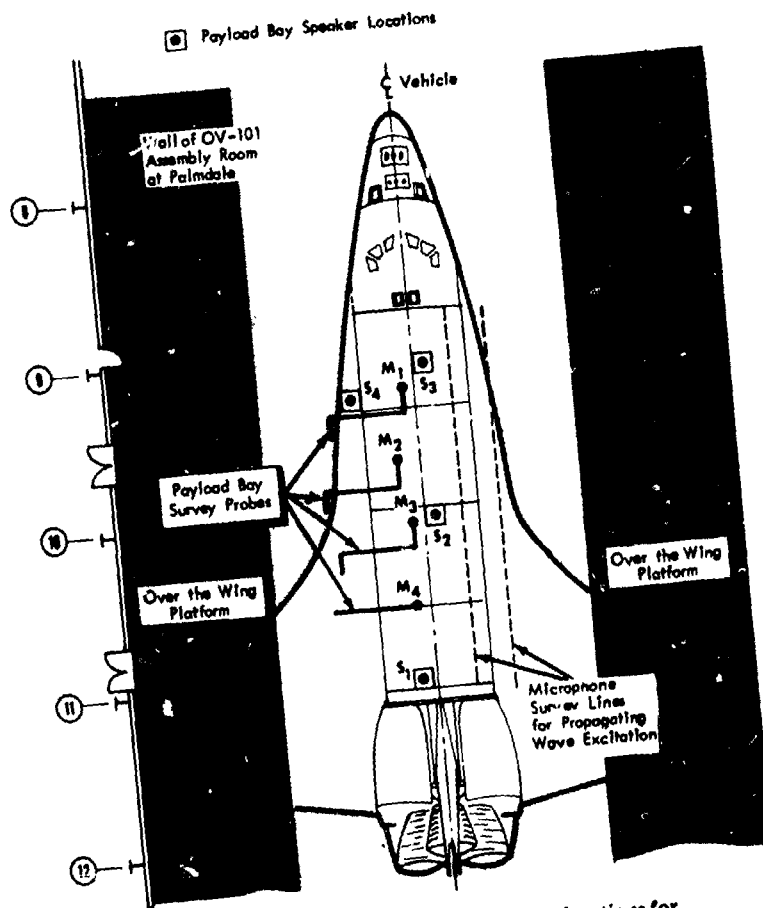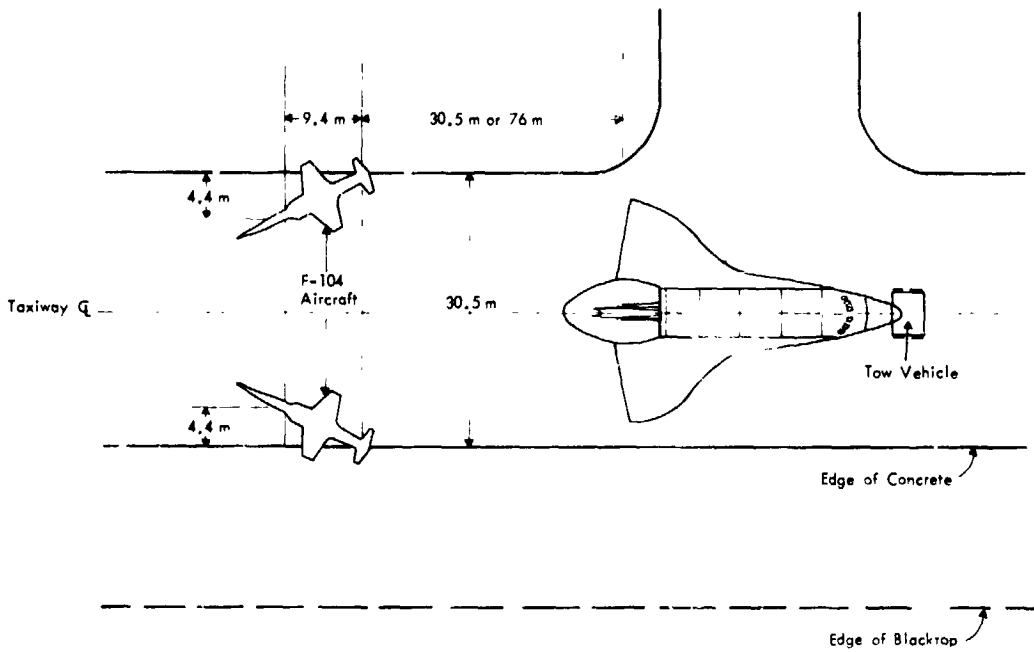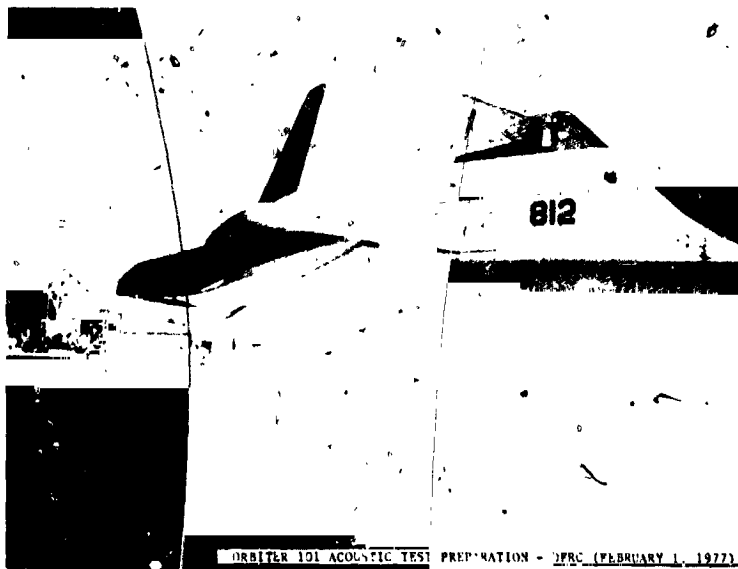compared with measured values. Sound pressure spectra measured inside and outside the OV 101 test vehicle are presented in Fig. 19.

### 5.3 Analytical Model Modifications

As a result of the OV 101 tests, two significant modifications were made to the analytical model to make it more representative of the orbiter vehicle. One modification was associated with the modeling of the payload bay doors for the calculation of the joint acceptances, and the other modification concerned the representation of structural damping. The two changes influenced the accuracy of the model in the mid to high frequency ranges.

In the initial representation of the payload bay doors, a low frequency model had been used for frequencies below the fundamental frequency of a door panel and a high frequency model had been used above this fundamental frequency. The door was represented as an equivalent orthotropic panel in both frequency regimes but the circumferential frames were included in the model only at the low frequency. The frames were excluded from the high frequency model on the assumption that they did not influence the response of the individual panels on the door. In the light of the OV 101 results this assumption was modified to include the representation of the frames for higher frequency ranges.

As indicated in Section 4.2, the structural damping terms had been represented in the early analytical model under the assumption that the loss factor was independent of frequency. This assumption was used because the available data did not show any well defined trend with frequency. The data from the OV 101 tests indicated that a frequency — dependent loss factor was probably a more appropriate relationship, and the damping model was

modified to include loss factors inversely proportional to frequency.

As a result of the two modifications identified above, the sound levels predicted by the analytical model were increased at frequencies above 200 Hz., as is shown in Fig. 20. The analytical model had previously underpredicted in this frequency range.

Statistical evaluation of the analytical model was performed in terms of the differences between predicted and measured space-averaged payload bay sound levels for the OV 101 jet noise tests. The results were presented as mean values and 99% confidence intervals (or 1% level of significance band) for the differences. These confidence intervals were introduced because the measurements were made at only a limited number of discrete locations.

The bounds associated with the 99% confidence intervals can be interpreted in the following way: there is a 1% chance that the actual difference between the measured and predicted space average levels will lie outside the bounds. If a discrepancy between the predicted and measured levels falls outside the bounds, the discrepancy should be considered statistically significant (at the 1% level of significance). However, if the discrepancy falls inside the bounds, there is not adequate evidence to state that the measured and predicted results are not in good agreement. It is seen in Fig. 21 that the results from the OV 101 test lie within the 1% level of significance band, except for the one-third octave bands centered at 80 and 100 Hz.

### 6.0 VALIDATION TESTS: PAYLOAD EFFECTS

The analytical model predicts not only the sound levels in the empty bay, but also the sound levels in subvolumes surrounding a given payload. As the prediction of sound levels

18

Fig. 19 — Interior and exterior space-averaged sound pressure levels
measured on OV101 during jet noise tests.

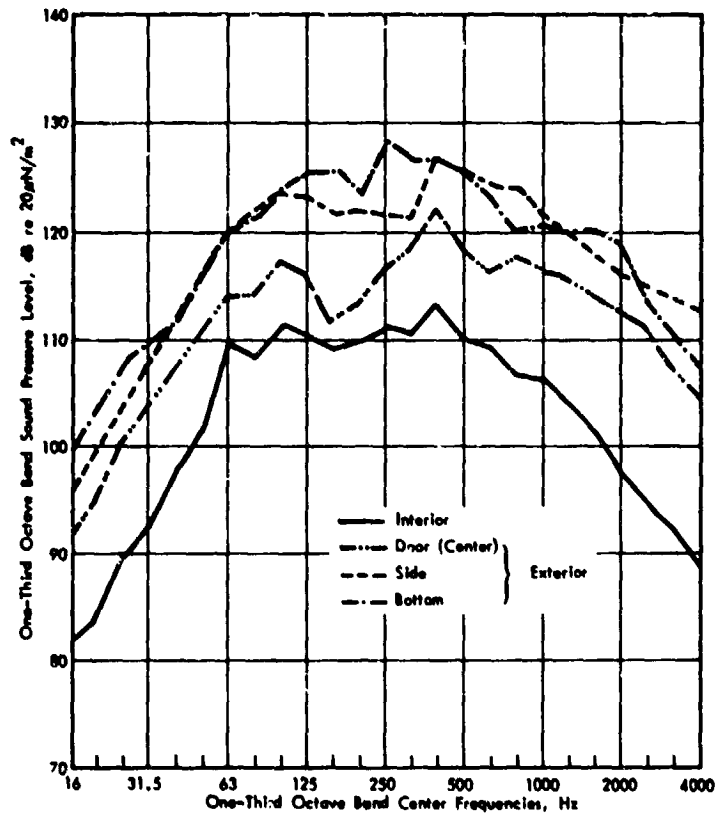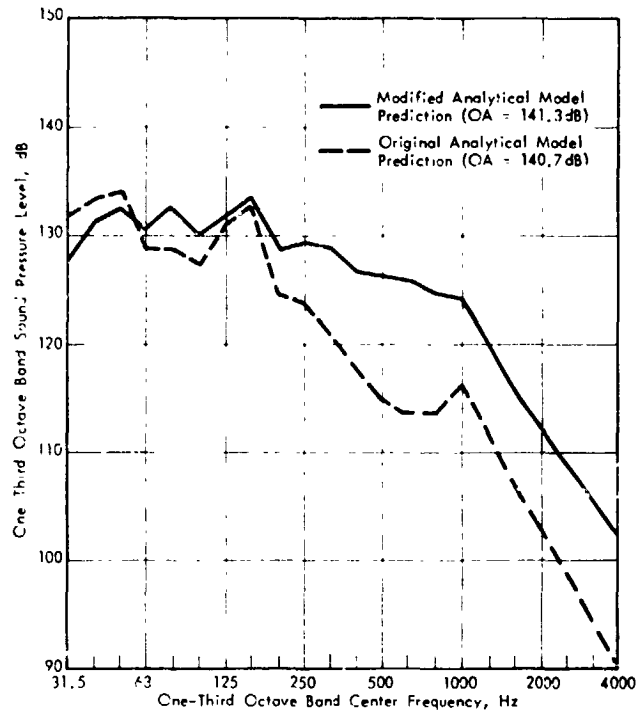Fig. 20 — Analytical model predictions of space-averaged sound
pressure levels in orbiter payload bay during launch
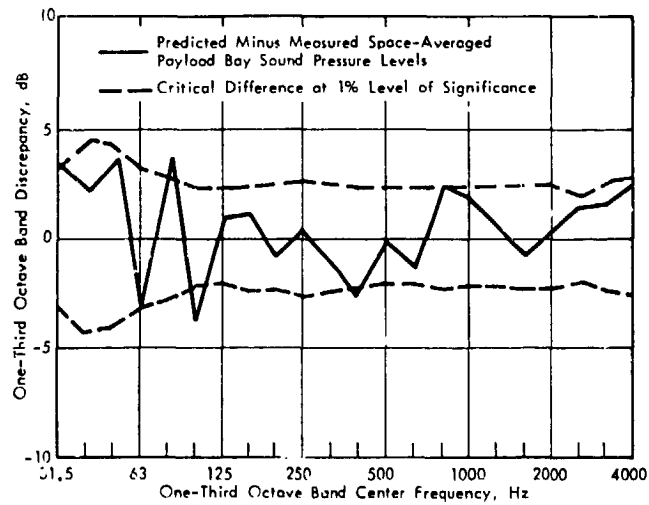(model modified as a result of OV101 tests)



Fig. 21 — Differences between predicted and measured payload
bay levels for OV101 jet noise tests

around payloads is probably the most important aspect of the analytical model, it is highly desirable to have some verification that the model is achieving this goal. Thus, two experimental investigations were conducted to validate the model for the case when a payload is present. The first investigation was performed at the beginning of 1976, early in the developmental stage of the analytical model, to provide initial guidelines for the model. Because a dynamic model was not available at that time, the payload bay was simulated by means of a one-fifth scale rigid model, and the acoustic power was introduced into the bay through a series of holes. Subsequently, a one-quarter scale flexible model became available and a series of tests was performed with a convected field on the exterior of the model orbiter vehicle.

By the time the one-quarter scale flexible model tests were performed the accuracy of the analytical model in predicting space-averaged sound levels for an empty payload bay had been established. Consequently it was adequate, when validating the analytical model for the case when a payload is present, to consider only the change in payload bay sound level when a payload is introduced. This simplification enables the constraints on the modeling of the exterior noise field and the orbiter vehicle dynamical characteristics to be relaxed to some extent. The approach of comparing payload bay sound levels with and without a payload present was followed also in the one-fifth scale rigid model tests.

## 6.1 One-Fifth Scale Model

The one-fifth scale rigid model simulated the interior contour of the payload bay of the Space Shuttle Orbiter Vehicle. The interior surface was constructed from 1.9 m thick plywood, stiffened on the exterior by 5.1 cm by 15.2 cm members. Scaled reproductions of the interior frames, wire trays, and pressurized bottles were included in the bay. In addition the sound absorption characteristics of the TCS material were simulated by the use of 0.6 cm thick foam with partially-open cells. The acoustic transmission characteristics (from inside to outside) of the full scale payload bay door were also represented by use of absorptive material [2].

Acoustic power was introduced into the payload bay by means of a series of hoses driven acoustically by eight loudspeakers. The hoses terminated in 1.3 cm diameter brass fittings which penetrated the plywood walls of the model. These fittings were plugged with steel wood to dampen the acoustic resonances in the tubes. Three payload configurations were represented by means of wooden models. The payloads were the Large Scale Telescope (LST) with Orbital Maneuvering System (OMS) kit, Spacelab Configuration No 2 (Fig. 10); and the USAF Defense Support Program Satellite with Interim Upper Stage (DSP/IUS). The Spacelab Configuration 2 model is shown in the one-fifth scale payload bay in Fig. 22.

## 6.2 One-Quarter Scale Model

The lack of dynamic similarity between the one-fifth scale model and the mid-fuselage of the orbiter vehicle left some uncertainty in the comparison between scale model and analytical results. However, an opportunity to reduce the uncertainty was provided by the availability in 1978 of the one-quarter-scale flexible model of the Space Shuttle vehicle. This model was constructed by Rockwell International for low frequency dynamic experiments related to problems such as flutter and "pogo", and was designed to give an accurately-scaled replica of the appropriate full-scale dynamic characteristics. Although this does not necessarily mean that the dynamic characteristics associated with noise transmission are scaled with the same high degree of accuracy, it is believed that the accuracy is sufficient for the measurement of changes in payload bay sound levels when a payload is introduced.

The one-quarter scale model is constructed mainly from riveted aluminum panels and stiffeners, as is the case for the full scale vehicle. However the model payload bay door is constructed from aluminum face sheets with a foam core, whereas the full scale door has graphite-epoxy face sheets and Nomex honeycomb core. Radiator panels were not installed on the door of the model, but weights were attached at appropriate locations on the door to represent the radiator weight distribution. The one-quarter scale model did not contain TCS material, so 0.64 cm foam was installed to simulate the acoustic absorption of the TCS material. For test purposes, the model orbiter vehicle was mounted on jacks and was located at a height of about 1.2 m above the floor in a high bay building. Figure 23 shows the model in position, with the payload bay doors open to show one of the test payloads.

Three payloads were selected for the study. One payload was the Spacelab Configuration No. 2 (Fig. 10) which had been used in one-fifth scale tests and in the analytical work. The other two model payloads, identified as Delta-D and Delta-L, were diagnostic payloads designed to study the effects of payload diameter and length, respectively. Side view sketches of the Spacelab and Delta-D payloads are shown in Fig. 24. The latter payload consisted of five circular cylinders with diameters equal to 10, 30, 60, 80 and 95% of the diameter of the available payload envelope.

The exterior sound field for these tests was generated by five loudspeakers located aft of the orbiter vehicle. The speakers were driven by independent random noise generators to produce grazing incidence acoustic wave excitation propagating forward along the orbiter vehicle, in a manner similar to that of the acoustic field anticipated from the five Space Shuttle engines during lift-off.

Noise levels were measured outside and inside the payload bay. The exterior sound field was measured in terms of level and correlation so that the actual excitation field

Fig. 22 — One-fifth scale model with spacelab payload
(end plates of payload bay removed)

Fig. 23 — One-quarter scale model with Delta-D payload

Forward
Bulkhead

Aft
Bulkhead

Tunnel

Spacelab

Instrument
Box

Forward
Pallet

Mid Pallet

Aft Pallet

(a) Spacelab Configuration 2 Model

Forward
Bulkhead

Aft
Bulkhead

30% dia.
cylinder

80% dia.
cylinder

60% dia.
cylinder

10% dia.

95% dia.
cylinder

Pallet
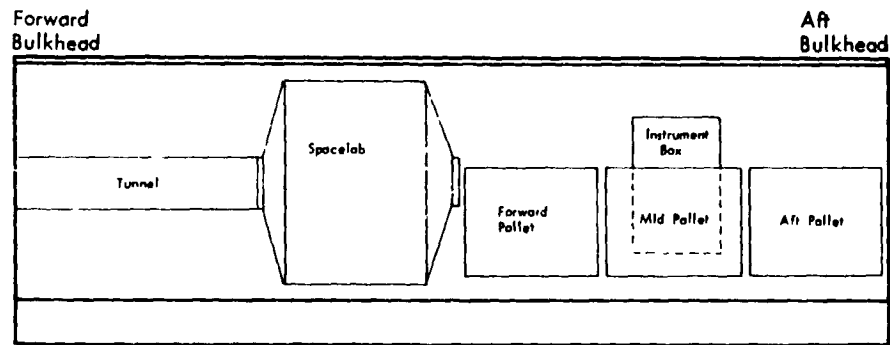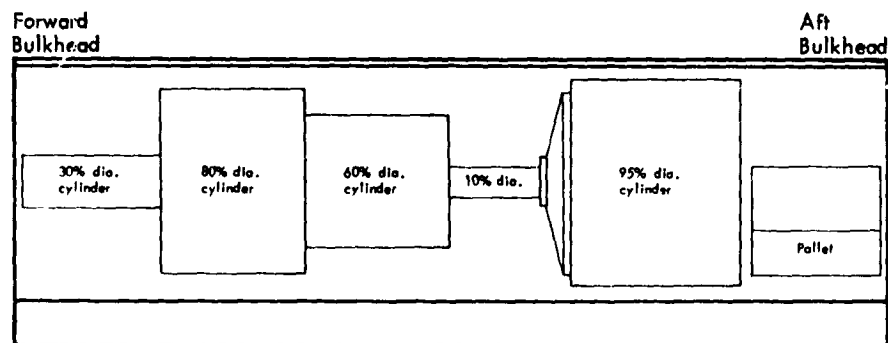
(b) Delta-D Diagnostic Model

Fig. 24 — Side Elevations of two one-quarter scale payload models

could be represented in the analytical model. Interior noise levels for the empty bay were measured at 42 locations and space-averaged values determined. These values were then compared with average levels measured in the subvolumes around the test payloads, in order to determine the influence of the payloads on the payload bay noise levels.

6.3 Experimental Trends

The payloads were chosen so that different approaches cculd be taken in defining the subvolume spaces in the pay-lo.id bay. These different approaches allow some form of diagnostic evaluation to be made of the analytical model, thereby validating the most suitable approach. For example, when the payload diameter is small, a subvolume is defined as extending all around the payload section, from the bottom of the bay to the door. As the payload diameter is ir ̲reased, a stage is reached at which the subvolume can no longer be considered as a single unit, but has to be divided into two subvolumes, one above and the other below the payload. Ultimately, as the diameter increases still further, the region above the payload becomes an annulus and it is difficult to envisage it as a subvolume with a well-defined modal structure. The analytical model has the capability of representing these annular subvolumes simply as "nodes" which transfer

acoustic power between connecting subvolumes but which do not accept acoustic power from outside the bay. The choice of representation for a subvolume can have a significant influence on the sound levels predicted for that subvolume.

As the goal of the model scale tests was the validation of the analytical model, measurements of sound levels around a giver  ̃: vload were made in such a manner that the data could be readily compared witn predictions. With this in mind, the following observations can be made regarding the data from the one-quarter and one-fifth scale tests.

a) The changes in sound level when a payload is introduced show large vari  ̃ ions from band to band at frequencies below 31.5 Hz (full scale).

b) Sound levels above large diameter payload sections are consistently higher than tl ɔse below.

c) Sound levels above large diameter payloads are consistently higher than those in the empty bay.

d) Sound levels around small diameter payloads tend to be slightly lower than those in the empty bay.

Typical spectra for changes in measured average sound levels are shown in Fig. 25. These spectra show the characteristics identified above.

## 6.4 Comparison with Analytical Model

Results of the analytical model were compared with measured data from both the one-fifth and one-quarter scale model tests. However, as the one-fifth scale tests provided mainly an interim approach in the model development, only the results from the one-quarter scale test will be discussed here.

In order to validate the analytical model by means of the one-quarter scale model tests, it was necessary to apply the analytical model to the specific test situation, rather than to the full-scale orbiter vehicle. Several test parameters required for the analysis were measured for data input, but others had to be assumed. Measured inputs included the exterior field and the acoustic absorption provided by the

simulated TCS material and the payload. One of the more troublesome assumptions was that of the structural damping of the model orbiter vehicle. Determination of structural damping is a problem often encountered in dynamics investigations. It was assumed eventually that the structural loss factor for all structural regions was given by $\eta = 2/f$. This compares with assumed values of 2/f for the full scale payload door and 4/f for the sidewall, bottom and aft bulkhead [3]. In other words, the damping for a given mode was assumed to be similar for full scale and model configurations.

Predicted and measured changes in payload bay noise levels were obtained from space-averaged levels in the empty bay and in the subvolume of interest when a payload is present. For the comparison between measurement and analysis the measured data were presented in sound level and the 99% confidence intervals for the change, in a manner similar to that discussed in Section 5.3 for the OV 101 tests.

Initial comparisons between measured and predicted changes in sound level associated with the introduction of a
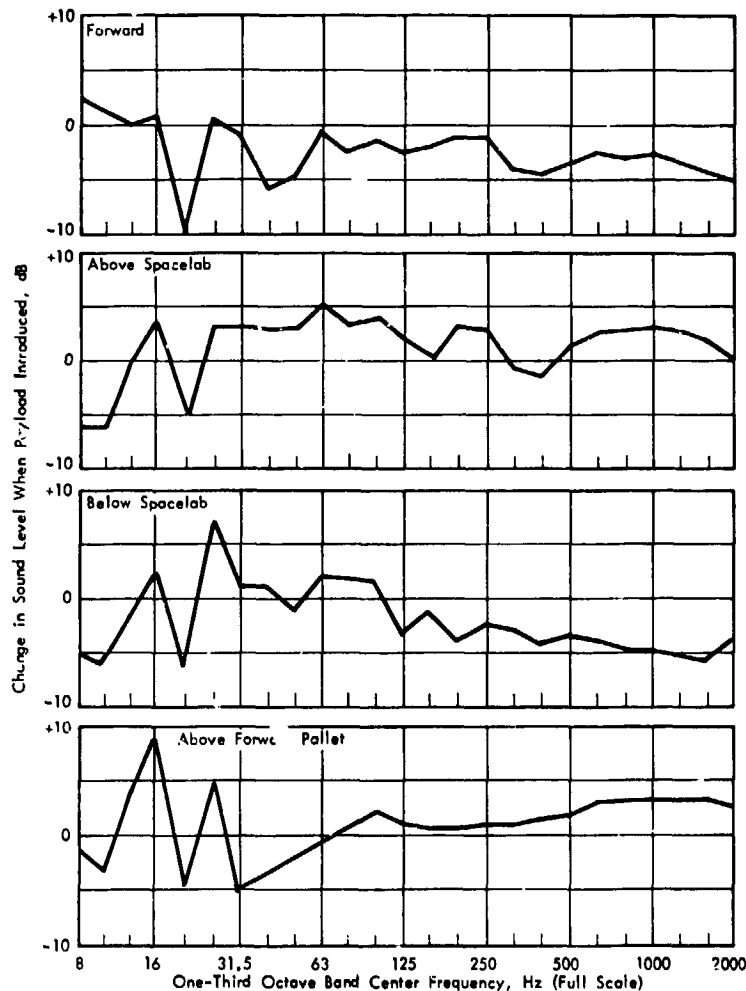


Fig. 25 — Measured change in payload bay sound levels when payload introduced (one-quarter scale model, spacelab configuration 2 payload)

25

payload indicated that the modeling of a subvolume as a connecting node was unsatisfactory. The agreement was much improved if the subvolume was modeled as other subvolumes, even though the analytical model in its present form was not strictly applicable to subvolumes such as nodes which have ill-defined boundaries with neighboring subvolumes.

The comparisons also showed that when the payload diameters was equal to, or greater than, 80% of the available payload diameter, the surrounding region in the payload bay should be considered as two subvolumes, one above and the other below the payload.

Figure 26 presents comparisons of experimental and analytical results for the change in sound level when a payload is inserted into the bay. The data are associated with the Delta-D payload and represent cases where there are no subvolumes modeled as nodes. The experimental data are presented in terms of the range of values bounded by the 99% confidence limits, as discussed earlier. The results show that the analytical model is reasonably accurate in predicting the average sound levels in a subvolume surrounding a payload. The accuracy is best for those subvolumes which are well-defined from the analytical modeling viewpoint and which have the payload bay door as one bounding surface. Poorest accuracy is associated with subvolumes which are formed below payloads and are difficult to model analytically.

One factor which seems to have a signficiant effect on the ability of the analytical model to predict noise levels in subvolumes below a payload is the absence of a representation for the response of the payload bay sidewall at frequencies below 200 Hz. This deficiency arose because of the unavailability of modal information for the sidewall at low frequencies. In its present form the analytical model assumes that there is no acoustic power flow through the sidewall in the low frequency range.
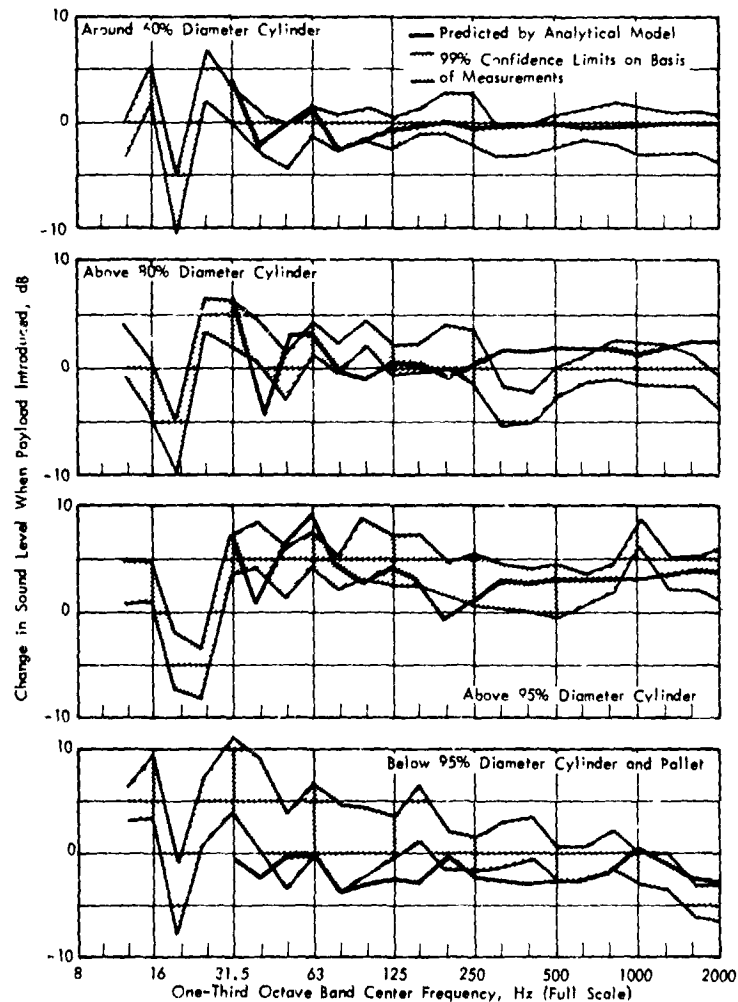


Fig. 26 — Comparison of predicted and measured changes in sound level when Delta-D payload installed in one-quarter scale test model

26

This comparison between experimental and analytical results covers the frequency range from 31.5 to 2000 Hz (full scale). Test data, however, were recorded for frequencies down to 12.5 Hz and the measurements will be available for future validation of a low frequency extension to the analytical model.

## 7.0 NOISE CONTROL APPROACHES

Consideration of noise control approaches formed a very small part of the overall program, but mention of this aspect of the work effort can be made as a brief aside to the general theme of this paper. The noise control study was conducted only as a part of the experimental investigation on the one-fifth scale rigid model. The study was not very successful in identifying highly effective noise control approaches, but the results did indicate that noise reductions could be achieved, particularly where control was required in a narrow frequency band.

Three concepts were evaluated. These were tuned absorbers, broadband absorbers, and mode disruptors. Tuned absorbers were introduced by installing material with a high flow resistance at modal pressure nodes, and broadband absortpion was achieved by the installation of large amounts of glass fiber blankets in the bottom of the payload bay. Finally, mode disruption was tested by the use of horizontal baffles along the centerline of the Large Scale Telescope and Spacelab payloads. Noise reductions of 1 to 5 dB were achieved in limited frequency ranges, the greatest reductions being associated with the horizontal baffles where strong vertical modes were disrupted.

## 8.0 COMPUTATION METHODS

### 8.1 General Approach

Two computation procedures have been developed from the analytical model. One method requires the use of a digital computer with fairly large storage capacity [5], whereas the other is a simple graphical approach [4] which makes use of results from the digital computer program.

The objective of each method is to determine the space-averaged sound levels in the subvolumes which surround a given payload at lift-off. The structural characteristics of the orbiter mid-fuselage and the correlation characteristics of the external acoustic pressure field are regarded as fixed inputs which are not available to the operator as variables. The excitation sound pressure levels can, however, be varied if need be. The main task to be accomplished by the user is the idealization of the payload of interest into several elements, each of which is surrounded by one or more well-defined subvolumes. The adjective "well-defined" is used here in the acoustical sense in that the subvolume should have surfaces which act as reflecting boundaries for acoustic waves in the subvolume, thereby generating fairly strong modal characteristics. The two procedures differ markedly in the computational effort involved but, by the same token, they also have large differences in the flexibility allowed to the user and the detail allowed in describing the payload. Consequently the resulting estimates for space-average

sound levels will be more accurate when obtained by means of the computer program than by the simplified method.

At the present time the two methods represent the development stage of the analytical model as it existed in mid-1977. That is to say, the methods do not include refinements in payload effect made as a result of the one-quarter scale model tests which have been analyzed only recently. Nor do they take into account nonresonant response of the cavities. This nonresonant response will be incorporated when the extension of the analytical model to lower frequencies has been completed. Finally, neither procedure includes low frequency transmission through the fuselage sidewall, since this item is not yet a part of the analytical model.

### 8.2 Computer Program

The analytical model has been developed into a computer program which can be used to calculate space-averaged sound levels in an empty payload bay, or in the bay with payload present. The objective of the computer program is to calculate the sound levels to which a given payload will be exposed to lift-off, and the main effort required of a user is the definition of the subvolumes which surround the payload when it is in the payload bay.

A very simplified flow diagram for the procedure is shown in Fig. 27. The computer program consists of a main program and a series of 13 subroutines which, among other things, calculate structural and volume resonance frequencies, structural joint acceptance functions, and coupling factors for the structure and subvolume. When a CDC-6600 computer is used, the total number of cards, excluding control cards is 2655, and computer storage required for the program and data is 257330 octal words. For IBM 360/370 series computers the storage required is 400,000 bytes. A microfiche listing of the program and subroutines is included as part of the software package provided for prospective users.

Two sets of input data are required for the program. One set describes most of the basic structural parameters required for the program, and the second set is associated mainly with the payload under consideration. The structural parameters for the mid-fuselage are fixed and are not available to the user for variation. Only the payload data cards can be selected by the user. The set of structural data parameters includes the response and acoustic radiation characteristics of the mid-fuselage structure including sidewall, bottom, payload bay doors and aft-bulkhead. The response characteristics include joint acceptances associated with the selected convective acoustic field and a diffuse acoustic field, mass-law transmission losses, and modal densities for each structural region.

A description of the data input required for the second set of data cards is given in the Computer User's Manual [5]. The excitation field is defined in terms of one-third octave band spectrum levels for the six structural regions of the mid-fuselage. Correlation characteristics are also input at this stage but they are used in a very limited manner in the main
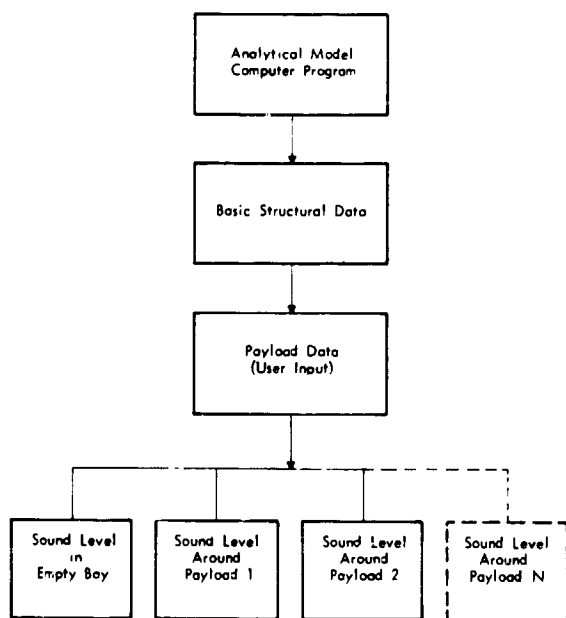
Fig. 27 — Simplified flow diagram for operation of
computer program

program. In any case the correlation characteristics have to
be identical to those used in preparing the structural data
input. Conse~··^ntly choice of correlation characteristics
is not open to the user except that diffuse field excitation
can be selected as opposed to a convected acoustic field.

The main effort required of the user is the idealiza-
tion of the payload into a series of elements, each of
which is surrounded by a well-defined subvolume. An
example of the breakdown of the interior space into a
series of subvolumes is given in Fig. 10. Each subvolume is
given a basic parallelepiped shape, and then any surface of
the parrallelepiped can be given single or double curvature
by specifying the displacement at the center of the surface.

In the present format of the computer program, each
subvolume has to be designated as being active or inactive.
Active subvolumes are those which are large enough to have
several resonance frequencies within a given frequency band
and thus can accept acoustic power from the exterior of the
bay. Inactive subvolumes have a paucity of resonanr . fre-
quencies, at least in the lower frequency bands, and, since
the present computer program is restricted to resonant
response of a subvolume for a given frequency band, the
subvolume cannot accept acoustic power from the exterior
field. Consequently inactive subvolumes act only to transfer
acoustic power between neighboring active subvolumes.

Calculation of the transfer of acoustic power between
subvolumes requires the specification of the location, shape
and dimensions of the connecting areas. These have to be
specified by the user for the particular idealization formed
to represent the payload. Also to be specified are the
absorbing areas and associated absorpttion coefficients for
the surfaces of each subvolume.

The output of the computer program gives the space-
averaged one-third octave band sound level spectrum for each
subvolume, in the frequency range from 31.5 Hz to 4000 Hz.
Calculations for lower frequency bands will be available when
the low frequency extension is complete. The calculated
sound levels result from resonant and nonresonant trans-
mission through the fuselage structure and the contributions
from each regime are identified separately in the computer
output.

## 8.3 Simplified Procedure

The simplified procedure was developed by converting
results obtained from the full computer program into a
graphical format which consists of three items — an exterior
sound pressure spectrum, an interior space-averaged sound
pressure spectrum for the empty bay, and the incremental
changes in spectrum level to account for the effects of a
payload.

The procedure allowed designers to make a first
estimate of the sound levels around a payload but, as
indicated earlier, the meth.,d suffered from certain disadvan-
tages which are not presented in the full computer program.
The simplified procedure was provided mainly as an interim
measure until the full computer program became generally
available. As the computer program is now in use by several
investigators, the simplified procedure has declined in use-
fulness, and further discussion is not warranted here.
Interested readers can refer to [4] for a detailed description
of the method.

## 9.0 MODEL IMPROVEMENTS

There are two obvious improvements which can be
made to the analytical model. One is the extension of the
model to lower frequencies which are still of importance in
determining payload response. The other improvement is the
inclusion of a dynamic model for the sidewall structure of
the payload bay at frequencies below 200 Hz.

The low frequency extension is currently under develop-
ment. In making the extension, consideration has to be given
to the possibility that a given frequency band may not
contain a resonant acoustic or structural mode. Thus the
model has to have provision for non-resonant acoustic
response of a subvolume and nonresonant vibrational re-
sponse of the structure. In the latter case the addition to the
analytical model consists only of stiffness-controlled re-
sponse, as mass-controlled response is already included in the
model. With the inclusion of non-resonant response of the
subvolume it should be possible to provide a more realistic
representation of the annular subvolumes which, under
some circumstances, have been considered as inactive sub-
volumes or connecting nodes, in the past.

It has been observed in earlier discussion that the
absence of a low frequency dynamic model for the side-
wall of the payload bay is probably responsible for the poor
agreement between measured and predicted sound levels
for subvolumes beneath payloaos. Inclusion of a sidewall
representation is dependent on obtaining an adequate
description of th. structural mode shapes and resonance

28

frequencies. These data were obtained for the bottom panels from finite element analyses performed by Rockwell International. A similar approach is proposed for the sidewall. For example, the mode shapes predicted by the finite element analysis will be approximated by sinusoidal forms so that existing joint acceptance formulations in the analytical model can be used to predict the sidewall response. It is anticipated that the low frequency sidewall model will be added to the analytical model for the payload bay acoustic environment during 1979.

## 10.0 CONCLUDING REMARKS

The discussion presented in the preceding sections has outlined the development of an analytical model for the prediction of sound levels in the payload bay of the Space Shuttle Orbiter Vehicle. The development has included both the formulation of the analytical model and its validation by means of model scale and full scale tests. Although the analytical model is not yet in its final and complete version, it is apparent that the systems — type approach used in the development effort has resulted in a prediction procedure which can be expected to give reliable estimates of payload bay sound levels, even when a payload is present. Furthermore the analytical model has the capability of being readily modified to include other excitations such as turbulent boundary layers and propeller near-field pressures, and to other aerospace vehicles. The analytical model is a significant step forward in the analysis of vehicle interior noise levels.

## ACKNOWLEDGMENTS

## REFERENCES

1. F. J. On, "Shuttle Orbiter Payload Bay Internal Acoustic Environment during Lift-off," NASA Report X-321-75-116, May 1975.

2. A. G. Piersol, P. E. Rentz, J. F. Wilby, "Space Shuttle Payload Bay Acoustics Prediction Study, Vol. I Problem Definition and Experiments," BBN Report 3286 Vol. I, December 1976.

3. L. D. Pope, J. F. Wilby, "Space Shuttle Payload Bay Acoustics Prediction Study, Vol. II Analytical Model," BBN Report 3286, Vol. II, December 1976.

4. J. F. Wilby, L. D. Pope, "Space Shuttle Payload Bay Acoustics Prediction Study, Vol. IIIA Manual for Simplified Prediction Procedure," BBN Report 3286, Vol. IIIA, August 1977.

5. L. D. Pope, "Space Shuttle Payload Bay Acoustics Prediction Study, Vol. IV Computer User's Manual," BBN Report 3286, Vol. IV, February 1977.

6. A. G. Piersol, L. D. Pope, J. F. Wilby, "Space Shuttle Payload Bay Acoustics Prediction Study, Vol. V. Verification of Analytical Model and Overview of Study," BBN Report 3286, Vol. V, August 1977.

7. A. G. Piersol, L. D. Pope, P. E. Rentz, E. G. Wilby, J. F. Wilby, "Space Shuttle Payload Bay Acoustics Prediction Study, Verification of Analytical Model and Overview of Study: Addendum," BBN Report 3286 Vol. V Addendum, October 1978.

8. A. G. Piersol, P. E. Rentz, "Assessment of the Space Shuttle Orbiter Payload Bay Noise Reduction Based upon OV 101 Acoustic Experiments," BBN Report 3300, September 1976.

9. A. G. Piersol, P. E. Rentz, "Prediction of Space Shuttle Orbiter Payload Bay Launch Acoustic Levels based upon OV 101 Acoustic Tests," BBN Report 3424, April 1977.

10. L. D. Pope, J. F. Wilby, "Band-Limited Power Flow into Enclosures," J. Acoust. Soc. Am. 62, 4, 906-911, October 1977.

11. A. G. Piersol, P. E. Rentz, "Experimental Studies of the Space Shuttle Payload Acoustic Environment," SAE Paper 770973, November 1977.

12. H. C. Allen et al., "An Interim Report on Shuttle Orbiter Vibroacoustics," The Shock and Vibration Bulletin, No. 47, Part 3, 157-201, September 1977.

13. S. H. Guest, J. H. Jones, "Space Shuttle Noise Suppression Concepts for the Eastern Test Range," Proceedings 13th Space Congress, Cocoa Beach, Florida, April 1976.

14. J. A. Cockburn, A. C. Jolly, "Structural-Acoustic Response, Noise Transmission Losses and Interior Noise Levels of an Aircraft-Fuselage Excited by Random Pressure Field," AFFDL-TR-68-2, 1968.

15. J. A. Hay, "Experimentally Determined Damping Factors," Chap. 12 of Symposium of Acoustic Fatigue, AGARD-CP-11, A73.

16. Anon., "Damping in Acoustically Excited Structures," Engineering Sciences Data Item No. 73011, July 1973.

17. Anon., "A Survey of Data on Damping in Spacecraft Structures," Fokker-VFW Space Division Report ESRO CR(P) 539, 1974.

18. C. E. Rucker, J. S. Mixson, "Vibroacoustic Testing of Space Shuttle Thermal Protection System Panels," AIAA/ASME/SAE 17th Structures, Structural Dynamics, and Materials Conference, May 1976.

19. J. Soovere, "Dynamic Properties of Graphite Fiber Honeycomb Panels," AIAA Paper 73-326, March 1973.

20. C. W. Best, W. C. Crisman, D. J. Wilkins, "Damping in Sandwich Beams with Shear Flexible Cores," J. Eng. for Industry 89, 662-670, November 1967.

## PROBABILITY OF FAILURE PREDICTION FOP STEP-STRESS
## FATIGUE UNDER SINE OR RANDOM STRESS

Ronald G. Lambert
General Electric Company
Aircraft Equipment Division
Utica, New York 13503

A previously proposed cumulative fatigue damage law is extended to predict the probability of failure or fatigue life for structural materials with S-N fatigue curves represented as a scatterband of failure points. The proposed law applies to structures subjected to sinusoidal or random stresses and includes the effect of initial crack (i.e., flaw) sizes. The corrected cycle ratio damage function is shown to have physical significance.

### INTRODUCTION

A cumulative fatigue damage law was previously derived by applying Fracture Mechanics theory to structures subjected to several levels of sequentially applied sinusoidal or random stress. The proposed damage law was similar to Miner's linear cycle ratio law but contained a correction term which accounted for the dependency upon the values of stress range, initial crack (flaw) length, a geometrical parameter and the material's fracture toughness. The significance of the proposed damage law was that it made corrections for known deficiencies in existing damage laws.

The only condition imposed at the discontinuity of the two levels of step-stress was that the crack length not change, which is an accurate representation of the physics involved. However, the value of cycle ratio damage was shown to change at the stress level discontinuity by a calculable amount.

The proposed damage law treated the cycle ratio damage expressons as deterministic quantities. This paper considers the material's fatigue curve as a scatterband of failure points, not as a single line, by treating the fatigue curve constant as a random variable.

This paper shows that the cycle ratio damage function is related to the probability of failure (or fatigue life) and, therefore, has physical significance as well as being a convenient and practical mathematical expression

### APPROACH SUMMARY

The analytical approach to be used in deriving probability of failure expressions in the two levels of step-stress is summarized as follows: The material being stressed has its fatigue curve represented as a scatterband of failure points. The corresponding single stress level failure probability $F(N)$ is derived as a function of stress cycles N. It is shown that $F(N)$ can also be expressed in terms of the cycle ratio damage function D. The cycle ratio damage functions in the two step-stress levels are computed utilizing previously derived expressions described in the Appendices. These damage functions include Fracture Mechanics' effects; the most significant from a practical viewpoint is the initial crack (flaw) length. The damage functions are used to compute the desired failure probability expressions, Eqs. (14) and (15). Examples are worked out to establish the reasonableness of the derived $F(N)$ expressions.

### FATIGUE CURVES

Fig. 1 shows the single level sinusoidal and random fatigue curves for 7075-T6 Aluminum Alloy. These curves are of the following form:

$$S = \frac{\Delta S}{2} = \bar{A}\, N_S^{-1/\beta} \tag{1}$$

$$\sigma = \bar{C}\, \tilde{N}_T^{-1/\beta} \tag{2}$$

where $\bar{A}$ and $\bar{C}$ are material fatigue curve

constants and $\beta$ is a slope parameter [1]. $\Delta S$ is the cyclic sine stress range. Refer to the Symbols section for Metric – Conventional Units conversion factors as well as definitions for all symbols. $\sigma$ is the random rms stress. $N_S$ is the sine cycles to failure. $N_T$ is the median number of random stress cycles to failure. The above fatigue curves are zero-width (i.e., nonscatterband) lines of failure points.
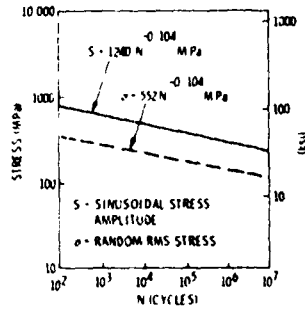


Fig. 1 – Sinusoidal and random fatigue curves for 7075-T6 Aluminum Alloy

Table 1 shows typical parameter values for several materials that will be used for subsequent examples.

TABLE 1
Typical Fatigue Curve Constants

| | $\bar{A}$ | | $\beta$ | $\bar{C}$ | |
|---|---|---|---|---|---|
| | (ksi) | (MPa) | | (ksi) | (MPa) |
| Copper Wire | 81 9 | 565 | 9.28 | 36.9 | 254 |
| 7075-T6 Aluminum Alloy | 180 | 1240 | 9.65 | 80 | 552 |

DETERMINISTIC FAILURE

The fatigue curves of Fig. 1 can be used in a deterministic fashion to predict failure. Define the cycle ratio damage function as follows:

$$D = \frac{N}{N_T} \qquad (3)$$

where $N$ = applied cycles

$N_T$ = cycles to failure

Define $F(N)$ = probability of failure at N cycles

The value of $N_T$ corresponds to a particular value of stress $\sigma$ in Fig. 1. Curves of D and F(N) versus applied stress cycles N are shown in Figs. 2 and 3. Failure is shown to occur when $N = N_T$ (i.e., when D = 1.0). These figures are presented to contrast the probabilistic treatment which follows.
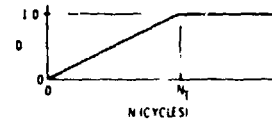


Fig. 2 – Cycle ratio damage function versus applied stress cycles
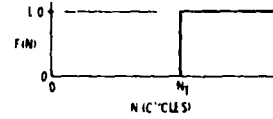


Fig. 3 – Deterministic probability of failure versus applied stress cycles

SCATTERBAND FATIGUE CURVE

A material's S-N fatigue curve is typically not a single line as shown in Fig. 1 but a wider scatterband of failure points. The single lines of Fig. 1 can be thought of as the median of the scatterband. This scatterband can be represented by letting the constant A in Eq. (1) become a random variable. For $\bar{A}$ having a Gaussian probability density function with average value $\bar{A}$ and standard deviation $\Delta$, it can be shown [1] that the probability density function of cycles to failure $p(N_T)$ for a random applied stress of rms value $\sigma$ is expressed as

$$p(N_T) = \frac{\bar{A}}{N_T \, \beta \, \Delta \, \sqrt{2\pi}} \left( \frac{N_T}{\tilde{N}_T} \right)^{1/\beta}$$

$$\exp \left[ - \frac{\bar{A}^2 \left\{ \left( \frac{N_T}{\tilde{N}_T} \right)^{1/\beta} - 1 \right\}^2}{2\Delta^2} \right] (4)$$

where

$$\tilde{N}_T = \left( \frac{\bar{C}}{\sigma} \right)^\beta \qquad (5)$$

$\tilde{N}_T$ = median cycles to failure

Refer to Table 1 for typical values of $\bar{A}$, $\bar{C}$, and $\beta$.

The corresponding probability of failure is defined as follows:

F(N) = probability of failing at N cycles

F(N) = probability that $N > N_T$ (i.e., that the number of applied cycles exceeds the cycles to failure of the material)

$$F(N) = \int_0^N p(N_T) \, dN_T \tag{6}$$

$$F(N) = 0.5 + \text{erf}_p\left[\frac{\bar{A}}{\Lambda}\left\{\left(\frac{N}{\tilde{N}_T}\right)^{1/\beta} - 1\right\}\right] \tag{7}$$

where $\text{erf}(\alpha)$ = Papoulis' [2] Error
Function

$$\text{erf}_p(\alpha) = \frac{1}{2\pi}\int_0^\alpha e^{-y^2/2} \, dy$$

$$\text{erf}_p(0) = 0; \quad \text{erf}_p(\infty) = 0.5$$

$$\text{erf}_p(-\alpha) = -\text{erf}_p(\alpha)$$

Both the average number of applied stress cycles N and cycles to failure $N_T$ in Eq. (3) are random variables for the random stress case. However, for reliable equipment design where N is usually greater than, say, 100 cycles, the value of N can be considered as a constant. The cycles to failure $N_T$ can be expressed in terms of a median value $\tilde{N}_T$. The corresponding cycle ratio damage function of Eq. (3) can be expressed in terms of its median value $\tilde{D}$.

$$\tilde{D} = \frac{N}{\tilde{N}_T} \tag{8}$$

The relationships between the parameters of Eqs. (4), (5), (6), (7), and (8) are shown in Fig. 4. The values of the curve $p(N_T)$ are independent of the value of N. The shaded area $F(N)$ increases as N increases. $F(N) = 0.5$ for $N = \tilde{N}_T$ (i.e., for $\tilde{D} = 1.0$). This was not the case for deterministic failure as
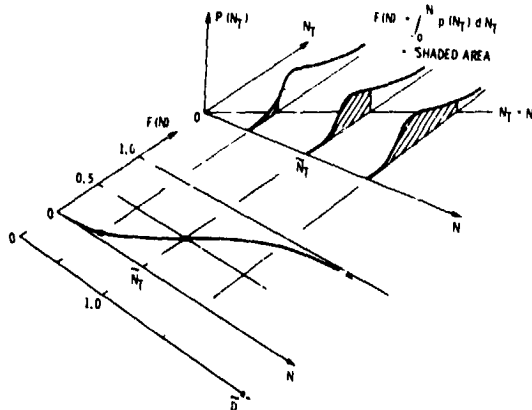


Fig. 4 - Relationships between $p(N_T)$, $F(N)$, $N$, $N_T$, $\tilde{D}$

shown in Figs. 2 and 3, because the scatterband representation of the fatigue curve places failure both before and after the median cycles to failure $\tilde{N}_T$. Fig. 3 represents the case for $\Delta = 0$.

DAMAGE FUNCTION

The damage function of Eq. (3) can be treated mathematically by using Eqs. (3), (4), and (8) along with the appropriate transformation. The derived probability density function of D is as follows:

$$p(D) = \frac{\bar{A}}{D\beta\Delta \sqrt{2\pi}}\left(\frac{\tilde{D}}{D}\right)^{1/\beta}$$

$$\exp\left[-\frac{\bar{A}^2\left\{\left(\frac{\tilde{D}}{D}\right)^{1/\beta} - 1\right\}^2}{2\Delta^2}\right] \tag{9}$$

EXAMPLE 1

Copper wire is subjected to a random stress of rms value $\sigma = 48.3$ MPa (7 ksi). Calculate $p(D)$ versus D for $N = 10^6$, $5 \times 10^6$, and $5 \times 10^7$ average applied stress cycles.

Given:

$$\bar{A} = 565 \text{ MPa } (81.9 \text{ ksi})$$

$$\bar{C} = 254 \text{ MPa } (36.9 \text{ ksi})$$

$$\beta = 9.28$$

$$\Delta = 56.5 \text{ MPa } (8.19 \text{ ksi})$$

$$\bar{A}/\Delta = 10$$

$$\sigma = 48.3 \text{ MPa } (7 \text{ ksi})$$

$$\tilde{N}_T = 5 \times 10^6 \text{ cycles from Eq. (5)}$$

| N | $\tilde{D}$ |
|---|---|
| $10^6$ | 0.2 |
| $5 \times 10^6$ | 1.0 |
| $5 \times 10^7$ | 10.0 |

Plots of $p(D)$ versus D using Eq. (9) are shown in Figs. 5, 6, and 7 for the above three cases. The median value D falls above the mode of the nonsymmetrical $p(D)$ curve.

PROBABILITY OF FAILURE -

Eq. (7) can also be expressed as:

$$F(N) = 0.5 + \text{erf}_p\left[\frac{\bar{A}}{\Delta}\left\{(\tilde{D})^{1/\beta} - 1\right\}\right] \tag{10}$$

Eq. (10) could equally be defined as $F(D)$.
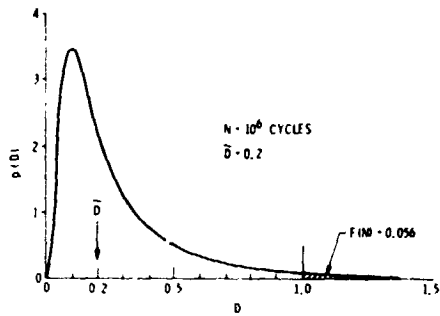
Fig. 5 – Plot of p(D) versus D for $\tilde{D} = 0.2$
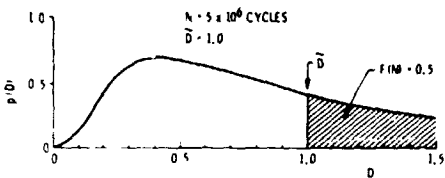
Fig. 6 – Plot of p(D) versus D for $\tilde{D} = 1.0$
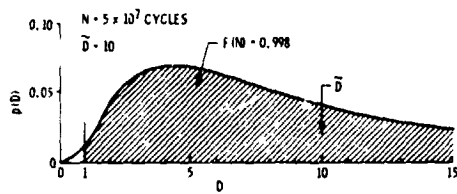
Fig. 7 – Plot of p(D) versus D for $\tilde{D} = 10$

It should be noted that the slope of the curve in the vicinity of $F(N) = 0.5$ is inversely related to $\Delta$, the standard deviation of the scatterband fatigue curve. $F(N) = 0.5$ for $\tilde{D} = 1.0$.

EXAMPLE 2

Same as Example 1 except calculate $F(N)$ for values of $\tilde{D}$ from 0.1 to 10. Fig. 8 is a plot of $F(^N)$ versus D using Eq. (10) for $\overline{A}/\Delta = 10$ and $\overline{A}/\Delta = 30$. Note that these curves are not straight lines on Weibull probability paper.

Eq. (9) was numerically integrated for values of D above 1.0. These values of area are equal to the values of $F(N)$ using Eq. (7) or (10). Three such values are shown by the shaded areas of Figs. 5, 6, and 7.

Therefore, the following is true:

$$F(N) = \int_{1.0}^{\infty} p(D) \, dD = \int_{0}^{N} p(N_T) \, dN_T \quad (11)$$
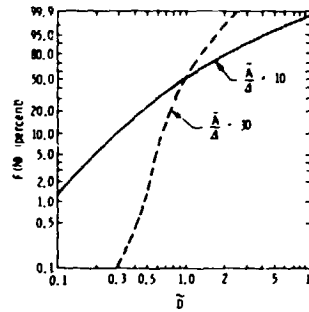
Fig. 8 – Plot on Weibull graph paper of $F(N)$ versus $\tilde{D}$ for $\overline{A}/\Delta = 10,20$ and $\beta = 9.28$

This is shown pictorially in Figs. 4 and 9.
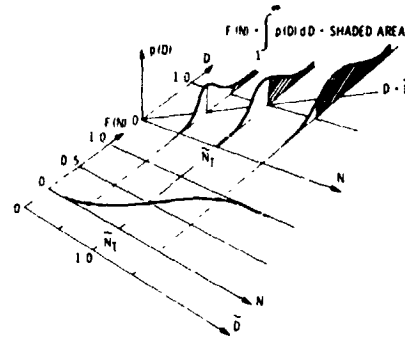
Fig. 9 – Relationships between p(D), F(N), N, $\hat{N}_T$, $\tilde{D}$

The cycle ratio damage function is related to the probability of failure (or fatigue life) and, therefore, has physical significance as well as being a convenient and practical mathematical expression. If was shown in Ref. 1 that the expression of $F(N)$ as a function of $p(N_T)$ as shown in Eqs. (6) and (11) agreed well with experimental data.

Fig. 10 illustrates the same relationships between parameters as Fig. 9
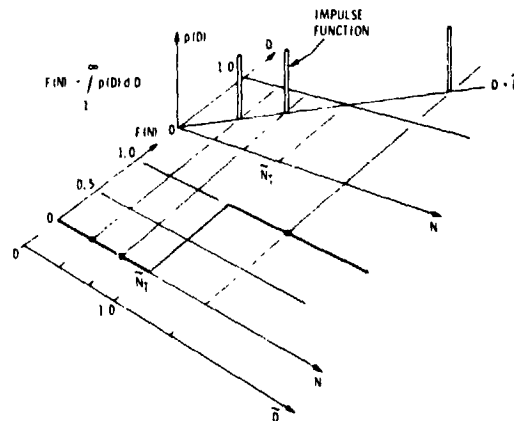
Fig. 10 – Relationships between parameters for $\Delta = 0$

34

except for $\Delta = 0$, the deterministic case. Here $p(D)$ becomes an impulse function of infinite height, zero width, and unity area. The area of $p(D)$ above $D = 1.0$ is zero for $N < \tilde{N}_T$ and is unity for $N > \tilde{N}_T$. Thus, there is a discontinuity at $N = \tilde{N}_T$. Fig. 10 is a different way of representing Figs. 2 and 3.

## STEP-STRESS FAILURE PROBABILITIES

Appendix A describes step-stress cycle ratio damage functions. Appendix C describes the previously proposed cumulative fatigue damage law used for computing fatigue life in a deterministic fashion. Appendix D describes the relationship between random and sinusoidal stress to produce the same crack growth. Ref. 3 describes the constants of these Appendices in more detail.

All of these relationships will be used to compute the probability of failure in the two applied stress levels for random or sinusoidal step-stress with a scatterband fatigue curve.

Define:

Level I: $\Delta S = S_1$; $0 \le N_1 \le N_{f_1}$

Level II: $\Delta S = S_2$; $0 \le N \le \infty$

$F(N_1)_I$ = probability of failure at $N_1$ cycles in Level I

$F(N)_{II}$ = probability of not failing in Level I and failing in Level II.

Eqs. (10) and (11) show that the probability of failure can be calculated if the median value of the random variable damage function is known.

$\tilde{D}_I$ = median value of Level I damage function

$\tilde{D}_{II}$ = median value of Level II damage function

$$F(N_1)_I = 0.5 + \text{erf}_p\left[\frac{\bar{A}}{\Delta}\left\{(\tilde{D}_I)^{1/\beta} - 1\right\}\right] \quad (12)$$

$$F(N)_{II} = 0.5 + \text{erf}_p\left[\frac{\bar{A}}{\Delta}\left\{(\tilde{D}_{II})^{1/\beta} - 1\right\}\right] \quad (13)$$

Equivalently,

$$F(N_1)_I = 0.5 + \text{erf}_p\left[\frac{\bar{A}}{\Delta}\left\{\left(\frac{N_1}{Nf_1}\right)^{1/\beta} - 1\right\}\right] \quad (14)$$

$$F(N)_{II} = 0.5$$
$$+ \text{erf}_p\left[\frac{\bar{A}}{\Delta}\left\{\left(\frac{N_1 X}{Nf_1} + \frac{N}{Nf_2}\right)^{1/\beta} - 1\right\}\right] \quad (15)$$

## INITIAL CRACK LENGTH

Including initial cracks (flaws) in design guidelines, standards, and codes as well as manufacturing process inspection criteria is becoming more prevalent, because such cracks reduce fatigue life. The larger the crack, the shorter the fatigue life. Initial cracks either exist in the structural material as dislocations or metallurgical inclusions or are introduced during manufacturing fabrication or assembly operations. Their sizes can range from microscopic to macroscopic.

In some cases, relatively large initial cracks go undetected for a variety of reasons. In other cases, it is impractical to repair the crack or replace the part even if the crack is detected. These situations occur frequently enough to be of practical importance.

In complex welded structures nondestructive testing procedures cannot detect cracks less than 1.27 mm (0.050 in.) in depth with a high degree of confidence, even under optimum conditions [4]. For hard-to-inspect areas like blind welds, cracks as deep as 2.54 mm (0.100 in.) can be expected to escape detection on a regular basis [4].

## EXAMPLE 3

For the configuration shown in Fig. 11, calculate the probabilities of failure for random step-stress of rms values 15.3 MPa (2.22 ksi) and 30.6 MPa (4.44 ksi) respectively with initial crack lengths of 1.27 mm (0.05 in.) and 2.54 mm (0.10 in.) The material is 7075-T6 Aluminum Alloy. Consider the specimen width to be 5 inches. The average number of applied stress cycles in Level I is $N_1 = 6 \times 10^3$ cycles. Let $\bar{A}/\Delta = 10$.
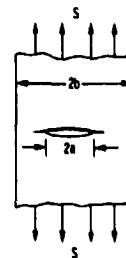
Fig. 11 - Center cracked strip loaded in tension

$\Delta S_1 = 4.5$ $\sigma_1 = 68.9$ MPa (10 ksi)

$\Delta S_2 = 4.5$ $\sigma_2 = 137.8$ MPa (20 ksi)

$Y = 1.77$

$a_{c_1} = 32.5$ mm (1.28 in.)

$a_{c_2} = 8.1$ mm (0.319 in.)

Define:

$N_I$ = applied stress cycles in Level I

$N_{II}$ = applied stress cycles in Level II

$N_{TOTAL} = N_I + N_{II}$ = total stress cycles

The value for the damage function $\tilde{D}_1$ in Table 2 shows that 18.4 percent of the fatigue life "on the average" was consumed after 6000 cycles at stress level $\sigma_1$ for $a_i = 1.27$ mm (0.50 in.).

Thus, 82.6 percent of the fatigue life "on the average" remains at stress level $\sigma_1$. The stress level referred to must not change in order for the fatigue life consumed and remaining to add up to 100 percent. The 18.4 percent of life consumed at level $\sigma_1$ is equivalent to 21 percent (refer to the $\tilde{D}_{1e}$ value) at stress level $\sigma_2$. Thus 79 percent of the fatigue life "on the average" remains at stress level $\sigma_2$. "On the average" in actuality refers to median values, not average values.

Similarly for $a_i = 2.54$ mm (0.100 in.) 51.4 percent of the fatigue life was consumed in Level I with 48.6 percent remaining in Level II at stress level $\sigma_2$.

The damage function values of Table 2 correspond to the deterministic median line of the material's fatigue curve. Table 3 indicates failure probabilities for the scatterband of the fatigue curve.

The results of Table 3 are plotted in Fig. 12. The discontinuity in failure probability can be seen at the inter-

TABLE 2
Calculated Parameters

| $a_i$ (mm) | $a_i$ (in.) | $N_{f_1}$ (cycles) | $N_{f_2}$ (cycles) | $\tilde{D}_1$ | X | $\tilde{D}_{1e}$ | $\tilde{D}_2$ |
|---|---|---|---|---|---|---|---|
| 1.27 | 0.050 | $32.6 \times 10^3$ | $1.8 \times 10^3$ | 0.184 | 1.14 | 0.210 | 0.790 |
| 2.54 | 0.100 | $15.7 \times 10^3$ | 729 | 0.383 | 1.34 | 0.514 | 0.486 |

TABLE 3
Failure Probabilities

| $N_{TOTAL}$ | $N_I$, $N_{II}$ | $a_i = $ 1.27 mm (0.050 in.) F(N) | $a_i = $ 2.54 mm (0.10 in.) F(N) |
|---|---|---|---|
| 0 | 0 | 0 | 0 |
| 1000 | 1000 | 0.001 | 0.007 |
| 2000 | 2000 | 0.006 | 0.027 |
| 3000 | 3000 | 0.014 | 0.057 |
| 4000 | 4000 | 0.025 | 0.093 |
| 5000 | 5000 | 0.038 | 0.132 |
| 6000 | 6000 | 0.053 | 0.171 |
| 6000 | 0 | 0.067 | 0.252 |
| 6100 | 100 | 0.099 | 0.331 |
| 6200 | 200 | 0.133 | 0.403 |
| 6350 | 350 | 0.186 | 0.500 |
| 6500 | 500 | 0.237 | 0.576 |
| 7000 | 1000 | 0.394 | 0.752 |
| 7400 | 1400 | 0.500 | 0.836 |
| 8000 | 2000 | 0.617 | 0.904 |
| 9000 | 3000 | 0.752 | 0.958 |
| 10,000 | 4000 | 0.835 | 0.980 |
| 11,000 | 5000 | 0.887 | 0.990 |
| 12,000 | 6000 | 0.921 | 0.994 |
| 13,000 | 7000 | 0.943 | 0.997 |
| 14,000 | 8000 | 0.959 | 0.998 |
| 15,000 | 9000 | 0.970 | 0.999 |

face between Level I and II. Level II F(N) values are markedly greater than Level I values due to the increase in applied stress level. The larger initial flaw or crack size significantly increases F(N) at a given value of cycles or decreases fatigue life for a given failure probability.

less than unity for this stress level sequence. The corresponding failure probabilities are shown in Fig. 13. The direction of the discontinuities at the stress region boundary and the slopes of the curves in crossing the boundary are different from those in Fig. 12.
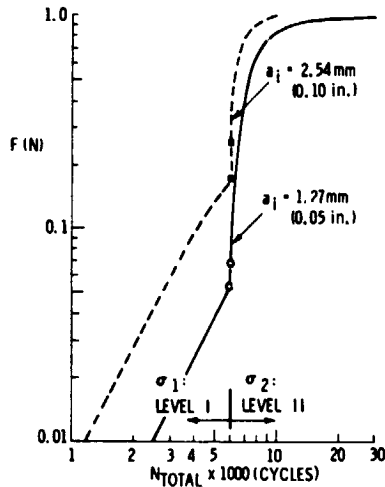


Fig. 12 - Failure probabilities for $\sigma_1$ = 15.3 MPa (2.22 ksi) rms and $\sigma_2$ = 30.6 MPa (4.44 ksi) rms
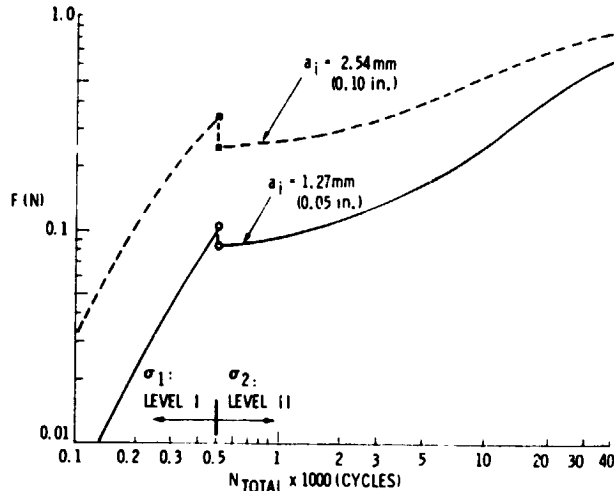


Fig. 13 - Failure probabilities for $\sigma_1$ = 30.6 MPa (4.44 ksi) rms and $\sigma_2$ = 15.3 MPa (2.22 ksi) rms

## EXAMPLE 4

The same as Example 3 except that the stress level sequence is reversed with $N_I$ = 500 cycles.

$\sigma_1$ = 30.6 MPa (4.44 ksi) rms

$\sigma_2$ = 15.3 MPa (2.22 ksi) rms

Table 4 shows the calculated parameters. Note that the values for $\chi$ are

## CONCLUDING REMARKS

It is believed that the derived failure probability expressions, Eqs. (14) and (15), are simple, practical and accurate. These expressions indicate that a large value of initial crack (flaw) size has a significant effect on probability of failure and fatigue life which is consistent with experimental observations.

TABLE 4
Calculated Parameters

| $a_i$ (mm) | $a_i$ (in.) | $N_{f_1}$ (cycles) | $N_{f_2}$ (cycles) | $\tilde{D}_1$ | X | $D_{1e}$ | $\tilde{D}_2$ |
|---|---|---|---|---|---|---|---|
| 1.27 | 0.050 | $1.8\times10^3$ | $32.6\times10^3$ | 0.278 | 0.878 | 0.244 | 0.756 |
| 2.54 | 0.100 | 729 | $15.7\times10^3$ | 0.686 | 0.745 | 0.511 | 0.489 |

## SYMBOLS

| | |
|---|---|
| a | crack half-length |
| $a_c$ | critical value of crack half-length at stress level $\Delta S$ or $\sigma$ |
| $a_{c1}$ | critical value of crack half-length at stress level $\Delta S_1$ or $\sigma_1$ |
| $a_{c2}$ | critical value of crack half-length at stress level $\Delta S_2$ or $\sigma_2$ |
| $a_i$ | initial crack half-length |
| A | material constant |
| $\bar{A}$ | average value of A |
| b | specimen half-width |
| $\bar{C}$ | constant of random fatigue curve |
| $c_o$ | constant of crack growth rate curve |
| D | cycle ratio damage function |
| $D_1$ | cycle ratio damage function at stress level $\Delta S_1$ or $\sigma_1$ |
| $D_2$ | cycle ratio damage function at stress level $\Delta S_2$ or $\sigma_2$ |
| $\tilde{D}$ <br> $\tilde{D}_1$ <br> $\tilde{D}_2$ | median values of the above cycle ratio damage functions |
| $\tilde{D}_I$ | median value of the cycle ratio damage function during the first of two sequentially applied step-stress levels |
| $\tilde{D}_{II}$ | median value of the cycle ratio damage function during the second of two sequentially applied step-stress levels |
| $\tilde{D}_{1e}$ | median value of the equivalent damage done at stress level $\Delta S_2$ or $\sigma_2$ |
| $\dfrac{da}{dN}$ | crack growth rate |
| $erf_p$ | error function defined by Papoulis [2] |
| F(N) | probability of failure in N cycles |
| in. | inches |
| $\Delta K$ | range of stress intensity factor |
| $\Delta K_c$ | fracture toughness |

| | |
|---|---|
| ksi | thousands of pounds per square inch |
| $p(\alpha)$ | probability density function of $\alpha$ |
| N | number of stress cycles |
| $N_1$ | number of stress cycles at stress level $\Delta S_1$ or $\sigma_1$ |
| $N_I$ | total number of applied stress cycles in the first of two sequentially applied step-stress levels |
| $N_{II}$ | total number of applied stress cycles in the second of two sequentially applied step-stress levels |
| $N_{TOTAL}$ | sum of $N_I$ and $N_{II}$ above |
| $N_{f1}$ | number of stress cycles to failure at stress level $\Delta S_1$ or $\sigma_1$ |
| $N_{f2}$ | number of stress cycles to failure at stress level $\Delta S_2$ or $\sigma_2$ |
| $N_S$ | number of sine cycles to failure at stress level $\Delta S$ |
| $N_T$ | number of cycles to failure at random stress level $\sigma$ |
| $\tilde{N}_T$ | median value of $N_T$ |
| S | sinusoidal stress amplitude |
| $\Delta S$ | sinusoidal stress range |
| sec | trigonometric secant |
| rms | root-mean-square |
| X | damage law correction factor |
| y | dummy variable |
| Y | geometrical parameter |
| $\alpha$ | dummy variable |
| $\beta$ | fatigue curve slope parameter |
| $\Delta$ | standard deviation of A |
| $\sigma$ | random rms stress value |
| $\theta$ | constant of crack growth rate curve |
| m | metre |
| mm | millimeter |
| MPa | mega Pascals |

| | |
|---|---|
| 1.0988 | $\dfrac{\text{MPa }\sqrt{\text{metre}}}{\text{ksi }\sqrt{\text{in.}}}$ |
| 6.895 | $\dfrac{\text{MPa}}{\text{ksi}}$ |
| 25.4 | $\dfrac{\text{mm}}{\text{in.}}$ |

## REFERENCES

1. R.G. Lambert, "Analysis of Fatigue under Random Vibration," The Shock and Vibration Bulletin, Naval Research Laboratory, Washington, DC, August 1976.

2. A. Papoulis, Probability, Random Variables, and Stochastic Processes, McGraw-Hill Book Co., New York, 1965.

3. R.G. Lambert, "Fracture Mechanics Applied to Step-Stress Fatigue under Sine/Random Vibration," Presented at 48th Shock and Vibration Symposium, Huntsville, Ala., October, 1977.

4. T.W. Crooker, "Fracture Mechanics Fatigue Design," Mechanical Engineering, June, 1977.

5. P.C. Paris, "The Fracture Mechanics Approach to Fatigue," Proc. 10th Sagamore Army Mater. Res. Cong., p 107, Syracuse University Press, Syracuse, NY, 1964.

6. P.C. Paris and H.H. Johnson, "Sub-Critical Flaw Growth," Engineering Fracture Mechanics, Vol. 1, p 3, 1968.

## APPENDIX A
## FRACTURE MECHANICS EXPRESSIONS

A detailed discussion of the application of fracture mechanics is given in Ref. 3. A brief summary will be described herein. Fig. 11 shows a particular loading and crack configuration. The crack half-length, a, will be referred to as the crack length to simplify the wording. The actual crack length is 2a. The stress away from the vicinity of the crack is S. $\Delta S$ is the stress range; that is, it is the double amplitude of the sinuoidal stress variation with time. Static stresses are not included. Y is a dimensionless parameter that depends upon the specimen and crack shape and dimensions, the type of crack and its location within the specimen, and the type of loading [5,6]. For the case shown in Fig. 11, the expression for Y is:

$$Y = \sqrt{\pi}\left(\sec\frac{\pi a}{2b}\right)^{1/2} \qquad (16)$$

The stress intensity range $\Delta K$ is a function of Y, $\Delta S$, and crack length.

$$\Delta K = Y\,\Delta S\sqrt{a} \quad \text{MPa}\sqrt{\text{metre}}\ (\text{ksi}\sqrt{\text{in.}}) \qquad (17)$$

In the stable crack propagation region, the rate of crack growth is

$$\frac{da}{dN} = c_o(\Delta K)^\theta \quad \text{metre/cycle (in./cycle)} \qquad (18)$$

where N is the number of applied stress cycles, and $c_o$ and $\theta$ are material constants. Eq. (18) can be integrated and expressed as:

$$N = \frac{2}{c_o\Delta S^\theta Y^\theta(\theta - 2)}$$
$$\left[\left(\frac{1}{a_i}\right)^{\frac{\theta-2}{2}} - \left(\frac{1}{a}\right)^{\frac{\theta-2}{2}}\right]\text{cycles} \qquad (19)$$

where

$a_i$ = initial crack length

$a$ = crack length at N cycles

The crack will grow in a stable fashion until the crack length "a" reaches a critical value "$a_c$" and $\Delta K$ reaches the material's critical value $\Delta K_c$ (fracture toughness) at which time the crack growth becomes unstable and the part fails catastrophically.

$$a_c = \left[\frac{\Delta K_c}{Y\Delta S}\right]^2 \quad \text{metre (inches)} \qquad (20)$$

$a_c$ = critical crack half-length

For 7075-T6 Aluminum Alloy,

$c_o = 1.5 \times 10^{-10}$ m/cycle

$\qquad (6.0 \times 10^{-9}$ in./cycle)

$\theta = 4$

$\Delta K_c = 2.2$ MPa $\sqrt{m}$ (20 ksi $\sqrt{\text{in.}}$)

If two values of stress range ( $\Delta S_1$ and $\Delta S_2$) were independently applied, the corresponding cycles to failure ($N_{f_1}$ and

$N_{f_2}$) would be calculated for 7075-T6 using Eqs. (19) and (20),

$$a_{c1} = \left[\frac{\Delta K_c}{Y\Delta S_1}\right]^2 \qquad (21)$$

$$a_{c2} = \left[\frac{\Delta K_c}{Y\Delta S_2}\right]^2 \qquad (22)$$

$$N_{f_1} = \frac{1}{c_o \Delta S_1^4 Y^4}\left[\frac{1}{a_i} - \frac{1}{a_{c1}}\right] \qquad (23)$$

$$N_{f_2} = \frac{1}{c_o \Delta S_2^4 Y^4}\left[\frac{1}{a_i} - \frac{1}{a_{c2}}\right] \qquad (24)$$

The above expressions are limited in application to those cases where the crack growth is in the stable crack propagation region [3] and where Y remains at a relatively constant value.

## APPENDIX B
## STEP-STRESS DAMAGE FUNCTIONS

Consider the situation where a sinusoidal stress of range $\Delta S_1$ is applied for $N_1$ cycles at a stress of range $\Delta S_2$ [3]. These two sequential stress levels will be defined as Levels I and II respectively. Define $N_2$ as the value of $N$ at which failure occurs in Level II.

Level I:    $\Delta S = \Delta S_1$; $\; 0 \leq N_1 \leq N_{f_1}$

Level II:   $\Delta S = \Delta S_2$; $\; 0 \leq N \leq \infty$

$$0 \leq N_2 \leq N_{f_2}$$

$N_{f_1}$ and $N_{f_2}$ are described in Appendix A. The corresponding median cycle ratio damage functions are:

Level I:    $\tilde{D}_I = \tilde{D}_1 = \dfrac{N_1}{N_{f_1}}$

Level II:   $\tilde{D}_{II} = \tilde{D}_{1e} + \tilde{D}_2 \qquad (25)$

$$\tilde{D}_2 = \frac{N}{N_{f_2}} \qquad (26)$$

$\tilde{D}_{1e}$ = equivalent damage at $\Delta S_2$ that is done by $N_1$ actual cycles as $\Delta S_1$

$$\tilde{D}_{1e} = \tilde{D}_1 X = \frac{N_1 X}{N_{f_1}} \qquad (27)$$

where X = correction factor to account for the crack propagation and fatigue failure dependency upon the values of Y, $\Delta K_c$, $a_i$, $\Delta S_1$, and $\Delta S_2$.

$$X = \left[\frac{1 - \left(\dfrac{a_i}{a_{c1}}\right)^{\frac{\theta-2}{2}}}{1 - \left(\dfrac{a_i}{a_{c2}}\right)^{\frac{\theta-2}{2}}}\right]$$

$$= \left[\frac{1 - \left(\dfrac{a_i Y^2 \Delta S_1^2}{\Delta K_c^2}\right)^{\frac{\theta-2}{2}}}{1 - \left(\dfrac{a_t Y^2 \Delta S_2^2}{\Delta K_c^2}\right)^{\frac{\theta-2}{2}}}\right] \qquad (28)$$

Thus

$$\tilde{D}_{II} = \frac{N_1 X}{N_{f_1}} + \frac{N}{N_{f_2}} \qquad (29)$$

Stress Level Interface:

At the discontinuity of sequential stress Levels I and II (N = 0):

$$\tilde{D}_I = \tilde{D}_1 = \frac{N_1}{N_{f_1}}$$

$$\tilde{D}_{II} = \tilde{D}_{1e} = \frac{N_1 X}{N_{f_1}}$$

$$\tilde{D}_I \neq \tilde{D}_{II}$$

The only condition imposed at the interface was that the crack length not change. $\tilde{D}_I \neq \tilde{D}_{II}$ because the value of critical flaw size changes (i.e., $a_{c1} \neq a_{c2}$).

## APPENDIX C
## PROPOSED CUMULATIVE FATIGUE DAMAGE LAW

The previously proposed damage law [3] for the step-stress case of Appendix B is:

$$D_1 X + D_2 = 1 \qquad (30)$$

Given that $a_i$, Y, and $K_c$ are constants for a particular configuration, it can be noted that

$$X > 1 \text{ for } \Delta S_2 > \Delta S_1; \ D_1 + D_2 < 1$$

$$X < 1 \text{ for } \Delta S_2 < \Delta S_1; \ D_1 + D_2 > 1$$

$$X = 1 \text{ if } a_i << a_{c_1} \text{ and } a_i << a_{c_2}$$

The above law is useful for computing the fatigue life $N_2$ of Appendix B in a deterministic fashion for a single line fatigue curve. It accurately applies for cases where $\Delta S_1$ and $\Delta S_2$ are both in either the elastic or plastic stress-strain region but not for cases where they are in different regions [3].

## APPENDIX D
## RANDOM-SINUSOIDAL STRESS CRACK GROWTH RELATIONSHIP

Fig. 1 and Eqs. (1) and (2) show the relationship between a material's sinusoidal "S-N" and random "$\sigma$-N" fatigue curves. At a given number of cycles, Eqs. (1) and (2) show

$$\frac{\Delta S}{\sigma} = \frac{2\bar{A}}{\bar{C}} \qquad (31)$$

For 7075-T6, $\bar{A}$ = 1240 MPa (180 ksi); $\bar{C}$ = 552 MPa (80 ksi).

$$\Delta S = 4.5\sigma$$

In this case, a sinusoidal stress range that is equal in magnitude to $4.5\sigma$ will propagate a crack the same length as a random stress of rms value for the same number of cycles [3]. Thus the fracture mechanics equations may be used for random stress cases by the substitution of $\Delta S = (2\bar{A}/\bar{C})\sigma$ from Eq. (31).

# ON THE USE OF COHERENCE FUNCTIONS

## TO EVALUATE SOURCES OF DYNAMIC EXCITATION*

Stanley Barrett
Martin Marietta Corporation
Denver, Colorado

The objective of the study described in this paper was to investigate the use of coherence functions for identifying the relative contributions of multiple dynamic inputs to the measured vibration response of spacecraft components on a practical, complex structure. Data for the study were generated by applying simultaneous vibratory and acoustic excitation to a test model (a modified Titan instrumentation truss). Up to three inputs were used. In some cases mutually coherent inputs were generated.

A digital computer program was written to analyze the test data, using an approach based on iterative computational algorithms developed by Bendat. This approach is simpler than earlier matrix methods and is believed to be more economical in terms of computer time.

The results showed that the coherence function technique was effective in identifying and evaluating sources of excitation, for both independent and coherent inputs. The effect of varying the number of data samples used in the necessary averaging process was briefly investigated and is discussed in the paper.

## INTRODUCTION

In the field of environmental dynamics it is frequently desirable to be able to identify and rank the dynamic sources contributing to the measured output of a system. For instance, a noise control engineer may be required to estimate the relative severity of various noise sources making up the acoustics environment in a factory so he can decide how to assign his available noise-reduction resources. Another example in the aerospace industry might be the problem of protecting a sensitive electronic assembly being excited by simultaneous acoustic and vibration inputs; this can be solved more easily if the dynamicist knows how the various inputs contribute to the overall response.

A number of techniques are available for performing this source identification. If the sources have narrowband frequency characteristics, frequency spectrum analysis is satisfactory and is often used. The resulting spectra can be ambiguous, however, when the inputs and the outputs exhibit peaks at coincident frequencies. In this situation a time-domain approach can be applied using auto- and cross-correlation functions. Unfortunately, there are some serious practical limitations inherent in correlation techniques, as discussed by Broch [ref 1]; consequently, attention has recently been directed to using various forms of the coherence function to solve the problem. This is a frequency-domain function that provides the same basic information as the correlation function approach, but presents it in a form generally more useful for practical purposes.

The coherence function has applications in other areas. For example, it can be used to evaluate the fidelity of measured transfer functions. However this paper concentrates on solving the source identification problem. Similar work in this area was reported recently [ref 2] in which several sources of vibration that were causing an airborne antenna to malfunction were investigated. Coherence functions (CFs) based on a matrix treatment were used. Our study was somewhat more general and used a nonmatrix method

originated by Bendat [ref 3], which is judged to be more economical than the matrix approach.

## DISCUSSION OF COHERENCE FUNCTIONS

Three forms of the coherence function are used in this paper--the ordinary coherence function (OCF), the multiple coherence function (MCF) and the partial coherence function (PCF). The PCF is sometimes referred to as the conditional coherence function in the literature. Other kinds of coherence functions have been defined [ref 4] but will not be discussed here. *The OCF, MCF and PCF are all measures of the linear dependence between spectral components of random processes, and are real valued functions of frequency varying in magnitude between zero and one.* The standard symbol for CF is $\gamma^2(f)$, with appropriate subscripts used to indicate the form and the parameters involved.

Consider a set of stationary random inputs $x_i(t)$ ($i = 1,2,3,...p$) and one output $y(t)$, acting on the constant parameter linear system shown in Fig. 1.
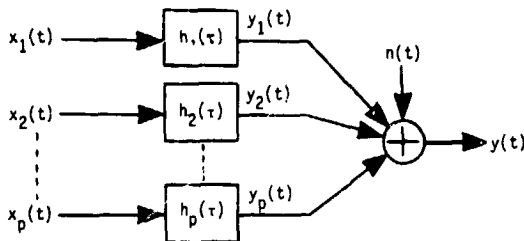


Fig. 1 -
Multiple-input/single-output system

The "noise" term $n(t)$ shown in Fig. 1 is intended to account for any deviations from the ideal model; it would include measurement noise at the output, time delays in the measured data, nonlinear effects, statistical errors, etc. We assume $n(t)$ to be statistically independent of the total measured output $y(t)$.

The system could equally well be described in frequency domain terms by taking Fourier transforms so that $x_i(t)$, $y_i(t)$, $y(t)$ and $n(t)$ would become $X_i(f)$, $Y_i(f)$, $Y(f)$ and $N(f)$ respectively. The impulse response functions $h_i(\tau)$ would transform to frequency response functions $H_i(f)$. Shifting to the frequency domain introduces useful simplifications in the input/output relationships. For example, in the time domain a local output $y_i(t)$ is related to the input $x_i(t)$ in terms of the impulse response $h_i(\tau)$ by the convolution integral

$$y_i(t) = \int_0^\infty h_i(\tau) \, x_i(t - \tau) \, d\tau, \qquad (1)$$

whereas, in the frequency domain, the corresponding relationship is a simple product of Fourier transforms

$$Y_i(f) = H_i(f) \, X_i(f). \qquad (2)$$

The spectral density functions associated with the time functions are

$G_{ii}(f)$ = auto-spectrum of $x_i(t)$,

$G_{yy}(f)$ = auto-spectrum of $y(t)$,

$G_{nn}(f)$ = auto-spectrum of $n(t)$,

$G_{ij}(f)$ = cross-spectrum of $x_i(t)$ with $x_j(t)$,

$G_{iy}(f)$ = cross-spectrum of $x_i(t)$ with $y(t)$.

We could also define $G_{ny}(f)$ as the cross-spectrum of $n(t)$ with $y(t)$, but this would vanish since $n(t)$ and $y(t)$ were assumed to be statistically independent. Note that we are using one-sided spectra involving only positive frequencies. Although theoretical studies often work with two-sided spectra, since the correction is a factor of two, which would always cancel out in the equations because of the way the spectra are used, we can safely use the more physically meaningful one-sided spectra immediately.

The ordinary coherence function between any two inputs $x_i(t)$ and $x_j(t)$ is given by

$$\gamma^2_{ij}(f) = \frac{|G_{ij}(f)|^2}{G_{ii}(f) \, G_{jj}(f)}. \qquad (3)$$

In what follows, the (f) dependency will generally be omitted for brevity. If the inputs are completely independent, the OCF will vanish for all combinations of i and j since $G_{ij}$ will be zero. Thus any variation from zero indicates some degree of mutual coherence between the inputs. Note that $\gamma^2_{ij} = 1$ would mean that $x_i(t)$ and $x_j(t)$ contain redundant information and one of the inputs should be eliminated from the model.

The OCF between any input $x_i(t)$ and the total output $y(t)$ is

$$\gamma^2_{iy} = \frac{|G_{iy}|^2}{G_{ii} \, G_{yy}}. \qquad (4)$$

In this case $\gamma^2_{iy} = 1$ implies that the other inputs are not contributing to the output and

44

the model should be viewed as a single-input/single-output system.

If the inputs are completely independent, the sum of the input/output OCFs should be unity for all frequencies. When this result is not obtained, it means that noise is present in the input or output data, other inputs exist that have not been included, or the system is nonlinear. The OCF $\gamma_{it}^2$ shows the proportion of the total output resulting from $x_i(t)$; the actual output power contributed by $x_i(t)$ is given directly by $\gamma_{iy}^2 G_{ii}$.

The multiple coherence function shows the CF relationship between the complete set of inputs $x_i(t)$, $x_2(t)$, ... $x_p(t)$ and the total output $y(t)$. It can be used as a diagnostic tool to examine how closely an assumed model matches the actual system by evaluating the noise in the system as follows

Let $x(t) = x_i(t)$, $x_2(t)$, ... $x_p(t)$ be the set of inputs to the model in Fig. 1, excluding noise, and

$\hat{y}(t)$ = the predicted output in the absence of noise,

$y(t)$ = the actual measured output,

$n(t)$ = effects causing deviations from the predicted output

$\quad = y(t) - \hat{y}(t)$.

Corresponding auto-spectra are $G_{xx}$, $G_{\hat{y}\hat{y}}$, $G_{yy}$, $G_{nn}$.

Since $\hat{y}(t) = y(t) - n(t)$

$\therefore G_{\hat{y}\hat{y}}(f) = G_{yy}(f) - G_{nn}(f)$.

The MCF is defined as

$$\gamma_{x:y}^2 = \frac{G_{\hat{y}\hat{y}}}{G_{yy}} = \frac{G_{yy} - G_{nn}}{G_{yy}} \qquad (5)$$

$$= 1 - G_{nn}/G_{yy}$$

$$\therefore G_{nn} = G_{yy}\left\{1 - \gamma_{x:y}^2\right\}. \qquad (6)$$

If all the inputs are independent, the MCF will equal the sum of the individual input/output OCFs

$$\gamma_{x:y}^2 = \gamma_{1y}^2 + \gamma_{2y}^2 + \ldots + \gamma_{py}^2. \qquad (7)$$

The system noise can thus be evaluated from (6) and (7).

Equation (7) does not apply if the inputs are not completely independent; however, a similar relationship can be developed for this case between the MCF and various partial coherence functions. Before the PCFs can be calculated, the inputs must be modified or "conditioned" to remove the coupling effects caused by the lack of independence between the inputs. Each PCF will then show the proportion of the output caused by a specific input, with the effects of all other inputs eliminated.

Special subscript notation is used to indicate a PCF and to show how the data records have been conditioned. For example, $x_{3.12}(t)$ indicates that input $x_3(t)$ has been conditioned on $x_1(t)$ and $x_2(t)$ to eliminate their effects. The corresponding conditioned auto-spectrum would be $G_{33.12}$. The PCF between $x_3(t)$ and $y(t)$, conditioned on $x_1(t)$ and $x_2(t)$ is given by

$$\gamma_{3y.12}^2 = \frac{|G_{3y.12}|^2}{G_{33.12}\,G_{yy.12}}. \qquad (8)$$

Thus, the PCF between the preconditioned quanities is equivalent to the OCF between the postconditioned quantities.

The numerical conditioning process is quite complicated for a mutliple-input system. Matrix methods for performing this operation have been developed [4, 5, 6] and an application is described in reference 2. These methods are very effective in keeping the computational process organized but can be expensive in computer time because they involve a considerable number of complex matrix inversions. An alternative approach was developed recently by Bendat [3, 7] in which iterative algorithms are used to calculate conditioned spectral density functions and partial coherence functions. The technique uses Fourier transforms of the data records and performs the conditioning by removing an optimum least-squares prediction of the "contaminating" inputs from each input in turn. A unique feature of Bendat's method is the use of "ordered" inputs. In this process, the original set of input records is rearranged in a particular order and then each record is conditioned on the preceding records. Thus $x_1(t)$ is unchanged, $x_2(t)$ is conditioned on $x_1(t)$ to become $x_{2.1}(t)$, $x_3(t)$ is conditioned on $x_1(t)$ and $x_2(t)$ to become $x_{3.12}(t)$, and so on. The noise term $n(t)$ is equivalent to the output conditioned on all of the inputs.

A revised model involving ordered, conditioned, frequency-domain inputs is shown in Fig. 2.
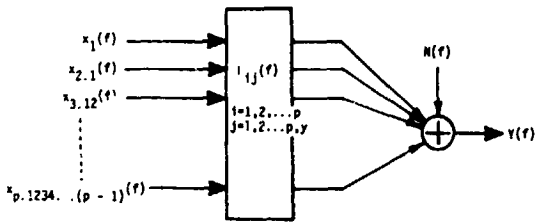
Fig. 2 -
Multiple-input/single-output system with
ordered conditioned inputs

The following procedure is used to establish the new order for the inputs:

1) Calculate the OCF between each input $x_i(t)$ and the output $y(t)$;

2) For the frequency range of primary interest, arrange the calculated OCFs in order of magnitude;

3) The new $x_1(t)$ is the input that gives the highest OCF, $x_2(t)$ is the input giving the next highest OCF, and so on for the remaining inputs.

This gives a set of ordered inputs that now must be conditioned by the process developed in reference 3 and summarized here.

The box labeled $L_{ij}(f)$ in Fig. 2 represents frequency response functions connecting the conditioned inputs $X_{i.123...(i-1)}(f)$ with each other and with the output $Y(f)$. The $L_{ij}$ terms are used to estimate the effects of the preceding $(i-1)$ inputs, which are to be eliminated from the $\underline{ith}$ input in the iterative conditioning pro$\underline{cess}$. The $L_{ij}$ must be optimized on the basis of minimizing the error in these estimates.

From the model, we can write

$$Y = \sum_{i=1}^{p} L_{iy} X_{i.123...(i-1)} + N. \qquad (9)$$

Let $\quad N_{iy} = Y - L_{iy} X_{i.123...(i-1)}, \qquad (10)$

which is the difference between the total output Y and the output due to the $\underline{ith}$ conditioned input passing through $L_{iy}$.

Then $|N_{iy}|^2 = |Y - L_{iy} X_{i.123...(i-1)}|^2$

$$= |Y|^2 - L_{iy}^* [X_{i.123...(i-1)}^* Y]$$

$$- L_{iy} [Y^* X_{i.123...(i-1)}] + L_{iy}^* L_{iy}$$

$$|X_{i.123...(i-1)}|^2 \qquad (11)$$

where the asterisks indicate complex conjugates.

Taking expected values of both sides give an expression for the mean square system error for any $L_{iy}$, in terms of auto- and cross-spectra of the conditioned input and the output

$$E\left\{|N_{iy}|^2\right\} = \epsilon^2$$

$$= G_{yy} - L_{iy}^* G_{iy.123...(i-1)}$$

$$- L_{iy} G_{iy.123...(i-1)}^*$$

$$+ L_{iy} L_{iy}^* G_{ii.123...(i-1)}. \qquad (12)$$

To minimize $\epsilon^2$, differentiate (12) partially with respect to $L_{iy}$ and equate to zero

$$\frac{\partial}{\partial L_{iy}} \cdot (\epsilon^2) = - G_{iy.123...(i-1)}^*$$

$$+ L_{iy}^* G_{ii.123...(i-1)} = 0.$$

Taking complex conjugates and solving for the optimum $L_{iy}$ gives

$$L_{iy}(opt) = \frac{G_{iy.123...(i-1)}}{G_{ii.123...(i-1)}}. \qquad (13)$$

The optimum input/output frequency response functions for the model will thus be

$$L_{iy} = \frac{G_{1y}}{G_{11}}$$

$$L_{2y} = \frac{G_{2y.1}}{G_{22.1}}$$

$$L_{3y} = \frac{G_{3y.12}}{G_{33.12}} \; ...etc.$$

In a similar manner we can find the optimum frequency response functions connecting the coherent inputs by setting $y=j$

$$L_{ij}(opt) = \frac{G_{ij.123...(i-1)}}{G_{ii.123...(i-1)}} \qquad (14)$$

where $i = 1,2,...,p$, $j > i$
leading to

$$L_{12} = \frac{G_{12}}{G_{11}} \qquad L_{13} = \frac{G_{13}}{G_{11}} \; .....$$

$$L_{23} = \frac{G_{23.1}}{G_{22.1}} \qquad L_{24} = \frac{G_{24.1}}{G_{22.1}} \; .....$$

$$. . . . . . . .$$

$$L_{(p-1)p} = \frac{G_{(p-1)p.123...(p-1)}}{G_{(p-1)(p-1).123...(p-1)}}.$$

At this point we have developed expressions for the optimum frequency response functions in terms of conditioned auto- and cross-spectra; now we need to be able to obtain these spectra from the original nonconditioned spectra. An iterative algorithm is used to do this; the derivation is rather lengthy and so will be omitted. Details may be found in reference 3. The general expression to be used is

$$G_{ij.123...r} = G_{ij.123...(r-1)}$$
$$\cdot L_{rj}G_{ir.123...(r-1)} \qquad (15)$$

where    $i = 1,2,3,...p,y; \quad j \leq i; \quad r < j.$

Spec'-' ises are

r=1:    $G_{ij.1} = G_{ij} - L_{1j}G_{i1}$

r=2:    $G_{ij.12} = G_{ij.1} - L_{2j}G_{i2.1}$

r=3:    $G_{ij.123} = G_{ij.12} - L_{3j}G_{i3.12}$

where

$i,j = 2,3,...p,y$

$i,j = 3,4,...p,y$

$i,j = 4,5,6,...p,y$ respectively.

. . . . . . . . . . . . . . .

r=p:    $G_{yy.123...p} = G_{yy.123...(p-1)}$
$$- L_{py}G_{yp.123...(p-1)}$$

To obtain the general auto-spectrum form, set i=j in (15)

$$G_{jj.123...r} = G_{jj.123...(r-1)}$$
$$- L_{rj}G_{jr.123...(r-1)}. \qquad (16)$$

Now rewrite equation (14) with i replaced by r

$$L_{rj} = \frac{G_{rj.123...(r-1)}}{G_{rr.123...(r-1)}}. \qquad (17)$$

Take complex conjugates and solve for $G_{jr.123...(r-1)}$, then substitute into (16) to obtain

$$G_{jj.123...r} = G_{jj.123...(r-1)}$$
$$- |L_{rj}|^2 G_{rr.123...(r-1)}. \qquad (18)$$

Again, we could evaluate special cases by setting r-1,2...p and then varying j so that j=r+1, r+2,...p,y. The iterative process of obtaining the ordered conditioned auto-spectra from the original auto-spectra is illustrated in Fig. 3.



Fig. 3 -
Diagram showing how ordered conditioned auto-spectra are obtained from original auto-spectra [3]

The PCFs between the conditioned inputs and outputs are now defined as

$$\gamma^2_{iy.123...(i-1)} \tag{19}$$

$$= \frac{|G_{iy.123...(i-1)}|^2}{G_{ii.123...(i-1)} \; G_{yy.123...(i-1)}}.$$

A general formula connecting multiple coherence functions with associated ordinary and partial coherence functions is derived in reference 7. For a system with p inputs, this formula is

$$\gamma^2_{y:x} = 1 - \left\{ (1 - \gamma^2_{1y}) \; (1 - \gamma^2_{2y.1}) \right. \tag{20}$$

$$\left. (1 - \gamma^2_{3y.12}) \dots (1 - \gamma^2_{py.123... \; p-1}) \right\}.$$

Note that $\gamma^2_{y:x} = 1$ if, and only if, the OCF or one of the PCFs equals unity, and $\gamma^2_{y:x} = 0$ if, and only if, all of these functions equal zero. For the case where the inputs are independent, equation (20) reduces to the simpler result of equation (7).

## APPLICATION TO A THREE-INPUT/SINGLE-OUTPUT SYSTEM

The general theory discussed in the previous section was applied to the special case of a system with three inputs, which may be either independent or mutually coherent, and a single output. This system corresponds to the test setups used to obtain data from which the computational technique was developed. The test results provide inputs $x_1(t)$, $x_2(t)$, $x_3(t)$ and an output $y(t)$; both independent and coherent inputs were applied as separate cases. These time histories were then processed to yield average estimates of auto-spectra $G_{11}(f)$, $G_{22}(f)$, $G_{33}(f)$ and $G_{yy}(f)$ and (for the coherent case) cross-spectra $G_{12}(f)$, $G_{13}(f)$, $G_{1y}(f)$, $G_{23}(f)$, $G_{2y}(f)$ and $G_{3y}(f)$. For the independent input case, the OCFs were computed using equations (3) and (4) and then the MCF was calculated from equation (7).

In the coherent input case, the OCFs were computed for use in reordering the inputs. The ordered, conditioned auto- and cross-spectra were next calculated from equations (15) and (16). To start the iteration process it was necessary to calculate the first set of optimized frequency response functions from (14)

$$L_{12} = \frac{G_{12}}{G_{11}} \quad L_{13} = \frac{G_{13}}{G_{11}} \quad L_{1y} = \frac{G_{1y}}{G_{11}}. \tag{21}$$

Note that these are ratios of nonconditioned spectra only.

The relationships in (21) were used with equations (15) and (18) to calculate the first set of conditioned auto- and cross-spectra

$$\left. \begin{aligned} G_{22.1} &= G_{22} - |L_{12}|^2 \; G_{11} \\ G_{33.1} &= G_{33} - |L_{13}|^2 \; G_{11} \\ G_{yy.1} &= G_{yy} - |L_{1y}|^2 \; G_{11} \end{aligned} \right\} \tag{22}$$

$$\left. \begin{aligned} G_{23.1} &= G_{23} - L_{13} G^*_{12} \\ G_{2y.1} &= G_{2y} - L_{1y} G^*_{12} \\ G_{3y.1} &= G_{3y} - L_{1y} G^*_{13}. \end{aligned} \right\} \tag{23}$$

The next set of frequency response functions was then obtained

$$L_{23} = \frac{G_{23.1}}{G_{22.1}} \quad L_{2y} = \frac{G_{2y.1}}{G_{22.1}}. \tag{24}$$

Knowing these, we computed the next set of conditioned spectra

$$\left. \begin{aligned} G_{33.12} &= G_{33.1} - |L_{23}|^2 \; G_{22.1} \\ G_{yy.12} &= G_{yy.1} - |L_{2y}|^2 \; G_{22.1} \\ G_{3y.12} &= G_{3y.1} - L_{2y} \; G^*_{23.1}. \end{aligned} \right\} \tag{25}$$

Using (22), (23) and (25), the two partial coherence functions were calculated

$$\gamma^2_{2y.1} = \frac{|G_{2y.1}|^2}{G_{22.1} \; G_{yy.1}} \tag{26}$$

$$\gamma^2_{3y.12} = \frac{|G_{3y.12}|^2}{G_{33.12} \; G_{yy.12}}. \tag{27}$$

Finally, the multiple coherence function was computed

$$\gamma^2_{y:x} = 1 \tag{28}$$

$$- (1 - \gamma^2_{1y})(1 - \gamma^2_{2y.1})(1 - \gamma^2_{3y.12}).$$

The data analysis process is summarized in Fig. 4.

## EXPERIMENTAL PROGRAM

A typical complex aerospace structure (a modified Titan instrumentation truss) was tested to provide data for use in demonstrating the computational technique. A panel

carrying a simulated component was mounted on the top of the truss. It was designed so its first three resonances would occur in the range from 50 to 300 Hz. The assembly was hung inside Martin Marietta's acoustic chamber on a 2-Hz suspension system and was connected via two pushrods to two shakers. The shakers were mounted on rubber isolation pads to minimize feedback of mechanical vibration through the floor.

Record Analog Time Histories, $x_i(t)$ & $y(t)$

Low-Pass Anti-Aliasing Filter

Digitize Data, Subdivide Each Channel into n Records

Compute Auto-Spectra $G_{ii}$ & $G_{yy}$ Averaged Over n Records

Independent Inputs

Coherent Inputs

Compute Cross-Spectra $G_{iy}$ Averaged Over n Records

Compute OCFs $\gamma_{iy}^2$

Compute MCF $\gamma_{y:x}^2$

Compute Cross-Spectra $G_{iy}$ & $G_{ij}$ Averaged Over n Records

Compute OCFs $\gamma_{iy}^2$ & Use to Reorder Inputs

Compute Optimum Transfer Functions $L_{iy}$ & $L_{ij}$

Compute Ordered Conditioned Auto-Spectra $G_{ii.123...}$

Compute Ordered Conditioned Cross-Spectra $G_{iy.123..}$ & $G_{ij.123..}$

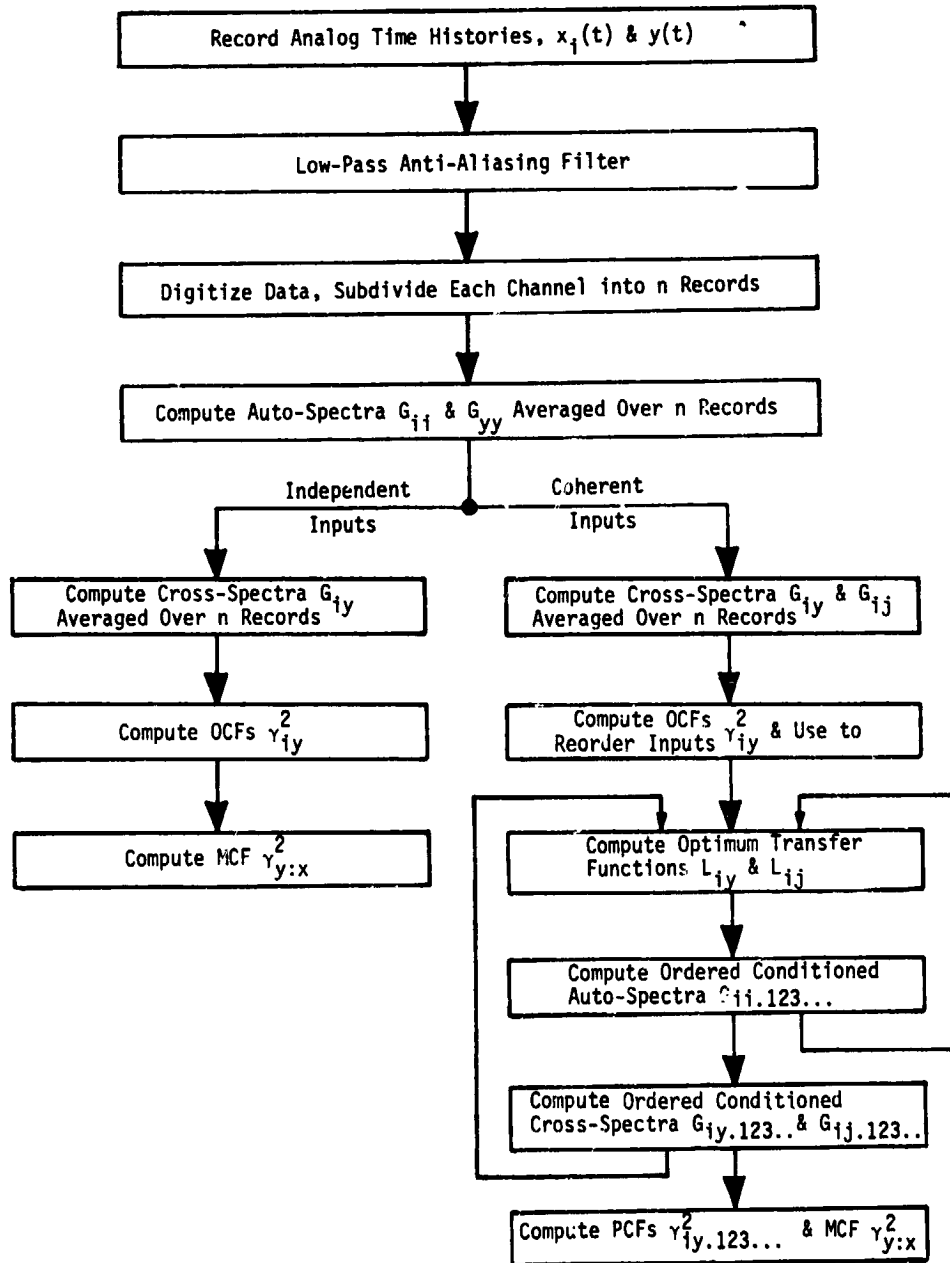Compute PCFs $\gamma_{iy.123...}^2$ & MCF $\gamma_{y:x}^2$

Fig. 4 - Data analysis flow chart

The test setup was designed to be capable of applying two separate random mechanical vibration inputs through the truss to the panel, combined with direct acoustically induced vibration. Thus as many as three inputs could be applied simultaneously. For the coherent input case, the two shakers were driven through a single power amplifier/random noise generator system. For the case of three independent inputs, separate power amplifiers and random noise generators were used. The output was defined as the response acceleration measured at the simulated component on the panel.

A sketch of the test setup is shown in Fig. 5 in which the transducers used to measure the inputs and the output are identified in the notation used for data analysis.
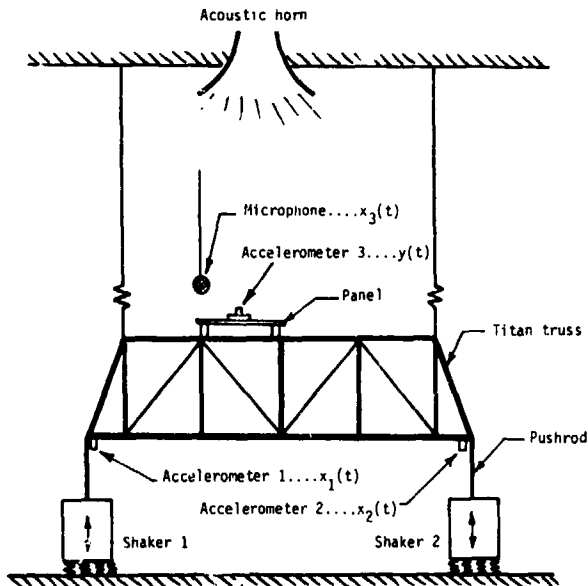


Fig. 5 - Sketch of test setup

DISCUSSION OF RESULTS

The technique used on the test data consisted of first calculating the averaged auto- and cross-spectra for the inputs and output signals, then computing the OCF between each pair of inputs $(\gamma_{ij}^2)$ and between each input/output combination $(\gamma_{iy}^2)$. The $\gamma_{ij}^2$ were then reviewed to determine whether the two inputs $x_i$ and $x_j$ should be treated as being independent or correlated (i.e., mutually coherent). According to Bendat in private discussions, a value of $\gamma_{ij}^2$ of 0.1 is low enough for an assumption of independance; a higher value indicates significant coherence between the inputs. At the other end of the scale, $\gamma_{ij}^2 \geq 0.9$ means that the two inputs are effectively fully coherent and

should therefore be treated as a single input to the system.

Six different combinations of inputs were used in the test program, but for the purposes of this paper it will suffice to discuss the results obtained from analyzing three cases.

Case 1 used two vibration inputs that were intended to be correlated with an independent acoustic input, while case 2 used two nominally independent vibration inputs. Case 3 was a single-input/single-output test setup.

Case 1 Data

Acceleration and pressure spectral density plots for the three inputs and the response are given in Fig. 6. The two shaker inputs were very similar in spectrum shape. The panel response exhibited prominent peaks at approximately 68, 160, 230, 290 and 420 Hz.

The OCF between the two shaker inputs is plotted in Fig. 7. This shows that the coherence between the inputs was quite low in the frequency range below 100 Hz, and relatively high at some higher frequencies. However the OCF was in the desired range of 0.10 to 0.90 over most of the frequency band. The OCFs between each individual shaker input and the acoustics input were examined next; these are presented in Fig. 8 and 9. Although the shaker inputs and the acoustic input were theoretically independent, a significant degree of mutual coherence is indicated. This is thought to be caused by the acoustically induced panel response being transmitted through the truss structure and coupled into the vibration environment as recorded by the shaker input accelerometers. It was therefore decided that case 1 data should be regarded as representing a system with three correlated inputs and a single output.

The resulting coherence functions are shown in Fig. 10 through 13. When these are examined in conjunction with the panel response plot [Fig. 6(d)], several features become apparent:

1) Figure 10 indicates $\gamma_{1y}^2 = 0.78$ at 68 Hz, showing that the high response at this frequency resulted mainly from the shaker 1 input. Figures 11 and 12 are plots of the partial coherence functions between shaker 2 and panel response with the effects of shaker 1 removed, and between the acoustic input and panel response with the effects of both shakers removed. Both of the PCFs have quite low values at 68 Hz;

50

(a) Shaker 1 Input

(b) Shaker 2 Input

(c) Acoustic Input

(d) Panel Response
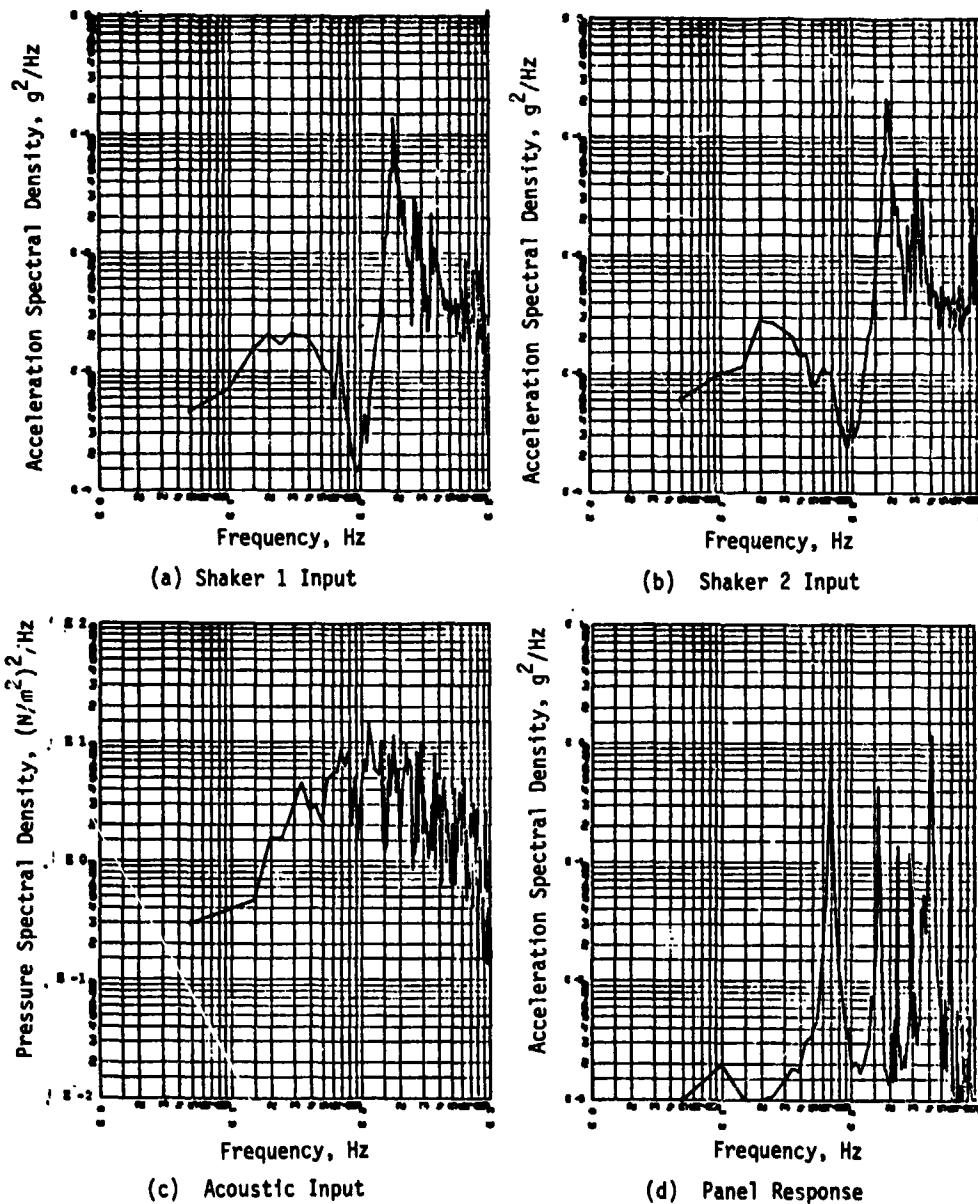
Fig. 6 - Input and response data for case 1

2) The next response peak is at approximately 160 Hz. Figures 10, 11 and 12 show that the two shakers were primarily responsible for this peak, having OCF and PCF values of 0.44 and 0.47 respectively. The PCF associated with the acoustic input at this frequency is less than 0.10. It is interesting to note that (Fig. 7) the mutual coherence between the two shakers was very high ( 0.98) in the 150 to 180-Hz range, whereas the mutual coherences between the individual shakers and the acoustic input (Fig. 8 and 9) were close to zero ( 0.02). Thus in this frequency band the system should

actually be analyzed as a model having two independent inputs and a single output;

3) The third response peak, occurring at about 230 Hz, was evidently due mainly to the input from shaker 2 since $\gamma^2_{2y.1}$ = 0.53, whereas $\gamma^2_{1y}$ = 0.15 and $\gamma^2_{3y.12}$ = 0.26 at this frequency;

4) Another narrow response peak is seen at approximately 290 Hz. The CF values at 290 Hz are $\gamma^2_{1y}$ = 0.02, $\gamma^2_{2y.1}$ = 0.01

51

and $\gamma^2_{3y.12} = 0.85$; thus this peak was clearly caused by the acoustic input;

5) A rather broad response peak is centered at about 420 Hz. This also was obviously caused by the acoustic input, which has $\gamma^2_{3y.12} = 0.6$ at 420 Hz. The OCF and PCF for the shakers are approximately $\gamma^2_{1y} = 0.05$ and $\gamma^2_{2y.1} = 0.06$ at this frequency.
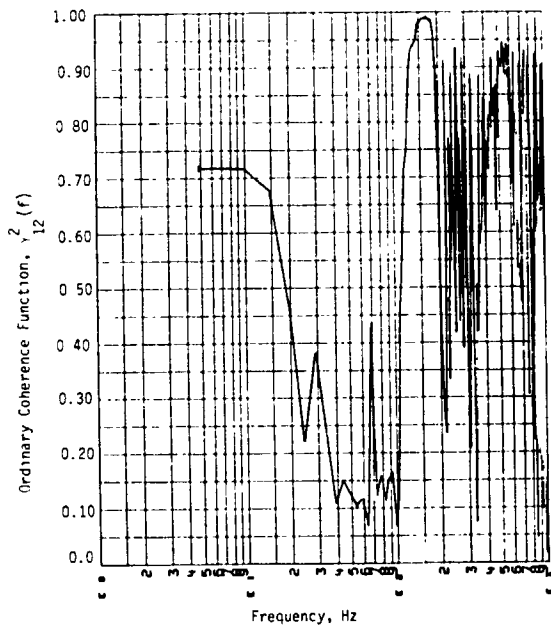


Fig. 7 -
Ordinary coherence function between shaker 1 and shaker 2 inputs (case 1)

Table 1 summarizes the ordinary and partial coherence functions associated with the first five response peaks on the panel. The multiple coherence function values from Fig. 13 at these frequencies are also tabulated.

TABLE 1
Values of Coherence Functions at
Panel Resonance (Case 1)

| Frequency, Hz | $\gamma^2_{1y}$ | $\gamma^2_{2y.1}$ | $\gamma^2_{3y.12}$ | $\gamma^2_{y:x}$ |
|---|---|---|---|---|
| 68 | 0.78 | 0.09 | 0.04 | 0.81 |
| 161 | 0.44 | 0.47 | 0.08 | 0.73 |
| 230 | 0.15 | 0.56 | 0.26 | 0.72 |
| 290 | 0.02 | 0.01 | 0.85 | 0.86 |
| 420 | 0.05 | 0.06 | 0.60 | 0.64 |

The amount by which the MCF is less than one represents the effects of noise and nonlinearities in the system. Since these effects may be assumed to be statistically independent of the inputs, they do not contaminate the individual coherence functions as-
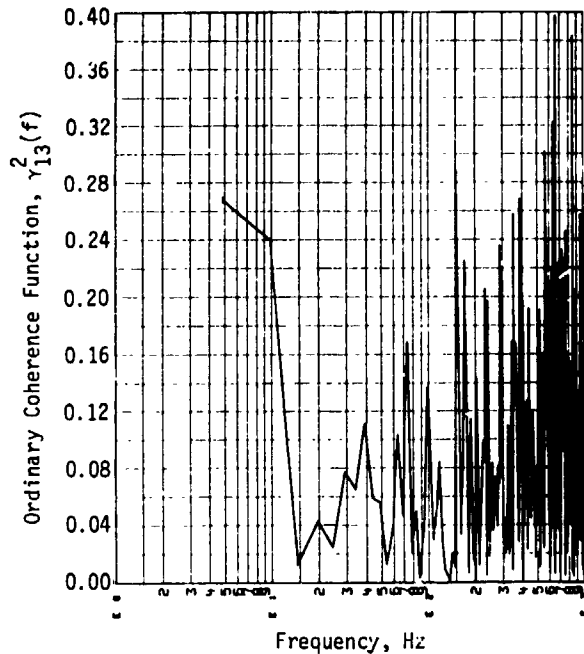


Fig. 8 -
Ordinary coherence function between shaker 1 and acoustics (case 1)
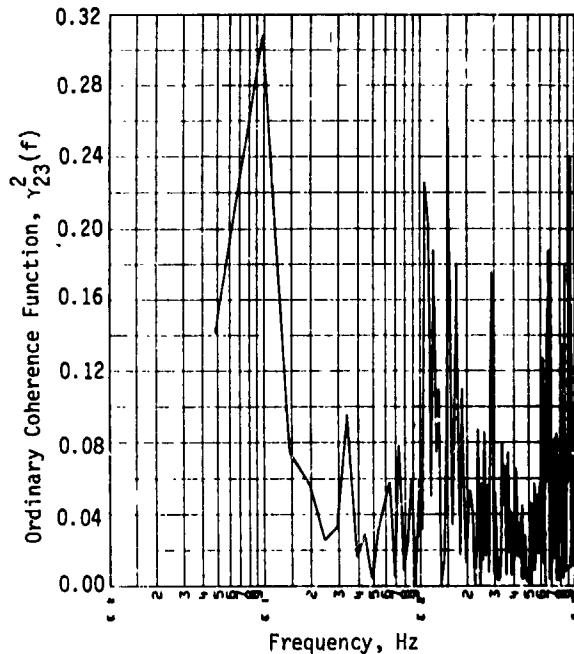


Fig. 9 -
Ordinary coherence function between shaker 2 and acoustics (case 1)

sociated with the inputs. They contaminate only the multiple coherence function, which represents the coherence between the full set of inputs and the measured output.
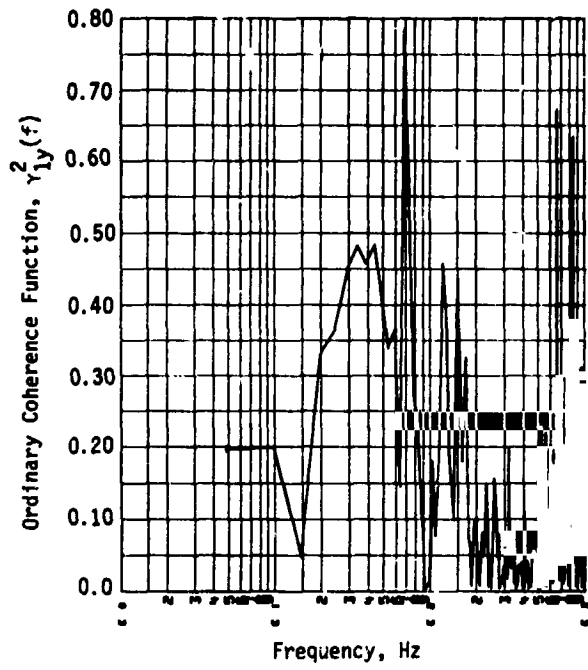
Fig. 10 -
Ordinary coherence function between shaker 1
and panel response (case 1)
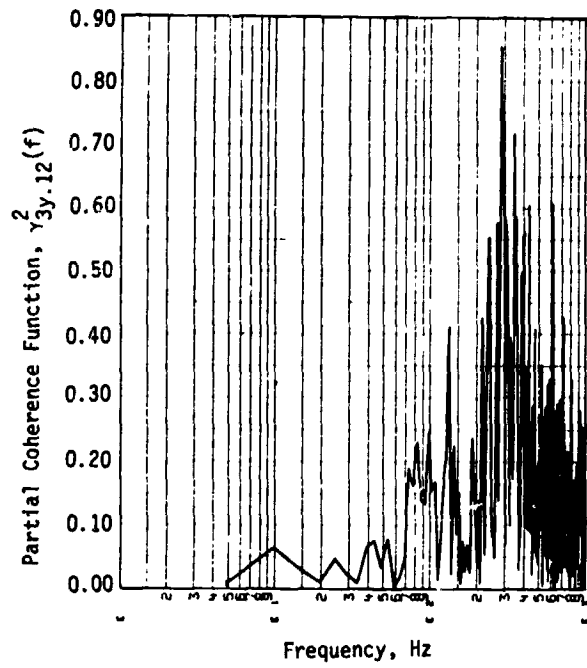


Fig. 12 -
Partial coherence function between
acoustics and panel response (case 1)



Fig. 11 -
Partial coherence function between shaker 2
and panel response (case 1)
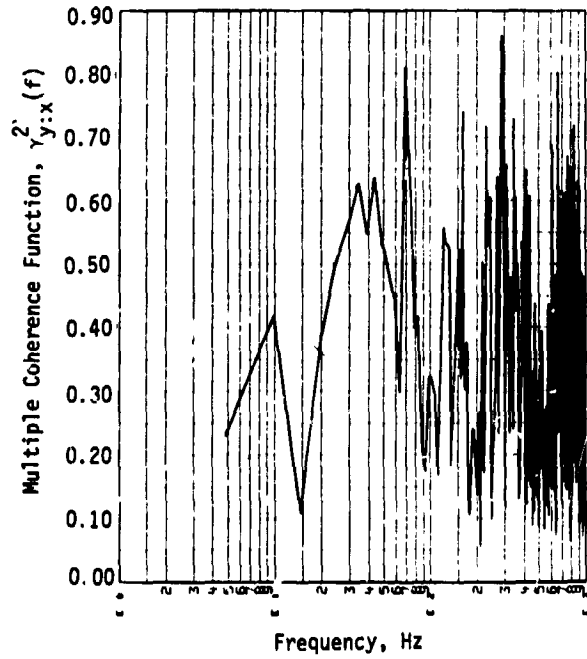


Fig. 13 -
Multiple coherence function between
total set of inputs and panel response
(case 1)

## Case 2 Data

Two nominally unco.related inputs were used for this test run. Fig. 14 shows the input and response data. As usual, the coherence between the inputs was first calculated to verify that the assumption of independence was correct. Fig. 15 shows that this was the case except at the 4.8-Hz point and at some frequencies above 500 Hz when the value of the OCF exceeded the Bendat criterion of 0.10 by a small margin. It was concluded that it would be reasonable to ignore this degree of mutual coherence and treat the system inputs as uncorrelated.

The OCF plots between each input and the output appear in Fig. 16 and 17. When these are reviewed in conjunction with the panel response plot in Fig. 14(c), it is clear that the response peaks at 70 and 160 Hz are due primarily to the shaker input, while the resonance at 410 Hz appears to be driven most efficiently by the acoustics. The MCF plot in Fig. 18 again shows that a high degree of "noise" is present in the data. The CF values of the first three resonances are given in Table 2.



(a) Shaker 1 input          (b) Acoustic Input
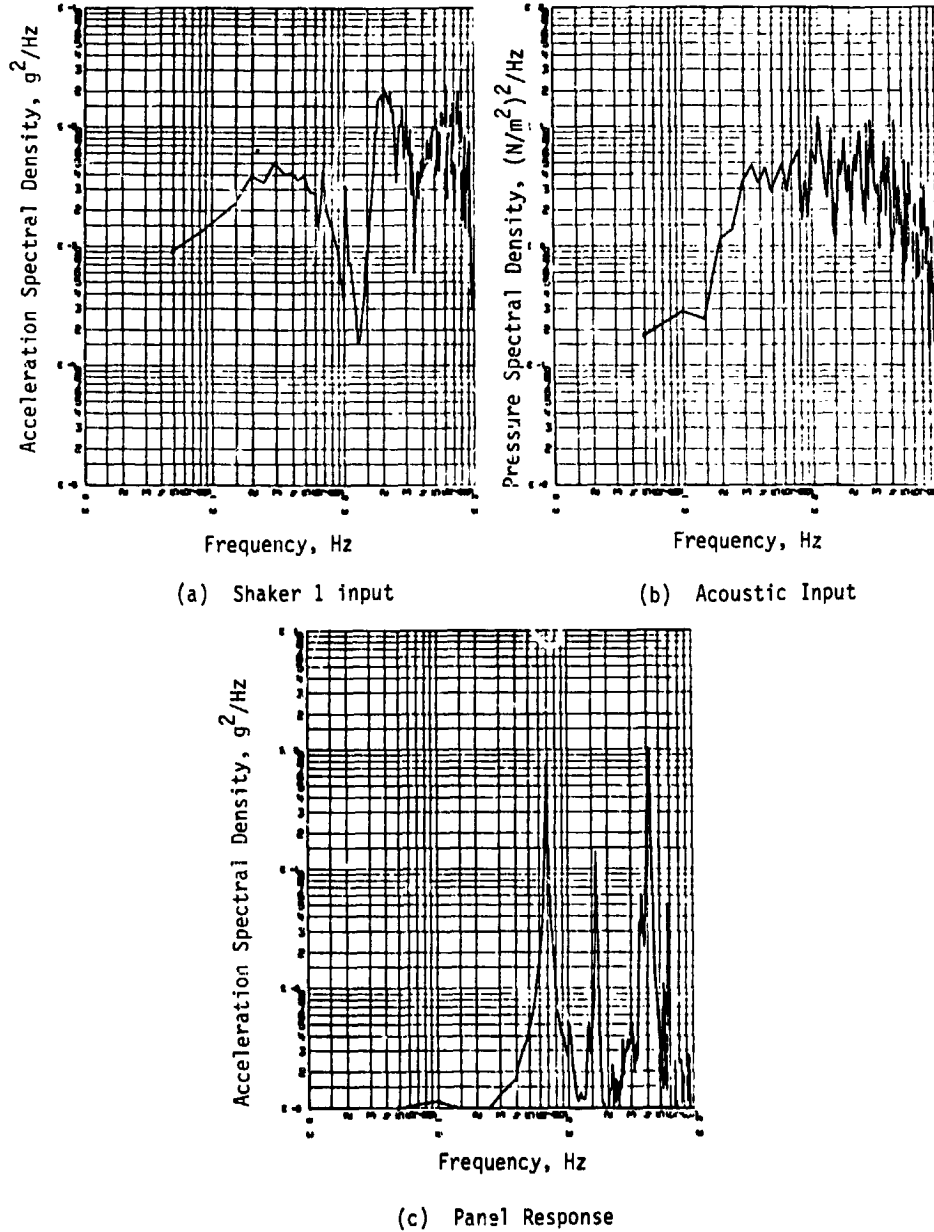


(c) Panel Response

Fig. 14 - Input and response data for case 2

TABLE 2
Values of Coherence Functions
at Panel Resonance (Case 2)

| Frequency, Hz | $\gamma^2_{1y}$ | $\gamma^2_{3y.1}$ | $\gamma^2_{y:x}$ |
|---|---|---|---|
| 70 | 0.55 | 0.05 | 0.61 |
| 160 | 0.47 | 0.05 | 0.52 |
| 410 | 0.08 | 0.58 | 0.66 |

## Case 3 Data

The data taken from this case were used to investigate the effect of varying the number of data segments used in the averaging process prior to calculating the OCF. Fig. 19 shows four versions of the OCF, in which 10, 50, 100 and 200 averages were used. With only four different cases, the results were not conclusive; however, as illustrated in Table 3, the variation at some frequencies was large enough to suggest that a number of averages in the region of 200 are necessary to ensure reasonable accuracy. On the other hand, if a fixed record length of data is available for analysis, the accuracy of the results will be degraded if the length of each segment is reduced. A detailed error analysis is necessary to ensure that the best tradeoff is made (see reference 9).

## CONCLUSIONS

From the study results it was concluded that the coherence function technique is ef-



Fig. 16 -
Ordinary coherence function between shaker 1 and panel response (case 2)



Fig. 15 -
Ordinary coherence function between shaker 1 and acoustics (case 2)
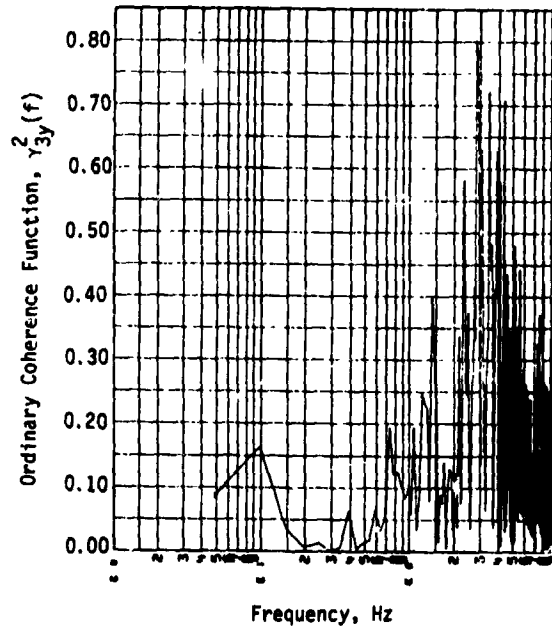


Fig. 17 -
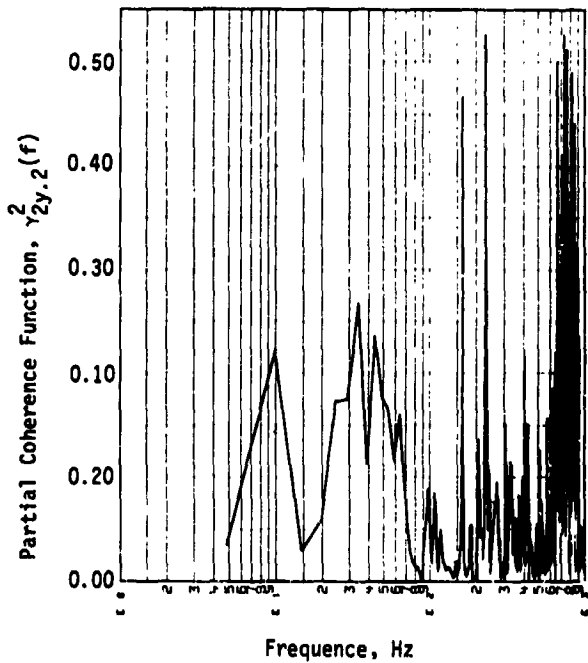Ordinary coherence function between Acoustics and panel response (case 2)

55

**Fig. 18 -**
Multiple coherence function between total
set of inputs and panel response (case 2)

TABLE 3
Effect of Averaging on OCF
Values

| Frequency, Hz | No. of Averages | Value of OCF |
|---|---|---|
| 44 | 10 | 0.69 |
| | 50 | 0.52 |
| | 100 | 0.52 |
| | 200 | 0.55 |
| 110 | 10 | 0.41 |
| | 50 | 0.43 |
| | 100 | 0.48 |
| | 200 | 0.58 |
| 400 | 10 | 0.60 |
| | 50 | 0.50 |
| | 100 | 0.46 |
| | 200 | 0.40 |
| 660 | 10 | 0.91 |
| | 50 | 0.85 |
| | 100 | 0.77 |
| | 200 | 0.74 |

fective in identifying the relative contri-
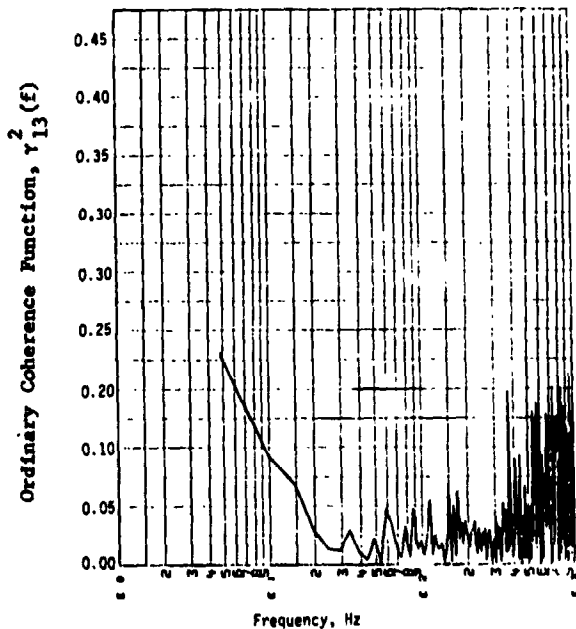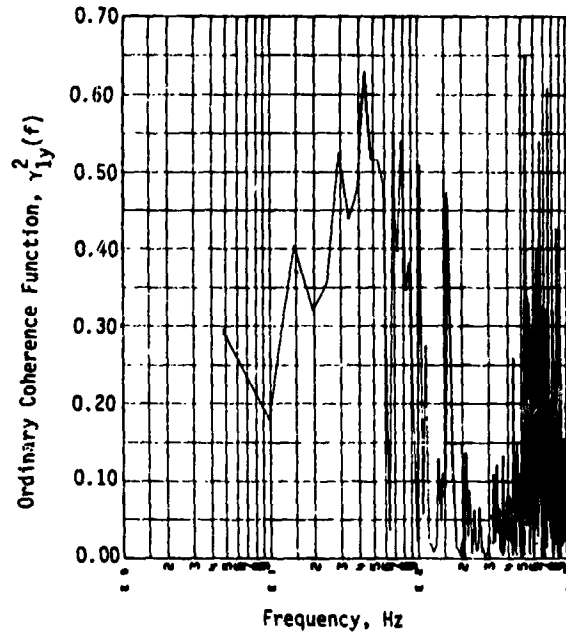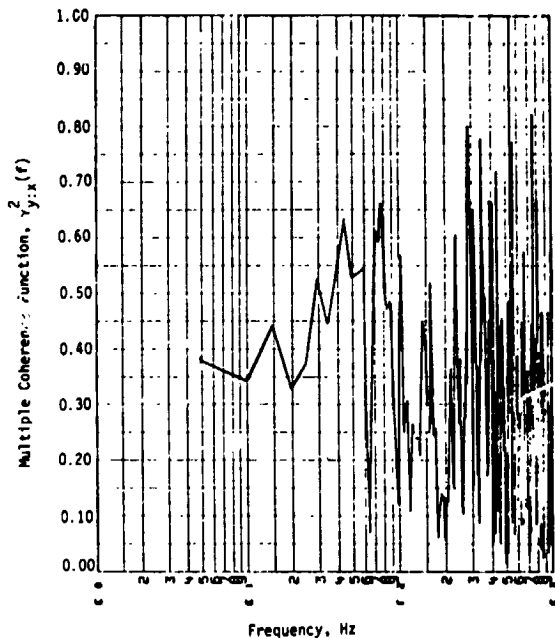butions of multiple sources of dynamic ex-
citation to the response of a practical me-
chanical system. However, this was found to
be true for the system tested only in the
region of resonant response frequencies. The
technique did not give good results at fre-
quencies between resonance when errors in-
duced by noise and/or system nonlinearities
were apparently similar in magnitude to the
quantities being used in the calculation.
This is not a serious handicap when using the

technique strictly for source identification
since such information is generally of great-
est interest at resonant frequencies. The
"noise level" was high in all of the test
cases, as indicated by the fact that the mul-
tiple coherence function approached unity
only at a relatively few frequency points.
For an ideally linear and noise-free system,
the MCF should have a value of 1.0 across
the full frequency band if all the appro-
priate inputs have been properly included.

The iterative approach developed by
Bendat [3 and 7] was used to calculate the
partial coherence functions for the case in-
volving correlated inputs. A comparison of
this approach with the other matrix-based for-
mulation [4, 5 and 6] showed the iterative
method to be conceptually simpler and probably
more economical in computer time, especially
as the number of correlated inputs increases.
To verify this conclusion it would be neces-
sary to analyze an appropriate model by both
methods and make a direct cost comparison.

To determine whether the inputs to the
system were correlated it was necessary to
calculate the OCFs between the various inputs;
if the value of the OCF was no greater than
0.1, it was assumed that the two inputs in-
volved were uncorrelated so the source identi-
fication could be carried out in terms of
OCFs. If the OCF > 0.1, the inputs were as-
sumed to be correlated and the more complex
PCFs had to be calculated. This test must be
performed as a routine part of the analysis.
It was found that in some cases inputs de-
signed to be independent were actually quite
well correlated at certain frequencies due to
structural feedback between the measurement
points. When the test indicates that the in-
puts are well-correlated at some (but not all)
frequencies, the problem can be broken down
into two parts on a frequency basis, and the
appropriate coherence functions (ordinary or
partial) can be calculated for each part. If
the two frequency ranges are not well separ-
ated, a practical approach would be to assume
that the inputs are correlated at all frequen-
cies and analyze accordingly. At frequencies
where this is not true, the appropriate terms
will drop out and the correct solution will be
obtained at the expense of some increase in
computer time.

The effect of increasing the number of
data segments used for averaging was demon-
strated. The input/output OCF was plotted
for 10, 50, 100 and 200 averages. It was con-
cluded from variations in the plots that it
is desirable to use 150 to 200 averages to
ensure that the CF estimate is reasonably ac-
curate without incurring excessive computer
costs. Since the duration of the data seg-
ments affects the accuracy of the results, as
well as the number of segments, a tradeoff
between the two is necessary. A thorough in-
vestigation of this problem would be desir-
able but was beyond the scope of this study.
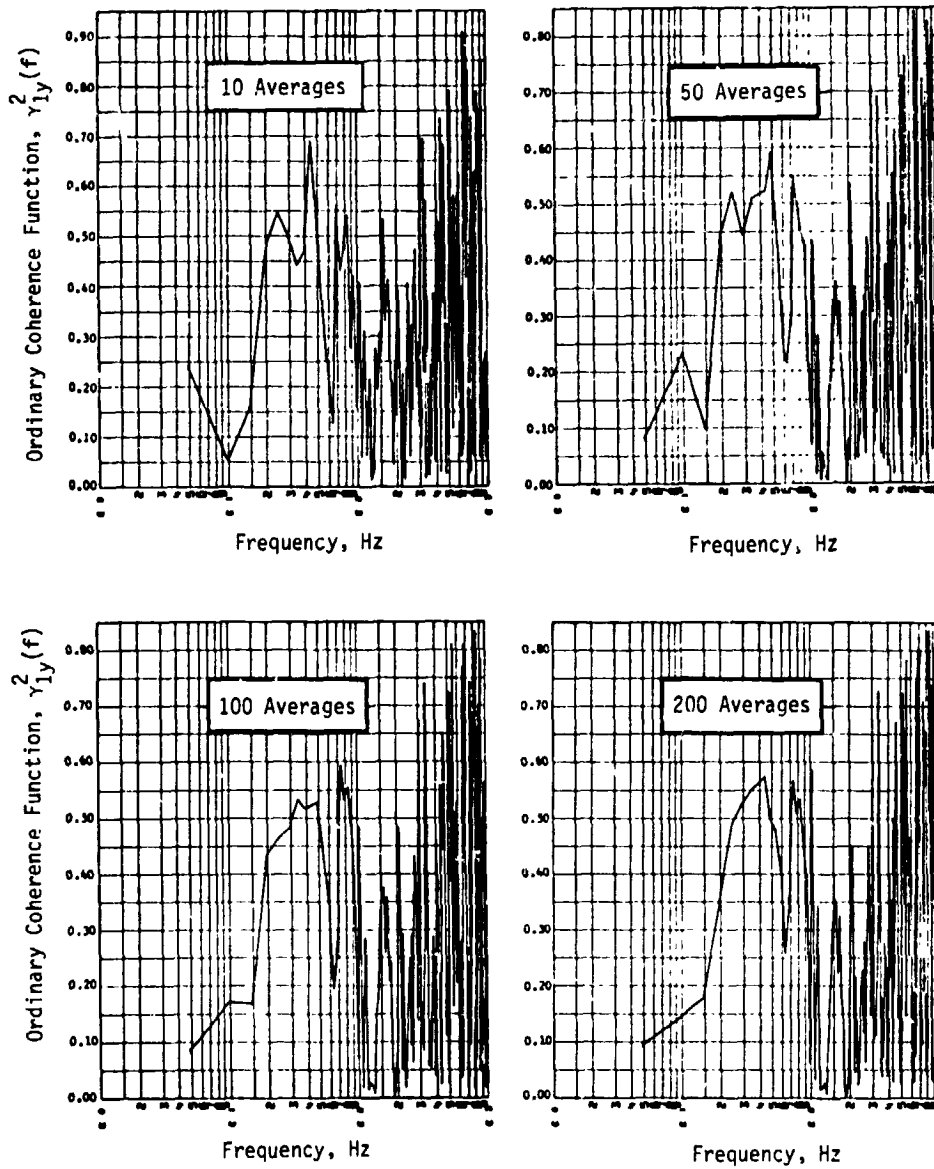
Fig. 19 -
Effect of number of samples on the estimate of ordinary
coherence function (case 2)

REFERENCES

1. J. T. Broch, "On the Applicability and Limitations of the Cross-Correlation and Cross-Spectral Density Techniques," Bruel and Kjaer Technical Review No. 4, pp. 3-27, 1970

2. R. E. Thaller and J. Pearson, "Coherence Functions Used to Define Sources of Airborne Antenna Vibration," U.S. Air Force Report AFFDL-TR-75-143, December 1975

3. J. S. Bendat, "System Identification from Multiple Input/Output Data," J. Sound & Vib., 49(3), pp. 293-308, 1976

4. N. R. Goodman, "Measurement of Matrix Frequency Response Functions and Multiple Coherence Functions," U.S. Air Force Report AFFDL-TR-65-56, June 1965

5. J. S. Bendat and A. G. Piersol, Random Data: Analysis and Measurement Procedures, pp. 136-167, Wiley and Sons, New York, 1972

6. R. Potter "Matrix Formulation of Multiple and Partial Coherence," J. Acoust. Soc. Am., Vol. 61, No. 3, pp. 776-781, March 1977

7. J. S. Bendat, "Solutions for the Multiple Input/Output Problem," J. Sound & Vib., 44(3), pp. 311-325, 1976

8. W. G. Halvorsen and J. S. Bendat, "Noise Source Identification Using Coherent Output Power Spectra," Sound and Vibration, Vol. 8, No. 8, August 1975

9. J. S. Bendat, "Statistical Errors in Measurement of Coherence Functions and Input/Output Quantities," J. Sound & Vib., 59(3), pp. 405-421, 1978

# STATUS OF CAVITY NOISE PHENOMENA MEASUREMENT AND SUPPRESSION ON THE B-1 AIRCRAFT

A. G. Tipton and C. H. Hodson
Los Angeles Division, Rockwell International
El Segundo, California

During the B-1 aircraft development, an extensive program of weapons bay cavity noise measurement and suppression studies was performed using wind tunnel models, flight test measurements, and aircraft design modifications. Substantial cavity noise reduction was demonstrated during flight test operations. The unsuppressed cavity noise level of 170 dB was reduced to values less than 150 dB with external retractable spoilers upstream of the cavity opening. This paper presents an overview of the cavity noise investigation and the development of the B-1 weapons bay noise suppressor. Flight test data obtained with and without the noise suppressor are shown.

## SUMMARY

High-speed flow over open cavities generates intense discrete and broadband pressure fluctuations that adversely affect aircraft systems. During the B-1 aircraft development, an extensive program of weapon bay cavity noise measurement and suppression studies was performed using wind tunnel models, instrumented aircraft, and design modifications.

Initial noise-level measurements for unsuppressed cavities at low dynamic pressures and mach numbers indicated the presence of four discrete cavity oscillation modes superimposed on broadband turbulence pressure. Extrapolation of the low-q d    o high-q flight conditions showed good c       son with calculated values based on empiri  .1 prediction techniques for the maximum cavity discrete and broadband pressures. The maximum extrapolated overall level for the unsuppressed cavity was 170 dB.

The high noise levels caused unacceptable weapons bay door vibration, high crew station vibration, and concern for internal stores and aircraft subsystems in the vicinity of the weapons bays.

Initial wind tunnel investigation of several cavity noise reduction concepts indicated substantial attenuation was possible using external spoilers. The concepts evaluated consisted of simple 45 and 90 degree ramps on the forward bulkhead, and on both the forward and aft bulkheads of an open cavity, as well as a more sophisticated deflector-diffuser concept.

Flight test measurements with retractable spoilers installed upstream of the cavity front bulkhead showed substantial noise reductions in both the broadband pressures and discrete cavity resonances. The broadband pressures were reduced 10 dB, and the discrete cavity resonances were reduced approximately 20 dB. The cavity noise-level reduction achieved by the retrofitted spoiler reduced door vibration amplitudes and crew station vibration to acceptable levels. The maximum bay acoustic environment of stores and equipment was reduced from 170 to approximately 150 dB.

## INTRODUCTION

High-speed flow over open cavities generates intense discrete frequency and broadband pressure fluctuations. The design of aircraft structure and equipment for adequate life in the severe noise environment can require unacceptable time, cost, and weight increments. Supression of the cavity noise is a possible alternative to design for tolerance of the environment. In the case

of the B-1 weapons bays, the environmental problem was particularly severe without noise suppression because of the high flight dynamic pressures at which the weapons bays were required to be opened.

A noise-suppression device was developed and tested for the B-1 weapons bays. The purpose of this paper is to describe the development program for the B-1 weapons bay noise-suppression device, and to report some of the test results which have been obtained.

WEAPONS BAY LOCATION AND DESCRIPTION

Figure 1 shows the location of the three weapons bays on the aircraft. Although all three bays are the same internally, there are differences in the boundary layer characteristics at each bay location. The differences in flow field over the forward and center bay are not appreciable. Therefore, the internal bay acoustics would be expected to be very similar in the forward and center bays. However, the aerodynamic characteristics over the aft bay are significantly different from those over the forward and center bays. The boundary layer is thicker at the aft bay location. The engine nacelles cause a venturi effect so that the local mach number and dynamic pressure over the aft bay are higher than the freestream values. At supersonic mach numbers, shock waves from the engine inlets also influence the flow over the aft bay. These external aerodynamic differences over the aft bay area would be expected to cause the acoustic characteristics in the aft bay to be significantly different from those in the forward and center bays.
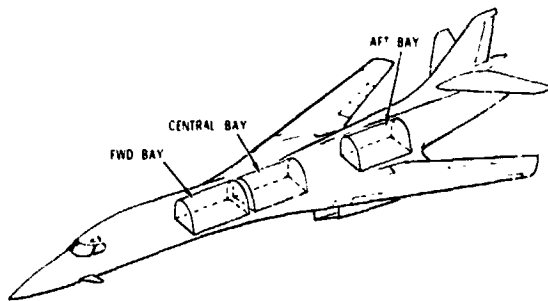
Fig. 1 - Weapons bay locations

The weapons bay doors may be opened in flight to the fully open position, or to a nominally "half-open" position, depending on the operational requirement. Figure 2 illustrates the two door positions. The width of the cavity which is open to the airstream is different for the two door positions, and results in different cavity noise levels. Figure 3 shows the shape and dimensions of the weapons bay cavities,

which are the same for all three bays. The locations of the microphones used for noise measurements within the bays are also shown in Figure 3.
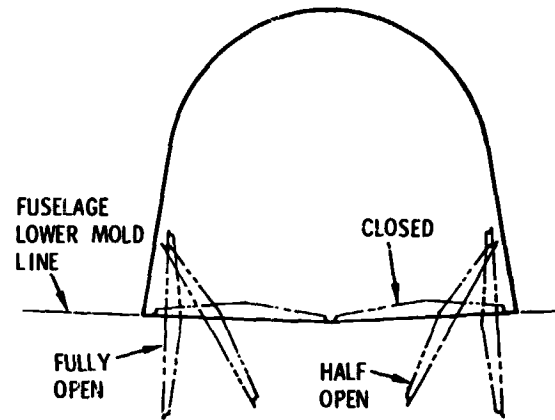
Fig. 2 - Weapons bay door positions
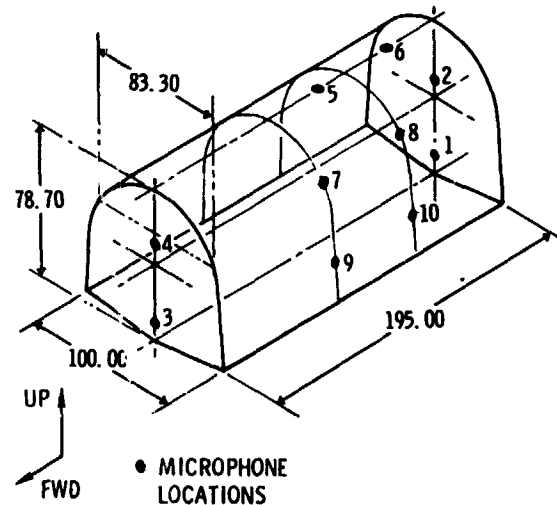
Fig. 3 - Weapons bay geometry and microphone locations

UNSUPPRESSED CAVITY NOISE LEVELS

The first B-1 weapons bay noise-level measurements were made at low dynamic pressure without noise suppression devices. Figure 4 shows the acoustic levels measured for half-open and fully open weapons bay doors. The first four natural frequencies of the doors were determined during ground resonance tests. The resulting frequencies are shown in figure 4. It may be noted that the cavity resonance frequencies are in the same range as the door natural frequencies. This resulted in excessive door vibration at low dynamic pressures. Extrapolation of the

60

door vibration response to higher dynamic pressures indicates premature failure of the doors or operating mechanism.
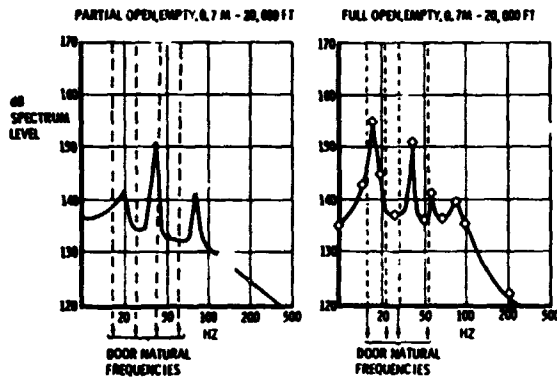


Fig. 4 - Weapons bay acoustic levels - unsuppressed

The acoustic levels for broadband noise and discrete frequency cavity resonance were predicted by the methods of reference 1 for the B-1 weapons bay with fully open doors. The predictions for M = 0.85 at sea level are shown in figure 5. The flight test measurements taken at lower dynamic pressures were extrapolated to M = 0.85 at sea level. The extrapolation is based on the assumption that acoustic pressure is linearly dependent on flight dynamic pressure, and on mach number effects developed from the data of reference 1. A subsequent section of this paper shows experimental data on the variation in the weapons bay acoustic pressures with flight dynamic pressure at M = 0.85. The data show that over the dynamic pressure range of 367 psf to 1,015 psf, the acoustic pressures are very nearly proportional to flight dynamic pressure. The extrapolated flight test data are compared with the predicted acoustic levels in figure 5. The flight test data shown were measured by the microphone at the lower aft bulkhead location which is designated as microphone location 1 in figure 3. The noise levels on the bay lower aft bulkhead were at least as high as at any of the other locations in the bay. Figure 5 shows good correlation between measured and predicted levels for empty bays with fully open doors. The door position and the presence of stores influenced the acoustic levels of the discrete frequency cavity resonances. As shown in figure 5, the fundamental and third cavity resonance for empty cavities was suppressed by the half-open door position. Stores inside the bay with half-open doors suppressed all discrete resonances to values close to the broadband pressure levels. The presence of stores inside a fully open bay, however, resulted in no appreciable reduction in discrete cavity resonances

relative to an empty bay. The broadband levels were only slightly affected by door-opening position and the presence of stores. The broadband levels with internal stores were in close agreement with predictions for empty cavities.
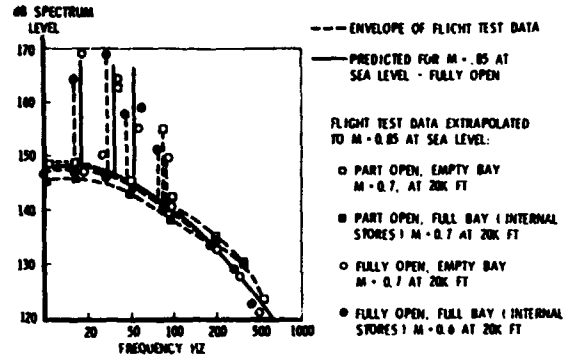


Fig. 5 - Comparison of measured and predicted unsuppressed acoustic levels

Vibration levels were measured at the pilot's station with weapon bays open and closed. The vibration amplitudes with fully open doors were extrapolated with dynamic pressure to the levels which would be expected for M = 0.85 at sea level. The vibration levels in the vertical direction are shown in figure 6, compared with vibration tolerance levels from reference 2. The highest vibration level occurs with fully open doors at the fundamental cavity resonant frequency, and is above the voluntary tolerance level. With closed weapon bays, the vibration response in the frequency range of the 20 to 40 Hz cavity resonances is not measurable. The low-frequency response at approximately 3 Hz, shown in figure 6, corresponds to the first fuselage bending mode, and is the same amplitude with open or closed bays.
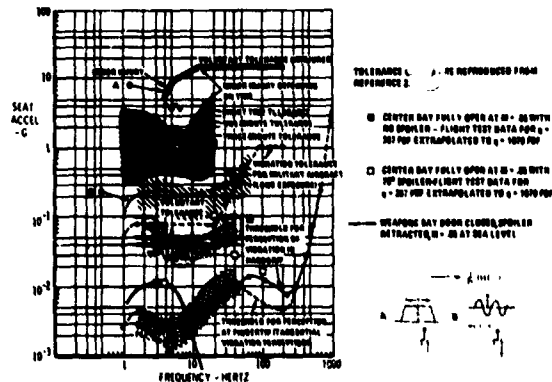


Fig. 6 - Crew station vibration environment compared with tolerance levels

## NOISE SUPPRESSOR DEVELOPMENT

Initial wind tunnel tests showed substantial noise attenuation could be obtained with external spoilers immediately forward and aft of the weapons bay. Several types of spoiler, and variations of the types were tested. Simple 45 and 70 degree ramps, 90 degree fences, and a more complicated deflector diffuser concept were tested. Although the wind tunnel tests indicated the deflector-diffuser type of spoiler to be the most effective noise-reduction device, the associated weight and installation complications were prohibitive. The space available for the spoiler and its required retraction mechanism was severely limited, particularly for the aft bay. The 90 degree fence-type spoiler, which could be retracted vertically, required the least installation space, and was the most compatible with the existing aircraft structure which reacts the aerodynamic loads on the spoiler. Consequently, the wind tunnel tests emphasized testing variations of the 90 degree spoiler. Variations in spoiler extension distance and span were tested over subsonic and supersonic mach number ranges. The most significant results of the wind tunnel tests indicated that (1) a 90-degree spoiler with a span approximately half the width of the weapons bay provided better noise attenuation than a 90-degree spoiler which spanned the full width of the weapons bay, (2) the spoiler panel in front of the bay provided the major part of the noise suppression, and (3) a spoiler panel at the rear of the bay is not required for the B-1 weapons bays. These results were of great significance to the weight, complexity and cost of the spoiler installation. In addition to the savings allowed by fewer and smaller panels, even greater savings are realized in the actuation system and internal structure required to react the spoiler airloads. The wind tunnel tests also indicated that small improvements in spoiler performance could be obtained by making the panel porous, and leaving an open gap between the fuselage surface and the top edge of the spoiler. These features were desired to reduce the static and buffeting loads on the spoiler.

Several wind tunnel tests were conducted with the adjacent forward and center bays open simultaneously, with and without spoilers. In general, the wind tunnel tests indicated the spoilers to be less effective for adjacent bay operation, particularly in suppression of the fundamental cavity resonance mode.

Aerodynamic wind tunnel tests were conducted to determine the effects of the spoiler on aircraft trim loads, engine inlet airflow, and weapons separation. These tests showed that the

effects of the spoiler were acceptable. Weapons separation characteristics were actually shown to be slightly improved by the spoiler.

A temporary flight-test spoiler was installed on the central bay of A/C-1 shortly after the weapons bay wind tunnel tests were completed. The installation is illustrated in figure 7. This spoiler installation was tested over a wide range of subsonic and supersonic speeds. Test data were acquired at dynamic pressures up to 1,015 psf with half and fully open weapons bay doors. The flight tests were conducted with spoiler spans equal to the weapons bay width, and the spoiler span half the weapons bay width. As predicted by the wind tunnel tests for the part open door position, the half-span spoiler provided better noise attenuation than the full-span spoiler. For the fully open door position, the half-span spoiler provided approximately the same suppression as the full-span spoiler. Both solid spoiler panels and panels with 20-percent porosity were tested. The porous panels provided more improvement over the solid panels than was predicted by the wind tunnel tests. In general, the flight test spoiler installation provided greater noise attenuation than measured in the wind tunnel tests. A 10- to 15-dB noise reduction in the discrete frequency cavity resonance noise was measured in the tunnel test for the subsonic range, whereas the flight test spoiler installation provided a 20- to 25-dB reduction in the discrete frequency cavity resonance noise.



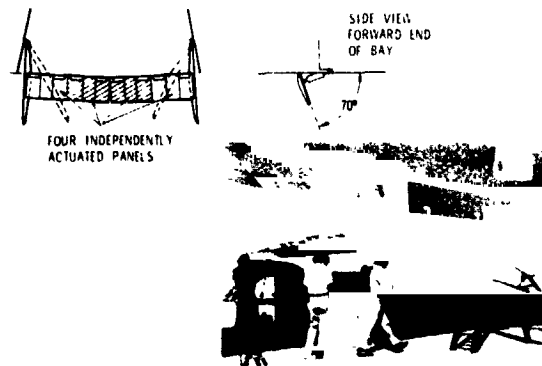Fig. 7 - 70-degree porous spoiler installation

The weapons bay door vibration and the crew station vibration levels were significantly reduced with the 70-degree flight test spoiler. Figure 8 shows the weapons bay door vibration amplitude variation with flight dynamic pressure which was measured with the weapons bay spoiler installed. The door vibration, measured at low dynamic pressure and mach number without the

spoiler, is also shown in figure 8 for comparison. With fully open doors, the door vibration is approximately an order of magnitude higher without the spoiler deployed.
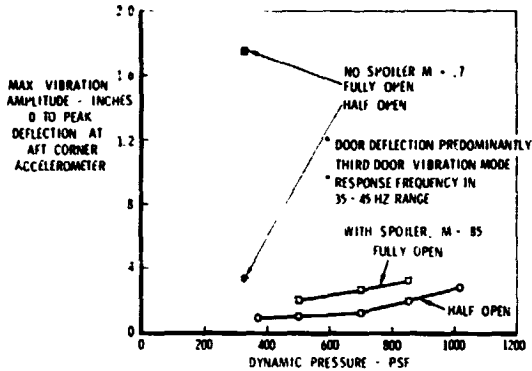


Fig. 8 - Weapons bay - door maximum vibration amplitude versus dynamic pressure

The crew station vibration levels with spoiler extended are shown in figure 6 relative to the unsupp·essed case. Approximately an order of magnitude vibration reduction was achieved with the 70° spoiler.

FLIGHT TESTS OF FINAL SPOILER CONFIGURATION

The final spoiler configuration developed for the production design is illustrated in figure 9. The spoiler panel extends at a 90-degree angle with respect to the fuselage undersurface, and has the same area as the projected frontal area of the inboard two panels on the 70-degree spoiler installation shown in figure 7. The panel extends 14 inches below the fuselage mold line, is 42 inches wide, and has a 3.5-inch gap between the top edge of the spoiler ... 1 the fuselage. The panel has approximately 20 percent of its area removed by 1.35-inch-diameter holes approximately as shown in figure 9. The spoiler is extended prior to opening the weapons bay door, and completely retracted after closing the bay. Extensive flight tests have been conducted with this spoiler installation. Figures 10 and 11 show acoustic levels in the aft bay for half and fully open doors at M = 0.85 with the 90-degree porous spoiler and without a spoiler. The suppressed acoustic levels are substantially below the unsuppressed noise levels for both the cavity discrete frequency resonances and the broadband turbulence pressures in the aft bay. Figure 12 shows the acoustic levels in the forward bay for fully open doors at M = 0.85 with the 90-degree porous spoiler. The forward bay acoustic levels without spoilers are not available for comparison. However, it is expected that acoustic levels in the forward and center bays with no spoiler

should be very similar. Therefore, the acoustic levels in the center bay without a spoiler and with doors fully open at M = 0.85 are shown in figure 12 for comparison. The unsuppresed acoustic levels in the center bay exceed the suppressed levels in the forward bay by more than 10 dB for all discrete and broadband pressures.



Fig. 9 - 90-degree porous spoiler installation



Fig. 10 - Aft bay acoustic levels - doors half open



Fig. 11 - Aft bay acoustic levels - doors fully open

63

The center bay acoustic data with the 70-degree porous spoiler are also compared in figure 12 with data for the forward bay with the 90-degree porous spoiler. The noise levels for the two spoiler/bay combinations are approximately the same except at lower frequencies, where the levels are somewhat lower with the 70-degree spoiler. It is expected that the forward and center bays would have very nearly identical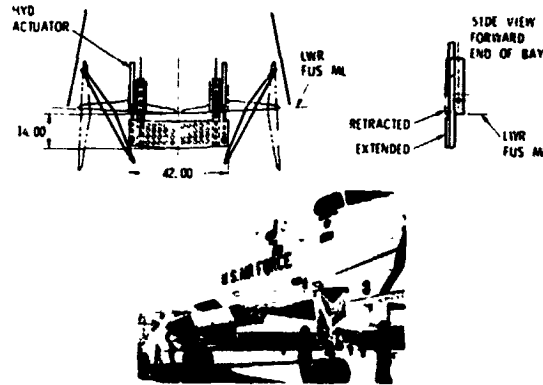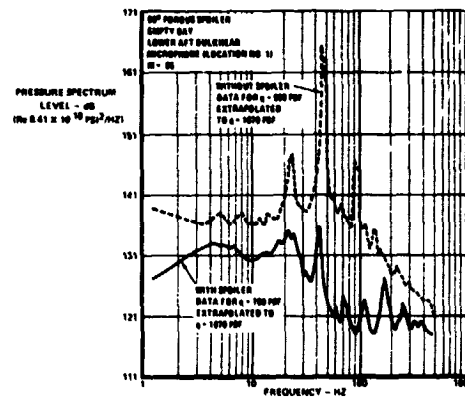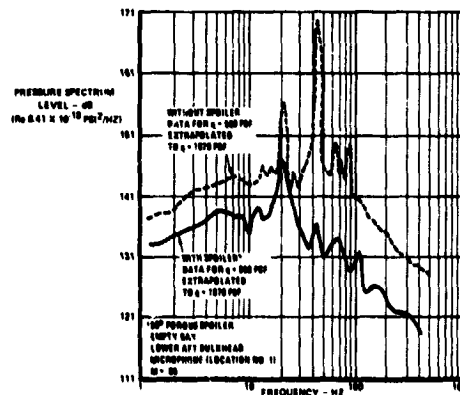 acoustic levels if the spoiler configuration were the same on both bays. Therefore, the small differences in the suppressed acoustic levels shown in figure 12 are attributed to the difference in spoiler configuration, rather than the difference in bay location.
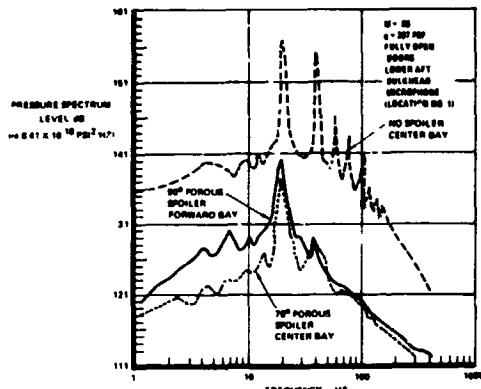


Fig. 12 - Forward and center bay acoustic levels

The acoustic noise in the aft bay and forward bays with noise suppressors is approximately the same. The unsuppressed noise level in the aft bay differs from the forward bay values. The first cavity resonance and the broadband pressure in the aft bay are lower than the forward bay values, but the second cavity resonance is higher in the aft bay. The data illustrated are for a single mach number, and significant variation of cavity noise is expected with mach number for constant dynamic pressure.

The acoustic levels shown in figures 10, 11, and 12 were measured at the lower aft bulkhead microphone, designated location 1 in figure 3. In general, the locations on the forward bulkhead and sidewalls experience broadband and discrete frequency noise levels equal to or lower than those at the lower aft bulkhead location.

Figure 13 shows how the levels of the first three discrete frequency cavity resonances vary with mach number for the unsuppressed center bay, and for the forward bay with spoilers, for the half-open door position. The acoustic levels are expressed in terms of decibels normalized to dynamic pressure, for data obtained at dynamic pressures ranging from 367 to 1,015 psf.

The unsuppressed cavity noise levels decrease with mach number at constant dynamic pressure, while the suppressed bay noise levels remain relatively constant. A plot of normalized acoustic levels versus mach number for the first two cavity resonances in the aft bay with half-open doors is shown in figure 14. The second cavity resonance in the aft bay shows the same tendency to decrease in amplitude with increasing mach number. However, the first mode is relatively constant with increasing mach number. Supersonic data for the aft bay with spoiler are not yet available.
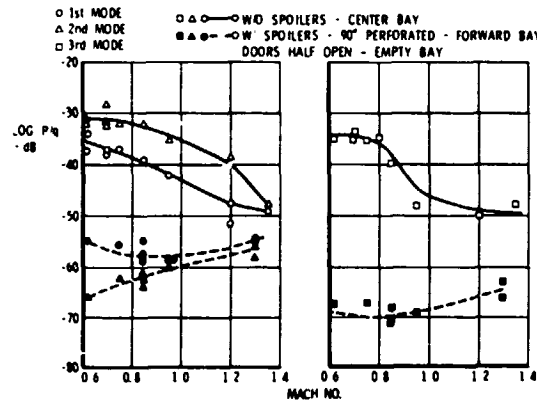


Fig. 13 - Aft bay discrete cavity resonance acoustic levels versus Mach number
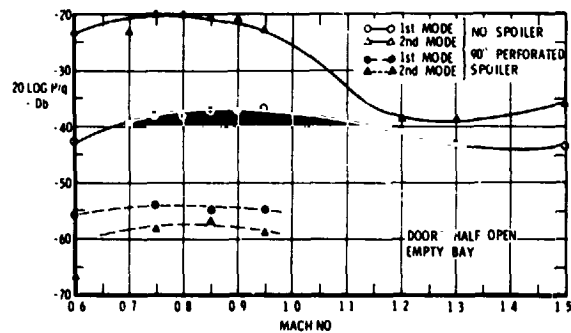


Fig. 14 - Aft bay discrete cavity resonance acoustic levels versus Mach number

Figure 15 shows acoustic levels at three dynamic pressures ranging from 367 to 850 psf for M = 0.85. These data are for the aft bay with doors fully open, and are taken from the microphone designated as location 1 on figure 3. The data of figure 15 are expressed in decibels normalized to dynamic pressure in figure 16. Figure 16 illustrates that acoustic pressures in the bay are proportional to flight dynamic pressure over the dynamic pressure range spanned by the data for a constant mach number. The deviations from this proportionality are no greater than those which would be expected from limita-

tions on measurement accuracy. In general, the acoustic flight test data are accurate within 3 dB.
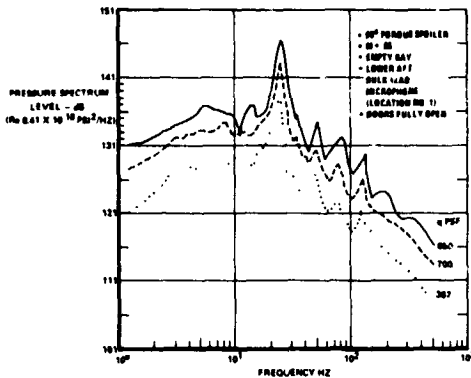


Fig. 15 - Aft bay acoustic levels for three flight dynamic pressures
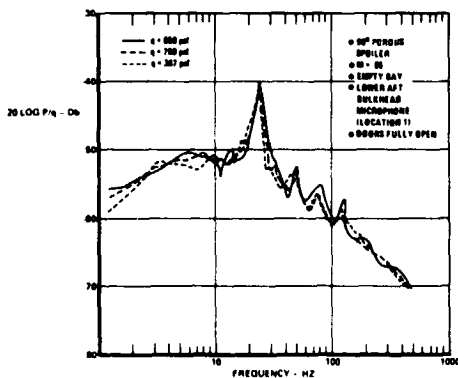


Fig. 16 - Normalized aft bay acoustic levels for three flight dynamic pressures

Door vibration levels on the forward and aft bay with 90-degree porous spoilers installed are comparable to those measured on the central bay and shown in figure 8.

A minimum amount of flight test data have been acquired thus far in the flight test program for multiple open bay configurations. With the forward and aft bays open simultaneously, the acoustic levels measured in both bays with spoilers extended are very nearly the same as with the bays open individually.

Several weapons separations have been made from the forward and aft weapons bays with deployed spoilers. All store separations have been completely successful.

Acoustic levels have been measured with several internal store configurations with the spoiler extended. In general, unless the store loading nearly fills the cavity, acoustic levels are essentially the same as the empty bay levels shown in figure 10 through 16. With a full load of internal stores, the acoustic levels are somewhat lower than with an empty bay. It has been observed that when the store in the launch position is ejected, the acoustic levels are very nearly the same as with the bay empty.

CONCLUDING REMARKS

A summary of the B-1 weapon bay noise levels, effects, and methods of suppression has been presented. The flight test data obtained show large reductions in the acoustic levels are provided by the weapons bay spoiler. The acoustic environment with the spoiler extended is well within the maximum predicted which was used for design and qualification of aircraft structure and equipment.

Only a small portion of the data obtained during the B-1 weapons bay test program is referenced in this paper. A large amount of more detailed data remains to be analyzed and correlated. It is anticipated that systematic evaluations of full-scale and wind tunnel data will be conducted. These should include more complete studies of the acoustic trends with mach number, the acoustic distribution within the bay with and without stores, correlation of wind tunnel and full-scale data, and comparison of measured data with predictions resulting from methods presented in current literature.

The acoustic levels illustrated in this report for fully open, empty bays show good correlation with predictions made by the methods of reference 1. However, the studies of wind tunnel and flight test data with noise suppressors have not yet furnished enough data to provide a thorough understanding of the aerodynamic phenomena involved in the operation of the spoiler-type noise suppressors. Additional work is required to explore the aerodynamic mechanisms which determine the effectiveness of spoilers. The areas which seem most likely to provide improved insight are (1) flow visualization studies, (2) more detailed static and oscillatory pressure surveys in and near the weapons bays, and (3) more extensive correlation of available B-1 data with published data on noise suppressors, such as the data of references 3, 4, and 5. Such improvement in understanding the phenomena involved in noise suppression could lead to general methods for predicting noise suppressor performance, and the capability for optimizing noise suppressor configurations.

65

Flight tests of the B-1 weapons bays are in progress as part of the continuing research, development, testing, and evaluation program. Additional testing with various store configurations is planned. Acoustic measurements within the aft bay are also planned for supersonic speeds with doors half and fully open. This will complete the data base for all bays over the operating speed range of the aircraft.

---

REFERENCES

1. Heller, H. H., Holmes, G., and Covert, E., "Flow Induced Pressure Oscillations in Shallow Cavities," AFFDL-TR-70-104, 1970

2. System Safety Handbook DH1-6, 3rd Edition, Rev 5, AFSC DH 1-6, Criteria for Vibration Tolerance, 20 January 1974

3. Heller, H. H., and Bliss, D. B., "Aerodynamically Induced Pressure Oscillations in Cavities - Physical Mechanisms and Suppression Concepts," AFFDL-TR 74-133, 1975

4. Clark, R. L., "Weapons Bay Turbulence Reduction Techniques," AFFDL-TM-75-147-FXM, 1975

5. Buell, D. A., "An Experimental Investigation of the Airflow Over a Cavity with Antiresonance Devices," NASA TN D-6205, 1971

# SPACE SHUTTLE SOLID ROCKET BOOSTER AFT SKIRT REENTRY NOISE
## INDUCED BY AN AERODYNAMIC CAVITY-FLOW INTERACTION

L. A. Schutzenhofer, P. W. Howard
W. W. Clever, and S. H. Guest
Structural Dynamics Division
Systems Dynamics Laboratory
George C. Marshall Space Flight Center
Marshall Space Flight Center, Alabama  35812

High amplitude discrete frequency cavity induced noise was osbserved during wind tunnel testing of the reentry flight phase conditions of the Solid Rocket Booster (SRB) of the Space Shuttle vehicle system. These wind tunnel tests were designed to acquire aerodynamic noise data for the development of vibroacoustic design and qualification test criteria for the SRB.

The reentry trajectory characteristics of the SRB are random with the angle of attack varying from approximately 96° to 180° and with the dynamic pressure varying from approximately 360 to 1,020 lb/ft$^2$ for a 95 percentile envelope for a Mach number of 3.5. The SRB model was a 2.8 percent scale model with all the external protuberances. It was tested with internal motor volumes of 5, 50, and 100 percent of the burnt-out SRB motor volume. Results of tests are given for two cavity volumes, i.e., 5 and 100 percent.

## INTRODUCTION

The Space Shuttle Vehicle (SSV) is currently being developed by the National Aeronautics and Space Administration (NASA) and it will serve as the primary space transportation system for the 1980's. The SSV is a multi-component system which consists of an orbiter, an external tank (ET), and two solid rocket boosters (SRB's). At the end of the first phase of the aerodynamic ascent, the SRB's will be jettisoned from the orbiter and ET, and the empty motor cases will reenter the atmosphere while the orbiter and ET continue their ascent flight. Subsequently, the SRB's are recovered for eventual reuse in future SSV flights. This sequence of flight events is shown in Figure 1.

Since the SRB vehicle will be reused in the SSV program, all structural and avionic/hydraulic system components (thrust vector control power supply, actuator, booster separation motors, etc.) are required to remain intact and below design limits for ascent and reentry flight phases. During the reentry flight, the SRB experiences a "coning" motion together with high dynamic pressures. These high dynamic pressures and vehicle attitudes result in high pressure fluctuations together with subsequent structural vibrations.

Preliminary aeronoise screening tests in the Marshall Space Flight Center's (MSFC's) low noise trisonic wind tunnel (TWT) facility [1] indicated that high aeronoise levels exist in the vicinity of the SRB aft skirt. These levels were approximately 189 dB at certain angles of attack for supersonic reentry Mach numbers of 2.75 and 3.5. These high levels were induced by an unstable shock wave attaching and detaching at the SRB motor nozzle extension as the vehicle went through the coning motion. Through systematic testing, it was determined that jettisoning the SRB rocket motor nozzle extension at reentry flight apogee and using the already present heat shield were sufficient to reduce the 189 dB to levels which are acceptable for design.

The specific wind tunnel results that are presented in this paper pertain to the aeronoise levels in the vicinity of the SRB aft skirt (Fig. 2) for the present reentry flight configuration at a flight Mach number of 3.5. This configuration is without the
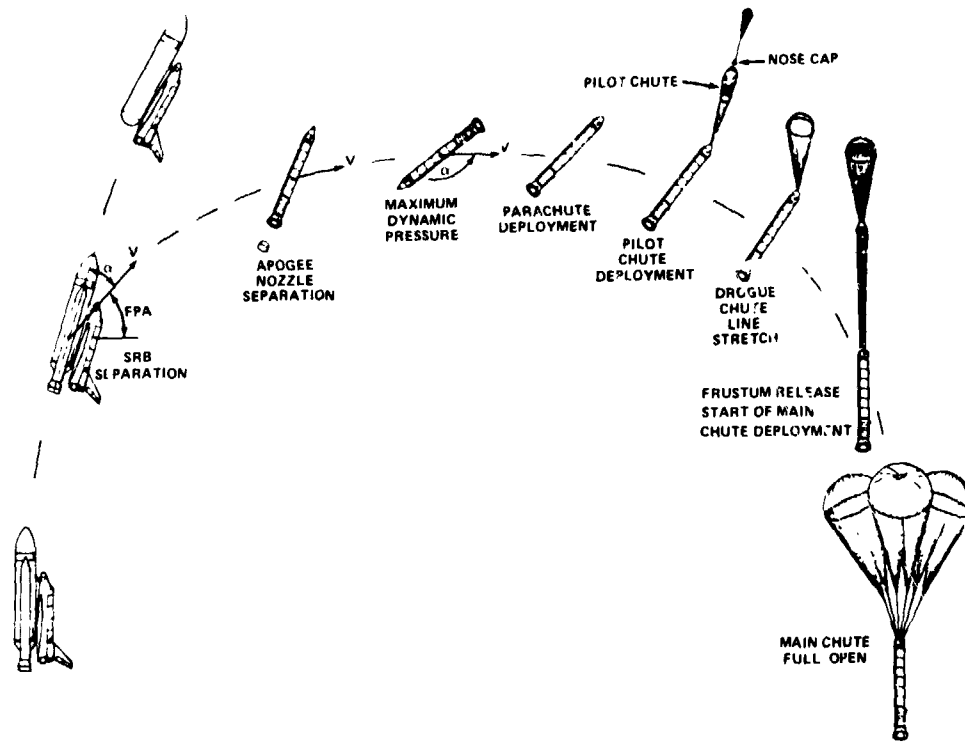
Fig. 1 - SSV flight sequence.



Fig. 2 - Typical wind tunnel test hardware.

nozzle extension, and the shock wave attachment and detachment during the coning motion are significantly more stable. Thus, the 189-dB levels are reduced to less than 170 dB. However, the pressure fluctuations that were observed are at discrete frequencies for certain vehicle configurations and aerodynamic conditions. These discrete frequency fluctuations are cavity-induced pressure fluctuations where the cavity is the SRB motor's internal volume. These discrete frequency results have been singled out of the SRB reentry aeronoise data base for presentation because one of the major goals of this paper is to delineate the conditions that precipitate these cavity induced pressure fluctuations as well as their amplitude and frequency characteristics.

Additional goals of this paper are to delineate (1) the application of random trajectory characteristics toward aeronoise environmental predictions, (2) the method of scaling the wind tunnel data to SSV flight conditions, (3) the wind tunnel testing techniques, (4) the data acquisition and data reduction systems, and (5) the aero/acoustic cavity noise coupling mechanism.

SRB REENTRY TRAJECTORY

After the SRB separates from the SSV, it reenters the atmosphere in a way that the

68

characteristics of the trajectory, i.e., dynamic pressure, angle of attack, etc., are expected to have random variations when considering the entire population of possible reentry conditions. The reason that these trajectory characteristics are random is that they depend upon parameters such as initial separation conditions (rates, etc.), atmospheric properties, center of pressure, center of gravity, aerodynamic pitch and yaw damping, and normal and axial force coefficients, which are random variables [2]. Since these independent trajectory parameters are input variables, the output characteristics (dynamic pressure, etc.) of the trajectory must be expected to be random.

The method of computing the reentry characteristics was through Monte Carlo analysis. In the Monte Carlo analysis, the input variables are selected randomly over certain limits; then the output characteristics for each sample function are similar to those of an actual flight. The entire population of flight output variables, i.e., dynamic pressure, angle of attack, etc., are then analyzed to compute reentry flight statistics.

A typical statistical output is a dynamic pressure, q, and angle of attack, $\alpha$, contour as shown in Figure 3 [3]. This q-$\alpha$ contour was determined by the method developed in Reference 4. Figure 3 represents a 95 percentile q-$\alpha$ boundary for a Mach number of 3.5. The 95 percentile boundary is a constraint for the SRB reentry design environments. From Figure 3 it is seen that the

range of dynamic pressure is $18 \times 10^3$ N/M$^2$ $\le$ q $\le$ $49 \times 10^3$ N/m$^2$ and the range of angle of attack is $96° \le \alpha \le 183°$ at a Mach number of 3.5. This type of data was applied in the design of the fluctuating pressure test to estimate various test conditions. Then, subsequent to the test, these data were applied to scale the wind tunnel results from the tunnel conditions to SSV reentry flight conditions. In addition to the q-$\alpha$ contour, the expected range of the reentry velocity, V, is from 1024 m/s $\le$ V $\le$ 1048 m/s and the expected Reynolds number range is $8 \times 10^6 \le R_N \le 24 \times 10^6$ at a Mach number of 3.5.

In considering Mach numbers other than 3.5, a 95 percentile dynamic pressure range can be constructed as shown on Figure 4 [5]. Similarly, one can construct a 95 percentile angle of attack variation with Mach number as shown in Figure 5. These figures clearly show the range of q and $\alpha$ over the Mach number range $0.6 \le M \le 3.5$.

HARDWARE DESCRIPTION AND SYSTEM ACCURACIES

The SRB reentry fluctuating pressure environments and the data presented in this paper were derived from wind tunnel tests of a 2.8 percent model with all the protuberances geometrically scaled. The data reported herein were acquired with a 100 percent and also a 5 percent internal motor volume simulation. Some significant dimensions pertaining
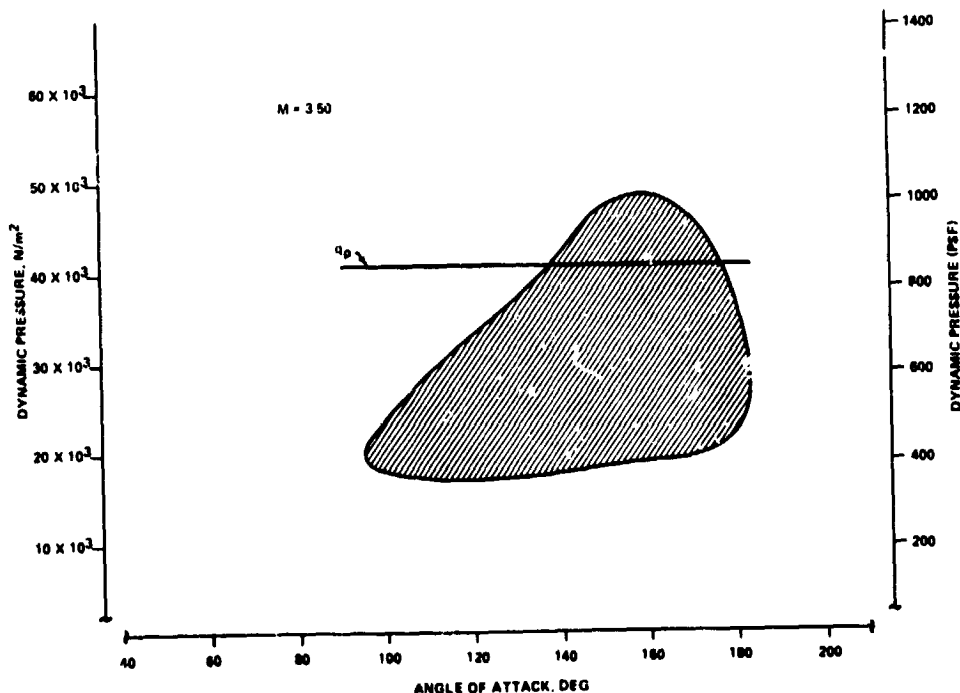


Fig. 3 - 95-percentile contour for angle of attack versus dynamic pressure.

69
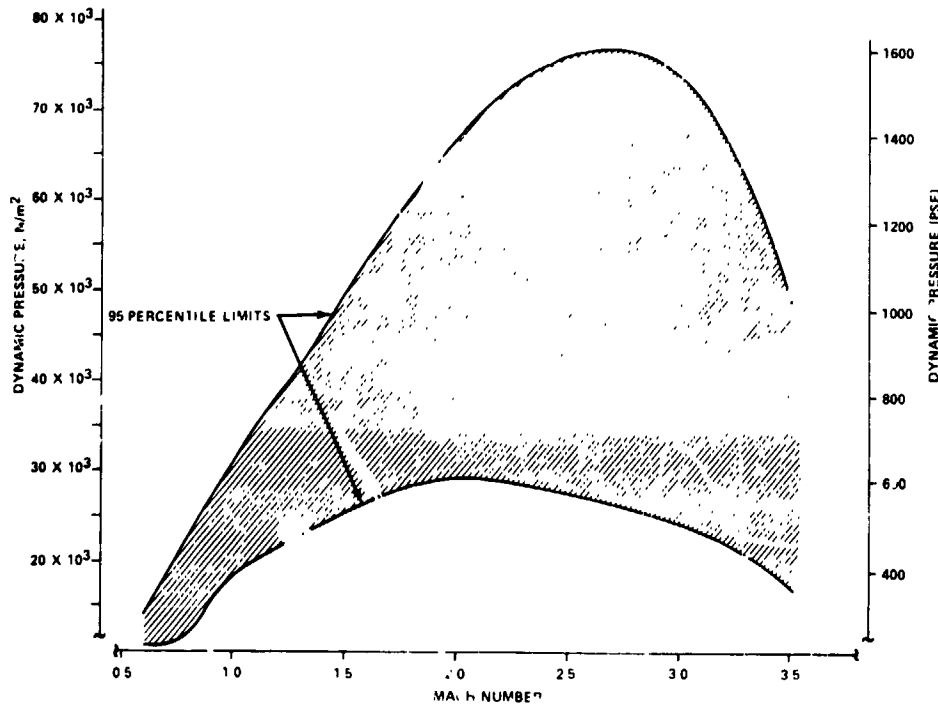
Fig. 4 - 95-percentile dynamic pressure boundaries for SRB reentry.
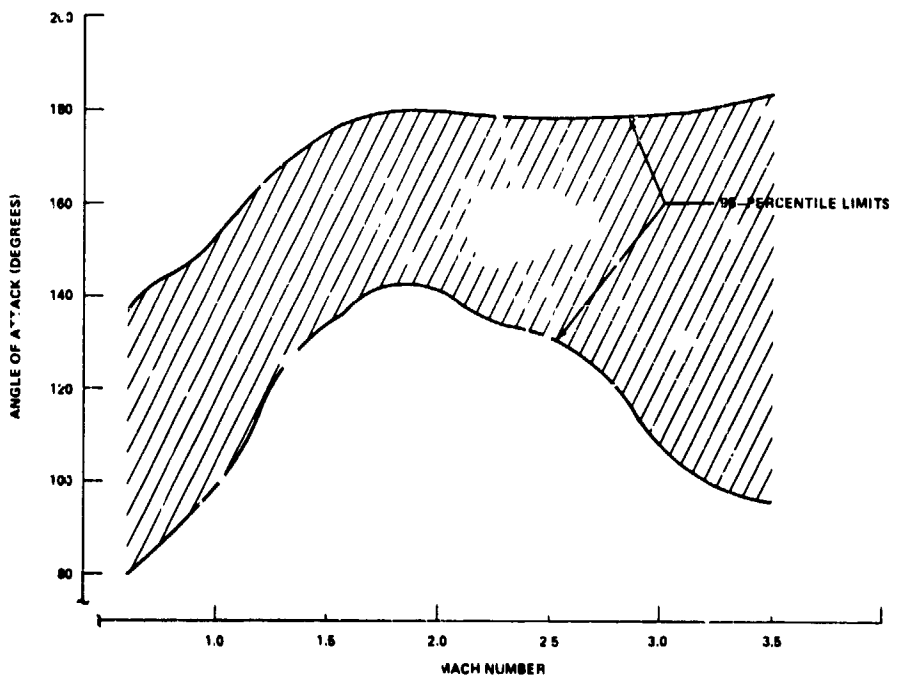


Fig. 5 - 95-percentile angle of attack range for SRB reentry.

to the geometrical features of these two configurations are shown in Figure 6 [5,6,7].

A significant feature of these wind tunnel models was the dynamically scaled SRB heat shield.

The SRB flight configuration heat shield is a quartz woven fabric and fiberfax which is hung between the rocket nozzle and skirt to protect the skirt and other components from high temperatures during the ascent and reentry flight phases. It was felt that the

70

100 07 cm
(39 397 in )

10 38 cm
(4 088 in )

14.81 cm
(5.83 in.)

100% MOTOR VOLUME SRB MODEL

8 46 cm
(3 33 in )

14 81 cm
(5 83 in )

3.87 cm
(1.524 in.)

12 51 cm
(4 925 in )

4.45 cm
(1.75 in.)

5.72 cm
(2.250 in.)

5% MOTOR VOLUME CONFIGURATION
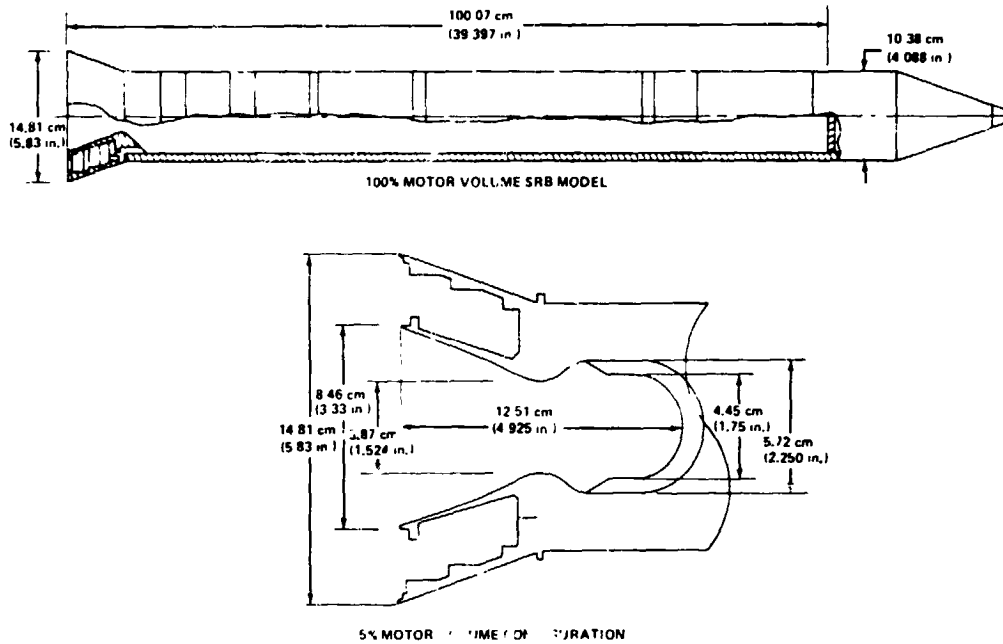
Fig. 6 – Schematic of SRB reentry acoustic wind tunnel test model.

dynamic motion of the heat shield would be important in determining the acoustic environment in the region of the aft skirt; consequently, the heat shield was dynamically scaled [5,6,7] for application in the wind tunnel testing.

All of the testing was accomplished using miniature pressure transducers. The type of transducer was a Kulite XCQL-17-093-25D. These transducers were operated in the ac coupled mode during data acquisition and dc coupled during the system calibration. The transducers had a screen cover that protected the diaphragm from particles in the air stream. During the testing, with the external configuration geometrically scaled, 120 pressure transducers were used to acquire the data. This configuration was for the 5 percent volume (Fig. 2). For details of the transducer locations, see Reference 6. For the 100 percent volume testing, 35 transducers were used [7] and the locations of the pertinent transducers are shown in Figure 7. In fact, the data presented herein were obtained from transducers 112 (nozzle), 114 (compliance ring), 119 (nozzle/skirt cavity) and 99 (external skirt), as shown in Figure 7.

The data acquisition and data reduction scheme-matic is shown in Figure 8 [8]. The basic concept of this system was to acquire on-line data for pertinent decision-making at the test site, in addition to data reduction and scaling at the test site in a day-to-day operational mode. Typical types of computer outputs are shown on Figure 8. They consist of "overall level versus angle of attack" and "one-third octave
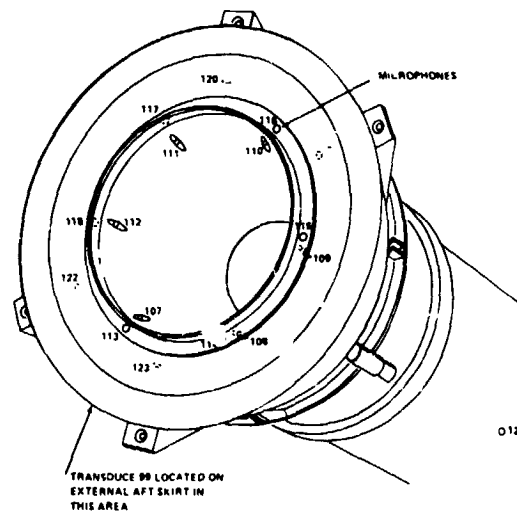


Fig. 7 – Instrumentation location.

band fluctuating pressure spectra." Much of the data were superimposed and cross-plotted for comparison purposes. This system was developed by the Experimental Aerophysics Branch at MSFC.

As seen in Figure 8, the data signals, i.e., transducer outputs, were processed through signal conditioning equipment consisting of line drivers and amplifiers. For the overall fluctuating pressure levels, in terms of angle of attack for a fixed Mach number and roll angle, the conditioned signals were recorded on magnetic tape and paralleled through a

71
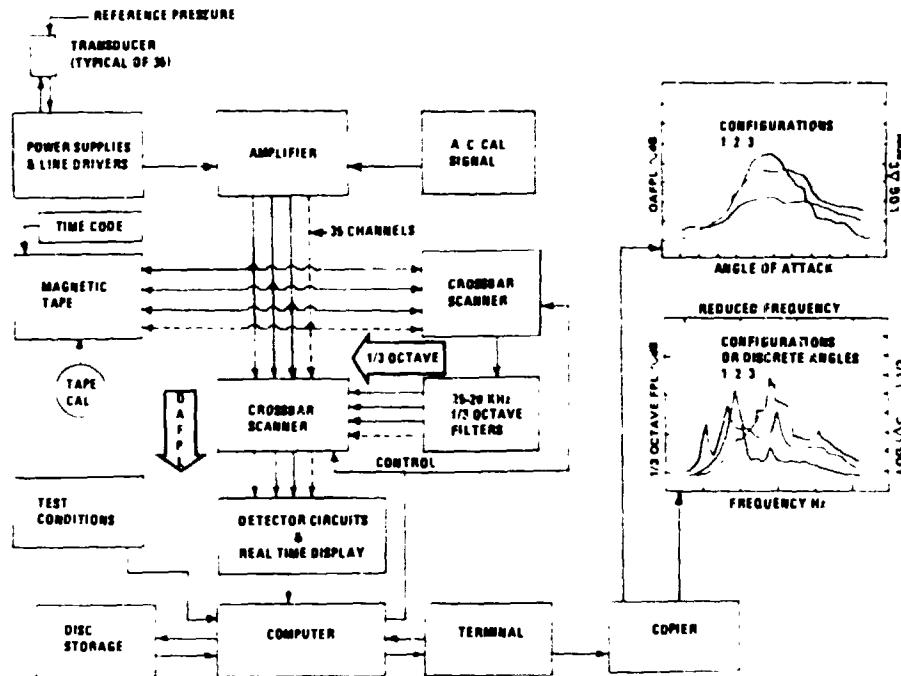
Fig. 8 - Data acquisition and reduction system.

crossbar-scanner for root-mean-square (rms) detection. It should be noted that the crossbar-scanner is used to service all inputs in a sequential fashion. The rms signals were then input to a mini-computer (also to the computer storage disc) for on-site display, i.e., fluctuating pressure level (FPL) versus angle of attack $(\alpha)$, to determine the model angle of attack position where the highest rms levels occurred to capture a long data sample for spectral analysis. The model was then positioned at those selected angles and 30-s data records were acquired. In this operation, the conditioned signals were again input to the magnetic tape recorder and again they were paralleled to a crossbar-scanner where each signal was sequentially input into a 1/3 octave filter bank and then into another crossbar-scanner. The output of this scanner was input to the rms detectors and in this way 1/3 octave spectra were acquired on-line. These spectra were then stored on a disc for easy access. The 1/3 octave spectra that were stored on the disc have an effective averaging time of approximately 1 s. These spectra were then scaled for environmental prediction.

The parameters that were used in scaling the model wind tunnel data to full scale are the dynamic pressure, velocity, and the characteristic length. The wind tunnel characteristic parameters were computed on-line from the wind tunnel conditions, while the SRB reentry characteristics were obtained from the trajectory characteristics (Fig. 3). These wind tunnel conditions are shown in Figure 8 as an input to the computer.

The uncertainty in the Mach number and total pressure was within 1 percent; the uncertainty in the total temperature was 2 percent. The power supply voltages, transducer sensitivities, cable losses, and amplifier gains were calibrated and operated where the worst-case error was 0.4 dB. The error and uncertainties result in a full scale SRB environmental error of approximately ±1.25 dB. This uncertainty leads to confidence interval estimations of approximately ±3.0 dB for a 95 percent confidence coefficient.

The frequency response of the data acquisition system was "flat" from 20 Hz to 20 kHz, model scale, and the uncertainty in the full scale frequencies was approximately 1 percent. The uncertainty in the roll angle and angle of attack was less than ±0.2 degree.

TEST FACILITIES, CONDITIONS, AND OPERATION

The results presented in this paper were acquired in tunnel A at the Arnold Engineering Development Center (AEDC) in Tullahoma, Tennessee, and at NASA's Ames Research Center unitary wind tunnel facility [9,10]. The test conditions used in the overall program were as follows: $0.6 \leq M \leq 3.5$, $88 \times 10^3 \leq P_T \leq 149 \times 10^3$ N/m², and $293 \leq T_T \leq 346°K$. The roll orientations of the model were 150°, 180°, 210°, and 270°; while the angle of attack varied from 90° to 180°. These conditions

were determined from the statistics of the SRB
reentry trajectory. The data presented herein pertain specifically to a Mach number of 3.5, a total
temperature of 322°K, $P_T = 149 \times 10^3$ N m$^2$,
Reynolds number $= 0.736 \times 10^6$, and a role angle of
180°. These conditions were selected because they
delineate the salient features of cavity induced
pressure fluctuations.

The test operation was designed in what can be
described as an angle of attack sweep mode and a
discrete angle mode. In the angle of attack sweep
mode, the model's angle of attack was varied over
three 30° ranges in segments of $90° \leq \alpha \leq 120°$,
$120° \leq \alpha \leq 150°$, and $150 \leq \alpha \leq 180°$, thus
encompassing the entire $\alpha$ range shown in Figure 5.
This was accomplished with a fixed Mach number and
a fixed roll angle orientation. During the angle of
attack sweep, rms data were taken and the data were
recorded on magnetic tape. The sweep rate of
approximately 0.2°/s was selected since the data
were quasi-stationary for this rate. These rms data
were analyzed on-line to select the angles of attack
where the highest levels occurred. The model was
then positioned at these selected angles where 30-s
data samples were acquired and put on tape, and, at
the same time, on-line 1 3 octave spectra were taken
and stored on a disc. This discrete mode of operation took approximately 55 s. A comparison of overall levels between data taken in the sweep mode and
discrete mode was always less than 1 dB and in most
cases the values were nearly identical, i.e., ±0.3
dB.

After data were acquired in the sweep and
discrete modes, the Mach number and roll orientation were changed and this procedure was repeated.
In some of the more recent tests, the model was
rolled automatically. This procedure significantly
reduced the tunnel down time, which increased the
test efficiency [5].

SCALING AND TEST RESULTS

The basis for estimating aeronoise environments is geometric model testing in conjunction with
fluid dynamic similarity which is achieved through
dimensional analysis. The dependent variable is the
fluctuating press. re environment and, in this application, it depends primarily upon Mach number,
geometric similitude, and model orientation. There
is a difference in Reynolds number between the model
and prototype; however, it is thought that this
difference is not significant in the consideration of
the cavity induced flow noise presented in this paper.
The Reynolds number effect is negligible because the
sharp edge of the SRB aft skirt fixes the separation
point of the shear layer at the leading edge of the
nozzle. In addition, there is no anticipated Reynolds

number effect in the leading edge approach flow at a
Mach number of 3.5. Thus, these wind tunnel model
test results are expected to produce reasonably
accurate environmental estimates with no significant
Reynolds number dependence.

Through dimensional analysis it can be shown
that the rms fluctuating pressure ($p_{rms}$) divided by
the free stream dynamic pressure (q) is the same
for the model and the prototype, i.e.,

$$\left[\frac{p_{rms}}{q}\right]_M = \left[\frac{p_{rms}}{q}\right]_P = \Delta Cp_{rms} \quad (1)$$

where the subscript M pertains to the model and the
subscript P pertains to the prototype. This quantity
is usually denoted as $\Delta Cp_{rms}$. It can also be shown
that frequency (f) multiplied by a characteristic
length (D) and then divided by the free stream velocity (V) is the same between the model and the
prototype, i.e.,

$$\left[\frac{fD}{V}\right]_M = \left[\frac{fD}{V}\right]_P \quad (2)$$

Equation (1) is the basis for scaling fluctuating
pressure data amplitudes. Equation (2) provides
the br or scaling frequencies from model scale
to full scale. It should be clear that exact scaling is
achieved only when exact fluid dynamic similarity is
achieved together with all the boundary conditions,
e.g., momentum, thermal, kinematic, etc., being
exactly scaled. This situation is rarely achieved in
practice because exact similarity is not actually
required. It is believed that the scaling procedures
(including the dynamically scaled heat shield) applied
in the testing described herein is sufficiently accurate to estimate the full scale SRB reentry acoustic
environments.

The data presented in Figures 9 through 15 are
overall fluctuating pressure level variations with
angle of attack and one-third octave band spectra,
in prototype frequency, taken at selected angles of
attack. They represent typical fluctuating pressure
level variations in the vicinity of the aft skirt. In
particular, transducer 112 (Fig. 7) represents the
nozzle, transducer 114 represents the compliance
ring, transducer 119 represents the cavity between
the nozzle and the aft skirt, and transducer 99
represents the external aft skirt. The data presented
in Figures 9 through 15 have been scaled with a model
dynamic pressure ($q_M$) of 15,513 N/m$^2$ (324 PSF)
and a full scale dynamic pressure ($q_P$) of 40,698
N/m$^2$ (850 PSF). This full scale $q_P$ is shown in
Figure 3. This one value of $q_P$ was used so that the
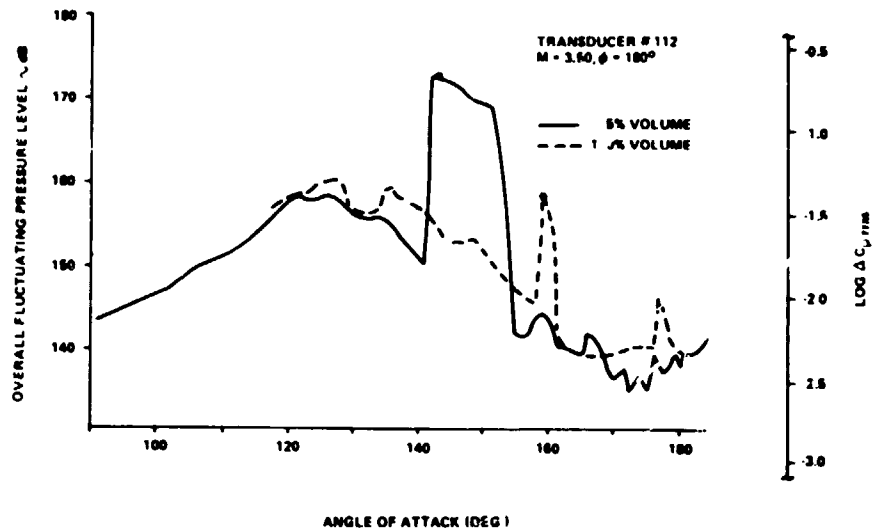
Fig. 9 – Nozzle overall fluctuating pressure level variation.
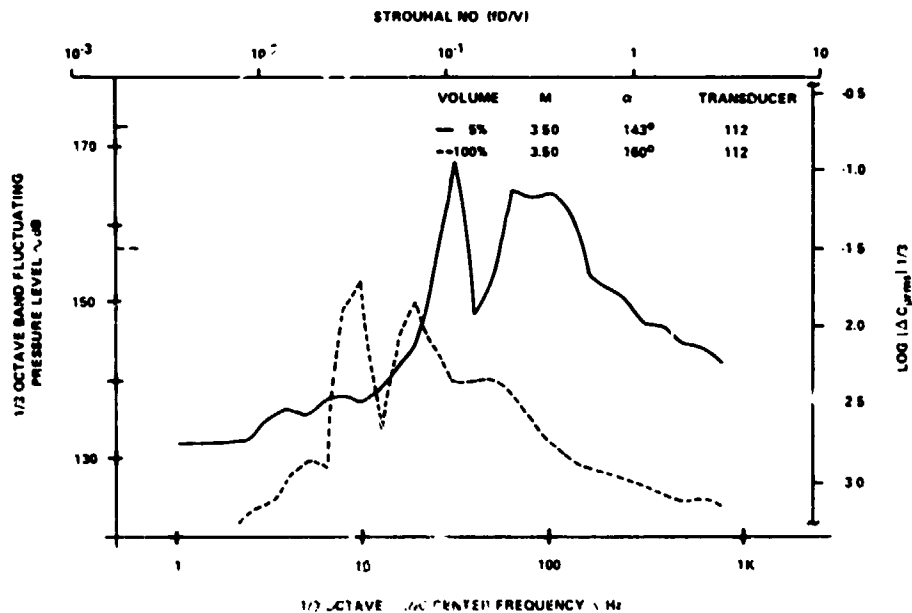


Fig. 10 – Nozzle 1/3 octave band spectra.

true picture of the cavity induced pressure fluctuation would be revealed and yet indicate the magnitude of the SRB reentry fluctuating pressure levels. For environmental estimation, however, the upper boundary of the q-α contour, also shown in Figure 3, was used. In this way, the data were dynamic pressure scaled for each angle of attack. All these data pertain to a Mach number of 3.5 and a roll angle of 180°.

In the nozzle, the overall fluctuating pressure variation is shown in Figure 9. It can be seen that

for the 5 percent volume a significant amplitude increase occurs at α ≈ 140° with levels in excess of 170 dB. At this angle of attack it is believed that the local Mach Number, $M_1$, is about unity. This high level is believed to be a cavity induced pressure fluctuation. For the 100 percent volume, the cavity induced pressure fluctuations occur at an angle of attack of approximately 160°. It is believed that the local Mach number over the nozzle exit plane is approximately 0.7. The one-third octave band spectra that correspond to the aforementioned conditions is shown in Figure 10. These

74
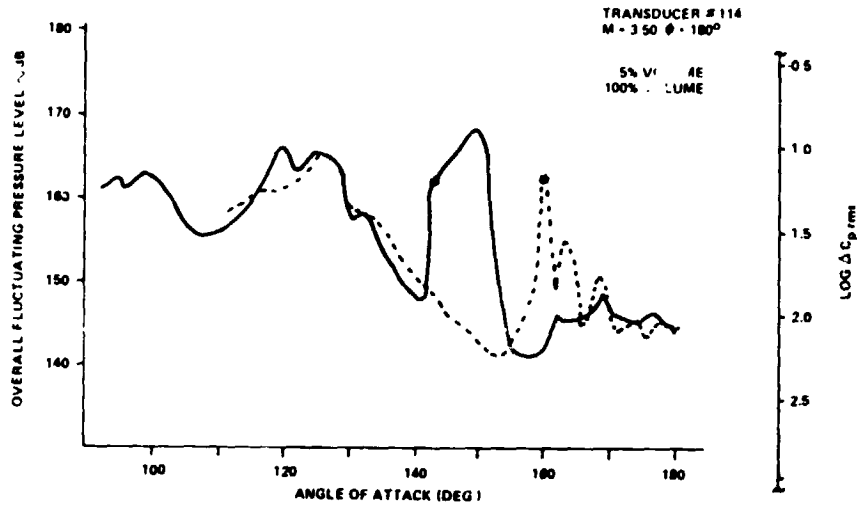
Fig. 11 - Compliance ring over..l fluctuating pressure variation.
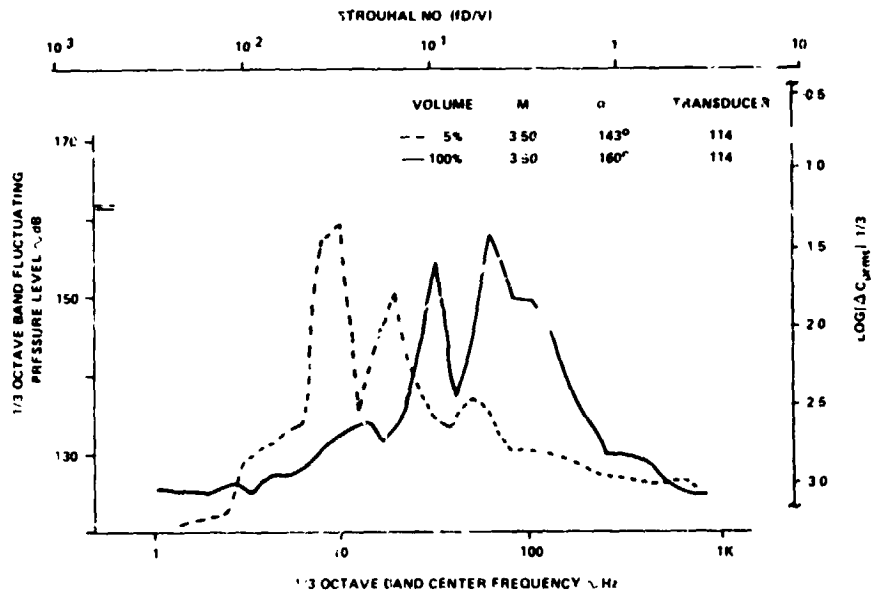


Fig. 12 - Compliance ring 1/3 octave band spectra.

spectra were taken at the angles indicated by the (x) in Figure 9. For the 5 percent volume, the peak in the one-third octave spectrum is approximately 27 to 32 Hz and the peak for the 100 percent volume is approximately 9 to 10 Hz. Narrow band analyses of these data indicate additional peaks at integral multiples of these dominant frequencies. It is believed that these harmonics probably represent waveform discortion of the pressure fluctuations and not a new and/or separate phenomenon. It is believed that this effect is similar to that reported in Reference 11.

In the vicinity of the compliance ring, the pressure amplitudes are similar to those in the nozzle shown in Figure 11; however, the levels are slightly less in the angle of attack ranges where cavity induced pressure fluctuations occur. The compliance ring spectra are shown in Figure 12, and the functional variation with frequency is similar to the spectra in the nozzle.

The environmental variation with $\alpha$ in the cavity between the nozzle and the aft skirt is shown in Figure 13. These levels are also slightly less

75
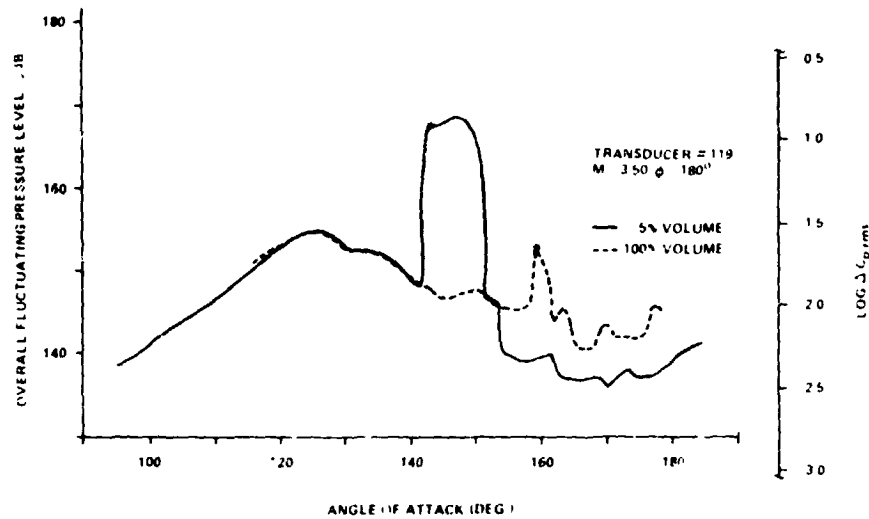
Fig. 13 - Skirt cavity overall fluctuating pressure variation.
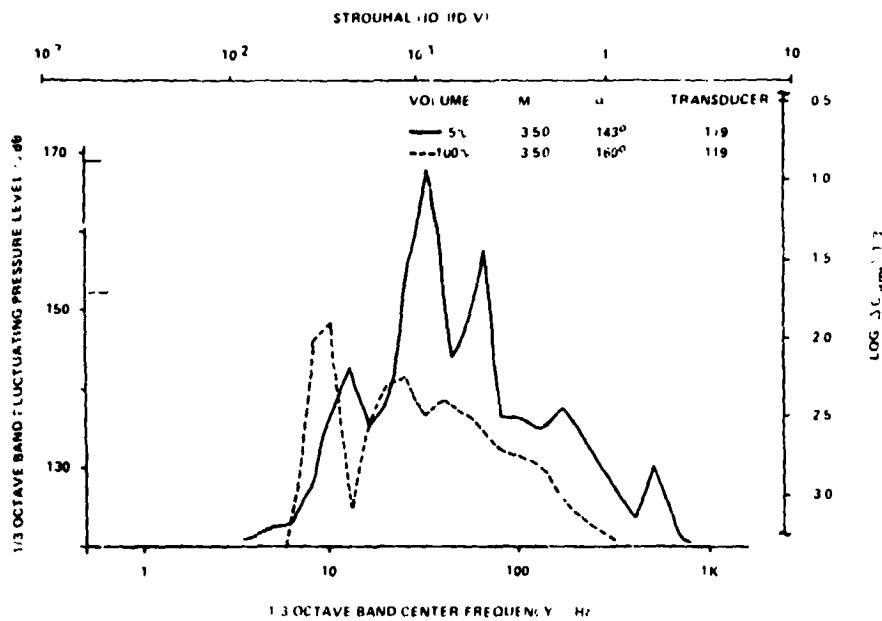


Fig. 14 - Cavity 1/3 octave band spectra.

than those in the nozzle as expected. The 1/3 octave band spectra corresponding to the (x's) on Figure 13 are shown in Figure 14. The harmonic content shown in this figure is similar to that of the data in the nozzle and compliance ring.

The fluctuating pressure level variation on the external portion of the aft skirt is shown in Figure 15. These levels are considerably less than the nozzle and compliance ring levels. In fact, while the 5 percent volume resonant effect at $\alpha = 140°$ can be seen, the 100 percent volume resonant effect at $\alpha = 160°$ is being masked by other effects.

The time variation of the fluctuating pressure data is shown in Figure 16. These data correspond to an angle of attack of 160° for a Mach number of 3.5 for the transducers 112, 113, and 114. This figure clearly indicates that the waveform has been distorted from that of a pure sine wave. Furthermore, the waveform distortion is most pronounced in the nozzle with a rounding effect on the compliance ring and then additional rounding in the nozzle/skirt cavity. The distorted waveform indicated by transducer 112 leads to harmonics of the predominant frequency as mentioned above.
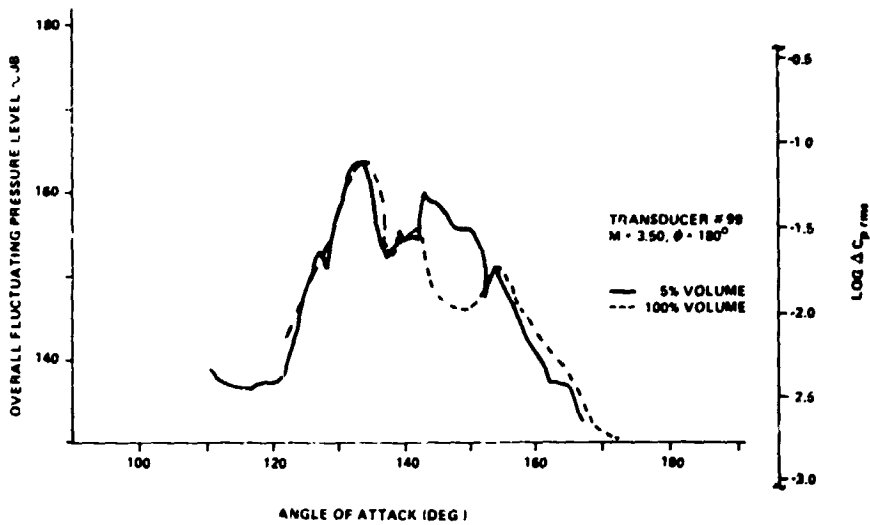
**Fig. 15 - External skirt overall fluctuating pressure variation.**
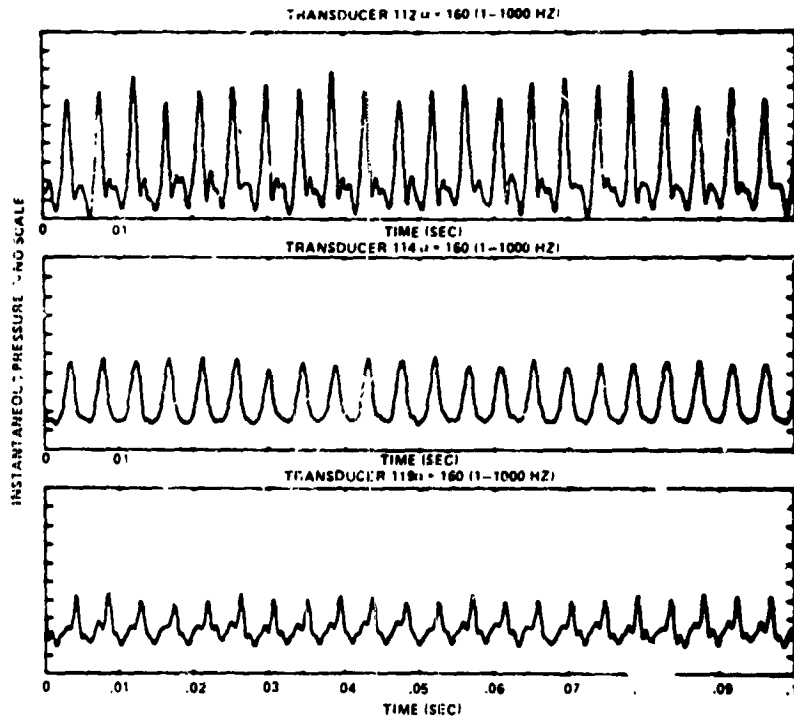


**Fig. 16 - Time variation of cavity induced pressure fluctuations.**

All of these data indicate that a cavity resonance effect exists in the vicinity of the aft skirt. The highest levels occur for the 5 percent volume and the predominant frequency is approximately 27 to 32 Hz. For the 100 percent volume, the levels decrease considerably and the predominant frequency is approximately 9 to 10 Hz. It is believed that the highest levels for the 5 percent volume are associated with a local Mach number of approximately unity at $\alpha = 140°$, and the levels for the 100 percent volume

while being lower are probably at a Mach number of approximately 0.7 for an $\alpha = 160°$.

For the 100 percent volume, there exists another independent resonant condition at an $\alpha = 169°$. This resonance is of considerably less amplitude than those shown in the figures, however, it does exist. The frequency of this resonance is approximately 3 Hz. This particular condition has not been shown in the data because of its low amplitude;

77

however, the presence of this resonant condition is important toward understanding the cavity induced fluctuating pressure phenomenon.

## INTERPRETATION OF RESULTS

The high amplitude fluctuating pressures, shown in the data of the previous sections, are thought to be induced by the SRB motor internal cavity. This deduction is supported by a comparison of frequencies measured in the vicinity of the SRB aft skirt and those calculated with empirical equations developed from smooth flow over rectangular cavities.

Rossiter [11] developed an empirical equation for estimating unsteady vorticity excitation by shear layer flow over a cavity. This equation was eventually modified [12] to include temperature differences between the external flow and the cavity. The modified equation, written in terms of the SRB notation, is of the form

$$\frac{f_\nu D_n}{V_1} = \frac{\nu - \gamma}{M_1\left(\frac{a_1}{a_c}\right) + 1/\beta} \quad ; \quad \frac{D_n}{H} > 1 \qquad (3)$$

where $f_\nu$ is the vorticity excitation frequency, $D_n$ is the diameter of the SRB nozzle at the severed nozzle plane, $V_1$ is the local velocity, $\nu$ is the mode number $(1, 2, 3, \ldots)$, $M_1$ is the local Mach number, $a_1$ is the local speed of sound, $a_c$ is the cavity speed of sound, $\gamma$ is a quantity that accounts for phase differences between upstream acoustic wave propagation and downstream vortex shedding or shear layer undulations in the local flow over the nozzle (this quantity depends on the cavity depth), $\beta$ is the ratio of eddy convection speed to the local velocity, and H is the depth of the cavity. It appears that equation (3) applies for shallow cavities where $D_n/H > 1$.

The 5 percent and 100 percent volume cases of the SRB cannot be classified as shallow cavities since $D_n/H = .6761$ and $D_n/H = .0845$, for the respective volumes. Experimental results in Reference 13 and the experimental results presented herein indicate that for deep cavities Rossiter's equation could be further improved. If equation (3) is modified for deep cavities as follows:

$$\frac{f_\nu D_n}{V_1} = \frac{(\nu - \gamma)(D_n/H)}{M_1\left(\frac{a_1}{a_c}\right) + 1/\beta} \quad ; \quad \frac{D_n}{H} < 1 \, , \qquad (4)$$

then equation (3) can be extended to deep cavities. Thus, equation (4) is an additional modification to Rossiter's equation to permit application to the deep cavity case. To apply equation (4) to the SRB reentry cavity induced fluctuating pressure frequency predictions, the frequency $f_\nu$ was nondimensionalized by D and V. It can be shown that the dimensionless frequencies are given by

$$\frac{f_\nu D}{V} = \left[\frac{1}{M^2} + \frac{K-1}{2}\right]^{1/2} \frac{(\nu - \gamma)(D/H)}{\left[1 + \frac{1}{\beta}\left\{\frac{1}{M_1^2} + \frac{K-1}{2}\right\}^{1/2}\right]} \quad ; \qquad (5)$$

$$\frac{D_n}{H} < 1$$

where K is the ratio of specific heats and M is the free stream Mach number. In the development of this equation, it was assumed that the cavity temperature was the total temperature. Equation (5) will be applied in this paper in the interpretation of the frequencies presented in the previous section. These frequencies are characteristic of the potential aerodynamic excitation in the shear layer flow over the nozzle exit plane. To realize excitation at these frequencies, there must be a coalescence with some type of acoustical mode of the cavity. If the cavity is deep, the depth modes of the cavity tend to become the predominant resonant acoustically excited modes. In fact, it will be shown that depth mode excitation occurs on SRB. If the cavity is shallow, the length modes across the cavity are usually the predominant resonant acoustically excited modes.

In the case of deep cavities, East [14] has shown that the first acoustic depth mode is given by

$$\frac{fH}{a_c} = \frac{1}{4}\left[1 + .65\left(\frac{D_n}{H}\right)^{.75}\right]^{-1} . \qquad (6)$$

If equation (6) is multiplied by $(2j - 1)$ where $(j = 1, 2, 3, \ldots)$ to approximate high order modes, and if the cavity acoustic response frequency is nondimensionalized by D and V, the dimensionless cavity frequency equation becomes

$$\frac{f_j D}{V} = \left[\frac{1}{M^2} + \frac{K-1}{2}\right]^{1/2}\left(\frac{D}{H}\right)\frac{(2j-1)}{4}\left[1 + .65\left(\frac{D_n}{H}\right)^{.75}\right]^{-1} \qquad (7)$$

where again the cavity temperature is assumed to be the total temperature.

The classical equation for an open-closed organ pipe acoustic mode [15] is given by

$$\frac{f_1 H}{a_c} = \frac{1}{4} \frac{(2j-1)}{(1 + \epsilon/H)} \qquad (8)$$

where $\epsilon$ is an end correction effect. Equation (8) can be nondimensionalized with D and V to obtain the equation

$$\frac{f_1 D}{V} = \left[\frac{1}{M^2} + \frac{K-1}{2}\right]^{1/2} \frac{D}{H(1 + \epsilon/H)} \frac{(2j-1)}{4} \qquad (9)$$

Equations (5), (7), and (9) will be applied to interpret the data discussed in the previous section. Recall, equation (5) represents the frequencies of the shear layer excitation, and equations (7) and (9) represent the frequencies of the cavity acoustical response. When these frequencies coalesce, a potential high amplitude acoustic resonance condition exists.

Figure 17 presents a plot of equations (5), (7), and (9) for $\nu = 1, 2,$ and 3 and for $j = 1, 2,$ and 3. The excitation frequencies and the response frequencies are plotted as a function of the local Mach number. In the 5 percent volume case, M = 3.5 and $D_n/H = .6761$. For this cavity depth ratio, $\gamma$ was selected to be .25 and $\beta$ was selected to be .57. These values were based upon References 11 through 14.

The dashed line in Figure 17 is the predominant frequency measured. The harmonics of this frequency are not shown since they result from waveform distortion. Equation (9) with $\epsilon/H = 0$ and .196 represents the cavity acoustical modes for $j = 1, 2,$ and 3 and they are shown by the dotted bands. Equation (7) is represented by the short lines to indicate its magnitude and equation (5) is represented by the solid curves lines for $\nu = 1, 2,$ and 3.

The predicted frequencies for the excitation [equation (5)] and for the acoustical response [equation (9) with $\epsilon/H = 0$ and .196] indicate coalescence for these first three modes. This indicates potential resonance conditions for these modes. In particular, the $\nu = 1, j = 1$ mode appears particularly strong because these frequencies coalesce at $M_1 = 1$ where it is believed that the most intense pressure fluctuations will occur [11-14].

The experimental results indicate a resonance at $\alpha = 140°$ at a frequency between 27 and 32 Hz. This indicates excitation of the first cavity depth mode at $M_1 = 1$ (see dashed line Figure 17).

Furthermore, this mode is the predominant and the only resonant excitation in this angle of attack range.

It is assumed, based on the measured results, that equation (9) with $\epsilon/H = 0$ predicts the cavity acoustical frequency and equation (5) predicts the aerodynamic vorticity excitation; then Figure 17 clearly indicates a resonance at $M_1 = 1$. Furthermore, consideration of the modes $\nu = 2$ and 3 together with $j = 2$ and 3 indicates that resonances are not expected (recall $\epsilon/H = 0$ is being considered) since these modes do not coalesce. Thus, the predicted frequencies and resonance conditions are remarkably consistent with the observed resonances for the first three modes.

The consistency between the measured frequencies and the calculated coalescence frequencies and conditions clearly indicates that the high amplitude pressure fluctuations measured on the SRB are induced by shear layer vorticity excitation.

Figure 18 presents a plot of equations (5), (7), and (9) for $\nu = 1, 2,$ and 3 and for $j = 1, 2,$ and 3. In the 100 percent volume case, M = 3.5 and $D_n/H = .0845$. For this cavity depth ratio, $\gamma$ was selected to be .57. The dashed lines in Figure 18 are the predominant frequencies measured. These frequencies are harmonically related and they occur at different angles of attack. When each of these predominant resonant frequencies exist, integral multiples also occur and it is thought that these harmonics are caused mostly by waveform distortion. Equation (9) with $\epsilon/H = 0$ and equation (7) represent the cavity modes for $j = 1, 2,$ and 3. Equation (5) is represented by a solid curve for $\nu = 1, 2,$ and 3.

The predicted frequencies for the excitation and for the acoustical response coalesce for the first three modes. This indicates potential resonance conditions for these modes. For the 100 percent volume, it appears that the second mode is the mode of predominant excitation since the coalescence occurs at $M_1 = 1$.

The experimental results indicate resonant frequencies (see dashed lines in Figure 18) for the first mode of approximately 3 Hz and for the second mode at approximately 9.0 to 10 Hz. The first mode is excited at an angle of attack of 169° and the second mode is excited at an angle of attack of approximately 160°. These angles of attack correspond to local Mach numbers of approximately .4 and .7 respectively.

The cavity acoustical frequencies estimated with equation (7) exceed the measured frequency by 14 percent for the first mode and by 9 percent for the second mode. These differences are considered tolerable since the internal geometry of the SRB includes a contoured nozzle and since equation (7) was developed for $M_1 < .2$. If equation (5) is increased by 11 percent so that it coalesces with the
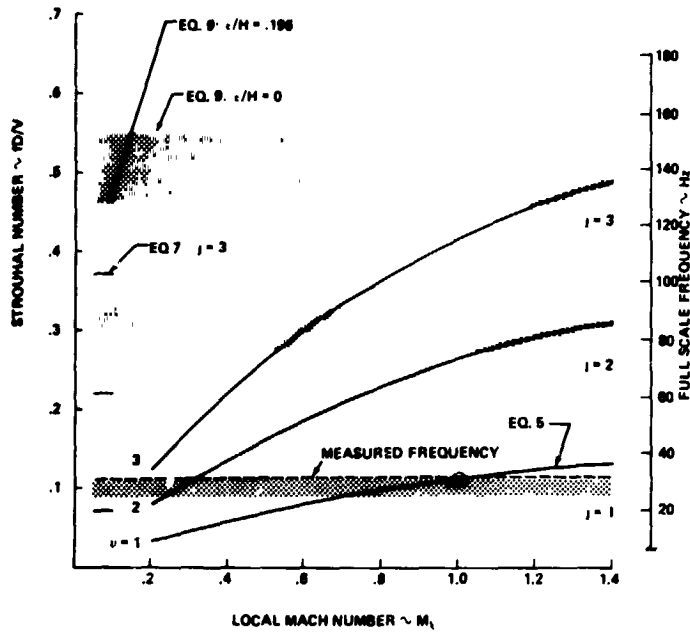
79

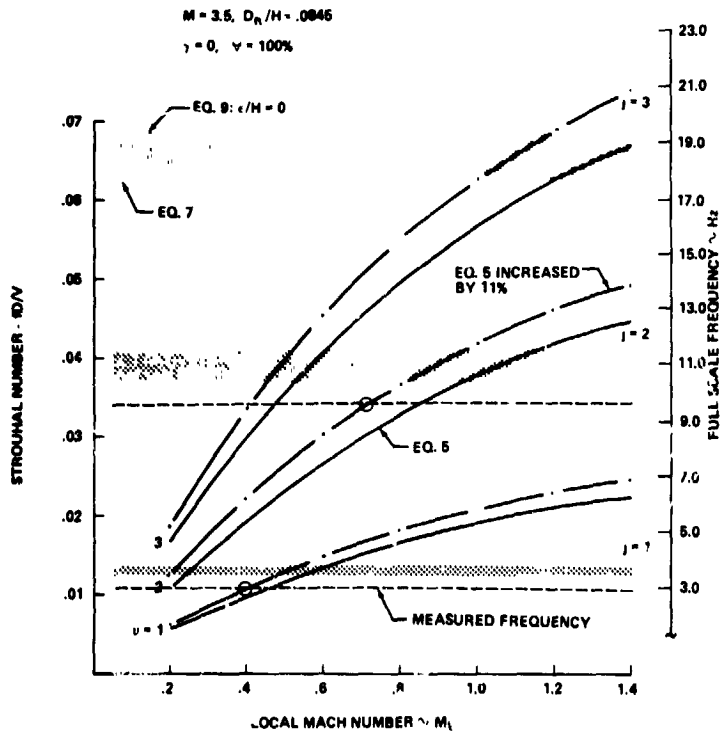Fig. 17 - Cavity noise mechanism for 5 percent volume.



Fig. 18 - SRP cavity noise mechanism for 100 percent volume.

measured frequencies, it can be seen that the coalescence occurs at local Mach numbers of approximately .4 for the first mode and approximately .72 for the second mode. These values of local Mach number are close to those believed to occur at angles of attack of 169° and 160°, respectively. It is possible that the third mode in the vicinity of 15 to 16 Hz may also be excited at a local Mach number of approximately .72 with this mode possibly being of a much lower amplitude than the second mode and thus being masked by the second mode. As a final observation, it is noted that the second mode excitation is higher in amplitude than the first mode. This can be expected because the second mode occurs at a higher Mach number as Mach one is approached from the low Mach number regime.

The results delineated in Figure 18 indicate that the cavity acoustical frequency predictions and the vorticity excitation frequency predictions adequately describe the cavity induced fluctuating pressure phenomenon. In fact, these equations predict the coalescence frequency range remarkably well considering that these equations were developed for smooth flow over rectangular cavities and not for the tested configuration which included: a sharp edge flow at a free stream Mach number of 3.5, the associated bow shock wave structure, and a fluttering flexible heat shield.

## CONCLUDING REMARKS

Methodologies and results are presented in this paper that deal with the practical aspects of defining and understanding aeronoise environments for the SRB vibroacoustic design and component test qualification program. The methodologies included: the application of random trajectory statistics for environmental prediction, the definition of the experimental technique and the hardware associated with acquiring aeronoise data, and the delineation of a sophisticated data acquisition and data reduction system for acquiring on-line overall (rms) data together with one-third octave spectra. The results presented pertain to fluctuating pressure data in the vicinity of the aft skirt of the SRB for a Mach number of 3.5 and a roll angle of 180° over the entire angle of attack range.

The SRB aeronoise environments have been derived from 2.8 percent model wind tunnel test data. A specific aspect relating to the specification of these environments was high amplitude discrete frequency aerodynamic pressure fluctuations in the vicinity of the SRB aft skirt. For the 5 percent volume, the predominant frequency was in the range of 27 to 32 Hz. For the 100 percent volume there were two predominant frequencies; one at approximately 3 Hz and the other between 9 and 10 Hz. The amplitude of the 5 percent volume was higher in

comparison to the 100 percent volume amplitude. One reason for this higher amplitude was that the resonance condition for the 5 percent volume occurred at a local Mach number near unity.

A shear layer vorticity excitation frequency prediction equation for deep cavities was put forth in this paper. Application of this equation in conjunction with the frequency equation for the acoustical modes of the SRB internal motor cavity results in calculations which clearly substantiate the mechanism associated with the high amplitude, discrete frequency pressure fluctuations measured during the wind tunnel testing. The mechanism is believed to be a resonant condition that results from the coalescence of vorticity excitation frequencies in the unstable shear layer over the SRB nozzle and the acoustical depth mode frequencies of the SRB internal motor cavity.

The method and equations presented in this paper were applied specifically to the SRB. They may, however, be applied to a variety of problems involving aero/acoustical interaction phenomenon and environmental estimation for which dynamic data are to be acquired, scaled, analyzed, and interpreted.

## REFERENCES

1. L. A. Schutzenhofer and P. W. Howard, "Suppression of Background Noise in a Transonic Wind Tunnel Test Section," AIAA Journal, Vol. 13, No. 11, pp. 1467-1471, Nov. 1975.

2. Verbal Communication with C. Hall and G. Watts, ED15, Marshall Space Flight Center, Sept. 12, 1978.

3. Memorandum ED15-77-21, "Reentry Trajectory Data for Generation of SRB Acoustic Environments," Marshall Space Flight Center, Apr. 27, 1977.

4. Memorandum ED15-77-26, "Procedures for Establishing Reentry SRB q-α Contours," Marshall Space Flight Center, June 23, 1977.

5. L. A. Schutzenhofer, ED23-78-40, "Pretest Report, Ames 2.8% SRB Reentry Acoustics Model Tests, SS27F and SS28F," Marshall Space Flight Center, Feb. 1978.

6. L. A. Schutzenhofer, "Pretest Report, 2.8% SRB Reentry Acoustic Model Test, SS13F," Marshall Space Flight Center, May 1976.

7. W. W. Clever, ED23-77-210, "Pretest Report, AEDC 2.8% SRB Reentry Acoustics Model Test, SS26F," Marshall Space Flight Center, Sept. 1977.

8. Verbal Communication with B. Neighbors, ED35, Marshall Space Flight Center, Sept. 6, 1978.

9. Test Facilities Handbook, 10th Edition, Vol. 3 (VKF), Arnold Engineering Development Center, Arnold Air Station, Tennessee, May 1974.

10. "Ames Research Facilities Summary 1974." Technical Information Division, NASA/Ames Research Center, Moffett Field, California, 94035.

11. J. E. Rossiter, "Wind Tunnel Experiments on the Flow Over Rectangular Cavities at Subsonic and Transonic Speeds." Royal Aircraft Est., Technical Report No. 64037, Oct. 1964.

12. H. H. Heller, G. Holmes, and E. E. Covert, "Flow-Induced Pressure Oscillations in Shallow Cavities," AFFDL-TR-70-104, Dec. 1970.

13. H. H. Heller and D. B. Bliss, "Aerodynamically Induced Pressure Oscillations in Cavities – Physical Mechanism and Suppression Concepts," AFFDL-TR-74-133, Nov. 1974.

14. L. F. East, "Aerodynamically Induced Resonance in Rectangular Cavities," J. Sound and Vibration, Vol. 3, No. 3, pp. 277-287, May 1966.

15. L. E. Kinsler and A. R. Frey, "Fundamentals of Acoustics," Wiley and Sons, Inc., New York, 2nd Edition, 1962.

## DEFINITION OF SYMBOLS

$a_1$      local speed of sound

$a_c$      speed of sound in cavity

$D$      diameter of SRB

$D_n$      diameter of SRB nozzle at severed nozzle plane

$f$      frequency

$f_j$      cavity response frequency for jth mode

$f_\nu$      vorticity excitation frequency for $\nu$th mode

$H$      depth of cavity

$j$      index 1, 2, 3

$K$      ratio of specific heats (1.4)

$M$      free stream Mach number

$M_1$      local Mach number

$p_{rms}$      root-mean-square fluctuating pressure

$P_T$      total pressure

$q$      dynamic pressure

$q_M$      dynamic pressure of a model

$q_P$      dynamic pressure of a prototype

$R_N$      Reynolds number based upon SRB diameter (D)

$T_t$      total temperature

$V$      free stream velocity

$V_1$      local velocity

$V$      percentage of motor internal volume

$\alpha$      angle of attack

$\beta$      ratio of eddy convection speed to local velocity (.57)

$\gamma$      phase angle of difference between acoustic wave and vortex shedding or shear layer wave propagation

$\epsilon$      end effect

$\nu$      index 1, 2, 3

$\phi$      roll angle

## BLAST AND SHOCK

## SNAPS IN STRUCTURES*

Michail Zak
Jet Propulsion Laboratory, California Institute of Technology
Pasadena, California

Snaps as a type of shock phenomena which arise in structures employing films, or strings are studied. The sources and the variety of such snaps are defined and a new mathematical model for their investigation is presented.

## INTRODUCTION

Structures employing films or strings with small resistance to compression are characterized by some special features which result from the instability of the above flexible bodies when subjected to certain types of disturbances. The two sources for the occurrence of snaps are connected with the following instabilities:

a) The effect of energy accumulation at the boundary of instability of a flexible body.

b) The effect of reflection in the course of the transition of the flexible body from an unstable to a stable state.

The first effect was explained physically and investigated mathematically in the Ref. (1). The investigations of the second effect are by necessity connected with the description of the behavior of a flexible body beyond the limits of its stability. The main theory of such behavior is given in Ref. (2). Snaps in structures with inextensible films and strings will be investigated based on that theory.

## THE BOUNDARIES OF INSTABILITY OF THE SHAPE OF FLEXIBLE BODIES

It can be shown (Ref. 3, 4) that any flexible body loses the stability of its shape in some direction $\underset{\sim}{n}$, if

$$T_n < - \frac{E}{2(1 + \nu)} \qquad (1)$$

*This paper presents the results of one phase of research carried out at the Jet Propulsion Laboratory, California Institute of Technology under Contract NAS7-100, sponsored by the National Aeronautics and Space Administration.

where $Tn = T \cdot \underset{\sim}{n}$ is the tension in the $\underset{\sim}{n}$-direction,

E is Young's modulus

$\nu$ is Poisson's ratio.

In the case of an ideally flexible body (E=0) condition (1) is simplified and can be written:

$$T_n < 0, \text{ or } T_{11} T_{22} < T_{12}^2 \qquad (2)$$

where $T_{11}$, $T_{22}$, $T_{12}$ are the two normal and the shearing stress, respectively. From the mathematical point of view the inequalities (1) and (2) state that a smooth solution of the governing differential equations (Ref. 3) does not exist. In practice this point displays itself in the appearance of wrinkles, the directions of which are normal to the directions of the loss of stability $\underset{\sim}{\eta}$.

## THE TYPES OF DEFORMATIONS LEADING TO INSTABILITY

All the types of deformations leading to the instability of a flexible body are encountered in a solar array for a NASA spacecraft which can be used as an illustration (Fig. 1) as follows:

A) A uniform contraction of the film (Fig. 2) in the course of which wrinkles appear normal to the direction of the contraction.

B) A uniform twist about the axis of symmetry (Fig. 3). Here the surface of the twisted form possess double curvature and wrinkles of variable intensity appear along and across the film.
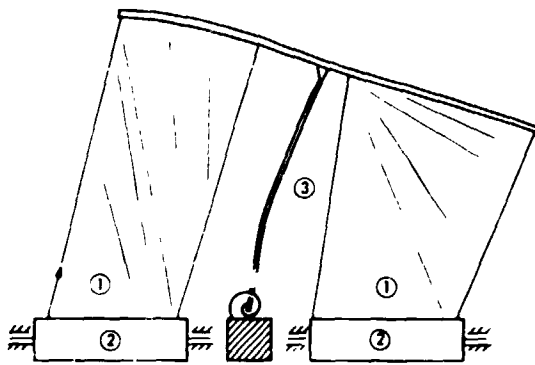
(1) FILMS
(2) DRUMS
(3) BI-STEM BOOM

Fig. 1.
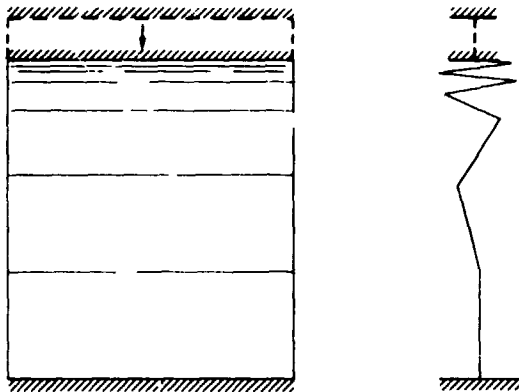


Fig. 2.
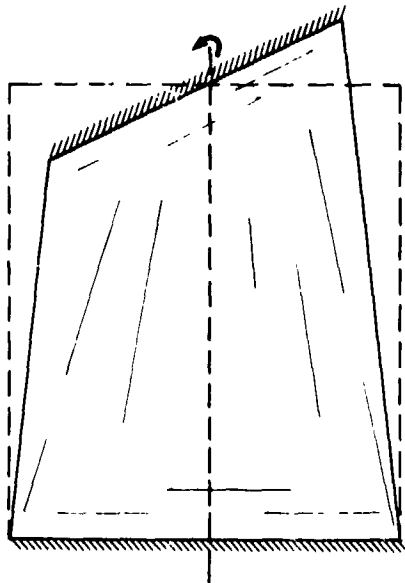


Fig. 3.

C) A uniform bending (Fig. 4). In this case the wrinkles of variable intensity appear from the edge toward the axis of the bending.

D) A uniform shearing (Fig. 5). Here the film is divided into two areas: the narrow diagonal tensioned area with uniform diagonal wrinkles and the out-of-diagonal slack area.

E) General Case.

In the most general case all of the above deformations can be nonuniform and act at the same time.

## THE MECHANISM OF SNAP FORMATIONS

Let us illustrate the mechanism of the formation of snap by examining the simplest case such as (a) of Figure 1, neglecting the extensibility of the film. After contraction of the film the process of restoration begins due to the elasticity of bi-stem boom. In the course of that restoration the film particles attain velocities which are in general nonzero at the moment of complete restoration. Hence by the virtue of inextensibility of the film at that moment a shock appears as the result of the reflection from the invariable length of the film. The shock (snap) leads to a discontinuity in the values and directions of the velocities of the film particles and the formation of new wrinkles. The above jump in the velocities is defined in accordance with the conservation of kinetic energy and the impulse at the moment of the shock taking into account of the elasticity of the entire structure. The above shock acts on other parts of the structure as a feedback to the film. Thus the whole structure as a coupled dynamic system is involved in the process of periodic shocks.

The situation becomes more complicated in the general case when the wrinkles possess a variable intensity, velocities and directions, but the mechanism of the generation of the snaps remains the same

Another source of snaps is connected with effect of the accumulation of energy due to a special type of tension distribution near the boundary of instability. That kind of snaps are encountered, for instance, in solar sails. As an illustration of such an effect, consider a film suspended in a gravity field. Suppose that an isolated transverse wave of small amplitude was generated at the point of suspension. The velocity of propagation of the leading front of the transverse wave will be smaller than the velocity of the trailing front because the tension decreases from the point of suspension to the free end. Hence the length of the above wave will be decreasing and in some cases will tend to zero. Then according to the law of conservation of energy the specific kinetic energy per unit of length will tend to infinity producing a snap (snap of knout).

C - 2
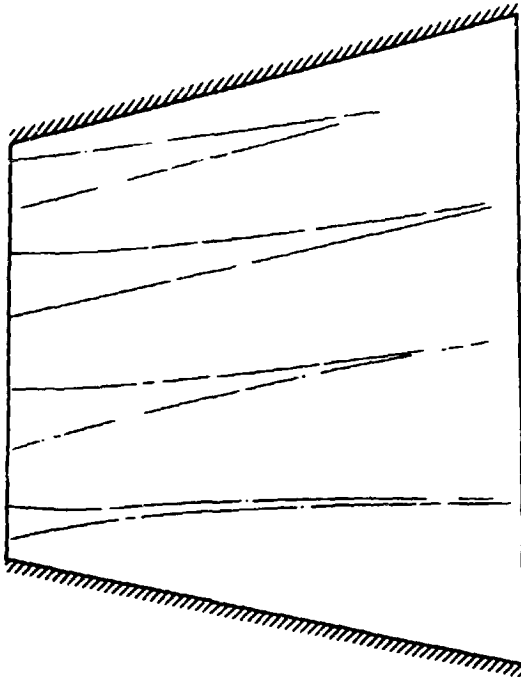
Fig. 4.
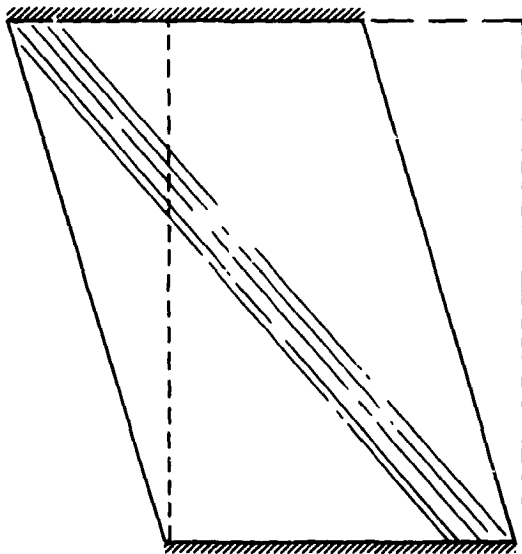


Fig. 5.

It is very important to emphasize that in both cases the snaps were generated by the structure itself as eigen-properties without external shock disturbances.

## THE MATHEMATICAL MODELS OF SNAPS

It is clear from the above that to describe snaps is to describe the behavior of a film beyond the limits of its stability. The latter problem was solved in Ref. (2). The main idea of the new governing equations is the introduction of an additional variable describing the intensity of the wrinkles. Utilization of a special moving (nonmaterial) system of coordinates connected to the running wrinkles allows one to take into account the transformations from the stable to the unstable state automatically. In the course of the transition of the boundary of instability the coefficients of the governing equations are changed by jumps leading to the corresponding jumps in the solution and thereby creating snaps.

The governing equations in an unstable state of a film are very close (but not equal) to the equations defining the motion of a fluid. In the simplest case when the study is confined to the model of a single wrinkle, the governing equations are degenerated into the equations of a system with variable mass.

From the point of view of the theory of structures, films or strings can be considered as unilateral constraints. Such a constraint realizes a rigid junction between parts of the structure in a stable state. In an unstable state the constraint is realized by means of wrinkles which are step-variable in their values, directions and intensity. Therefore, the above constraint also possesses the step-variable properties. Moreover, as a result of a variable moving mass of film such constraints lead to the dynamic "viscous" resistance.

## ANALYTICAL RESULTS

1.  Let us consider the snaps generated by the accumulation of energy (Fig. 6). According to the Ref. (1) a snap in this case is caused by the instability of the solution in a class of smooth functions (incorrectness of the Cauchy problem). The possibility of a snap appearance is given by the alternative:

    a)  the snap appears if the improper integral

$$\int_{\zeta_0}^{\zeta} \frac{d\zeta}{\sqrt{T(\zeta)/\rho(\zeta)}}$$

converges for $\zeta \to l$.

(Here $T$ is tension, $\rho$ is density, $\zeta$ is the current length, $l$ is the entire length.)

    b)  the snap is impossible if the above integral diverges. It can be shown that in a gravity field that integral coverages if $\rho$-constant, consequently, the motion of the film is accompanied by snaps near the free end. It can also be shown that the above result remains in force if the film moves in a

85

Fig. 7.

Fig. 6.

2. Turning to snaps as a result of reflections consider the simplest situation when unilateral constraints (ideal string) generates snaps in the course of axial harmonic oscillations (Fig. 8). Ignoring for simplicity the masses of the string AB and the spring BD and introducting the mass M of the body B we have the differential equation of motion of the body B:

$$m\ddot{x} + cx = 0, \ x > 0$$

or

$$m\ddot{x} + c|x| = 0 \qquad (4)$$

where c is the stiffness of the spring BD.

The solution of the equation (4) is given in the form:

$$x = x_0 \left| \cos \sqrt{\frac{m}{c}} t \right| \qquad (5)$$

if

$$x = x_0 > 0, \ \dot{x} = 0 \text{ at } t = 0$$

Thus one arrives at the oscillations with periodical snaps (Fig. 9) and the interval of time between shocks is defined by the formula:

$$T = \pi \sqrt{\frac{m}{c}} \qquad (6)$$

Taking into account the distributive density of the thread one gets the nonlinear governing equation instead of Equation (4):

$$\frac{d}{dt} \left[ (m + \rho x) \ \dot{x} \right] + cx = 0 \qquad (7)$$

resistive medium (air or water). All the above results will remain in force if one replaces the film or string of (Fig. 6) by the ideally flexible pipe within which liquid flows with only one difference: the point of the appearance of the snap shifts from the free end upward (Fig. 7).
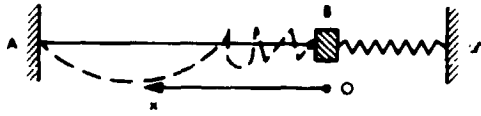
Fig. 8.
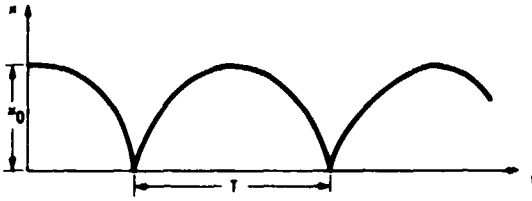


Fig. 9.



Fig. 10.

The exact solution of this equation can be expressed as elliptic functions (Ref. (2)). The nonlinear influence of the wrinkle formation displays itself in the appearance of damping and in a change of the period T (Fig. 10).

3. As a more complicated example where snaps have nonuniform intensity the transverse in-plane oscillations of a film can be considered (Fig. 11a). The governing equation for this case is a nonlinear equation in partial derivatives.

$$\frac{\partial}{\partial t}\left(u\frac{\partial u}{\partial t}\right) = \frac{T}{\rho}u\frac{\partial^2 u}{\partial x^2} \qquad (8)$$

where u is the transverse in-plane displacement.

The solution of this equation can be obtained by the method of separation of variables and presented in the form

$$u = u_0 \sin\frac{\pi}{l}x\sqrt{\left|\cos\frac{T}{\rho}\frac{\pi^2}{l^2}\sqrt{2}\,t\right|} \quad , \quad (9)$$

if

$$u(t = 0) = u_0 \sin\frac{\pi}{l}x, \quad \dot{u}(t = 0) = 0. \quad (10)$$

According to this solution (Fig. 11) the intensity of the periodical shocks decreases from the middle of the film to its ends.

CONCLUSION

Snaps in structure employing flexible bodies result from the internal properties of these structures and are connected with the states of their instability. The mathematical theory elaborated here allows the construction of models for such snaps and it describes the coupled nonlinear phenomena leading to snaps.



a)



b)
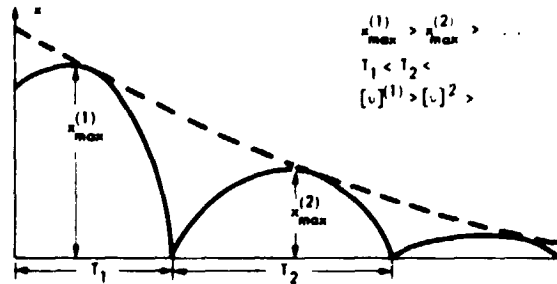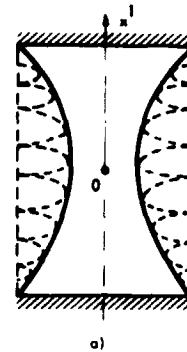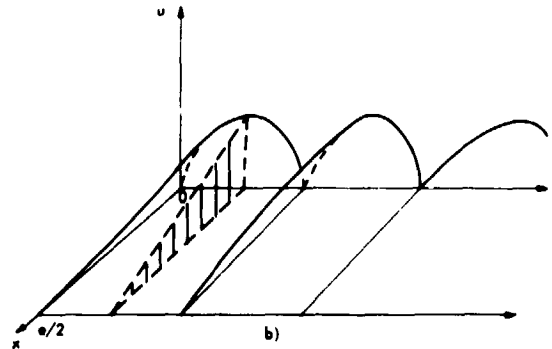
Fig. 11.

REFERENCES

1. M. Zak, "Uniqueness and Stability of the Solution of the Small Perturbation Problems of a Flexible Filament with a Free End," PMM, Vol. 39, No. 6, 1970, pp 1048-1052.

2. M. Zak, "Dynamics of Films," Journal of Elasticity, Noordnoff International Publishing (to be published).

3. M. Zak, "On the Loss of Stability of the Shape of an Ideally Flexible String," PMM Vol. 32, No. 6, 1968, pp 1092-1096.

4. M. Zak, "Non-Classical Problems in Continuum Mechanics," Monograph, 1974, Leningrad.

# A SIMPLIFIED METHOD OF EVALUATING THE STRESS WAVE
## ENVIRONMENT OF INTERNAL EQUIPMENT

J. D. Colton and T. P. Desmond
SRI International
Menlo Park, California

A simplified method called the Transfer Function Technique (TFT) has been devised for evaluating the stress wave environment in a structure containing internal equipment. The TFT consists of following the initial in-plane stress wave that propagates through a structure subjected to a dynamic load and characterizing how the wave is altered as it is transmitted through intersections of structural members. As a basis for evaluating the TFT, impact experiments and detailed stress wave analyses were performed for structures with two or three, or more members. Transfer functions that relate the wave transmitted through an intersection to the incident wave were deduced from the predicted wave response. By sequentially applying these transfer functions to a structure with several intersections, it was found that the environment produced by the initial stress wave propagating through the structure can be approximated well. The TFT can be used as a design tool or as an analytical tool to determine whether a more detailed wave analysis is warranted.

BACKGROUND

Many problems of predicting the response of equipment inside a structure have been solved by vibration analyses. However when structural response is induced by sudden motion of the primary structure in, for example, missiles or submarines under blast loading or in penetrators at impact, the inherent stiffness of these structures allows high-frequency stress-wave loading to propagate through the structure to the internal equipment. The initial stress wave that propagates through the structure may produce the most severe environment to which the equipment is subjected [1]. In this case, a stress-wave approach that focuses on the equipment-damaging stress waves themselves is desirable for predicting the equipment environment.

Available analytical techniques are capable of predicting the detailed stress wave response for many structures of interest [1,2]. However, for complex structures, the required numerical integration is often expensive and time consuming. Thus, for a preliminary evaluation of the severity of the stress wave environment, a simpler approach is desirable. Such an approach is developed in this paper.

OBJECTIVE AND APPROACH

The objective is to devise and demonstrate the usefulness of a simplified method for evaluating the stress wave environment in a structure containing internal equipment. This method is called the Transfer Function Technique of TFT.

The basis for the TFT is that the initial response of equipment inside a structure subjected to an external dynamic load is governed by the stress-wave propagation through the structure. The stress waves are created at the loaded surface and propagate, at a finite velocity, sequentially through the load-carrying structural members to the equipment. During this process, the amplitude and frequency content of the stress waves may be altered as the properties or dimensions of the structural members vary, or as the stress waves are transmitted through intersections from one structural member to another. The TFT is a straightforward method of accounting for sequential changes in the initial stress wave as it encounters new structural members and intersections.

The general approach to developing the TFT consists of two steps. The first step is to characterize the waves that are transferred through each of several common structural members and through intersections between members. These characterizations are obtained by performing exact analyses of the response when a stress wave impinges on structural members or intersections between members. Any analysis that can predict the details of the wave front is

acceptable. The analyses used in this paper are based on simple bar theories for in-plane response and Timoshenko-type theories for transverse response in which solutions were obtained by the method of characteristics. To ensure the accuracy of tne analyses, the response predicted by each analysis was compared with the response measured in a corresponding impact experiment.

The second step is to relate the transmitted waves to the incident wave by a relation called a transfer function. The transfer function is an approximate relation based on the results of the exact theoretical calculations. Sequential application of the transfer functions for each member and each intersection in a given structure allows one to determine how the stress waves are altered as they pass through the structure to the components.

Thus, an exact solution must first be obtained for each type of structural element or intersection. The usefulness of the TFT is that the transfer function obtained from the exact analysis can be applied to the same structural element or intersection in any other structure without repeating the exact analysis.

In the work discussed here, the development of the TFT was simplified in two ways. First, for simplicity, the investigation was restricted to wave propagation along one spatial dimension of each structural member, e g., in beams and rings, and in plates or shells in plane strain. Second, in the examples given here, all the structural members are straight beams of the same uniform cross section, so the in-plane waves are not altered as they propagate through each member. (As discussed in the next section, the TFT need characterize only the changes in the in-plane waves at the intersections of the structural members.) In principal the TFT can be applied to a more general class of structures, for example, structures with members of different cross-sections, however additional analyses would be required.

In the rest of this paper, we will compare the impor and of in-plane waves and transverse waves for equipment response problems; illustrate in detail the development of a transfer function for a two-member and a three-member intersection; and illustrate the application of the TFT to a multi-member structure.

COMPARISON OF IN-PLANE AND TRANSVERSE WAVES

It was found that the TFT could be simplified by including only the type of waves that produce the most severe environment for internal equipment. Equipment is generally mounted on a structural element that has at least one dimension that is much smaller than the others, such as a beam or plate. Such structural elements propagate two principal types of stress waves that excite equipment: waves that produce motion parallel to this plane (in-plane waves) and waves that produce motion normal to this

plane (transverse waves). The important features of these two types of waves can be illustrated by examining the response of a straight beam-column of circular cross section.

The response of a beam-column was calculated for an in-plane or axial load, as in Figure 1(a), and for a transverse load, as in Figure 1(b), of the same time history. For axial loading, Figure 1(a) shows the axial force-time history of the load at the end of the member and of the response at several locations in a straight, semi-infinite beam-column. The half-sine loading pulse is typical of that transmitted to an interior structural element from an exterior element, such as a shell, that is loaded suddenly on its exterior surface. The response shown is that predicted by simple bar theory. Because the half wave length of the pulse is much greater than the diameter of the beam-column (by about a factor of 10 here), the pulse propagated down the beam-column is nondispersive and is accurately predicted by bar theory. Thus, the axial force-time history is identical at each point on the structure. The time at which the pulse arrives depends on location and is given by $x/c_b$, where $x$ is the axial coordinate and $c_b = \sqrt{E/\rho}$ is the bar velocity. For in-plane waves, the particle velocity is proportional to the time derivitive of the axial force and the particle displacement is proportional to the time integral of the axial force. Therefore, the wave environment for equipment at any point on the structural member is characterized completely by the loading force only.

For transverse loading, Figure 1(b) shows the transverse shear force-time history at several locations in the same beam-column. The transverse wave response was predicted by Timoshenko beam theory. In contrast to the nondispersive axial wave response, the dispersive transverse wave response has a different transverse force-time history at each point on the structure. The character of the transverse wave differs from that of the axial wave in two ways. First, the amplitude of the transverse wave decreases, and the sign of the peak force amplitude alternates, as the wave propagates down the beam-column. For example, at $x/d = 30$, the peak shear force amplitude is only about 20 percent of the peak loading force amplitude and the peak amplitude is of the opposite sign. Second, the bulk of the energy of the pulse, in which the peak amplitude occurs, travels more slowly than the axial wave. For example, at $x/d = 30$, the peak amplitude of the shear force occurs at about $\Delta \tau = 18$ after the initial disturbance arrives: the peak amplitude of the axial force occurs at $\Delta \tau = 5$ after the initial disturbance. Thus, the bulk of the energy in the transverse pulse arrives about $\Delta \tau = 13$ later than that of the axial pulse. This difference in the time of arrival of energy in the pulses increases as the pulses propagate along the structure.
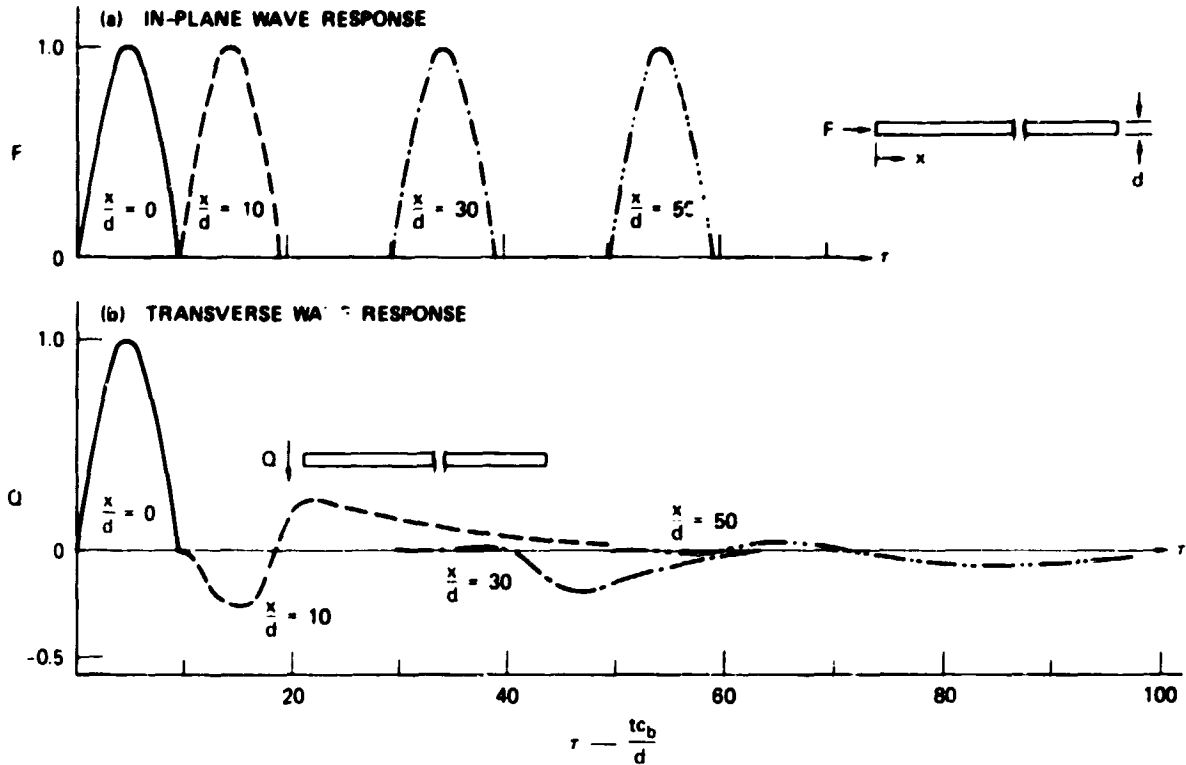
Fig. 1 - Comparison of Stress Waves Produced in a Bar by Axial Loading and by Lateral
Loading (t is time and $c_b$ is bar velocity)

These differences between responses of axial
and transverse waves permit an important simpli-
fication in developing and applying the TFT. Con-
sider two structural members joined at an arbi-
trary angle less than $\pi/2$ radians. When an axial
stress wave in the first member impinges on the
intersection, both an in-plane and a transverse
stress wave are produced in the second member.
However, except near the intersection, the exci-
tation of equipment by the transverse wave occurs
later than that by the in-plane wave and has a
much smaller amplitude. Therefore, in the appli-
cation of the TFT, it is necessary to follow
only the axial wave response in the second mem-
ber. For a more complex structure with several
intersections, effects are similar at each in-
tersection. Thus, it is necessary to follow
only the axial pulse on the load path from the
external load to the equipment.*

WAVF ̄OPAGATION THROUGH TWO- AND THRFE-MEMBER
INTL̲.̲ẓECTIONS

In this section we discuss an impact experi-
ment, a detailed wave analysis, and the determi-
nation of a transfer function for the two-member
intersection and for the three-member inter-
section.

Two-Member Intersection

A structure forming a two-member inter-
section is shown in Figure 2(a). To provide
baseline data against which theoretical calcu-
lations could be compared, we first performed an
impact experiment on a two-member structure made
of 6061-T6 aluminum straight members of 1.27-cm
square cross section with an intersection angle
of $\pi/4$ radians. The end of one member was im-
pacted by a 1.20 cm-diameter, 18.0 gram brass
projectile accelerated to 15.2 m/sec by a small
air gun. To produce a finite rise pulse, a
0.318-cm-thick Teflon disc was bonded to the end
of the member that was impacted. At one station
in each bar, either two or four strain gages were
used to measure the incident wave and the wave
transmitted through the intersection. Only the
ave.̲ge axial strains are discussed in this paper.

---

*For equipment mounted near the intersection, a
case of limited practical interest, the effect
of the transverse wave may not be negligible
compared with that of the in-plane wave. This
point is discussed in more detail in Reference 3.

91

GAGE No. 1
No. 2
No. 2
No. 1
No. 4 — P —
No. 3
No. 5
No. 6
No. 8
No. 7
STATION 3
No. 3
STATION 1    STATION 2

(a) STRUCTURAL CONFIGURATION



(b) AXIAL STRAIN PULSE AT STATION 1
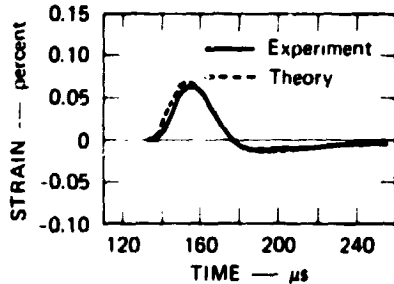


(c) AXIAL STRAIN PULSE AT STATION 3

Fig. 2 - Configuration and Response of
Two-Member Structure (axial
strains are the averaged strains
at each station)

The measured axial strain pulse that was
produced in the loaded member and was incident
on the intersection is shown in Figure 2(b).
The measured axial strain pulse transmitted to
the unloaded member is shown in Figure 2(c).

We then performed a detailed analysis of
the stress wave propagation through this two-
member intersection. The analysis is based on
simple bar theory, Timoshenko beam theory, and
a rigid element at the intersection. The
governing wave equations were integrated by the
method of characteristics.*

As indicated in Figure 2(b), the input
axial pulse used in the analysis was identical
to the measured axial pulse. Figure 2(c) com-
pares the predicted axial pulse transmitted into

---

*Details of the analysis are given in Reference 3.

TRANSFER FUNCTION



$$\frac{N_{2,max}}{N_{1,max}} = 0.39 \cos 2\theta + 0.61$$

$$N_1 = N_{1,max} \cdot \sin \frac{\pi C_p t}{\lambda}$$

$$\lambda = 20h$$
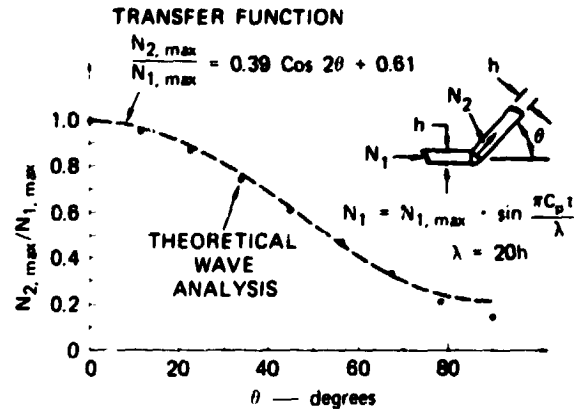
Fig. 3 - Transfer Function for Two-Member
Intersection

the unloaded member and the corresponding
measured pulse. The theory accurately predicts
the transmitted pulse.

Comparison of Figures 2(b) and 2(c) shows
that the shape of the main portion of the trans-
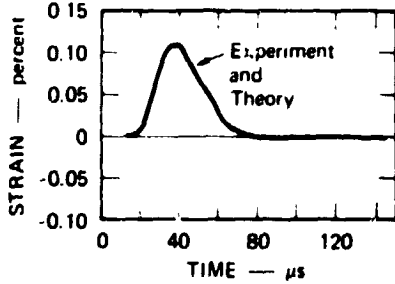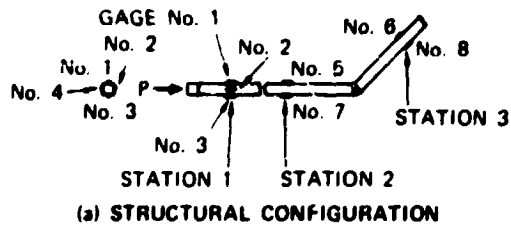mitted pulse closely approximates that of the
incident pulse. However, the wavelength of the
transmitted pulse is slightly less than that of
the incident pulse, and the amplitude of the
transmitted pulse is reduced to about 61 percent
of the amplitude of the incident pulse.

Analysis of nine similar two-member struc-
tures were performed for values of θ spaced
π/16 radians apart in the range 0 to π/2 radians.
The loading was an axial pulse in the shape of a
half-sine wave. As was true for the intersec-
tion with θ = π/4 radians, pulse shape and wave-
length change only slightly as the pulse is
transmitted through the intersection. The prin-
cipal effect of the intersection is to reduce
the amplitude of the transmitted pulse from that
of the incident pulse. This effect is summarized
by the calculated data points shown in Figure 3.

These observations suggest a simple method
for predicting the transmitted longitudinal wave
given the incident wave: the pulse shape and
wavelength are retained, and the amplitude is
reduced by a factor that depends on the inter-
section angle θ. The transfer function for this
intersection is therefore defined as the ratio
of the amplitude of the transmitted longitudinal
wave to that of the incident wave. The transfer
function of the two-member intersection was
constructed by fitting a curve to the calculated
data points of Figure 3; the expression for the
curve is also shown in the Figure. It was
found that although more complicated relations
could be found to relate the transmitted pulse
to the incident pulse more accurately (for ex-
ample by accounting for wave-length change), the
simplicity of the approach taken here makes it
particularly efficient for estimating the wave

(a) STRUCTURAL CONFIGURATION

(b) AXIAL STRAIN AT STATION 1

(c) AXIAL STRAIN AT STATION 2

(d) AXIAL STRAIN AT STATION 3

Fig. 4 - Configuration and Response of Three-Member Structure
(Axial strains are the averaged strains at each station)

environment for structures with several intersections.

## Three-Member Intersection

A structure forming a three-member intersection is shown in Figure 4(a). The structure was made of 6061-T6 aluminum straight members of 1.27-cm-square cross section, and the intersection angle was $\pi/4$ radians. The measured axial strain pulse that was produced in the loaded member and was incident on the intersection in the impact experiments is shown in Figure 4(b). The measured axial strain pulses transmitted to the unloaded members are shown in Figures 4(c) and 4(d).

As was true for the two-member structure, the axial loading pulse used in the analysis of the three-member structure, as shown in Figure 4(b), is identical to that measured in the experiment. Figures 4(c) and 4(d) compare the predicted axial pulses transmitted into the unloaded members and the corresponding measured pulses. The theory accurately predicts the transmitted pulses.

Comparison of Figures 4(b), 4(c), and 4(d) shows that, as was true for the two-member

structure, the shapes of the main portions of the transmitted pulses closely approximate that of the incident pulse; the wavelengths of the transmitted pulses are slightly less than that of the incident pulse; the amplitude of the pulse transmitted to the oblique member (station 2) is reduced to about 39 percent of the amplitude of the incident pulse; and the amplitude of the pulse transmitted to the in-line member (station 3) is reduced to about 80 percent of the amplitude of the incident pulse.

Analyses of three-member structures were performed for 15 values of $\theta$ spaced $\pi/16$ radians apart in the range $-7\pi/16$ radians $\leq \theta \leq + 7\pi/16$ radians. Again, the principal effect of the intersection was to reduce the amplitude of the transmitted pulse from that of the incident pulse with little affect on the pulse shape and wavelength. This effect is summarized by the calculated data points shown in Figure 5. The transfer functions of the three-member intersection were constructed by fitting a curve to the calculated points shown in Figure 5. The expressions for the curves are also shown in the figure.

93
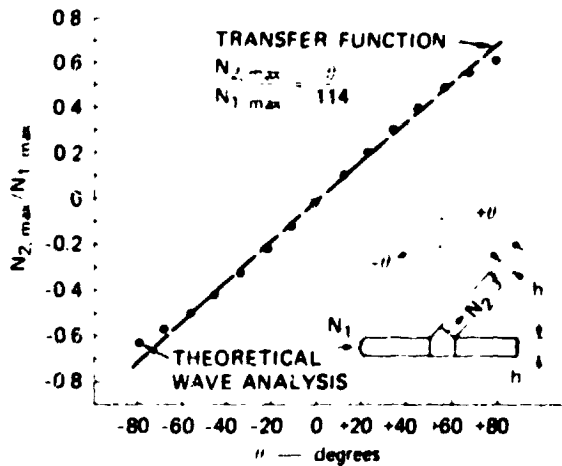
(a) OBLIQUE MEMBER
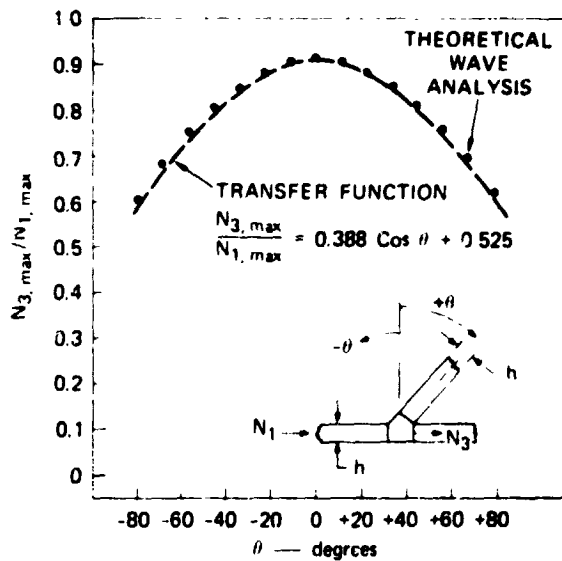


(b) HORIZONTAL MEMBER

Fig. 5 - Transfer Functions for Three-
Member Intersection

## APPLICATION OF THE TRANSFER FUNCTION TECHNIQUE

The application of the TFT can be illus-
trated by applying it to the structure shown in
Figure 6. As we did for the simple two- and
three-member structures, we first performed both
an impact experiment and a detailed wave
analysis* for the structure shown in Figure 6(a).
As before, the loading pulse used in the analy-
sis is identical to that measured in the experi-
ment. The measured and the predicted axial
strains in members 2, 4, and 5 are shown in
Figure 6.

───────────────

*A complete description of the analysis is
given in Reference 1.

In general, we obtained good agreement be-
tween the measured and the predicted strains.
The largest discrepancy occurs in member 5 when
the axial strain becomes tensile, about 35 μsec
after the arrival of the pulse. This portion of
the pulse in member 5 results from the combi-
nation of three effects: the small but nonzero
strain that occurs after the main portion of the
pulse that has propagated through members 2 and
4, an effect also shown in Figure 2(c); the wave
reflected off the junction of members 5, 3, and
6 after propagating through member 5; and the
wave that initially propagated through m·
then through member 5. The discrepancy b· ween
theory and experiment results from the combined
errors associated with predicting each of these
three effects. Nevertheless, good agreement is
obtained for the initial portion of the pulse,
when the environment for the equipment is most
severe.

We then used the TFT to predict the longi-
tudinal waves in the structure shown in Figure 6.
The prediction was made by sequentially applying
the appropriate transfer function to the inter-
sections between member 1 and the member of in-
terest. The TFT-predicted waves have the same
shape and wavelength as the incident wave.
Application of the TFT involves applying appro-
priate reduction factors to the amplitude of the
incident pulse. For example, for the $\pi/4$ radian
angle intersection formed between members 1 and
2, the transfer function given in Figure 5(a)
has a value of $N_{2,max}/N_{1,max} = 0.395$. For the
$\pi/4$ radian angle intersection formed between
members 2 and 4, the transfer function given in
Figure 3 has a value of $N_{4,max}/N_{2,max} = 0.610$.
Thus the amplitude of the wave transmitted to
member 4 is reduced from that of the incident
wave in member 1 by the factor

$$\frac{N_{4,max}}{N_{1,max}} = \left(\frac{N_{2,max}}{N_{1,max}}\right) \cdot \left(\frac{N_{4,max}}{N_{2,max}}\right)$$

$$= (0.395) \cdot (0.610)$$

$$= 0.241$$

In addition to being transmitted through
members 2 and 4, the wave in member 5 has also
been transmitted through a second two-member
intersection identical to the first two-member
intersection. Therefore, its amplitude is re-
duced from that of the incident wave by the
factor

$$\frac{N_{5,max}}{N_{1,max}} = (0.395) \cdot (0.610) \cdot (0.610)$$

$$= 0.147$$

(a) STRUCTURAL CONFIGURATION

(b) AXIAL STRAIN AT STATION 1

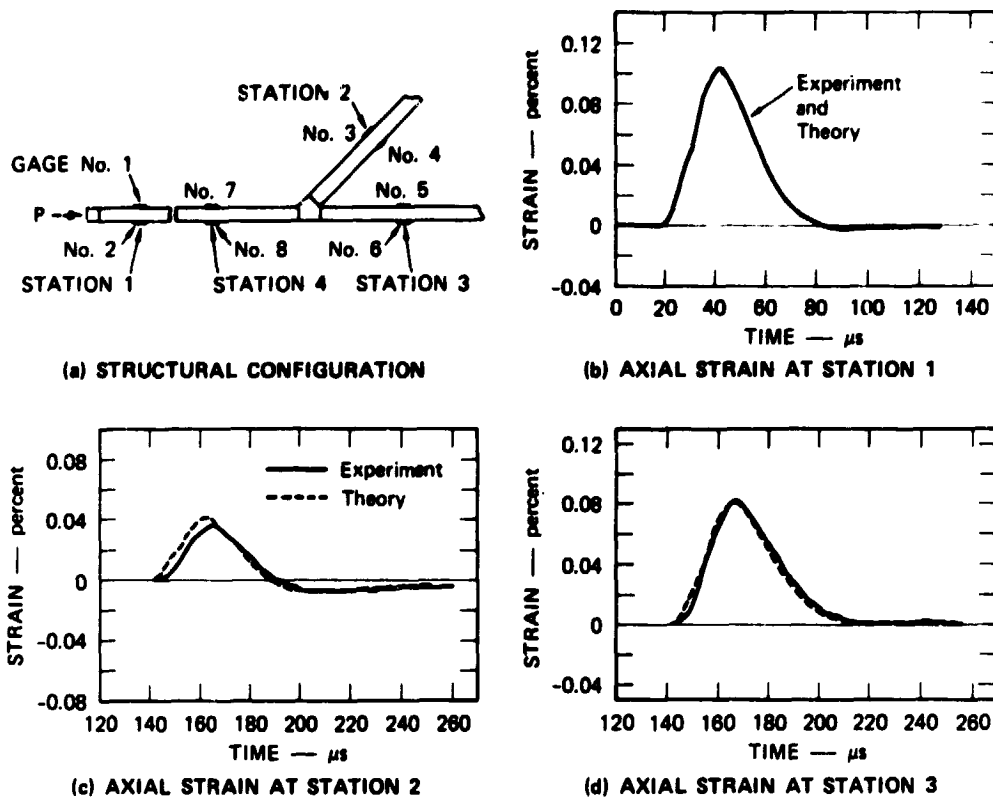(c) AXIAL STRAIN AT STATION 2

(d) AXIAL STRAIN AT STATION 4

(e) AXIAL STRAIN AT STATION 5
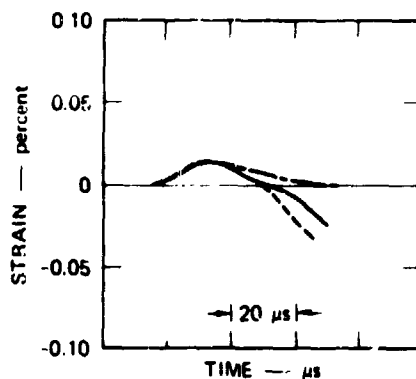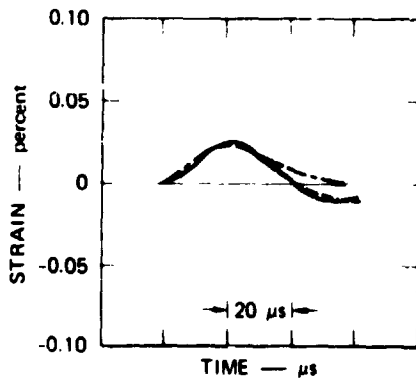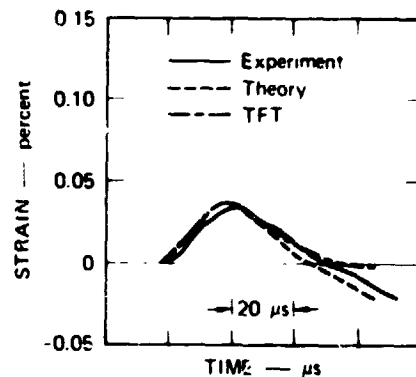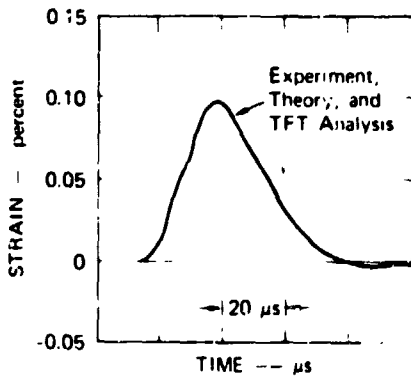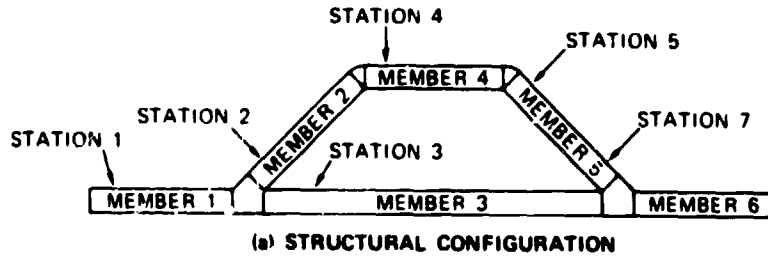
Fig. 6 - Configuration and Response of Six-Member Structure
(Axial strains are the averaged strains at each station)

95

The TFT-predicted waves are also shown in Figure 6. The figure shows that, as expected, there is good agreement among the initial waves in members 2, 4, and 5 as predicted by the detailed analysis, as predicted by the TFT, and as measured experimentally. Note that because the TFT-predicted pulses are proportional to the input pulse, they do not show significant tensile strain. They do, however, accurately predict the initial wave propagated through the structure.

## CONCLUSIONS

We have shown that, once the transfer functions are established for the required intersections, the TFT is useful for efficiently obtaining an initial evaluation of the wave environment in a structure subjected to a sudden dynamic load. Additional transfer functions for intersections of interest must be developed. Then the TFT can be used in two ways. First, it can be used as an analytical tool to determine whether the stress wave environment is so severe that further, more detailed analyses should be performed. Second, for potentially severe stress wave environments, the TFT can be used as a design tool for choosing sizes or configurations of structural members and of component mounting hardware to minimize the effect of the stress wave environment on the equipment.

## REFERENCES

1. J. D. Colton and J. E. Malinak, "Stress Wave Approach to the Analysis of Submarine Component Shock Response," Shock and Vibration Bulletin 46, Part 2, Naval Research Laboratory, Washington, D.C., March 1977.

2. J. D. Colton and H. E. Lindberg, "Stress Wave Approach to the Analysis of Internal Component Shock Response," Final Report DNA 3637F, SRI International, March 1976.

3. T. P. Desmond and J. D. Colton, "Generalization of the Wave Approach to the Analysis of Internal Equipment Response," Final Report (Draft) on SRI Contract No. DNA001-77-C-0198, October 1978

## BIBLIOGRAPHY

Abramson, H. N., H. J. Plass, and E. A. Ripperger, "Stress Wave Propagation in Rods and Beams," in Advances in Applied Mechanics, Vol. 5, H. L. Dryden and Th.vonKarman, eds. (Academic Press, New York, NY, 1958). pp. 111-194.

Achenbach, J. D., Wave Propagation in Elastic Solids (American Elsevier Publishing Co., New York, NY, 1973).

Atkins, K. J., and S. C. Hunter, "The Propagation of Longitudinal Elastic Waves Around Right-Angled Corners in Rods of Square Cross-Section," Quarterly J. Mech. and Appl. Mathematics, Vol. 28, pp. 245-260 (May 1975).

Kolsky, H., Stress Waves in Solids (Dover Publications, New York, NY, 1963).

Leonard, R. W., and B. Budiansky, "On Traveling Waves in Beams," NACA Technical Note 2874, (1953).

Timoshenko, S., "On the Transverse Vibrations of Bars of Uniform Cross Section," Phil. Mag., Ser. 6, Vol. 43, pp. 125-131 (1922).

# HIGH G PYROTECHNIC SHOCK SIMULATION
## USING METAL-TO-METAL IMPACT

Monty Bai and Wesley Thatcher
Motorola Government Electronics Division
Scottsdale, Arizona

This report presents a technique for simulating high g level pyrotechnic shocks, and the results of applying the technique to obtain the MIL-STD-1540A shock spectrum with a maximum acceleration of 18,000g at 2,000 Hz.

Designing the resonant beam and plate on which the test unit is mounted, and generating a proper impulsive load on them, were the essentials of the technique. One dimensional stress wave and Euler equations were employed in the design. A metal pendulum hammer was used to generate the impulsive load.

## INTRODUCTION

A given pyrotechnic shock spectrum can be obtained in an infinite number of ways, since there is no uniqueness between the shock transient and its shock spectrum. Drop table machines are often used to produce a given shock spectrum by generating a classical pulse such as a half sine. The distinct characteristics of the shock spectrum generated by this technique are a constant slope of 6 dB/octave (most of the slopes of pyrotechnic shock spectra are between 9 and 12 dB/octave) and a significant difference between the positive and negative spectra. The shock synthesis method, using an electromagnetic shaker controlled by a digital computer, can produce a shock spectrum of any shape. However, the amplitude of the spectrum is limited by the capacity of the shaker. A metal-to-metal impact technique can produce a very high g shock relatively easily. However, controllability and repeatability of the test are known to be rather poor. Without using an explosive, this technique seems to be the most promising approach in obtaining a high g level shock spectrum such as that specified in MIL-STD-1540A.

In order to control the shock response spectrum, understanding the response characteristics of single-degree-of-freedom spring mass systems was a fundamental step, since the shock response spectrum is defined as the absolute maximum dynamic response of many single-degree-of-freedom spring mass systems with damping. An ideal shock transient can be modeled for a given shock spectrum. The next step was to design a beam or plate which could produce such a transient, using one-dimensional wave propagation theory or the Euler equation. The final step was to develop an impulsive loading technique.

To produce the MIL-STD-1540A shock spectrum, the ideal transient should have a fundamental frequency of 2,000 Hz and highest energy at that frequency in its shock spectrum. Amplitudes of the frequencies higher than the fundamental frequency in the Fourier spectrum should be lower. To excite the fixture so that the dominant frequency matches the fundamental frequency, the duration of the impulsive loading should be approximately equal to half the duration of the fundamental frequency. Because of mathematical difficulties encountered in trying to theoretically predict the dynamic response of the beam or plate under a metal impact, the emphasis in this study was initially experimental.

## DESIGN OF THE RESONANT FIXTURE

To perform the required shock tests in the three orthogonal directions, a 48 X 6 X 1-in. aluminum beam and a 17 X 10 X 3-in. aluminum plate were designed for the resonant fixtures on which the test unit was mounted and excited. A 13-pound steel block pendulum hammer was arranged to generate an impulsive load on the fixture beam or plate. Schematic setups of the two fixtures and the pendulum are shown in Figs. 1 and 2.
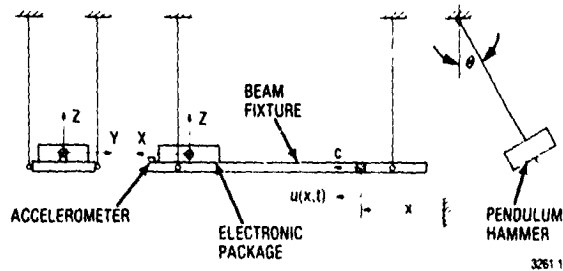
Fig. 1 - Diagrammatic Arrangement of Beam Fixture and Pendulum Hammer for Test in X Direction

The length of the resonant beam, L, was determined from the equation.

$$L = \frac{c}{2f_1} \tag{1}$$

where c is the speed of the dilatational wave in the beam and $f_1$ is the fundamental frequency. The harmonic frequencies can be calculated from the general form of Eq. (1).

$$t_n = \frac{nc}{2L}, \quad n = 1, 2, 3, \tag{2}$$

This equation is derived from the one-dimensional wave equation.

$$\frac{\partial^2 u(x,t)}{\partial x^2} = \frac{1}{c^2} \frac{\partial^2 u(x,t)}{\partial t^2} \tag{3}$$

with proper boundary conditions. The beam fixture can be used to perform in the X and Y directions by rotating the unit 90° along the Z axis

For the test in the Z direction, the 17 X 10 X 3-in. aluminum plate was used, the design of which was based on the Euler equation.

$$\frac{\partial^2 u(x,t)}{\partial t^2} + \frac{EIg}{\gamma} \frac{\partial^4 u(x,t)}{\partial x^4} = 0 \tag{4}$$

with completely free boundary condition.
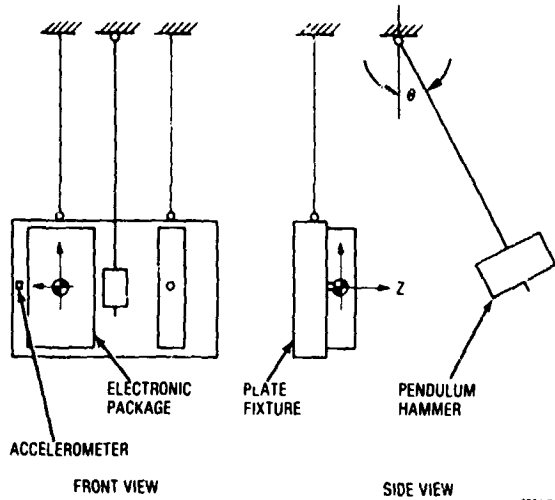


Fig. 2- Diagrammatic Arrangement of Plate Fixture and Pendulum Hammer for Test in Z Direction

## TESTS AND ANALYSIS

Shock transients were measured by the shock accelerometer, Endevco model 2292, with the shock amplifier, Endevco model 2740B, and analyzed with a Time/Data Digital Computer. A diagrammatic arrangement of the instrumentation is shown in Fig. 3 Three tests in each axis were conducted after calibrating the setup with a mockup unit.
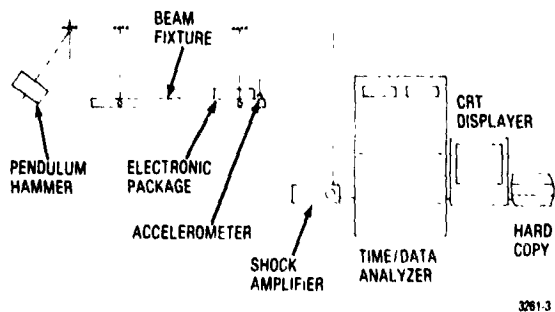


Fig. 3- Diagrammatic Arrangement of Instrumentation

A typical acceleration measurement in the X direction and its shock and Fourier spectra are shown in Figs 4, 5 and 6. The fundamental frequency of 2017 Hz with its harmonic frequencies of 4065, 6050 and 8010 Hz were measured in Fig. 5. These frequencies, which were predicted with Eq. (2) to be 2068, 4136, 6205 and 8272 Hz, are important characteristics of the beam that can only be changed by altering its length.
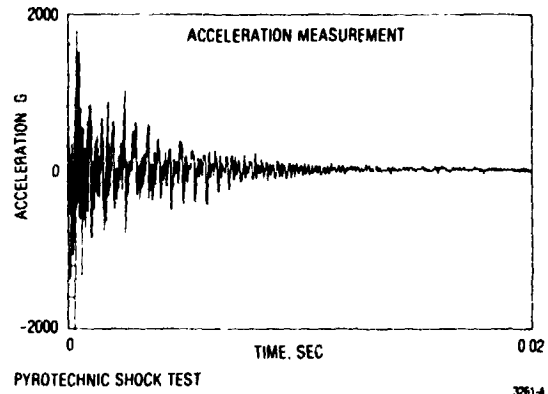


Fig. 4 - Shock Transient Measured in X Direction
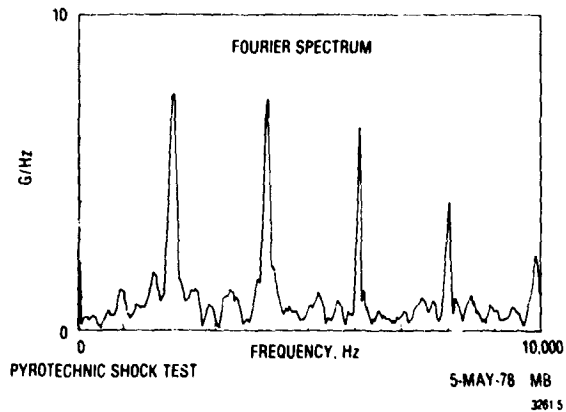


Fig. 5 - Fourier Amplitude Spectrum of Shock Transient Measured in X Direction

The shape of the shock spectrum can be predicted from the Fourier spectrum of the shock transient. The relative amplitudes of the frequencies in the Fourier spectrum can be effectively adjusted by placing a small aluminum block at the impact area, thus changing the impact loading duration. Wideband noise in the shock transients was generated by the test unit, especially during tests in the Z direction. The level of noise was considerably reduced by increasing the thickness of the fixture plate.

Test results in the X, Y and Z directions are shown in Figs. 7, 8 and 9. Seventy-two percent of the data points were in the tolerance bands of +6 dB from 100 to 5,000 Hz, +9 dB from 5,000 to 10,000 Hz, and -3 dB from 100 to 10,000 Hz. These results show more over-tolerance points than under-tolerance points, as was intended, although it was not planned to over-test that much, especially in the low frequency range (83% of the data points were within the tolerance bands with the mockup unit). It is believed that the differences in the two units caused the variation in the results.

98
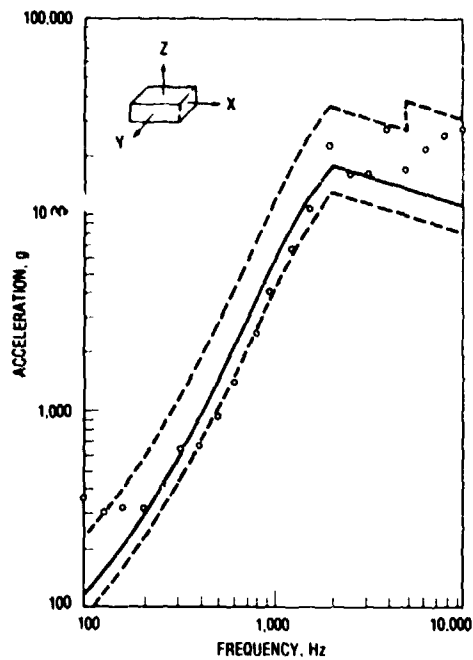
Fig. 6 - Shock Response Spectrum of Shock Transient
Measured in X Direction
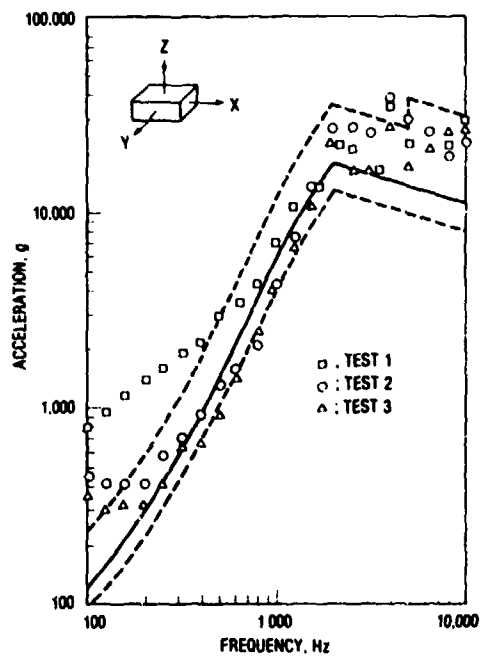


Fig. 7 - Shock Response Spectra of Tests in X Direction
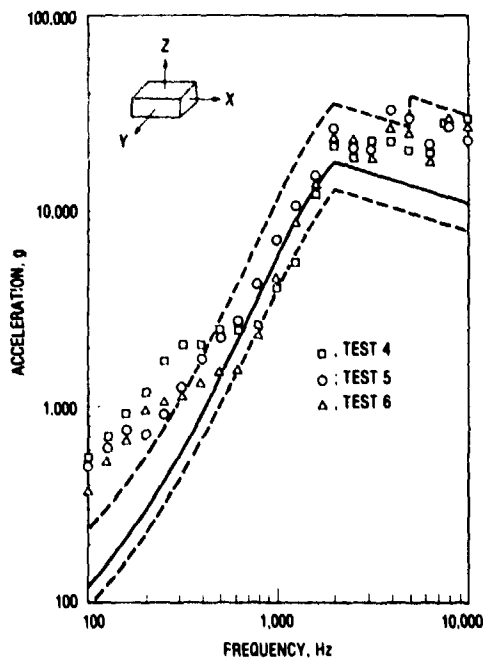


Fig. 8 - Shock Response Spectra of Tests in Y Direction
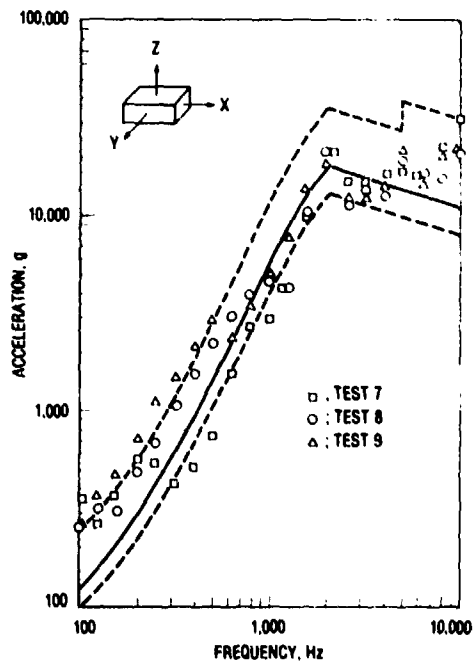


Fig. 9 - Shock Response Spectra of Tests in Z Direction

## DISCUSSION AND RECOMMENDATIONS

The capability for high g pyrotechnic shock simulation tests was demonstrated using the metal-to-metal impact technique and a Time Data Analyzer. This was done by performing the required pyrotechnic shock tests on a real unit according to MIL-STD-1540A, with a maximum acceleration of 18,000 g at 2,000 Hz. Designing the resonant fixtures and generating an optimum impulsive load on them were the essentials of the technique. It was relatively easy to obtain high g's of around 20,000 g in the shock spectrum. However, it was difficult to improve controllability and repeatability of the tests because of the nature of the metal impact and wideband noise generated by the test unit.

Seventy-two per cent of the data points were within tolerance bands while 7% of the data points were shown to be under the tolerance bands. These results from the real unit were considerably different from the shock spectrum      ted with a mockup unit (83% of the data points were w'-~ n the bands). It is believed that the cables and connectors attached to the actual unit, but not to the mockup unit, as well as

elongation of the mounting holes on the mockup unit were the main parameters contributing to the difference in the results from the two units.

Wideband noise in the shock transients was generated by the test unit, especially during tests in the Z direction. In this experimental study, a low level of noise appeared to help bring the spectrum level up about 2,000 Hz. This undesirable noise was minimized by increasing the thickness of the fixture plate and decreasing the contact area of the unit on the fixture. It is generally true that reducing the contact area reduces the shock level transmitted to the unit. Further improvement of the setup for generating an optimum impulsive load should be made. The pendulum hammer can be replaced by an air gun. A proper arrangement of the air gun with an acc··· i'e pressure gage and a device detecting the projectile impact velocity will eliminate alignment problems and improve the test repeatability.

A dynamic strain gage can be used to find the impulsive load. Therefore, the air gun arrangement and dynamic strain gage instrumentation are highly recommended for systematic and effective operation of pyrotechnic shock simulation tests.

# AN EXPERIMENTAL DESIGN FOR TOTAL CONTAINER
## IMPACT RESPONSE MODELING AT EXTREME
### TEMPERATURES

Virginia P. Kobler
U. S. Army Missile Research and Development Command
Huntsville, Alabama 35809

and

Richard M. Wyskida and James D. Johannes
The University of Alabama in Huntsville
Huntsville, Alabama 35807

A cushion behaves in one manner when tested as a flat pad (unconfined cushion) and in a different manner in an actual container (confined cushion). There have been few direct comparisons, the assumption being that the unconfined data results in conservative designs. Since unconfined cushion impact response has been modeled, it is now possible to attempt an extension to the confined cushion situation. An experimental design is developed to identify the actual effect of the outside container upon shock attenuation involving the protected item.

## INTRODUCTION

In designing a cushioning system, both the item to be protected and the external environment which it will encounter must be considered. The two stipulations of how much shock an item can survive and how much shock it is expected to experience in its environment are the prime considerations in the design of any cushioning system, commercial or military. In addition, extreme external environments must be considered in military cushion designs.

Modern package designers use dynamic cushioning curves to determine the appropriate material and material thickness to protect items from impact loads. Figure 1 is a typical set of dynamic cushioning curves for a given material, thickness and drop height. The three curves represent three different temperatures. Points on the curves correspond to the peak acceleration, given in G's, experienced by the cushioned item at the corresponding static stresses. The horizontal line depicts the fragility level to which the item under consideration must be protected. The package designer must choose a material and a material thickness which possesses dynamic cushioning curves for the temperature range for which he is designing, and furthermore, a portion of the curves must be below the specified fragility level. A separate set of curves is necessary for each unique set of parameters, i.e., drop height, cushion thickness, temperature, and material.

Extensive experimentation has been performed by McDaniel, Wyskida, Wilhelm, and Johannes [1-5] into the effect of temperature upon impact response for various bulk cushioning materials. McDaniel was the first to develop a mathematical model for the impact response of bulk cushioning materials which incorporated temperature effects. Cost [6] developed a viscoelastic theory to describe the temperature effects under impact loads.

The dynamic cushioning curves shown in Figure 1 were derived from data obtained when drop tests were conducted on a flat pad cushion. That is, the cushioning is placed on a plate, and the various platen weights corresponding to different stress levels are dropped onto the pad. The maximum acceleration achieved during the impact is measured. This method of obtaining impact response was not designed to take into consideration the effects of an outside container upon the impact response. Mazzei [7] found that there was a definite difference in confined (outside container) and unconfined test results. He attributed this difference to pneumatic effects within the container. Since there are known to be container effects, the lack of data on container effects and the inability to predict them has been a major concern to cushion system designers. Consequently, the authors' objective is to design a drop test experiment which extends the flat pad cushion impact response approach to that of an item enclosed in a container.

**MINICEL ENCAP**

H = 344K  A = 294K  C = 219K  D.H. = 762 mm
TOPT = 63.5 mm  GLMAX = 50.00  SSL = 4137 Pa  SSU = 7929 Pa
MIN. BEARING AREA = 56103 mm$^2$  MAX. BEARING AREA = 107535 mm$^2$
ITEM WEIGHT = 45.4 kg
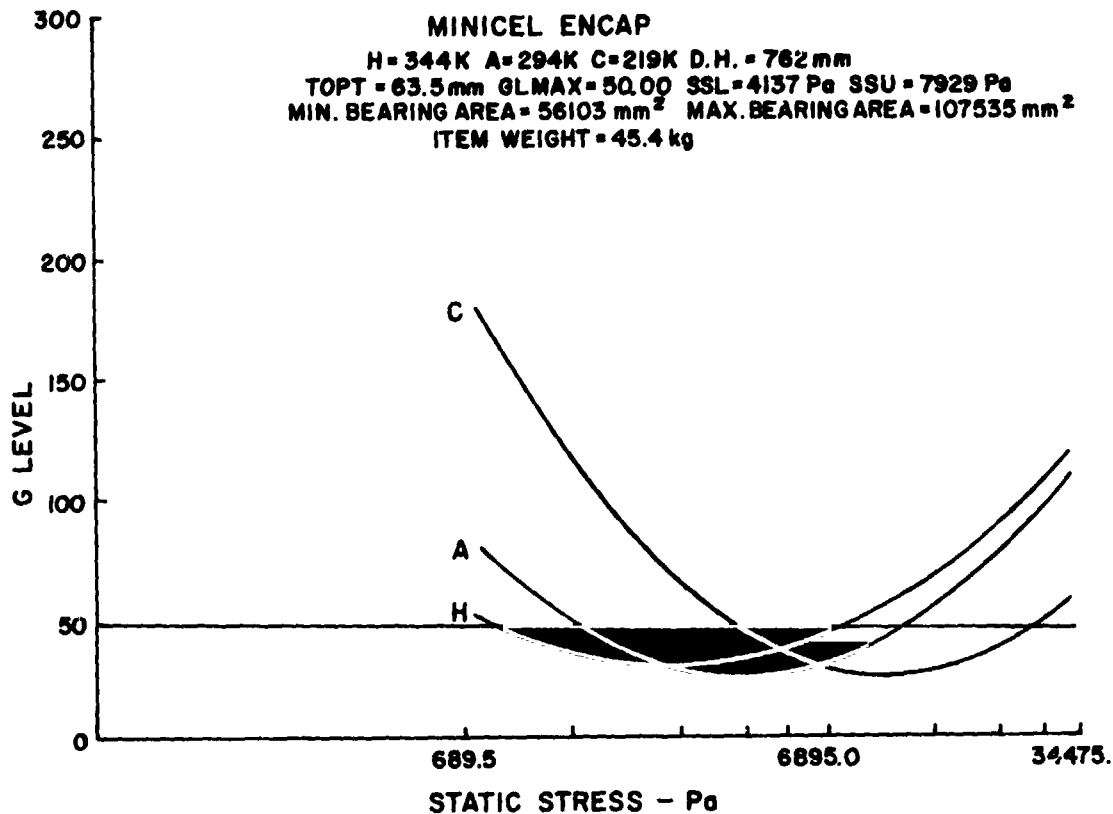
Fig. 1 - Typical dynamic cushioning curves at selected temperatures

McDaniel [4] developed a specific model for the impact response of Hercules Minicel, a cross-linked polyethylene foam, based upon flat pad cushion data. Minicel possesses the ability to withstand extreme temperatures, without a degradation in cushioning ability. Consequently, a 50.8 mm thick Minicel cushion was selected as the bulk cushioning material for use in the container experimental model.

PHYSICAL DESCRIPTION

The test specimen utilized in the container drop tests consisted of a 482.6 mm plywood cube protected by 50.8 mm cushions of Minicel configured as corner void pads. This test specimen was enclosed in a military standard cleated plywood shipping container as shown in Figure 2. Six static stress levels were obtained by varying the total area of the cushioning material on the six faces of the test specimen, so that each face of the container represents a different stress level. The relationship between static stress, σ, weight, W, and total cushion area, A, was used to determine the size of the corner pads in the following equation:

$$\sigma = \frac{W}{A}$$

Using the weight of the test specimen, 11.57 kg, and the following cushion pad dimensions, the resulting static stress levels are:

| Cushion Pad Side (mm.) | Total Area (mm.$^2$) | Static Stress Levels (Pa) |
|---|---|---|
| 215.9 | 186451.2 | 608.5 |
| 127.0 | 64516.0 | 1758./ |
| 88.9 | 31612.8 | 3589.1 |
| 76.2 | 23225.8 | 4885.2 |
| 69.8 | 19488.2 | 5822.1 |
| 57.2 | 13087.4 | 8669.6 |

It should be noted that the actual size of the corner void pads was determined prior to calculating the static stress levels, due to the physical dimension constraint on the surface of the test specimen. Should lower stress levels be desired, the dimensions of the test specimen must be increased accordingly, to accommodate the larger cushions which would be required.

The six temperatures at which drops were considered desirable were 219, 244, 266, 294, 316, and 344K. Four standard drop heights were used--304.8, 457.2, 609.6, and 762.0 mm. Three replicates were performed for each set of experimental conditions.

102
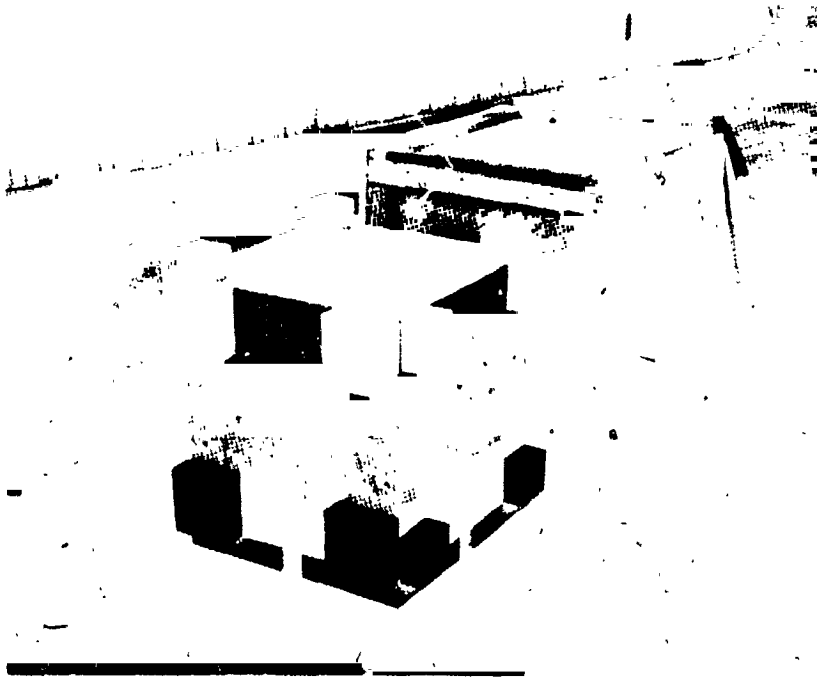
Fig. 2 - Test spec,men and outside container



Fig. 3 - Container systeni in environmental chamber

103
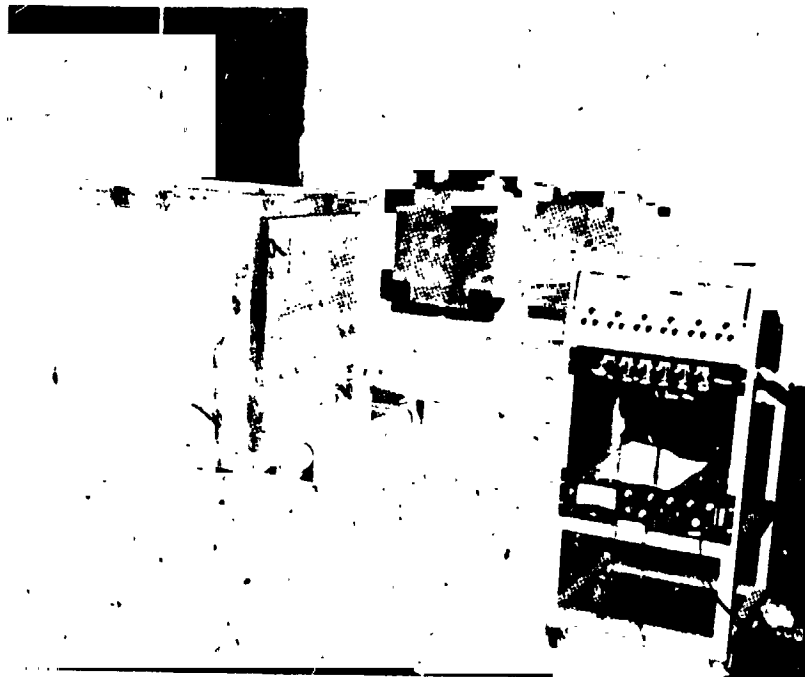
Fig. 4 - Drop tester and container system prior to drop

Twenty-four complete container systems were prepared for experimental testing. One set of twelve containers was utilized for temperatures 294, 244, and 344K, and the other twelve containers for 266, 316, and 219K. This prevents any one container system from experiencing the entire temperature range of 125K, which is unlikely to occur in an actual situation.

Prior to conditioning, the container system was instrumented with three accelerometers in the test specimen, and three in the outer container. The complete container systems were conditioned in environmental chambers (Fig. 3) at the required temperature for twenty-four hours prior to testing.

All tests were conducted at the U S. Army Missile Research and Development Command's Dynamic Test Facility. Fig. 4 shows the drop tester and the container positioned ready to drop. Fig. 5 shows the test apparatus after a drop.

EXPERIMENTAL DESIGN

The order of the drops was randomized as much as possible. One constraint on randomization was the use of the environmental chambers for each temperature. Chamber space necessitated the drop test procedure to consider all of one temperature simultaneously. That is, all three replicates for one temperature were conditioned as a group. Since each box required a cable to be attached, just prior to testing but after removal from the chamber, it was not feasible to randomize the boxes within the replicate. However, the static stresses and drop heights were randomized within each replicate. The randomized order of the drops was determined by the computer generated form shown in Fig. 6. One page of this form gives the order of drops for one replicate on four boxes. The order of drops for each box is given in the column under the box number. The letter for each drop indicates the face (or stress level) on which the box is being dropped, while the inches following the letter indicate the drop height.

104
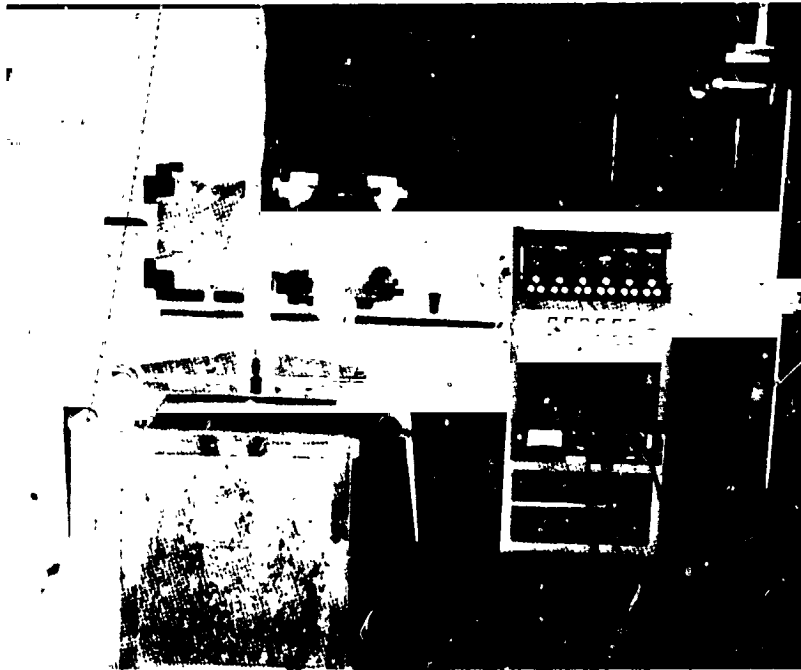
Fig. 5 - Test apparatus after drop

The time required to perform the necessary drops on all six surfaces of one box was less than two minutes. Since temperature is involved, experimentation was performed to determine if a significant change in temperature occurred prior to completion of the sequence of six drops on one container. Fortunately, the change in temperature was not significant in the required two minute interval.

PRELIMINARY RESULTS

Since this experiment was designed for a specific size test specimen and a specific size outside container, the entire dynamic cushioning curve range of static stress values is not included. In traditional flat pad cushion testing for dynamic cushioning curve development, additional static stress levels may always be obtained to complete the necessary data spectrum. Consequently, the entire cushioning curve is always obtainable. Such is not the case in this experimental design. The physical dimensions of the outside container were limited by the drop test apparatus and consequently constrained the physical size of the test specimen and the cushion system which was utilized. Thus, the dynamic cushioning curves to be developed from this experimental design are confined to static stress levels of 608.5 to 8669.6 Pa.

Preliminary calculations indicate that the corner void confined cushion data follows a mathematical form similar to the flat pad unconfined cushion data. After considerable experimentation with various transformation functions, in an attempt to acquire the best functional fit for the corner void confined data, the best function appears to be the $(1 - \cos x)$ expansion. It should be noted, however, that the two methods of testing (confined vs. unconfined), achieve minimum G-levels at different static stress levels. Fig. 7 depicts this phenomena for a 294K temperature and a 762.0 mm drop height situation. It is seen that the flat pad unconfined cushion data predicts a minimum G-level of 42 G's for a static stress of 2758.0 Pa, while the corner void confined cushion data predicts a minimum G-level of 35 G's at a 5516.0 Pa static stress level. At the higher static stress levels, the corner void confined curve is much flatter, and consequently anticipates a small G-level.

Preliminary results indicate a possible pneumatic effect for the confined situation. This pneumatic effect may vary as a function of drop height and temperature. However, data reduction has not proceeded far enough at this point to verify this conjecture. It is assumed, however, that the pneumatic effects augment the cushioning ability of the confined cushion, by

105

MATERIAL: MINICEL                    THICKNESS:
TEMPERATURE:                         REPLICATION:

                    DROP HEIGHT

| | BOX-1 | | BOX-2 | | BOX-3 | | BOX-4 | |
|---|---|---|---|---|---|---|---|---|
| : | | : | | : | | : | | : |
| : | C-304.8 | : | F-457.2 | : | B-457.2 | : | E-609.6 | : |
| : | F-304.8 | : | D-457.2 | : | A-45/.2 | : | D-304.8 | : |
| : | E-762.0 | : | B-304.8 | : | F-762.0 | : | F-609.6 | : |
| : | B-609.6 | : | E-304.8 | : | D-609.6 | : | A-304.8 | : |
| : | D-762.0 | : | C-762.0 | : | E-457.2 | : | B-762.0 | : |
| : | A-762.0 | : | A-609.6 | : | C-457.2 | : | C-609.6 | : |
| : | | : | | : | | : | | : |

Fig. 6 - Randomized drop test sequence
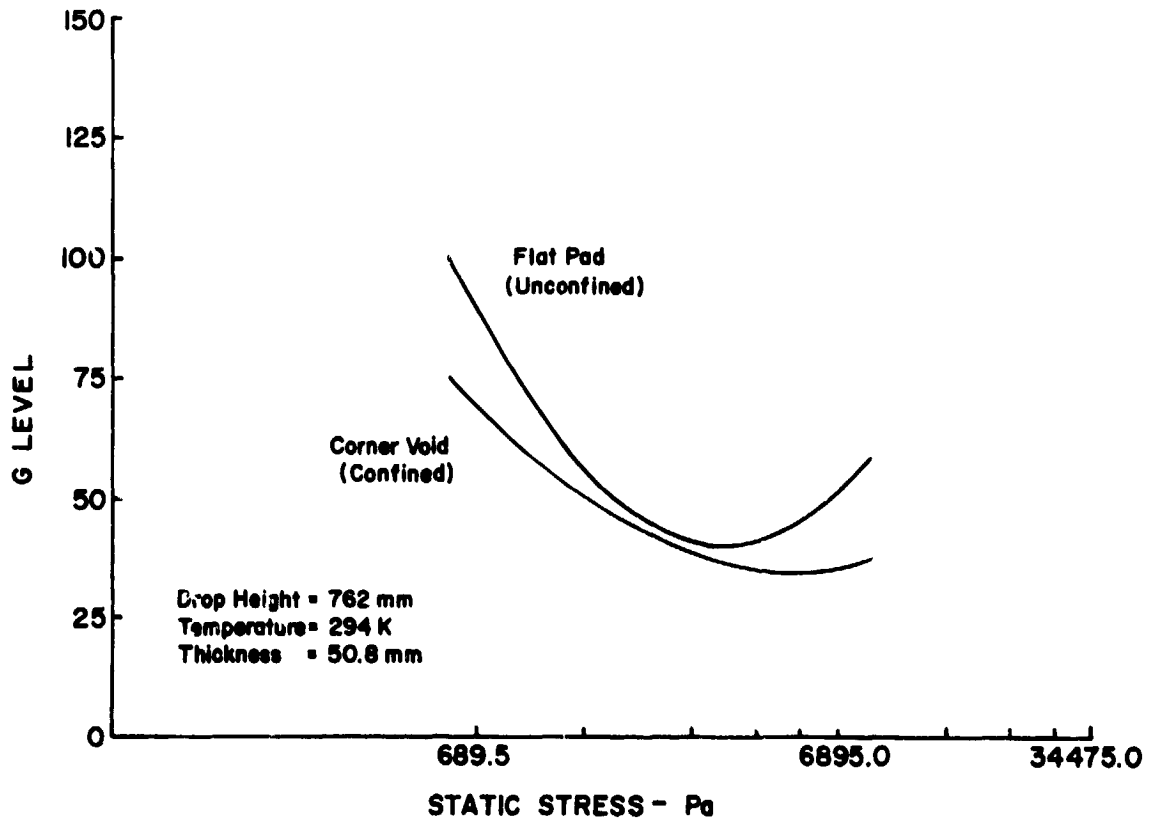


Fig. 7 - Confined vs. unconfined dynamic cushioning curves for Minicel

106

delaying the bottoming-out action of the cushion. The effect of temperature upon the cushioning system enclosed in the container has yet to be determined.

## CONCLUSIONS

The experimental design developed to test the effects of confinement upon cushions appears to be functioning satisfactorily. The drop test program has produced consistent corner void cushion data from which mathematical models may be developed. Since drop test data will be available for both the test specimen (item to be protected) and the outside container, it may be possible to explain the confined effects by means of models for both components. It is plausible that the confined effects follow a mathematical relationship as a function of temperature and drop height. Future research will follow this general approach as a means to isolate these effects upon confined cushioning materials.

## REFERENCES

1. McDaniel, D. M., and R. M. Wyskida, "A Study of Impact Test Effects Upon Foamed Plastic Containers," The Shock and Vibration Bulletin, January 1972.

2. McDaniel, D. M., R. M. Wyskida, and M. R. Wilhelm, "A Statistically Based Procedure for Temperature Sensitive Dynamic Cushioning Curve Development and Validation," The Shock and Vibration Bulletin, June 1975.

3. McDaniel, D. M., and R. M. Wyskida, "The Development of a Generalized Impact Response Model for a Bulk Cushioning Material," The Shock and Vibration Bulletin, August 1976.

4. McDaniel, D. M., "The Development of an Automated Program for the Optimal Design of Bulk Cushioning Systems," AIIE Transactions, March 1977.

5. Wyskida, R. M., D. M. McDaniel, and J. D. Johannes, "Impact Response Modeling of Bulk Cushioning Systems on a Programmable Desk-Top Calculator," The Shock and Vibration Bulletin, Spetember 1977.

6. Cost, T. L., "Dynamic Response of Container and Container Cushion Structures," Technical Report No. 74-003, Athena Engineering Company, Nortnport, Alabama, October 1974.

7. Mazzei, J. H., "A Comparison Study: Confined vs. Unconfined Test Data," Technical Report FRL-TR-45, Picatinny Arsenal, Dover, New Jersey, September 1961.

# EMPIRICAL PROCEDURES FOR ESTIMATING RECOILLESS RIFLE BREECH BLAST OVERPRESSURES

Peter S. Westine and Randall E. Ricker
Southwest Research Institute
San Antonio, Texas

The breech blast from recoilless rifles produces a more severe transient loading than the blast field from other types of guns. This paper presents an empirical equation for predicting breech blast overpressures aft of any recoilless rifle. Experimental test data from the literature on various recoilless rifles demonstrate that this solution is correct and a special series of tests on a variable nozzle and chamber recoilless rifle test fixture shows that the interior gun characteristics associated with the blast field are properly simulated. Model theory and past scaling effects for closed breech guns form a basis upon which this new solution is founded. The solution can also be extended for predicting blast pressure fields behind rocket motors.

## INTRODUCTION

This paper presents a new empirically derived relationship for predicting the peak free-field blast pressures behind the breech of a recoilless rifle. Experimental test data from the literature on various 57mm, 75mm, 90mm, and 105mm recoilless rifles are used together with measured blast pressures from a special test recoilless rifle chamber to develop a solution and demonstrate its validity.

The equation which results and will be discussed given by:

$A_e$ = exit area of the nozzle

$A_t$ = throat area of the nozzle

$P_c$ = maximum chamber pressure in the gun

$m$ = a shape factor for the chamber pressure time history. Approximately equals the average chamber pressure divided by the maximum chamber pressure

$N(\theta)$ = a nozzle shape factor. Equals 1.0 for central orifice but

$$\frac{P}{mP_c}\left(\frac{A_e}{A_t}\right)^2 = \left(4.055 - 3.939 \tanh \frac{\theta}{35}\right)\left[\frac{N(\theta)L}{\sqrt{A_e}}\right]^{-1.35 + 0.537 \tanh^2\left(\frac{\theta}{43.5}\right)} \tag{1}$$

where   $P$ = peak free field blast pressure

$L$ = distance from the breech

$\theta$ = angle in degrees from the center line of the rifle (0° is directly aft)

equals $e^{0.001287\ \theta^{3/2}}$ for kidney nozzles.

Equation (1) is valid for $\theta$ from 0 to 90 degrees and $\frac{L}{\sqrt{A_e}}$ from approximately 10 to 400.

## Comparison With Test Results

Equation (1) represents a three parameter space of nondimensional numbers. To demonstrate that the solution is a valid one, a series of plots was made in which the scaled pressure $\frac{P}{mP_c}$ $\left(\frac{A_e}{A_t}\right)^2$ was plotted versus the scaled standoff distance $\frac{N(\theta)L}{\sqrt{A_e}}$ along lines radiating away from the breech along constant angles $\theta$. Different weapon firings reported in the literature were used to obtain data for these comparisons. Included in the array of weapons are the 57mm T66E6 [1], 90mm T219 [2], 105mm specially modified M27 [3], 105mm T19 [4], 75mm T21 [5], 57mm M18A1 [6,7], and 106mm T170E1 [8]. The 57mm T66E6, 105mm T19, 75mm T21, and 57 mm M18A1 have kidney nozzles, whereas the other three weapons have central orifice nozzles. Table A lists the weapon parameters $P_c$, $A_e$, and $A_t$ associated with each of these weapon systems.

Figures 1, 2, 3, and 4 present the test results in plots of scaled pressure versus scaled standoff distance for constant angular directions from the breech. The shape of the symbol in all these figures indicates the source of the data and the reference from which the data were taken. The solid line through all of the data points is Equation (1) which is a curve fit to the test results. The results from these comparisons show that Equation (1) predicts the observed results and infers that a general solution is represented by these results.

Dividing the ordinate in some of these figures by a factor such as 3 does not change the results. This manipulation was only a method for shifting the plots so all data points would fit on the two cycle log-log paper.

Before the format used can be devised and understood, one must review some of the earlier empirical efforts for predicting blast fields around conventional closed breech guns. The format which was eventually used in this paper evolves from these earlier closed breech efforts and from the application of similitude theory to recoilless rifles.

## Previous Scaling Efforts

Apparently, the first attempts to scale blast waves around any source were during World War I by Hopkinson [9] in England and Cranz [10] in Germany. These laws for the blast field around H.E. charges are closely related to what we are using for recoilless rifles, as the same assumptions are required. Both individuals stated that for propagation of a blast with only one spatial coordinate, the peak overpressure would be a function of $R/W^{1/3}$. Because the energy density of most chemical explosives varies very little, another method of stating the Hopkinson-Cranz Law is to substitute charge diameter d for $W^{1/3}$ and state that the peak overpressure P is a function of $R/d$.

Reynolds [11] at Princeton and the Navy [12] at David Taylor Naval Ship Research and Development Center – formerly David Taylor Model Basin – were the first in the mid-40's to apply the Hopkinson-Cranz Law to determine the

TABLE A

WEAPON PARAMETERS USED TO SCALE RESULTS

| Weapon | Reference | $P_c$ (psi) | $A_e$ (in²) | $A_t$ (in²) | Nozzle Type |
|---|---|---|---|---|---|
| 57mm T66E6 | 1 | 7,100 | 7.05 | 2.95 | Kidney |
| 90mm T219 | 2 | 3,700 | 23.87 | 6.82 | C.O. |
| 105mm Modified M27 | 3 | Various | 35.5 | Various | C.O. |
| 105mm T19 | 4 | 9,260 | 17.48 | 9.30 | Kidney |
| 75mm T21 | 5 | 10,000 | 9.67 | 4.67 | Kidney |
| 57mm M18A1 | 6,7 | 6,500 | 7.05 | 2.95 | Kidney |
| 106mm T170E1 | 8 | 10,200 | 17.90 | 10.00 | C.O. |

Figure axis labels and data:

y-axis: $\dfrac{P}{9mP_c}\left(\dfrac{A_e}{A_t}\right)^2 \times 10^{+3}$

x-axis: $\dfrac{N(\theta)L}{\sqrt{A_e}}$

$\theta = 0°$

| SYMBOL | WEAPON | NOZZLE TYPE |
|--------|--------|-------------|
| ◆ | 57 mm T66E6 | Kidney |
| ◢ | 90 mm T219 | C.O. |
| ■ | 105 mm Modified M27 | C.O. |
| ◆ | 105 mm T19 | Kidney |
| ♦ | 75 mm T21 | Kidney |
| ✕ | 57 mm M18A1 | Kidney |
| ● | 106 mm T170E1 | C.O. |
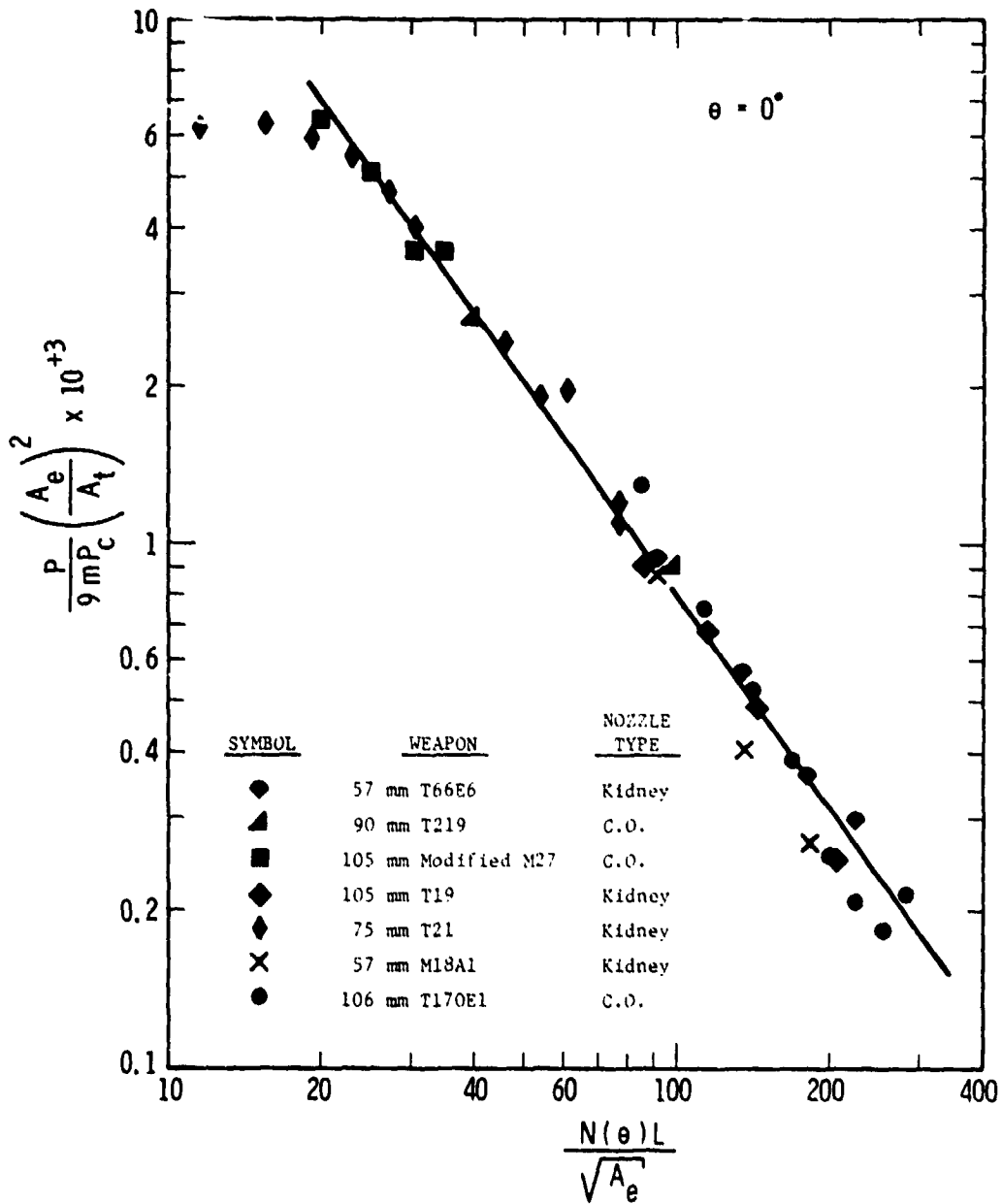
FIGURE 1. BREECH BLAST PRESSURE AT θ EQUAL 0 DEGREES

FIGURE 2.   BREECH BLAST PRESSURES AT θ EQUAL 30 DEGREES

112

$\theta = 60°$

$$\frac{P}{3mP_c}\left(\frac{A_e}{A_t}\right)^2 \times 10^{+3}$$

10

6

4

2

1

0.6

0.4

0.2

| SYMBOL | WEAPON | NOZZLE TYPE |
|--------|--------|-------------|
| ◢ | 90 mm T219 | C.O. |
| ● | 106 mm T170E1 | C.O. |
| ⬟ | 57 mm T66E6 | Kidney |
| ◆ | 105 mm T19 | Kidney |

20   40   60   100   200   400   600

$$\frac{N(\theta)L}{\sqrt{A_e}}$$
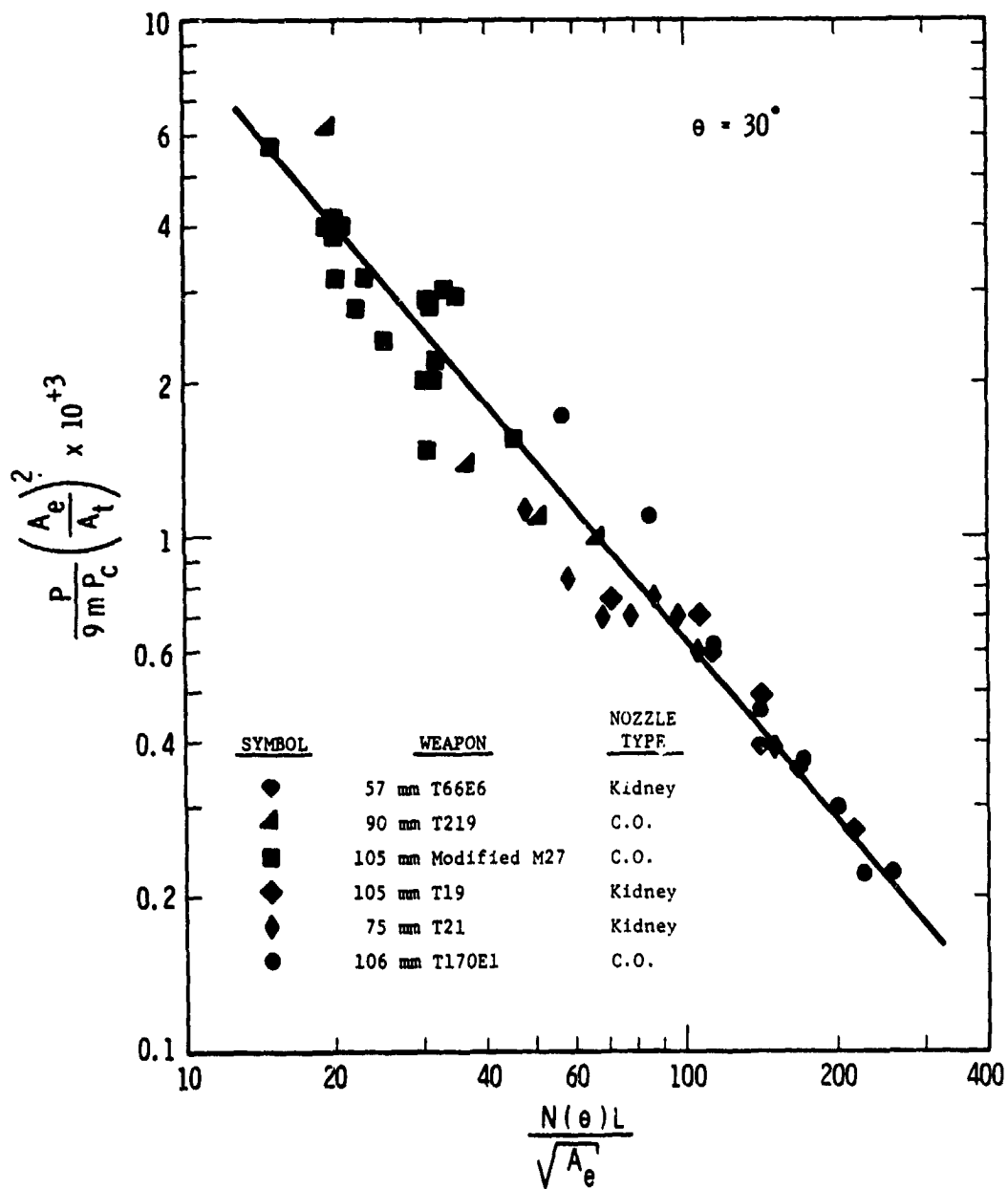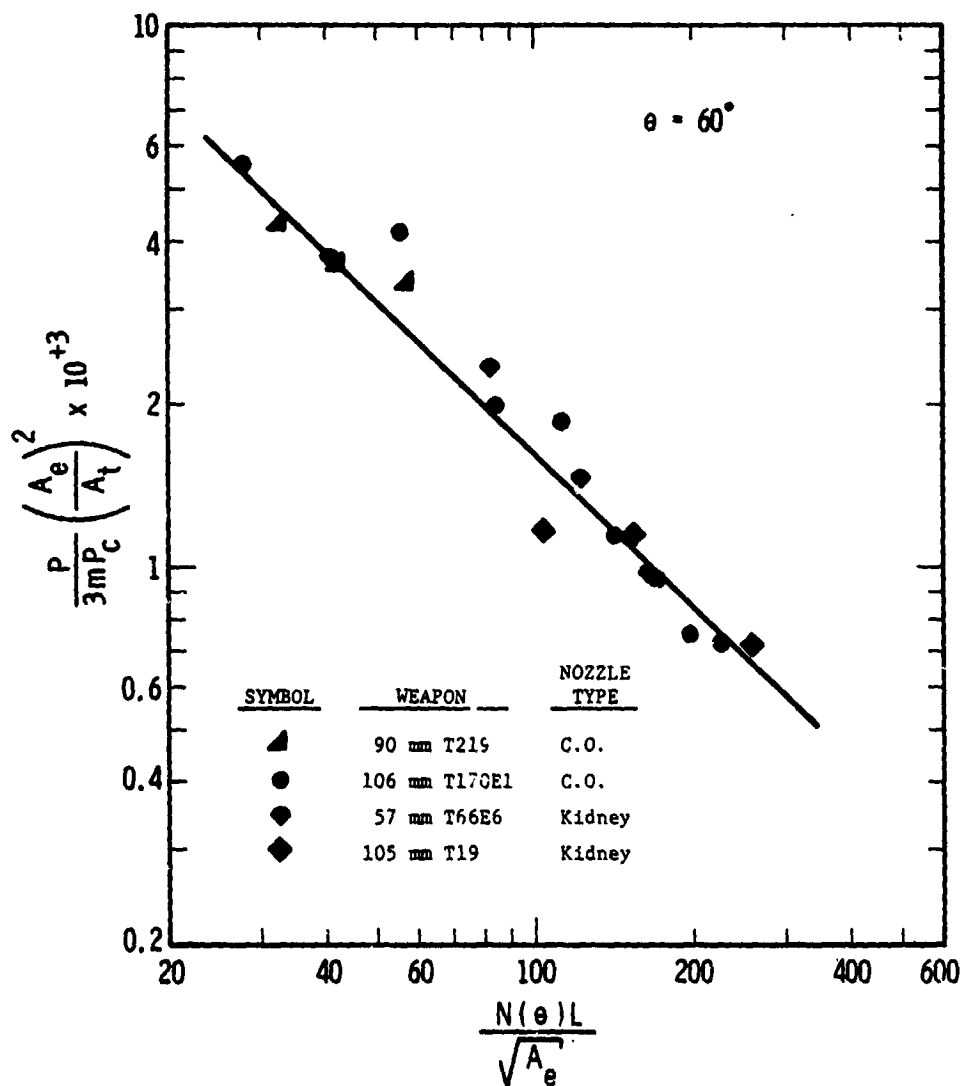
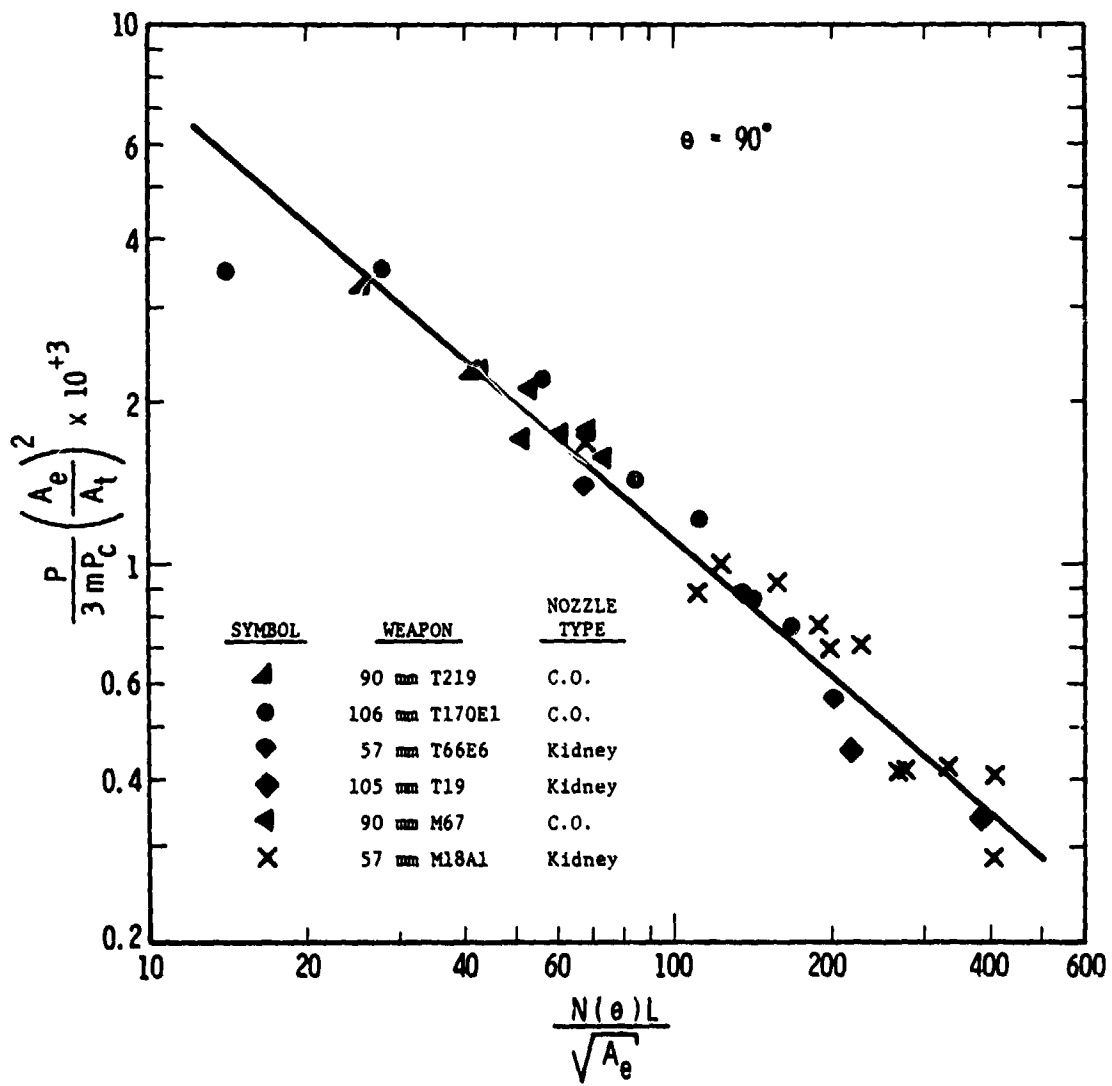FIGURE 3.   BREECH BLAST PRESSURE AT $\theta$ EQUAL 60 DEGREES

113

FIGURE 4.  BREECH BLAST PRESSURES AT θ EQUAL 90 DEGREES

the blast field around guns. Princeton applied the scaling law to obtain peak reflected pressures monitored by a flush mounted gauge in a panel under a closed-breech gun muzzle, while the Navy considered free-field overpressures and impulses around Naval guns. Both groups required geometric similarity to the extent that

$$\frac{M_1}{M_2} = \frac{E_1}{E_2} = \left(\frac{c_1}{c_2}\right)^3 = \left(\frac{\ell_1}{\ell_2}\right)^3 \qquad (2)$$

and replica scaling so that

$$V_1 = V_2 \qquad (3)$$

where

        $M$ = projectile mass

        $E$ = energy in the propellant

        $c$ = weapon caliber

        $\ell$ = length of bore

        $V$ = projectile muzzle velocity

and the subscripts denote specific weapons. If these numerous conditions were met, the maximum pressures, either side-on or reflected, were identical provided the distances were measured in calibers. Plots of isobars of constant overpressure and isoclines of I/c were constructed from 3"/50 Naval gun data on plots with an abscissa of $L_{||}/c$ and an ordinate of $L_{|}/c$. The Navy did believe falsely that barrel length could be disregarded in the scaling, but this observation was based on insufficient data from various guns of essentially the same scaled barrel length, $\ell/c$ equal to 50 give or take 10%. These scaling observations made in the mid-40's on the blast field around guns are correct, provided the interior ballistic restrictions expressed by Equations (2) and (3) are met. These laws are Hopkinson-Cranz extended to guns by requiring dynamic, kinematic, and geometric similarity to be maintained.

Unfortunately, scaling by calibers alone is satisfied in only a few cases. In order for the Princeton-Navy simulation to include all closed breech weapons, a large number of plots would have been required with a systematic variation in propelling charge, projectile mass, barrel length, and muzzle velocity. Armour Research Foundation [13] attempted to meet these limitations by representing the blast field around a gun muzzle with an equivalent weight of a spherical explosive charge located on

the bore axis at a distance $r_o$ from the muzzle. The distance $r_o$ evidently corresponded to the location of the stationary shock associated with the so-called "bottle" at the muzzle of a gun. To create an approximation to the peak pressure, Armour created a "reduced energy" W given by:

$$W = N(E - 1/2 \ mV^2) \qquad (4)$$

The parameter N was a correlation or fudge factor for a gun that is multiplied by the energy in the propellant minus the kinetic energy of the projectile to obtain an energy going into the blast wave. Actually, this "pseudo energy" is a fairly accurate representation of the energy going into blast because as a first approximation the other significant energy losses such as heat are nearly a constant percentage of the available energy. Armour applied the Hopkinson-Cranz Law to determine pressure distribution over a plate through the equation:

$$P = f(h/W^{1/3}, \ L/W^{1/3}) \qquad (5)$$

Equation (5) with h equal to the gun height over the deck was tested with data from 0.50 caliber, 20-mm, 37-mm, and 3.00-in. guns. Results were within 20% because all these guns had the same scaled barrel length $\ell/c$. Had Armour tested a grenade launcher, a 0.45 pistol, or other stubby gun, their prediction would have been poor. At that time, data were not available to show $\ell/c$ should be considered.

It was Westine [14] in 1969 who recognized that the Armour approach gave concentric circles for peak pressure contours, an observation which was obviously false. In addition, none of the short barrel weapon firings scaled with their long barrel counterparts. The Armour definition of an effective energy release was maintained; however, separate spatial parameters were inserted in the analysis to define barrel length, weapon caliber, and the observer's location parallel and perpendicular to the line of fire. The result of Westine's analysis which was conducted using similitude theory was the functional equation for free-field pressure.

$$\frac{Pc^2\ell}{W} = f\left(\theta, \ \frac{L}{c}\right) \qquad (6)$$

This equation had its validity demonstrated with experimental results in a manner similar to the approach used in presenting Figures 1 through 4 for recoilless rifles.

A first approximation at an attempt to extent the muzzle blast work of Westine to recoilless rifles was made by SwRI [7] personnel in 1971. Review of limited amounts of recoilless rifle data and another similitude analysis led to Equation (7) as the recoilless rifle counterpart to Equation (6) for closed breech guns.

$$\frac{P}{P_c} = f\left(\theta, \frac{L}{c}\right) \tag{7}$$

The parameter $P_c$ is the maximum chamber pressure in the gun. Data from 57-mm, 75-mm, 90-mm, and 105-mm recoilless rifle firings showed that Equation (7) was approximately correct provided unusual nozzle designs and propellant burns are not used in the guns to make their breech blast fields less severe. Subsequent work sponsored at Watervliet [15] and Picatinny Arsenal [3] shows that $P_c$ was at best only an approximation of the energy output for a recoilless rifle.

## Development of New Functional Relationships

If one studies Equation (6) for closed breech guns and contemplates an analogy which should exist between closed breech and recoilless rifles, Equation (6) can be used to suggest a relationship for predicting breech blast overpressures. The quantity $c^3\ell$ on the left hand side of Equation (6) is the volume of the gun tube at projectile exit. The quantity W is essentially an effective energy release which drives the muzzle blast. In addition, the $\sqrt{A_e}$ would be the recoilless rifle counterpart to the caliber c. These observations suggest that the recoilless rifle version of Equation (6) might be given by:

$$\frac{PV}{W_{eff}} = f\left(\theta, \frac{L}{\sqrt{A_e}}\right) \tag{8}$$

where V = volume of the recoilless rifle chamber

$W_{eff}$ = an effective energy release driving the breech blast

If Equation (8) is accepted as a logical relationship, the problem of developing a prediction equation becomes a problem in predicting the effective energy $W_{eff}$.

Our empirical approach to predict $W_{eff}$ began by conducting a similitude analysis. For most recoilless rifles, a typical chamber pressure history resembles the sketch in Figure 5. The duration T and peak chamber pressure $P_c$ depend upon the propellant type, and many gun chamber and nozzle geometric characteristics. Generally, engineers can predict $P_c$ and T from these weapon details. We conducted our model analysis by assuming that in addition to $P_c$ and T, the effective energy release $W_{eff}$ would depend upon the volume V of the rifle chamber, the throat area $A_t$ of the nozzle, the exit area of the nozzle $A_e$, and the ratio of specific heat $\gamma$ for the combustion products in the chamber as well as the speed of sound $a$ for combustion products. This definition of the problem leads to the following dimensional functional relationship for $W_{eff}$.

$$W_{eff} = f'(V, P_c, T, A_t, A_e, \gamma, a) \tag{9}$$

Equation (9) is an eight parameter space of dimensional numbers. It can be reduced to a five dimensional space of nondimensional numbers by conducting a model analysis. We will not repeat the algebraic procedures associated with such an analysis as several books exist on this topic [16]. Because no new assumptions are associated with such an analysis, we simply write one acceptable complete set of nondimensional terms.

$$\frac{W_{eff}}{P_c V} = f'\left(\frac{A_e}{A_t}, \gamma, \frac{V}{A_t^{3/2}}, \frac{aT}{A_t^{1/2}}\right) \tag{10}$$

Because the ratio of specific heats $\gamma$ for most propellant products is essentially a constant, we can drop it as a variable. Dropping $\gamma$ from the analysis and substituting Equation (10) into Equation (8) for $W_{eff}/V$ gives the result:

$$\frac{P}{P_c} = f\left(\theta, \frac{L}{\sqrt{A_e}}\right) f'\left(\frac{A_e}{A_t}, \frac{V}{A_t^{3/2}}, \frac{aT}{A_t^{1/2}}\right) \tag{11}$$

116
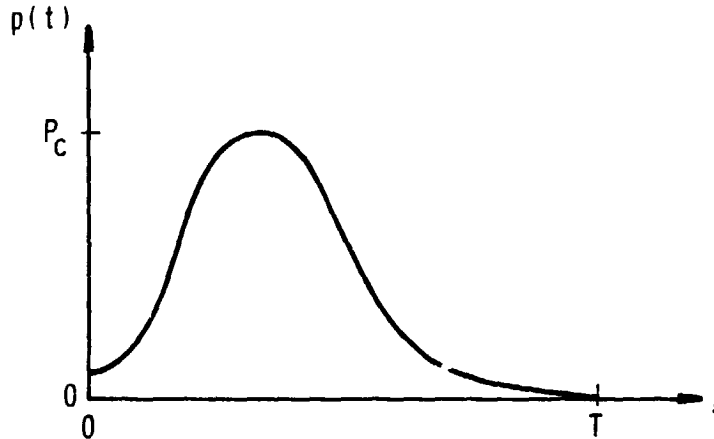
FIGURE 5. CONVENTIONAL RECOILLESS RIFLE CHAMBER PRESSURE HISTORY

The final format depends on a separate series of experimental observations. Notice that because two independent functions exist on the right hand side of Equation (11), the primed function for determining how gun chamber characteristics influence breech blast pressures can be studied independently from the unprimed function which maps the pressure field at different geometric locations around the breech. These were precisely the procedures which were followed to give the empirical relationship upon which this paper is based, Equation (1). We will describe first how Equation (11) was reduced to Equation (12) by conducting experiments on the primed relationship.

$$\frac{P}{P_c}\left(\frac{A_e}{A_t}\right)^2 = f\left(\theta, \frac{L}{\sqrt{A_e}}\right) \qquad (12)$$

## SwRI Variable Gun Tests

A nonprojectile firing recoilless rifle chamber was fabricated as seen in Figure 6. Basically, this device permitted us to accumulate test data while varying one parameter at a time. Three different nozzles were designed with three different expansion ratios $\frac{A_e}{A_t}$. A nozzle was changed by unscrewing the nozzle retaining ring so a new nozzle could be placed on the chamber and clamped with the retaining ring. The volume of the chamber could be changed by removing the B-1 and/or A-1 sleeves to change the diameter of the combustion chamber. Nozzle start pressures could be varied by changing the

rupture disk or diaphragm which separates the combustion chamber and the nozzle. The igniter tube contained black powder, and was part of the propellant train for igniting the propellant which surrounded the igniter. Three different types of propellants (M-1 light, M-1 dark, and M-10) were used in various experiments. The quantity of propellant also varied from 1/8 to 1/4 to 1/2 pound charges. In all experiments the nozzle throat area remained constant, $A_t = 2.826$ in.$^2$.

The other parameters in different combinations were all varied as in the summary in Table B. This test procedure permitted $\frac{A_e}{A_t}$ to be varied by changing nozzles, $\frac{V}{A_t^{3/2}}$ to be varied by changing the number of internal liners, and $\frac{aT}{A_t^{1/2}}$ as well as $P_c$ to be varied by changing the types and quantity of propellants.

All experiments were conducted by placing blast pressure transducers around the breech and making no variation in the parameters $\theta$ and $\frac{L}{\sqrt{A_e}}$. This procedure means that for any one scaled pressure transducer location, Equation (11) becomes:

$$\frac{P}{P_c} = f'\left(\frac{A_e}{A_t}, \frac{V}{A_t^{3/2}}, \frac{aT}{A_t^{1/2}}\right) \qquad (13)$$

117
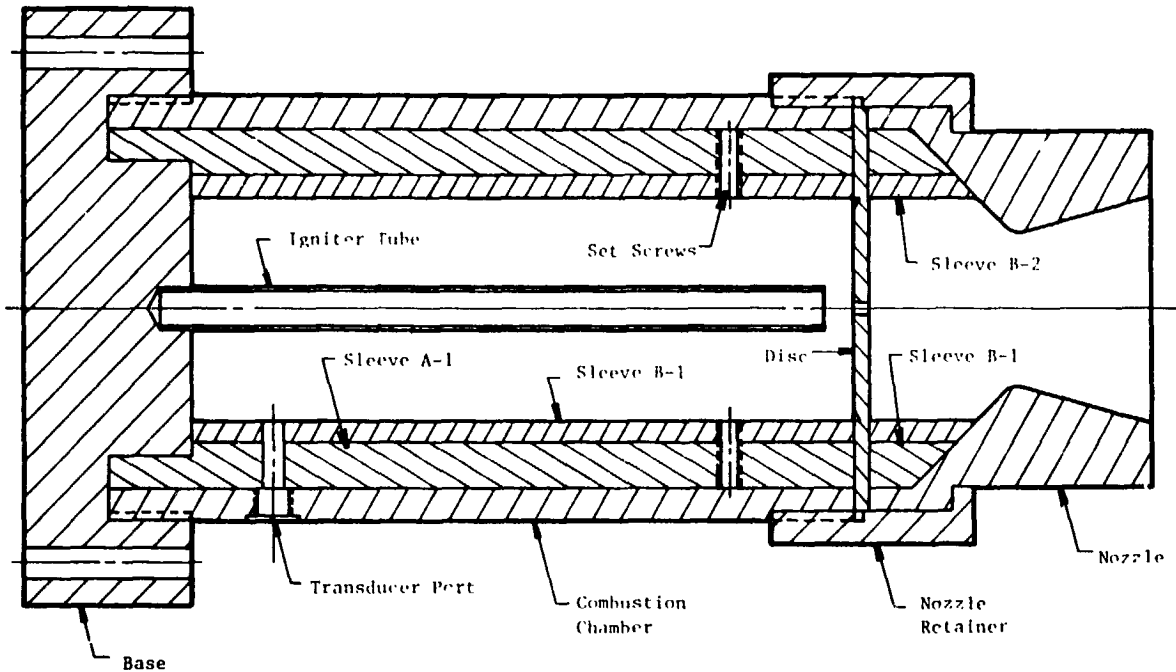
FIGURE 6. ASSEMBLY DRAWING RECOILLESS RIFLE CHAMBER TEST FIXTURE

TABLE B
VARIATION IN TEST PARAMETERS

| Parameter | Condition 1 | Condition 2 | Condition 3 |
|---|---|---|---|
| $A_t$ | 2.826 $in^2$ | 2.826 $in^2$ | 2.826 $in^2$ |
| $\dfrac{A_e}{A_t}$ | 1.80 | 2.10 | 2.30 |
| $\dfrac{V}{A_t^{3/2}}$ | 11.1 | 16.1 | 28.6 |
| Type Propellant | M-1 light | M-1 dark | M-10 |
| Quantity of Propellant | 1/8 lb. | 1/4 lb. | 1/2 lb. |

Figure 7 presents a view of the test setup with three Atlantic LC-33 pencil gauges around the breech of the gun. Because of symmetry, two of these gauges were in the same scaled location, $\dfrac{L}{\sqrt{A_e}}$ equal to 16.5 and $\theta$ equal to 30 degrees. The other gauge was located at $\dfrac{L}{\sqrt{A_e}}$ equal to 24.6 and $\theta$ equal to 83° to establish that conclusions were not based upon transducer location.

The purpose of these tests was to discover how the parameters $\dfrac{P}{P_c}$, $\dfrac{A_e}{A_t}$, $\dfrac{V}{A_t^{3/2}}$, and $\dfrac{aT}{A_t^{1/2}}$ interrelate. The results of these tests were that the scaled pressure was independent of scaled time $\dfrac{aT}{A_t^{1/2}}$ and scaled chamber volume $\dfrac{V}{A_t^{3/2}}$. The parameters $\dfrac{P}{P_c}$ and $\dfrac{A_e}{A_t}$ appeared to empirically combine to form the quantity $\dfrac{P}{P_c}\left(\dfrac{A_e}{A_t}\right)^2$ as in Equation (12).

Figure 8 presents test data in a plot of $\dfrac{P}{P_c}\left(\dfrac{A_e}{A_t}\right)^2$ versus $P_c$ to show

118

FIGURE 7. VIEW OF TEST SETUP
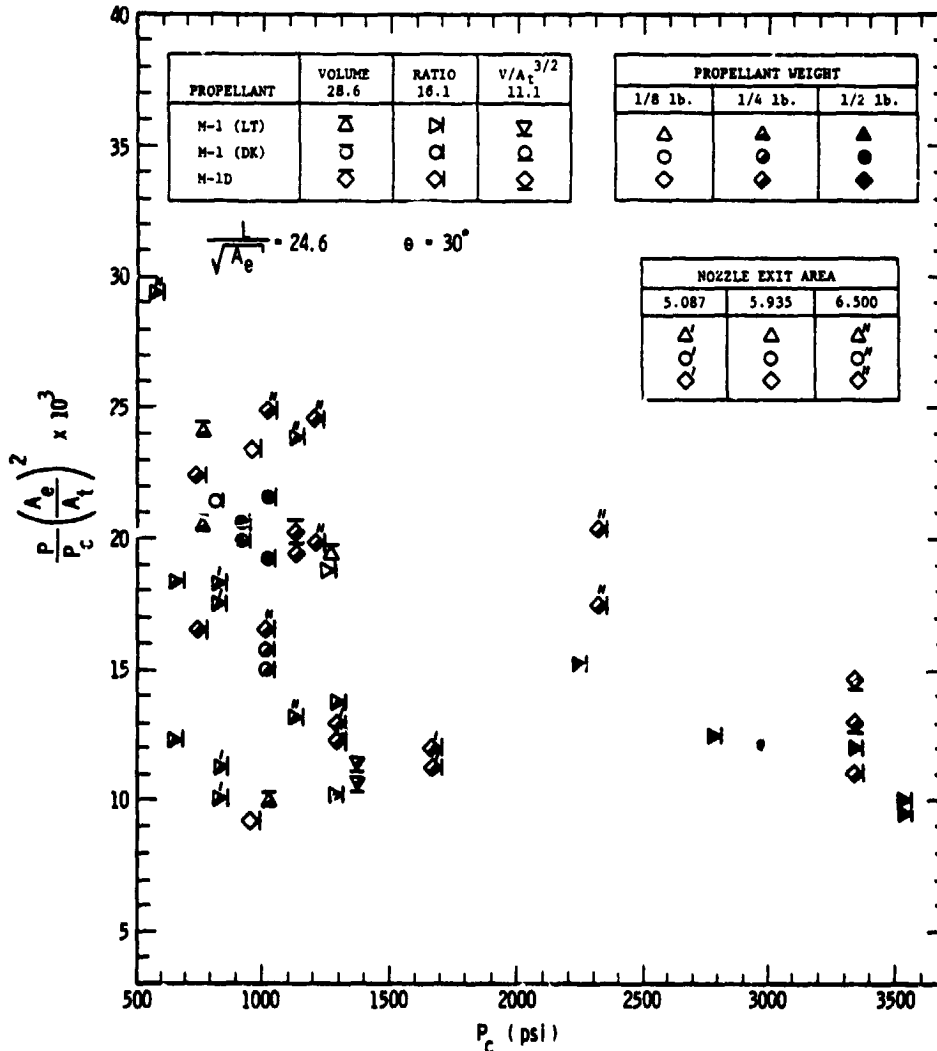


FIGURE 8. SCALING OF INTERIOR GUN CHARACTERISTICS

119

results are independent of $P_c$. Ones first reaction is that the results scatter greatly, but the ordinate on Figure 8 is an enlarged geometric scale rather than a log scale. Scatter does occur, but the same symbol can often be found at the bottom as well as at the top of this figure. Because many variations are being evaluated, the legion associated with this figure is complicated. The shape of the symbol, whether triangle, circle, or square, denotes type of propellant. The amount of shading indicates the amount of propellant used, 1/8, 1/4 or 1/2 pound. If a bar is placed on top of the figure, the large chamber volume was used; on the side the medium chamber volume, and on the bottom of the symbol, the small chamber volume was used. The number of primes added to a figure indicates which nozzle exit area was tested. All combinations were tested. Any scatter does appear to be random rather than systematic; hence, the conclusions which have been drawn about scaling interior gun characteristics appear to be correct.

As additional verification for our recoilless rifle interior ballistic observations, a one-dimensional, variable cross-section, Lagrangian, shock tube, computer program named GUN-WUNDY [17] was modified so it could be applied to this breech blast study. GUN-WUNDY is an artificial viscosity, finite difference code. Our modifications allowed us to approximate the flow field in the combustion chamber, nozzle, and external environment immediately aft of the breech. A combustion subroutine was added which puts both energy and mass in the combustion chamber flow field from the burning of propellant, and another subroutine was added to automatically rezone the flow field for more efficient running. The burning rate law used in these computations was of the format:

$$r = a + b\, p^N \qquad (14)$$

Table C summarizes the results from 10 different runs. The maximum overpressures are all being compared at the exit of the nozzle for different peak chamber pressures, nozzle expansion ratios, and scaled gun volumes. The throat area $A_t$ for the recoilless rifle in all these calculations equals 2.826 in.$^2$.

The quantity $\dfrac{P}{P_c}\left(\dfrac{A_e}{A_t}\right)^2$ does differ slightly, but not by much more than 10% from the average of 0.4610 in these

## TABLE C
## COMPUTED RECOILLESS RIFLE BREECH BLAST PRESSURES

| $P_{max}$ (psi) | $P_c$ (psi) | $\dfrac{A_e}{A_t}$ | $\dfrac{V}{A_t^{3/2}}$ | $\dfrac{P_{max}}{P_c}\left(\dfrac{A_e}{A_t}\right)^2$ |
|---|---|---|---|---|
| 551 | 5746 | 2.099 | 28.98 | 0.4224 |
| 556 | 5956 | 2.099 | 28.98 | 0.4113 |
| 505 | 5376 | 2.099 | 28.98 | 0.4139 |
| 1156 | 8326 | 1.800 | 16.01 | 0.4497 |
| 1146 | 8266 | 1.800 | 16.01 | 0.4490 |
| 1216 | 8716 | 1.800 | 16.01 | 0.4520 |
| 946 | 8596 | 2.099 | 16.01 | 0.4851 |
| 882 | 8626 | 2.300 | 16.01 | 0.5406 |
| 653 | 20386 | 4.000 | 16.01 | 0.5124 |
| 1026 | 7016 | 1.800 | 16.01 | 0.4736 |
| | | Average | | 0.4610 |

computations. This observation means that for engineering answers we computationally as well as experimentally have shown that the format given by Equation (12) is adequate. The routine scatter in one's ability to repeat measurements exceeds this error from these much more complex computational efforts.

## Effects of Combustion Chamber Pulse Shaping

All of the conclusions drawn so far in this discussion are based on conventional recoilless rifle chamber pressure histories with a shape similar to that shown in Figure 5. One of the better ways of reducing breech blast pressures is to tailor the pulse shape in Figure 5 so that the chamber pressure history becomes much more rectangular. The muzzle velocity of a projectile will be the same provided the impulse (area under the chamber pressure-time history) is the same, but breech blast pressures appear to be reduced. Generally, the shape of the chamber pressure pulse is modified by designing propellants so the burning surface area changes with time.

Figure 9 shows four different peak pressure recoilless rifle profiles studied at Watervliet Arsenal [15] in programs to reduce breech blast. Basically, a recoilless rifle was placed over a reflecting plane which represented a helicopter tail boom. Peak reflected overpressures were then measured for the four profiles at three positions, 48, 54, and 60 inches from the gun axis and 95, 241, and 312 inches behind the nozzle, identified as positions A, B,
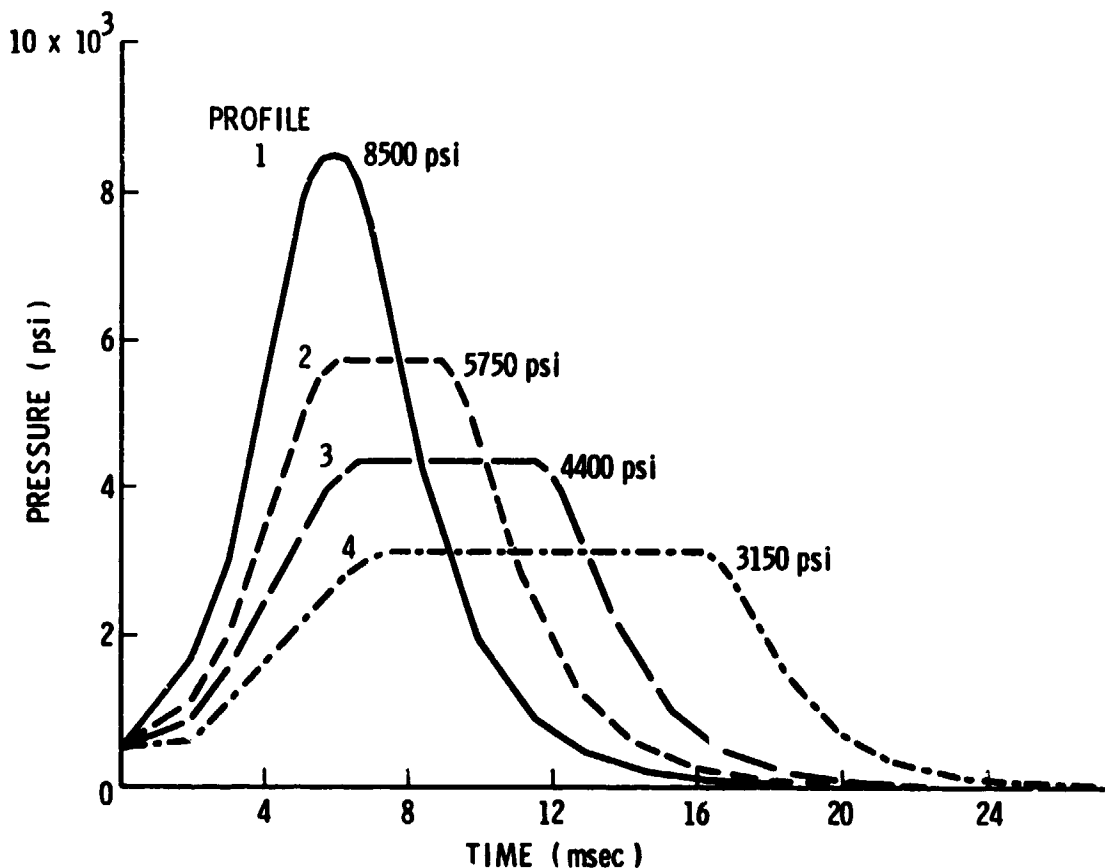
FIGURE 9. CHAMBER PRESSURE PROFILES FOR PEAK PRESSURE
STUDIES FOR CONSTANT MUZZLE VELOCITY

and C. The nozzle on the rifle was kept constant with an expansion ratio $\frac{A_e}{A_t}$ of 4.0. The only modification in the test conditions was to study how reflected overpressures changed because the chamber pressure profiles had been modified.

Table D presents in tabular format the results of this study. Notice that for each of the three locations $\frac{P}{P_c}$ is not a constant as would have been our previous conclusions. Table D indicates that at all three locations the peak breech blast pressure divided by the average chamber pressure is close to being constant. Only small errors exist when $\frac{P}{P_{avg}}$ for each pulse shape is compared to the average value for $\frac{P}{P_{avg}}$ at

any location. This observation indicates that the average chamber pressure is a better correlation coefficient than the peak chamber pressure. Because for most conventional recoilless weapons the pulse shape is self similar; $\frac{P_{avg}}{P_c}$ almost equals a constant 0.36.

The parameter m was added to the quantity $\frac{P}{P_c}$ in Equation (1) to account for pulse shape. For most weapons the peak chamber pressure $P_c$ is known rather than $P_{avg}$, thus Figures 1 through 4 and Equation (') continue to use $P_c$ as a reference pressure.

Although this paper concentrates on recoilless rifle breech blast pressures, it is capable of use for predicting breech blast around rocket motors.

121

## TABLE D
### EFFECTS OF CHAMBER PRESSURE PROFILE

| Profile Number | $P_c$ (psi) | $P_{avg}$ (psi) | Location A | | | Location B | | | Location C | | |
|---|---|---|---|---|---|---|---|---|---|---|---|
| | | | $P$(psi) | $\frac{P}{P_c}\times10^{+3}$ | $\frac{P}{P_{avg}}\times10^{+3}$ | $P$(psi) | $\frac{P}{P_c}\times10^{+3}$ | $\frac{P}{P_{avg}}\times10^{+3}$ | $P$(psi) | $\frac{P}{P_c}\times10^{+3}$ | $\frac{P}{P_{avg}}\times10^{+3}$ |
| 1 | 8500 | 2920 | 6.4 | 0.753 | 2.19 | 13.2 | 1.55 | 4.52 | 13.4 | 1.58 | 4.59 |
| 2 | 5750 | 2561 | 5.2 | 0.904 | 2.03 | 10.8 | 1.88 | 4.22 | 10.5 | 1.83 | 4.10 |
| 3 | 4400 | 2272 | 4.9 | 1.113 | 2.16 | 10.2 | 2.32 | 4.49 | 10.4 | 2.36 | 4.58 |
| 4 | 3150 | 1918 | 3.8 | 1.206 | 1.98 | 8.4 | 2.67 | 4.38 | 8.7 | 2.76 | 4.54 |
| | | | | | Avg. 2.09 | | | Avg. 4.40 | | | Avg. 4.45 |

Most rocket motors have a rectangular or almost constant thrust chamber pressure pulse. This observation means that provided an appropriate pressure pulse shape factor m is used, the breech blast pressure fields should be self similar.

To test this hypothesis, Figure 10 was created comparing breech blast pressures as predicted using Equation (1) with the average chamber pressure equal to the maximum chamber pressure to test data [7] for the LAW rocket, M72A1. The LAW rocket has a throat area of 0.607 in.$^2$, a nozzle exit area of 3.46 in.$^2$, and an average chamber pressure of 4500 psi. By using data from references 6 and 7, experimental test data could be compared directly to Equation (1) with a value of m = 1.0 assigned to the rocket motor. This comparison shows that the same decay with standoff distance exists for rocket motors as for recoilless rifles, and provided the correct parameters are substituted into Equation (1), it can be used to predict breech blast around both.

### Curve Fitting for Special Distribution

Equation (1) was developed empirically. Experimental test data were plotted as in Figures 1 through 4 and straight lines were curve fitted "by eye" to these results. Because the curves are straight lines on log-log plots in Figures 1 through 4, for any constant angle $\theta$, the equation to the data is given by:

$$\frac{P}{mP_c}\left(\frac{A_e}{A_t}\right)^2 = A\left(\frac{L}{\sqrt{A_e}}\right)^B \qquad (15)$$

After obtaining the constant coefficients A and B for each angle $\theta$, the coefficients A and B were then plotted as functions of the angle $\theta$. This relationship

$$A = 4.055 - 3.939 \tanh\left(\frac{\theta}{35}\right) \qquad (16)$$

and

$$B = -1.35 + 0.537 \tanh^2\left(\frac{\theta}{43.5}\right) \qquad (17)$$

are then empirical equations relating A and B to $\theta$ in these plots.

One other empirical observation was also made. At 0° directly aft of the breech, test data from all guns, whether they had a central orifice or kidney nozzle, appeared to form a single function, but at 90° or perpendicular to the breech, two separate curves appeared. After we recognized that one group of data points was kidney nozzles and the other was central orifice nozzles, a factor $N(\theta)$ was created to account for the changes in flow field which can occur aft of the rifle breech because of nozzle type. The relationship which was developed is an empirical one based solely on the fact that its use makes the data correlate. The equation for $N(\theta)$ is given by:

$$N(\theta) = \text{central orifice nozzle} \qquad (18a)$$

$$N(\theta) = e^{0.001287\theta^{3/2}} \text{ kidney nozzle} \qquad (18b)$$

Notice that at $\theta$ equal to 0 degrees, $N(\theta)$ equals 1.0 for either nozzle. The most pronounced effect is at $\theta$ equal to 90 degrees where the $N(\theta)$ values differ by a factor of 3.0.
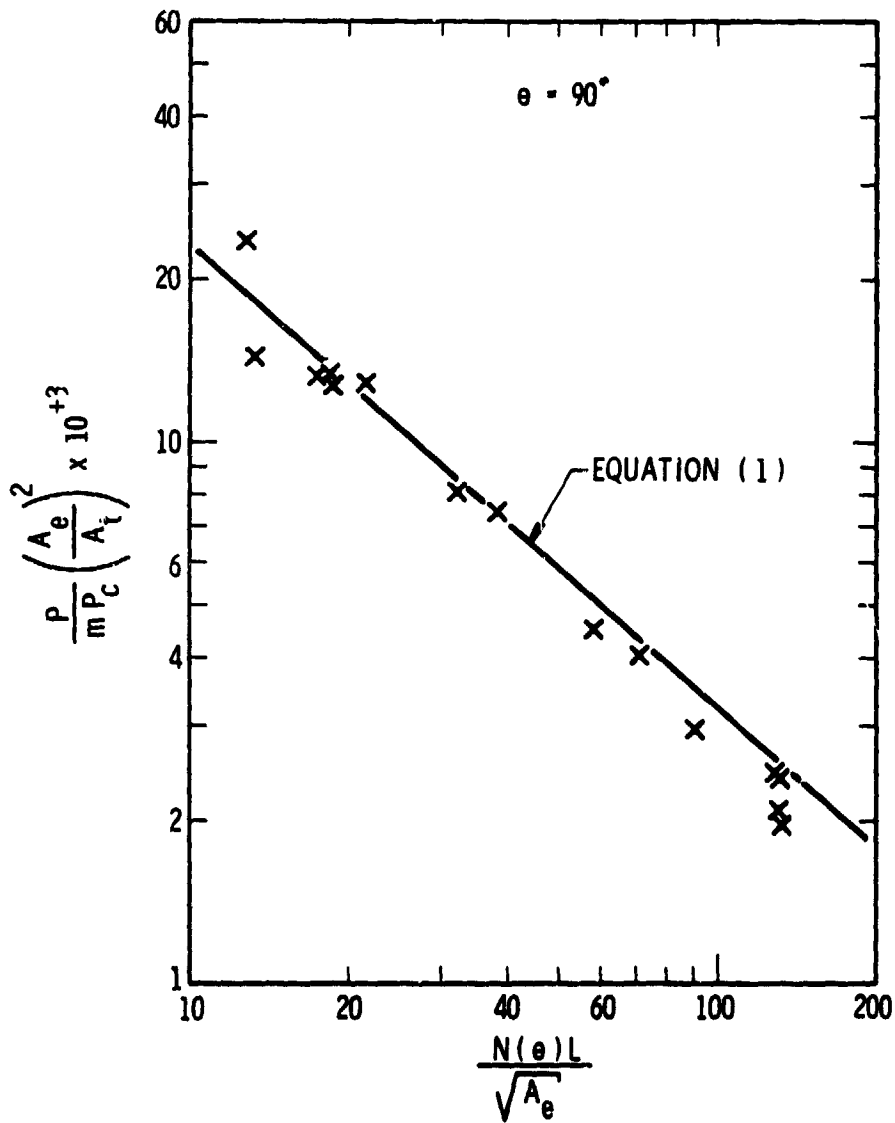
FIGURE 10.  BREECH BLAST PRESSURES AROUND LAW ROCKET

## Conclusions

An empirical solution has been presented for predicting breech blast overpressures aft of recoilless rifles. A wide variety of weapon data at various angles radiating from the breech demonstrate that the solution is valid for all recoilless rifles. The major interior ballistic characteristics influencing the breech blast appear to be the peak chamber pressure, the shape of the chamber pressure history, and the expansion ratio of the nozzle. Outside the weapon, the spatial distribution of the blast pressure field depends upon the type of nozzle, the exit area of the nozzle, and one's position relative to the breech. The solution does appear capable of being extended from recoilless rifles to rocket motors provided the correct shape factor is used for the chamber pressure pulse.

Currently, we are continuing with additional work to use these principals in defining the breech blast field in greater detail. Radial lines forward of the breech will have their pressures determined experimentally so more accurate estimates can be made of potential hearing loss from recoilless rifle firings. In addition, the free-field impulse distribution around recoilless rifles will be mapped so the entire blast pressure time history can be estimated for use in structural calculations and hearing loss determinations because of recoilless rifle firings.

## REFERENCES

1. "Ballistic Analysis of Blast Pressure Results for 57-mm Recoilless Rifle T66E6," Analytical Laboratory Report 55-B-67, January 10, 1956.

2. "Ballistic Analysis of Blast Results for 90-mm Recoilless Rifle, T219 (PAT)," Analytical Laboratory Report 56-B-120, October 18, 1956.

3. U. R. Zimmerman and R. A. Vecchio, "Back Blast Determination of a 105-mm Recoilless Rifle for an Aerial Artillery Weapon System," Picatinny Arsenal Technical Report 3420, August 1966.

4. "Firing Record No. M-46345," Project No. 6001 (428-M5-245), Ordnance Research and Development Center, Aberdeen Proving Ground, Maryland, August 10, 1945.

5. "Investigation of the Effect of Blast from Recoilless Rifles," Armor Research Foundation, Contract No. DA-11-022-ORD-1227, for Frankfort Arsenal, June 30, 1954.

6. "Engineer Design Test of Sound Pressure Level Measurement of Rockets and Recoilless Rifles," Firing Record No. P-74650, USATECOM Project No. 8-7-2320-02, Aberdeen Proving Ground, Maryland, August 1967.

7. W. E. Baker, P. S. Westine, and R. L. Bessey, "Blast Field About Rockets and Recoilless Rifles," Southwest Research Institute, Contract No. DAAD05-70-C-0120 for Ballistic Research Laboratories, May 1971.

8. "Peak Pressures for Breech and Muzzle Blast Measurements 106-mm Rifle, T170E1 Mount, 106-mm, T149E3," Analytical Section, A & A Division, Development and Proof Services, August 14, 1953 (no report number).

9. B. Hopkinson, British Ordnance Board Minutes 13565, 1915.

10. C. Cranz, Lehrbuch der Ballistik, Volume 2, Berlin, 1926.

11. G. T. Reynolds, "Muzzle Blast Pressure Measurements," Report No. PMR-21, Princeton University, April 15, 1944.

12. U. S. Navy Gun Blast Committee, "Survey of Research on Blast," First Interim Report 1946, pp 15-25.

13. H. J. Barton, R. J. Keyran, and T. Shiffman, "Correlation of Muzzle Blast Pressures Over Flat Surfaces," Armour Research Foundation of Illinois Institute of Technology.

14. P. S. Westine, "The Blast Field About the Muzzle of Guns," The Shock and Vibration Bulletin, No. 39, Part 6, pp 139-149, March 1969.

15. C. A. Andrade, G. C. Carofano, J. R. Ruetenik, and R. F. Smiley, "Ballistic Pulse Shaping to Reduce Blast Overpressure," Benet Labs, Watervliet Arsenal, 1974.

16. W. E. Baker, P. S. Westine and F. T. Dodge, Similarity Methods in Engineering Dynamics, Spartan Books Division of Hayden Books, Rochelle Park, NJ, 1973.

17. R. Piacesi, D. F. Gates, and A. E. Seigel, "Computer Analysis of Two-Stage Hypervelocity Model Launchers," Proceedings of Sixth Symposium on Hypervelocity Impact, pp 157-174, August 1963.

# BLAST FROM BURSTING FRANGIBLE PRESSURE SPHERES

E. D. Esparza and W. E. Baker
Southwest Research Institute
San Antonio, Texas

This paper describes laboratory experiments conducted to obtain incident overpressure data from frangible spheres pressurized with two different gases and a vapor. Glass spheres under internal pressure were purposely burst to obtain time histories of overpressure using side-on pressure transducers. A scaling law for pressure spheres bursting in free-air is derived and presented. This law is simplified and used to obtain a functional relationship for the non-dimensional blast parameters. Peak overpressure, arrival and duration times, and impulse data are presented for different initial conditions and blast source energies. These dimensionless data are also compared, wherever possible, with results of theoretical calculations and compiled data for Pentolite high-explosive. The scaled data are quite repeatable and show significant differences from blast waves generated by condensed high-explosives.

## INTRODUCTION

Bursting of thin-walled pressure vessels can occur accidently from excessive pressure, flaws or damages by external impacts from other sources. The sudden release of pressure can generate blast waves than can damage surrounding structures or personnel in the vicinity of the accident. A number of theoretical studies of the blast waves generated by this type of sudden energy release have been conducted [1-6]. However, only limited experimental data from carefully performed tests are available for verification of the theoretical predictions. Sources of data from bursting pressure vessels are limited to experiments with pressurized glass spheres ruptured on purpose with a striker by Boyer, et al [7] and some tests of bursting, thin walled metal vessels by Pittman [8]. Optical (shadowgraph and streak schlieren) instrumentation was employed by Boyer, et al, and Pittman measured overpressure time histories at several distances along three radial lines from each tank tested on the ground.

More recently, Esparza and Baker [9 and 10] conducted two series of small-scale experiments to obtain free field blast data at various distances from bursting pressurized spheres. Glass spheres of nominal 51 and 102 mm (2 and 4 in.) diameter under internal pressure were ruptured by a striker and complete time histories of over-

pressure were obtained with an array of side-on pressure transducers at different radial distances. This recent experimental work forms the basis for this paper.

The studies reported in References 9 and 10 were primarily experimental and were intended to provide a source of blast data from well-controlled experiments on bursting pressurized spheres. The fluids used in the experiments were high-pressure air and argon, and Freon®-12 in both vapor and liquid state. This paper includes a blast scaling law developed for frangible pressure spheres bursting in free air. The experiments and their setup are briefly described and the data are presented in non-dimensional form. Whenever possible, data are compared with results of theoretical calculations and compiled data for Pentolite high-explosive. The data presented include peak overpressures, arrival times, positive and negative impulses, and durations. These measured free-field blast parameters are the first known reported experimental data for frangible pressure vessels bursting in free-air.

## SCALING

The scaling of properties of blast waves from various explosive sources is a common procedure, and most blast data are reported in scaled parameters from

the Hopkinson-Cranz or Sachs' scaling laws. These laws, and others used in blast technology, are derived and discussed in detail by Baker [11]. Blast waves from explosions in the open are affected by the total energy E driving the shock wave, the distance R from the center of the explosive source, geometry and energy density of the explosive source, and ambient atmospheric conditions such as pressure $p_a$ and sound velocity $a_a$. For charges of different total energy but same type and geometry detonated under the same ambient conditions, the Hopkinson-Cranz scaling law applies. If ambient conditions differ between one experiment or analysis and another, Sachs' law is usually used.

Ir the model analysis developed for blast waves from spheres bursting in free-air, the blast source is idealized as a sphere of fluid at an initial pressure higher than atmospheric which is suddenly released from a massless spherical shell at time zero. The

TABLE 1   LIST OF PARAMETERS

| Parameter | Symbol | Dimensions |
|---|---|---|
| SOURCE: | | |
| Energy | E | FL |
| Radius | $r_1$ | L |
| Temperature | $\theta_1$ | $\theta$ |
| Pressure | $p_1$ | $FL^{-2}$ |
| Specific heats ratio | $\gamma_1$ | -- |
| Density | $\rho_1$ | $FT^2L^{-4}$ |
| Sound Velocity | $a_1$ | $LT^{-1}$ |
| AIR: | | |
| Pressure | $P_a$ | $FL^{-2}$ |
| Density | $\rho_a$ | $FT^2L^{-4}$ |
| Temperature | $\theta_a$ | $\theta$ |
| Specific heats ratio | $\gamma_a$ | -- |
| Sound Velocity | $a_a$ | $LT^{-1}$ |
| BLAST WAVE: | | |
| Overpressures (side-on and reflected) | $P_s, P_r$ | $FL^{-2}$ |
| Density | $\rho$ | $FT^2L^{-4}$ |
| Temperature | $\theta$ | $\theta$ |
| Shock Velocity | U | $LT^{-1}$ |
| Particle Velocity | u | $LT^{-1}$ |
| Arrival Time | $t_a$ | T |
| Duration | T | T |
| Impulse | I | $FTL^{-2}$ |
| Radius | R | L |

effects on the blast wave of the pressure container or the fragments from the container are not considered in the analysis. The first step in developing a scaling law is to list all pertinent physical parameters, together with their fundamental dimensions, in a force, length, time, temperature (F, L, T, $\theta$) system. This is done in Table 1. As will be seen later, some parameters are superfluous, but are retained for now and discarded later. The twenty-two parameters are grouped so that some describe the blast source, some describe ambient air conditions, and others describe the characteristics of the blast wave.

The dimensional parameters are next combined into a lesser number of dimensionless groups (often called pi terms) by the methods of dimensional analysis [12]. The intermediate steps are merely algebraic and will not be given here. The number of dimensionless groups equals the number of original dimensional parameters minus the number of fundamental dimensions. The actual grouping is not unique; one possible set is given in Table 2 with some physical description or interpretation for each term or set of terms. Table 2 can be considered as a model law which requires identity of all

TABLE 2.   DIMENSIONLESS (PI) TERMS

| Terms | Description |
|---|---|
| $\pi_1 = E/r_1^3 P_a$ | } Scaled energy |
| $\pi_2 = \theta_1/\theta_a$ | |
| $\pi_3 = P_1/P_a$ | |
| $\pi_4 = \gamma_1$ | } Scaled source properties |
| $\pi_5 = \rho_1/\rho_a$ | |
| $\pi_6 = a_1/a_a$ | |
| $\pi_7 = \rho_a a_a^2/P_a$ | } Scaled ambient conditions |
| $\pi_8 = \gamma_a$ | |
| $\pi_9 = P_s/P_a$ | |
| $\pi_{10} = P_r/P_a$ | |
| $\pi_{11} = \rho/\rho_a$ | |
| $\pi_{12} = \theta/\theta_a$ | |
| $\pi_{13} = U/a_a$ | } Scaled blast wave properties |
| $\pi_{14} = u/a_a$ | |
| $\pi_{15} = t_a a_a P_a^{1/3}/E^{1/3}$ | |
| $\pi_{16} = T a_a P_a^{1/3}/E^{1/3}$ | |
| $\pi_{17} = I a_a/P_a^{2/3} E^{1/3}$ | |
| $\pi_{18} = R\, P_a^{1/3}/E^{1/3}$ | } Scaled distance |

128

terms in the table if tests or analytical results on different scales are to be compared.

The number of terms can be reduced by applying some physical restrictions. Because all the experiments were conducted with the same ambient atmospheric conditions, $\pi_7$ and $\pi_8$ can be dropped from the analysis. Also, all experiments were conducted with the pressure sphere at ambient temperature. There-

fore, $\pi_2$ is superfluous. Finally, because the energy in the sphere for each test is computed using the thermodynamic properties of the source, the term $\pi_1$ can be eliminated. In the experiments, the blast properties measured were the side-on pressures, impulses, arrival times, and durations. Therefore, the other blast parameters were eliminated to formulate the general scaling law in Equation (1).

$$
\left.
\begin{aligned}
\bar{P}_s &= \frac{P_s}{P_a} \\[2em]
\bar{t}_a &= \frac{t_a a_a P_a^{1/3}}{E^{1/3}} \\[2em]
\bar{T} &= \frac{T a_a P_a^{1/3}}{E^{1/3}} \\[2em]
\bar{I}_s &= \frac{I_s a_a}{P_a^{2/3} E^{1/3}}
\end{aligned}
\right\}
= f_i \left[ \frac{R P_a^{1/3}}{E^{1/3}} , \frac{P_1}{P_a} , \gamma_1 , \frac{a_1}{a_a} , \frac{\rho_1}{\rho_a} \right]
\tag{1}
$$

where

$P_a$ = ambient pressure (absolute)

$a_a$ = ambient sound velocity

$P_s$ = peak side-on overpressure

$t_a$ = arrival time of the peak overpressure

$T$ = duration of the overpressure

$I_s$ = specific impulse

$R$ = radius of blast wave (stand-off distance)

$P_1$ = internal absolute pressure of sphere

$a_1$ = sound velocity of fluid in sphere

$\rho_1$ = density of fluid in sphere

$\rho_a$ = density of ambient air

$\gamma_1$ = ratio of specific heats of fluid in sphere

$E$ = internal energy in the sphere

and

$\bar{R} = \dfrac{R P_a^{1/3}}{E^{1/3}}$ = Sachs' scaled distance

The bars indicate non-dimensional quantities. The symbol $f_i$ indicates that each of the scaled blast wave properties on the left side of Equation (1) is a different function of the five scaled parameters on the right hand side. The first quantity is the scaled distance $\bar{R}$ and the last four are all scaled source properties. If these four properties do not change in a given set of experiments, the law reduces to Sachs' law.

THE EXPERIMENTS

Two sets of experiments were conducted using 51 and 102 mm (2 and 4 in.) nominal diameter glass spheres of several thicknesses as the blast source. In the first set consisting of 20 tests, two different gases, air and argon, were used to pressurize the 51 mm (2 in) spheres at room temperature with internal pressures from 1,930 to 5,171 kPa (280 to 750 psig). The 102 mm (4 in.) spheres were pressurized from 1,207 to 3,034 kPa (175 to 440 psig). Because of the lack of pressure-time data from non-ideal explosions, the general emphasis in this work was to obtain time histories of incident overpressure from pressurized spheres bursting in air at as many locations as possible per test. Also, it was desired that in each test some of the measurements be made as close to the glass sphere as was

129

physically possible with the transducers used.

The second set of experiments used Freon®-12 in the liquid and vapor state. However, because the sudden release of the liquid Freon® produced very weak waves (essentially sound waves), the overpressures measured were quite small and their damage potential negligible. Therefore, these liquid experiments will not be covered here. The other ten experiments used vaporized Freon®-12, also at room temperature, and internal pressures of 241 and 503 kPa (35 and 73 psig).

The experiments were set up in a fashion similar to those conducted by Boyer, et al [7]. The glass spheres were ruptured by a pneumatic striker while under high internal pressure. However, unlike the previous experiments, the instrumentation consisted of an array of pressure transducers at various distances along three radials from the sphere's centers. In addition to the pressure measurement system, high-speed cinematography was used in some of the tests to observe sphere breakup and obtain velocities of glass fragments. The velocity data were used to obtain the energy driving the blast wave by computing the fragment kinetic energy and subtracting it from the initial energy in the compressed fluid.

The tests were set up in a blast chamber as shown in Figure 1. The measuring equipment in the chamber included two aerodynamically-shaped, pencil-type blast pressure transducers and a double-wedge probe with six blast pressure transducers spaced along the upper surface. All eight of these transducers measured the side-on blast pressures generated by the bursting pressurized glass spheres. The high-speed movie camera was protected by a sheet of transparent plastic held in a wooden frame. The required lighting was provided by a high intensity spotlight.

The glass spheres were hand blown for this project. The thickness of each sphere was selected so that under pressure the spheres were close to the break point. Therefore, a slight tap against the sphere would burst it relatively uniformly all around and create small size fragments which would minimize the interference to the shock wave produced. Several spheres were pressurized to destruction to determine the approximate burst pressure of each size and thickness. The results of Boyer, et al [7], were used as a guideline for estimating the pressure which would burst each size sphere. However, because of non-uniformities in the spheres, (particularly in the thicker and larger ones), the maximum pressure spheres of the same size would withstand varied significantly.
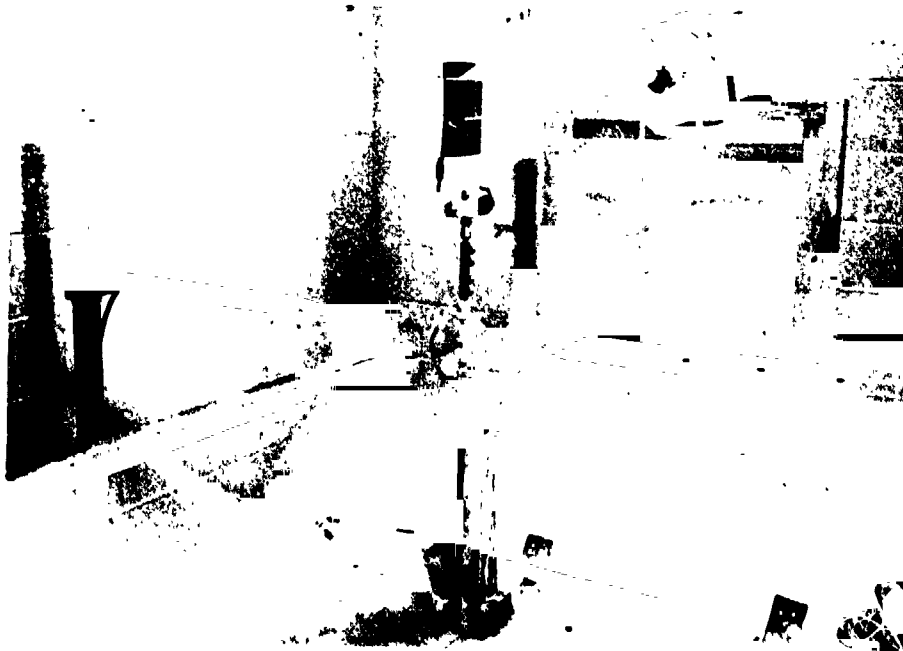


FIGURE 1. OVERVIEW OF EXPERIMENTAL APPARATUS

130

Because of the nonuniformity expected, each sphere tested was individually measured for mass, volume and thickness. The sphere assembly was weighed before each test and the remains (usually the neck and its fittings) were weighted after each test to determine the total mass of the fragments. The volume was measured by filling the sphere with water up to the bottom of the neck and then emptying the contents into a graduate. Using this volume, a mean diameter was computed using the formula for the volume of a sphere. With this mean diameter and the measured mass of the sphere, a mean sphere thickness was also computed. The actual thickness was also measured using ultrasonic sensors by taking several spot measurements around the sphere and averaging the results. The spheres used ranged in thickness from 0.3 to 4 mm (0.012 to 0.157 in.). For the majority of the spheres, these average values were very close to the computed mean thickness. All these measurements of sphere mass, volume and thickness were made

to obtain as accurately as possible the initial energy of the compressed fluid in the sphere.

Each experiment was set up in the test cell as shown in Figure 2. Once the sphere was properly connected and all instrumentation ready to record data, the pressuring system was purged several times and the sphere filled with the appropriate test fluid. After the temperature of the fluid stabilized to the ambient value, the solenoid valve in the filling line was closed remotely. The high-speed camera and the spotlight were then turned on to begin the actual test. At a preset point of film travel, the contacts in the camera closed which energized the solenoid on the pneumatic cylinder. The cylinder was pressurized and the striker burst the sphere releasing the high-pressure fluid.

The output of the pressure transducers was recorded on Polaroid film using several digital transient recorders and oscilloscopes. Minimum upper
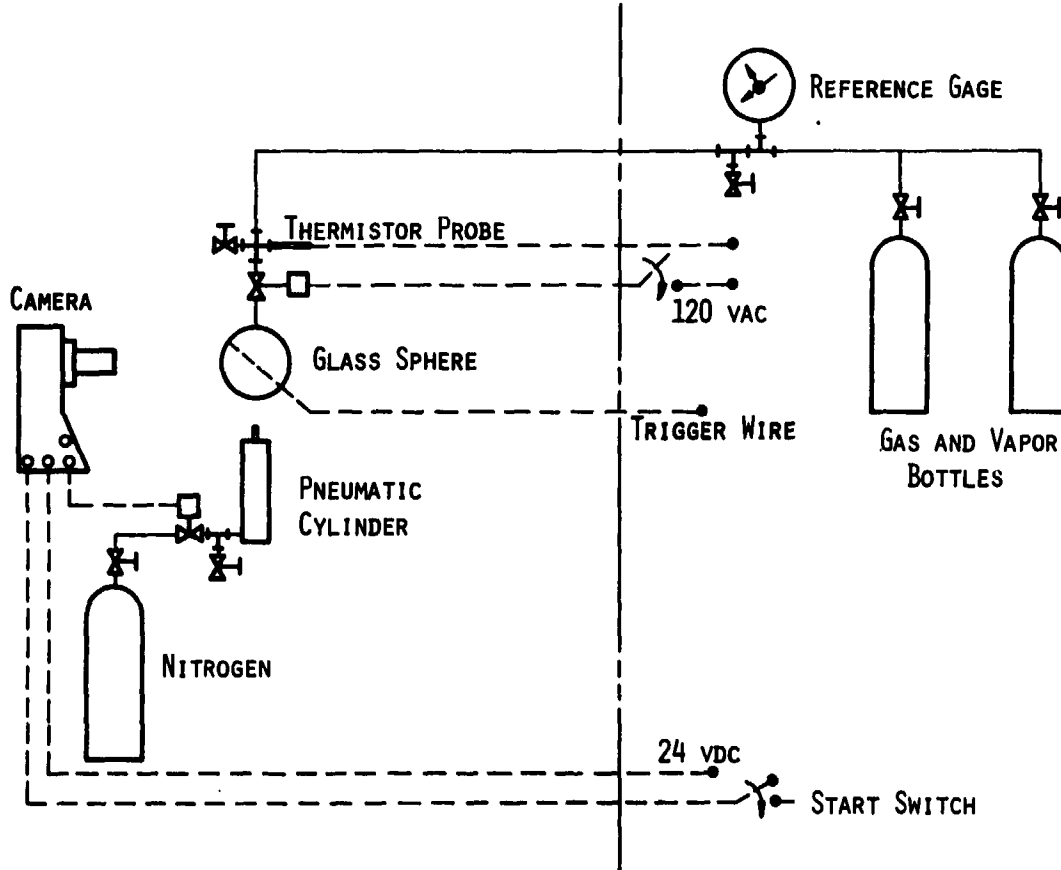


FIGURE 2. DIAGRAM OF EXPERIMENTAL SET-UP

131

frequency response of any one channel
was 25 kHz but the majority of the
record channels had an upper response
to at least 150 kHz. The data from the
photographs were digitized, manipulated
and plotted using a microprocessor-
based data processing system. The
resulting pressure and impulse versus
time plots were then used to read the
various blast parameters of interest.

TEST RESULTS

    The pressure-time histories that
were observed from the bursting spheres
were initially qualitatively similar
to those from ideal explosions in that
they contained a first shock which had
a measureable time-of-arrival, maximum
overpressure, and positive impulse.
However, the latter part of the records
differed from the usual point source
records in that they contained a large
negative phase impulse closely followed
by a strong second shock. This is
illustrated in Figures 3 and 4. The
blast parameters obtained in this ex-
perimental effort were non-dimensional
as indicated by the scaling law of
Equation (1). Because four of the
pi terms in this equation include the
energy E of the fluid in the sphere,
a determination of this quantity for
each test is required for computing the
non-dimensional quantities. The total
energy in the sphere does not all enter
the process of generating the shock
pressure wave. Because the glass
fragments are accelerated outward as
a result of the burst, their kinetic
energy represents a decrease in the
energy available to drive the blast
wave. Therefore, fragment velocities
were measured whenever possible to
compute the kinetic energy, $E_k$, of the
fragments for each test. Then, a cor-
rection was made to the energy (and
consequently the internal pressure)
available to the blast, in a manner
similar to that described by Boyer,
et al [7], by subtracting the kinetic
energy of the glass fragments from the
total energy, E, of the pressurized
gas volume. For those experiments in
which movies were not obtained, the
fragment velocity was estimated in
most cases from repeat experiments in
which the fragment velocity had been
measured and the test setup was almost
the same. Because the energy term
carries an exponent of 1/3, this
approximation results in very small
inaccuracies. Thus, the blast yield
is

$$E = E' - E_k \qquad (2)$$

    For the air and argon experiments,
the total energy E' in the pressure
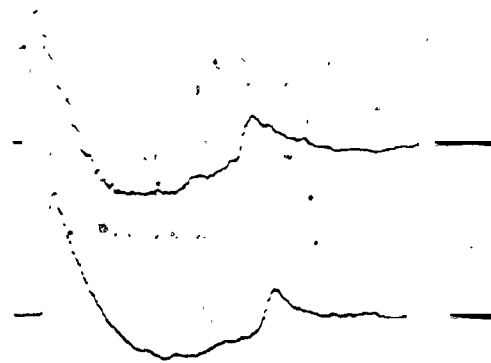


Air Sphere, 51 mm (2 in.) Diameter
$P_1/P_a$ = 53.5

Upper Trace:  $P_s/P_a$ = 0.4 @ $\bar{R}$ = 0.69

Lower Trace:  $P_s/P_a$ = 0.34 @ $\bar{R}$ = 0.82

Sweep:  200 μs/div.

FIGURE 3.   SAMPLE OF PRESSURE RECORDS
            FOR GAS SPHERE
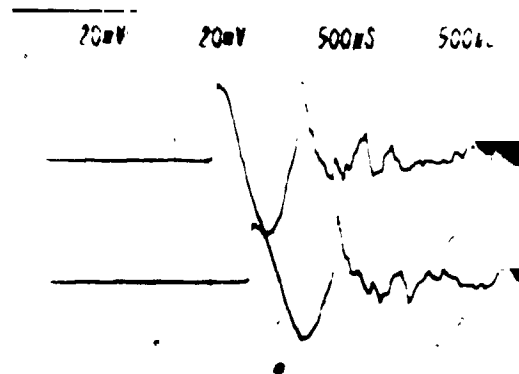


Freon®-12 Sphere, 51 mm (2 in.) Dia-
        meter  $P_1/P_a$ = 6

Upper Trace:  $P_s/P_a$ = 0.015 @ $\bar{R}$ = 6.8

Lower Trace:  $P_s/P_a$ - 0.011 @ $\bar{R}$ = 8.0

Sweep:  500 μs/div.

FIGURE 4.   SAMPLE OF PRESSURE RECORDS
            FOR VAPOR SPHERE

132

sphere was computed by the following formula originally proposed by Brode [13] and used by other investigators [3] to define the energy in a pressure sphere of volume $V_1$

$$E' = \left(\frac{p_1 - p_a}{\gamma_1 - 1}\right) V_1 \qquad (3)$$

For a perfect gas, the energy in the sphere given by this definition is very close to what would be computed by assuming the available energy is that which is released by an isentropic expansion of the gas in the sphere from a high pressure to an ambient pressure [14]. Equation (3) gives only slightly higher values than the isentropic expansion and is simpler.

For a bursting sphere containing a flashing vapor such as Freon®-12, perfect gas behavior cannot be used to determine the energy of the sphere. The maximum energy that can be released to drive a blast wave can be estimated by assuming an isentropic expansion from the initial state conditions to ambient pressure, and computing the corresponding work which could be done as a change in internal energy of the expanding fluid. Similar approximations have been used by other investigators to determine the energy of an expansion pressure wave from a flash-evaporation process [15,16]. Based on a unit mass of fluid, the energy change of a process starting at state 1 and expanding to state 2 is

$$u_1 - u_2 = {}_1\!\int^2 p\, dv \qquad (4)$$

where u is the internal energy and v is the specific volume. From tables [17] of thermodynamic properties the specific work, $u_1 - u_2$, was obtained knowing that enthalpy h is related to internal energy by

$$u = h - pv \qquad (5)$$

For a vapor starting in the super-heated region, expansion to ambient pressure can result in superheated vapor or wet vapor at state 2. In the first case, the process takes place along a constant entropy line and $\Delta u$ can be computed from direct table readings of h and v and the known pressures at both states. In the second case, the saturated vapor tables must be used to determine the final quality of the wet vapor by using the final entropy. With this quality,

the specific volume and enthalpy can then be computed, and $u_2$ determined. The total blast energy is obtained in both cases by computing the mass m of fluid, from the known sphere volume $V_1$ and the specific volume $v_1$, and multiplying by the change in internal energy

$$E' = m (u_2 - u_1) \qquad (6)$$

Once the total energy in the sphere was computed for both type of experiments, the kinetic energy of the fragments was subtracted, Equation (2), to obtain the estimated blast energy for each pressure sphere. This blast energy was then used to non-dimensionalize the data.

The scaling law of Equation (1) does not and cannot show that the functional forms $f_i$ are, nor does it tell the relative importance of varying each of the parameters. Either analysis or experiment or both must be conducted to get these answers. What it does do is to show a convenient way of presenting results of tests or analyses, or comparing results from various investigators. Ideally, one should vary each of the last four parameters in the bracket in Equation (1) while holding the other three constant, and determine the scaled blast parameters as functions of scaled distance. However, for the limited testing reported here the scaling law was simplified for each type of blast source. For the pressurized gas experiments, perfect gas behavior can be assumed and $p_1/p_a$ can then be eliminated because it is a function of the other three source terms. Only air and argon were used as pressurized gases in the blast wave source. For air $\gamma_1 = 1.4$ and for argon $\gamma_1 = 1.667$, which is a minor difference. The pi term $a_1/a_a$ equals one for air and very nearly one for argon. Therefore, these two terms can be eliminated. Finally, previous theoretical calculations [4] and the experimental data indicated that blast wave characteristics were only weakly dependent on the initial pressure ratio $(p_1/p_a)$. This effective ratio was varied in these experiments over a range of 9.9 to 42.0. Consequently, all the blast data are combined for the two gases and plotted strictly as a function of the Sachs' scaled distance in Figures 5 through 12. The parameters presented are the times of arrival of the first and second shock, the peak overpressures of both shocks, the first positive and negative phase impulses, and the durations of these two phases. The figures show the range of all test data within

133

FIGURE 5. SCALED TIME OF ARRIVAL OF
FIRST SHOCK WAVE FROM BURSTING GAS
SPHERES



FIGURE 6. SCALED SIDE-ON PEAK OVER-
PRESSURE FOR FIRST SHOCK FROM BURSTING
GAS SPHERES



FIGURE 7. SCALED SIDE-ON POSITIVE IM-
PULSE FROM BURSTING GAS SPHERES
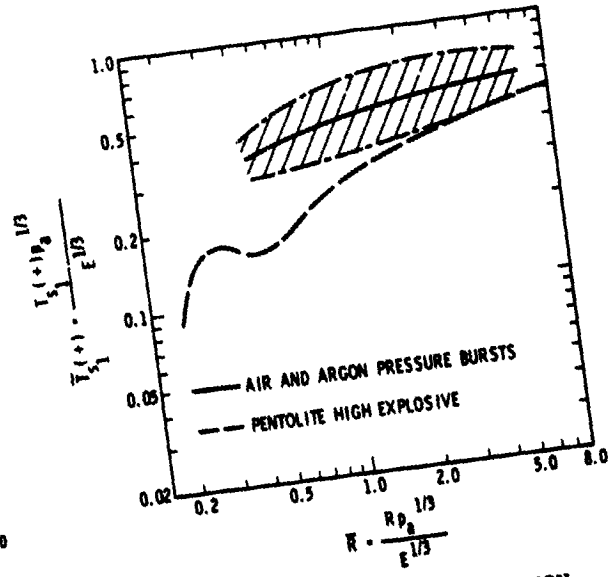


FIGURE 8. SCALED POSITIVE DURATION
FROM BURSTING GAS SPHERES

134

FIGURE 9. SCALED SIDE-ON NEGATIVE IM-
PULSE FROM BURSTING GAS SPHERES



FIGURE 10. SCALED NEGATIVE DURATION
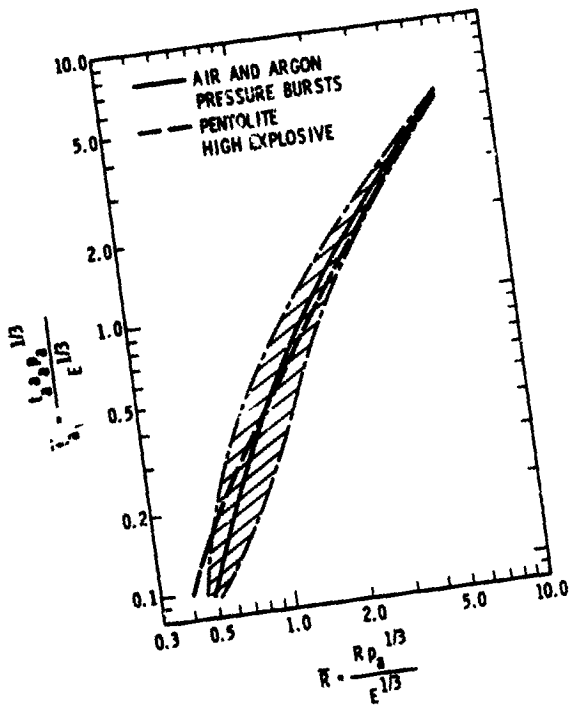FROM BURSTING GAS SPHERES



FIGURE 11. SCALED TIME OF ARRIVAL OF
SECOND SHOCK WAVE FROM BURSTING GAS
SPHERES.



FIGURE 12. SCALED SIDE-ON PEAK OVER-
PRESSURE OF SECOND SHOCK FOR BURSTING
GAS SPHERES.

135

the cross-hatched areas, and a "best fit" solid curve through the data.

Similarly, for the Freon®-12 vapor tests, the blast data can be presented as a function of only scaled distance because the ratios of specific heats, sound velocities, and densities are invariant among these experiments, and the internal pressure ratios used were only 3.5 and 6.0. These data are presented in Figures 13 through 20 as a function of scaled distance. Note that the data from the gas and vapor experiments, in general, will not plot together because each blast parameter will be a different function of the pi-terms from the scaling law, dependent on the fluid in the pressure sphere.

CONCLUSIONS

The characteristics of the recorded blast waves from the compressed gas and vapor experiments proved to be quite repeatable, and somewhat different from waves from condensed explosives such as Pentolite or TNT. The initial positive phase is followed by a very pronounced negative phase and a much more distinct second shock occurs. Furthermore, the data for each set of tests were somewhat different in appearance and relative amplitudes from each other.

Compared to available Pentolite data, the data from these non-ideal explosions are quantitavely similar in some respects but distinctly different in others. First shock arrival times and positive phase impulses are quite alike in amplitude with the pressure sphere data coinciding with the Pentolite curve over the range of scale distances used. Basic differences are lower initial overpressures and longer positive durations then for Pentolite. Because negative phase data for Pentolite are not available, no numerical comparisons can be made. However, qualitatively it is quite obvious that the pressures spheres generate much larger negative phase impulses and higher pressure second shocks than condensed explosives. This negative impulse is generally larger than the positive phase impulse.

The data presented appear to be the first sizeable set of measurements of the characteristics of blast waves from bursting, frangible pressure spheres. The differences cited between blast waves from bursting spheres and high explosives show that those from pressurized spheres are indeed non-ideal, even though they are quite

repeatable. Close to these sources the concept of "TNT equivalence" appears to have little meaning because the blast waves differ too greatly from those from condensed explosives. Because of the lower initial over-pressure, but larger negative phase and strong second shock, the damage caused by these waves can be significantly different, too, depending on the particular "target" placed in its path.

The results of the experiments reported here are limited to two gases, air and argon, and one flash-evaporating vapor, Freon®-12. These data form only the beginning of what should be a more substantial program into these types of explosions. Experiments using the basic test arrangement and methods covered here should be conducted with other gases with significantly different specific heat ratios and densities, with other vapors of higher saturation pressure, with fluids heated above ambient temperature, and with combustible gaseous mixtures. At the same time, theoretical investigation of these types of blast waves should continue and computation carried out for longer scaled times for comparisons with the experimental data. And, finally, the methodology for computing the energy driving the blast waves needs to be further analyzed to better apply the scaling law presented and to more accurately compute the non-dimensional blast parameters for better comparisons with high-explosive data or analytical predictions.

REFERENCES

1.  H. L. Brode, "The Blast from a Sphere of High Pressure Gas," Rand Corp., Report P-582, 1955.

2.  H. L. Brode, "The Blast Wave in Air Resulting from a High Temperature, High Pressure Sphere of Air," Rand Corp., Report RM-1825-AEC, 1956.

3.  S. L. Huang and P. C. Chou, "Calculations of Expanding Shock Waves and Late-State Equivalence," Drexel Institute of Technology, Report No. 125-12, April 1968.

FIGURE 13.  SCALED TIME OF ARRIVAL OF
FIRST SHOCK WAVE FROM BURSTING FREON-12
VAPOR SPHERES
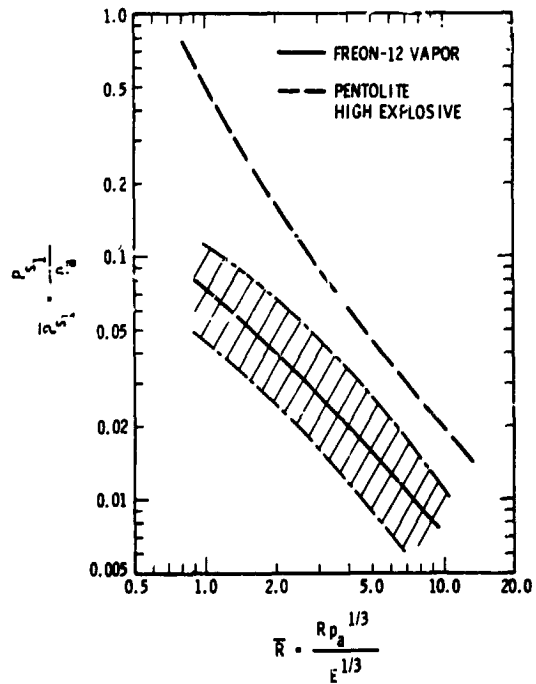


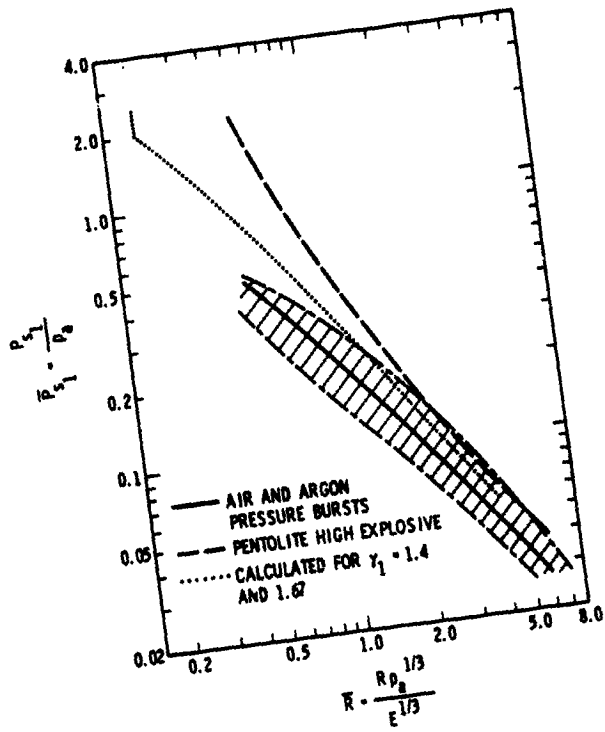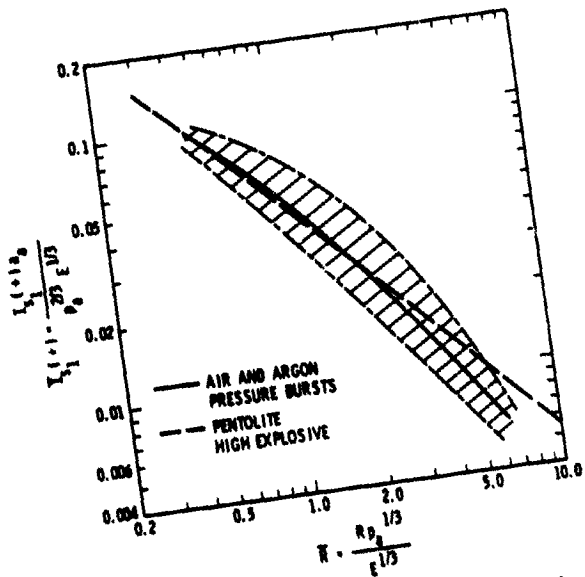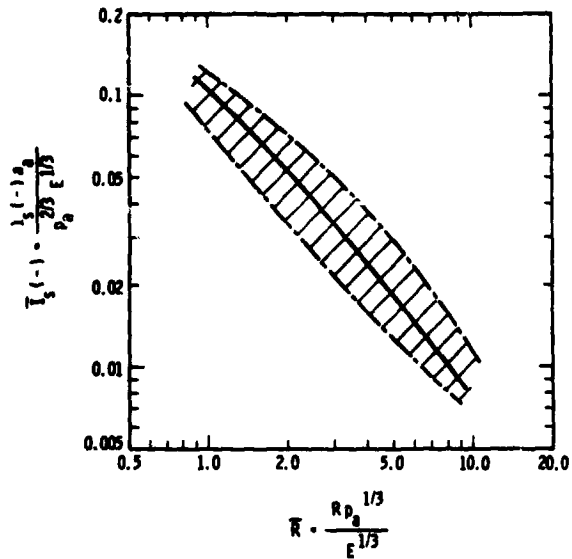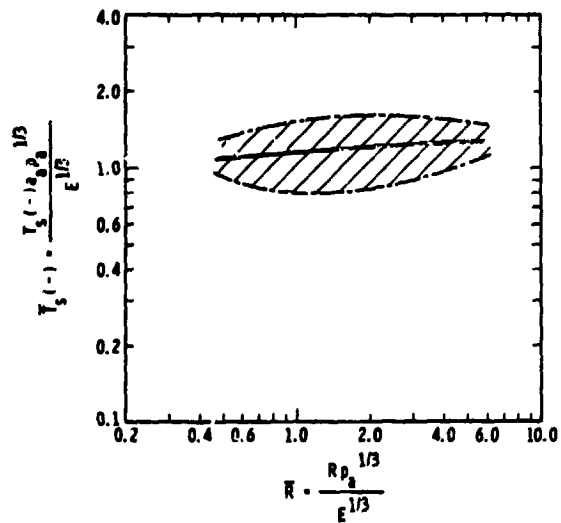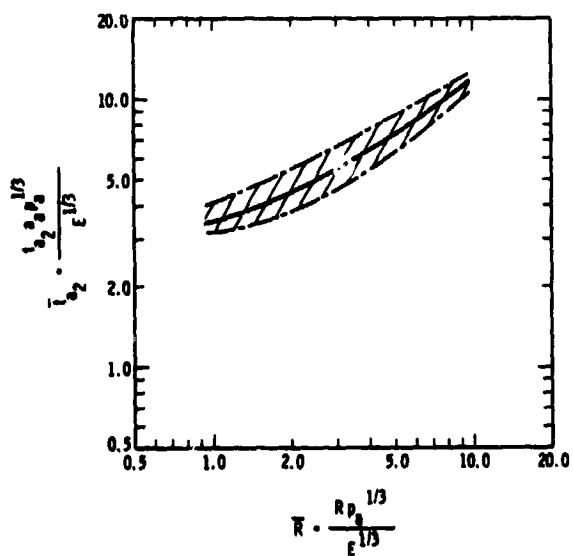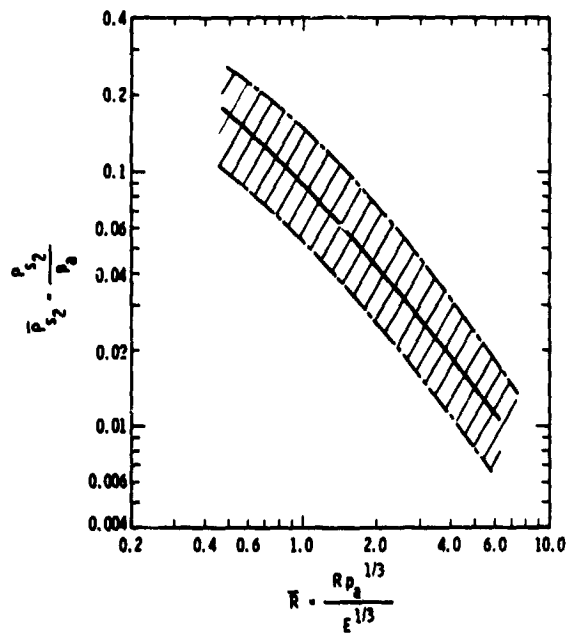FIGURE 14.  SCALED SIDE-ON PEAK OVER-
PRESSURE FOR FIRST SHOCK FROM BURSTING
FREON-12 VAPOR SPHERES



FIGURE 15.  SCALLD SIDE-ON POSITIVE IM-
PULSE FROM BURSTING FREON-12 VAPOR
SPHERES
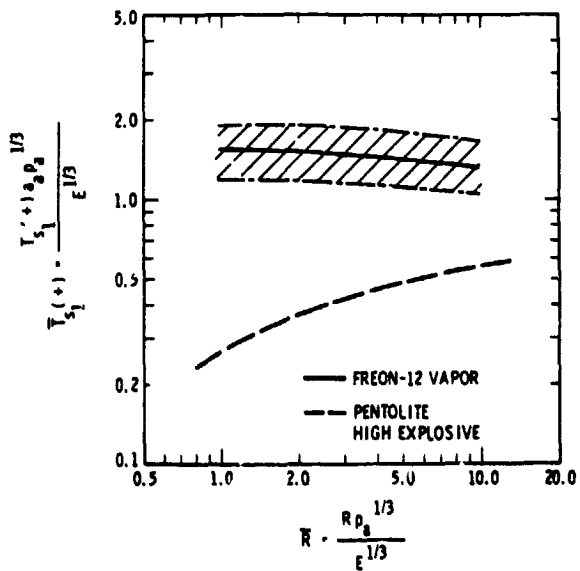


FIGURE 16.  SCALED POSITIVE DURATION
FROM BURSTING FREON-12 VAPOR SPHERES

137

FIGURE 17. SCALED SIDE-ON NEGATIVE
IMPULSE FROM BURSTING FREON-12 VAPOR
SPHERES
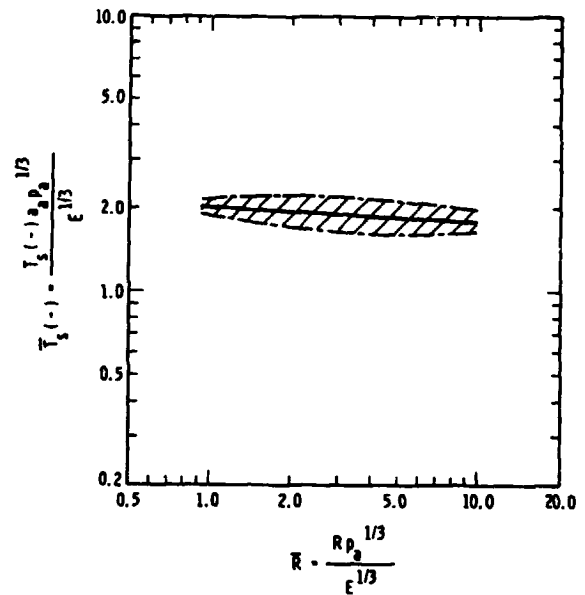


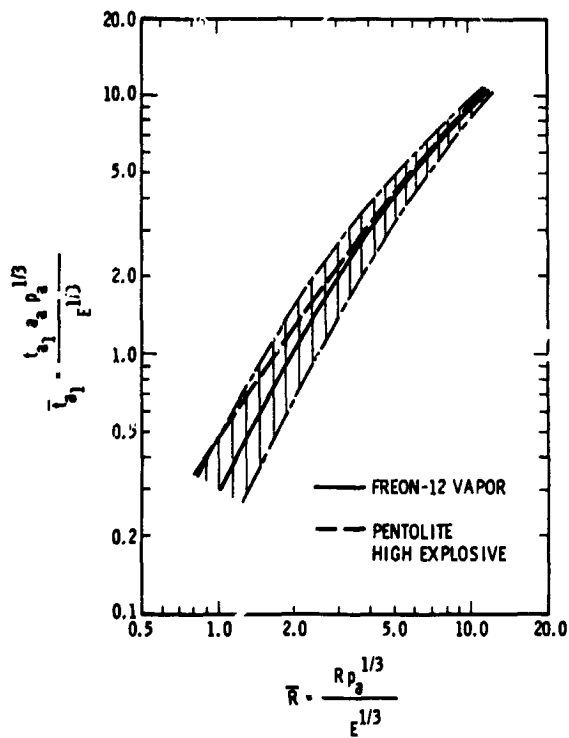FIGURE 18. SCALED NEGATIVE DURATION
FROM BURSTING FREON-12 VAPOR SPHERES
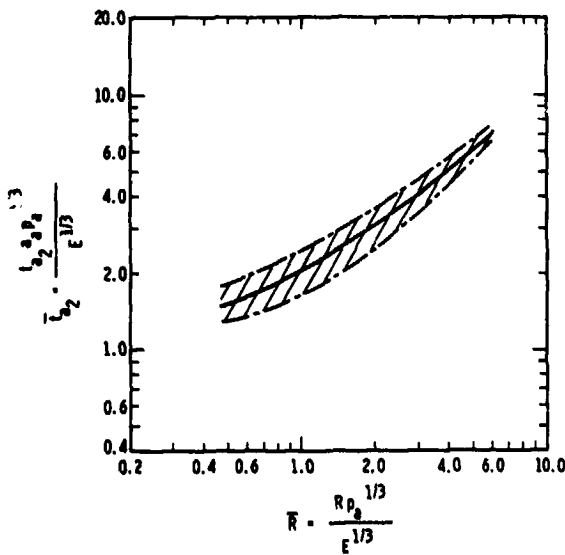


FIGURE 19. SCALED TIME OF ARRIVAL OF
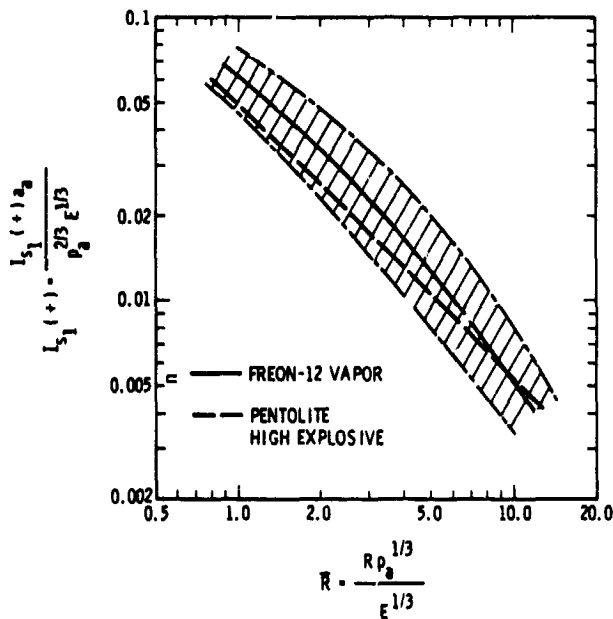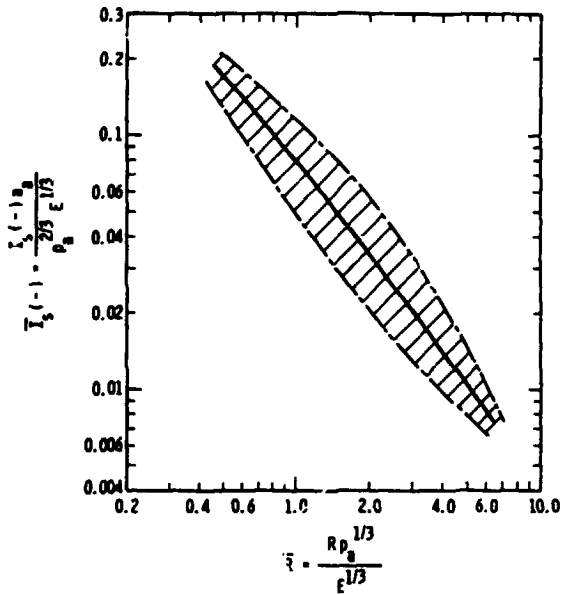SECOND SHOCK WAVE FROM BURSTING
FREON-12 VAPOR SPHERES
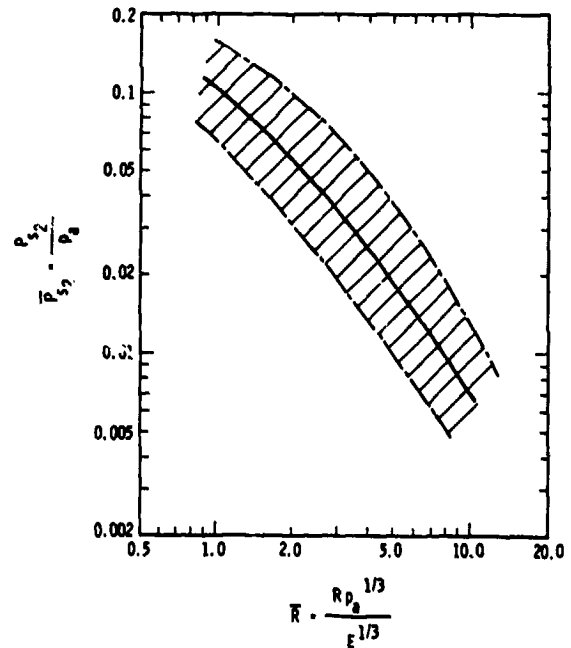


FIGURE 20. SCALED SIDE-ON PEAK OVER-
PRESSURE OF SECOND SHOCK FROM BURSTING
FREON-12 VAPOR SPHERES

138

4. R. E. Ricker, "Blast Waves from Bursting Pressurized Spheres," Master's Thesis, University of Illinois, Dept. of Aero. & Astro Eng., 1975.

5. W. E. Baker, J. J. Kulesz, R. E. Ricker, R. L. Bessey, P. S. Westine, V. B. Parr, and G. A. Oldham, "Workbook for Predicting Pressure Wave and Fragment Effects of Exploding Propellant Tank and Gas Storage Vessels," NASA CR-134906, Southwest Research Institute, San Antonio, Texas, November 1975, (Reprinted September 1977).

6. W. E. Baker, J. J. Kulesz, R. E. Ricker, P. S. Westine, V. B. Parr, L. M. Vargas, and P. K. Moseley, "Workbook for Estimating Effects of Accidental Explosions in Propellant Ground Handling and Transport Systems," NASA CR-3023, Southwest Research Institute, San Antonio, Texas 1978.

7. D. W. Boyer, H. L. Brode, I. I. Glass, and J. G. Hall, "Blast from a Pressurized Sphe.e," UTIA Report No. 48, Toronto, Canada, January 1958.

8. J. F. Pittman, "Blast and Fragment Hazards from Bursting Pressure Tanks," NOLTR 72-102, U. S. Naval Ordnance Lab., White Oak, MD, May 1972.

9. E. D. Esparza and W. E. Baker, "Measurement of Blast Waves from Bursting Pressurized Frangible Spheres," NASA CR-2843, Southwest Research Institute, San Antonio, Texas, May 1977.

10. E. D. Esparza and W. E. Baker, Measurement of Blast Waves from Bursting Pressurized Frangible Spheres Pressurized with Flash-Evaporating Vapor or Liquid," NASA CR-2811, Southwest Research Institute, San Antonio, Texas, 1977.

11. W. E. Baker, Explosions in Air, University of Texas Press, Austin, Texas, 1973.

12. W. E. Baker, P. S. Westine, and F. T. Dodge, Similarity Methods in Engineering Dynamics, Hayden Book Co., Rochelle Park, NJ, 1972.

13. H. L. Brode, "Blast Wave from a Spherical Charge," Physics of Fluids, 2, 217, 1959.

14. R. A. Strehlow and W. E. Baker, "The Characterization and Evaluation of Accidental Explosions," Progress in Energy and Combustion Science, Vol. 2, No. 1, pp 27-60, 1976.

15. B. Maurer, H. Schneider, K. Hess, and W. Leuckel, "Modelling of Vapor Cloud Dispersion and Deflagration after Bursting of Tanks filled with Liquefied Gas" (Translation by R. A. Mayer), Enlarged Version of Lecture before International Seminar: ELCALAP for Structural Safeguards and Containment Structures, Berlin, West Germany, September 1975.

16. W. E. Baker, E. D. Esparza, J. C. Hokanson, J. E. Funnell, P. K. Moseley and D. M. Deffenbaugh, "Initial Feasibility Study of Water Vessels for Arresting Lava Flow," AMSAA Interim Note No. F-13, Southwest Research Institute, San Antonio, Texas, June 1978.

17. ASHRAE Handbook of Fundamentals, Am. Soc. of Heating, Refrigerating and Air Conditioning Engineers, Inc., New York, 1972.

# TEST EVALUATION OF SHOCK BUFFERING CONCEPT FOR HYDRODYNAMIC RAM INDUCED BY YAWING PROJECTILE IMPACTING A SIMULATED INTEGRAL FUEL TANK

Patrick H. Zabel
Southwest Research Institute
San Antonio, Texas

A concept for containing the shock inputs due to hydrodynamic ram caused by an impacting projectile within a fuel cell is discussed. This concept is to provide a buffering layer of foam, flexible, rigid or a combination thereof, which is sealed from the liquid. A program is described in which this buffering concept was tested. The effectiveness of a novel muzzle-mounted, "tumble", test device is shown.

Twenty-six severely yawing 14.5 mm armor-piercing incendiary-tracer (API-T) projectiles impacted four combinations of rigid and flexible foam buffering assemblies mounted upon Z-stiffened aluminum plates or upon bare Z-stiffened plates. These targets represented unprotected aircraft integral fuel tanks and four candidate protected configurations of one and two-foot shotline thicknesses. Piezoelectric pressure transducers sensed the hydrodynamic ram pressures generated by the projectiles in three locations along the trajectory for the two-foot shotline tests and in two locations for the one-foot shotline tests. In each case, two transducers were at a common distance facing one another. Peak pressures are presented plus typical pressure recordings.

For the two-foot shotline tests, the test fixture had transparent sides through which motion pictures of the projectile penetration-cavitation sequences were taken.

A standard rifled 14.5 mm Mann gun was used. The barrel was modified to accept a muzzle-mounted attachment which caused the projectiles to yaw severely enough to meet standard test "tumble" requirements. Impact accuracy and yaw/ "tumble" data are presented. Projectile velocity was determined using a photoelectric chronograph screen array and electronic counter, and is presented.

Three test panels were mounted for each two-foot shotline test, front/bottom/rear; and, two for each one-foot shotline test, front/rear. Photographs of panel damage typical to each configuration for each shotline distance are presented.

Compression deflection data for the flexible and rigid foams used are presented and discussed. Both materials are in common use in aircraft, but these data are not readily available.
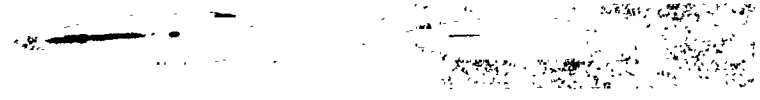
PROJECTILE                          PENETRATOR

a.  U.S. CALIBER .50 ARMOR PIERCING INCENDIARY M8


PROJECTILE                          PENETRATOR

b.  SOVIET 12.7 mm ARMOR PIERCING INCENDIARY


PROJECTILE                          PENETRATOR    TRACER CAP

c.  SOVIET 12.7mm ARMOR PIERCING INCENDIARY-TRACER
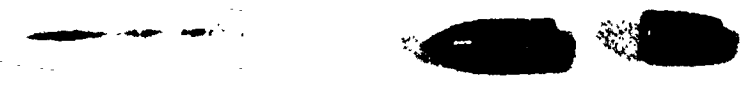

PROJECTILE                          PENETRATOR    TRACER CAP

d.  SOVIET 14.5mm ARMOR PIERCING INCENDIARY-TRACER


FRONTISPIECE.  TYPICAL SMALL-CALIBER PROJECTILES

142

Observations based upon these tests are:

(1) The hydrodynamic ram energy acted principally along the projectile trajectory. Minor damage was sustained at the impacted surface plate, less damage on a plate parallel to the shotline, but severe damage at the projectile exit plate.

(2) Hydrodynamic ram energy attenuates along a wetted shotline.

(3) Flexible foam is better than rigid foam in attenuating the hydrodynamic ram energy with this tested structure.

(4) A muzzle attachment may be used to convert a standard rifled Mann barrel into a "tumble" barrel and the impact location and "tumble"/yaw predicted or controlled within desirable limits.

## 1. INTRODUCTION

This paper describes a program in which a buffering concept for reduction of hydrodynamic ram effects was tested. [1] Upon ballistic penetration into a fuel tank below the liquid surface, kinetic energy is transferred from the projectile to the fuel, causing intense pressure waves, referred to as hydrodynamic ram. The projectile usually becomes unstable, yawing severely or tumbling -- either action increases the rate of transfer of kinetic energy, thereby increasing the hydrodynamic ram pressure level. When the projectile is armor piercing incendiary-tracer with the tracer element within a separate cup, separation of the projectile components and opening of the jacket present a much greater area for transfer of the projectile kinetic energy to the liquid since much less energy remains with the projectile components. This hydrodynamic ram traverses the fuel to the tank wall, potentially resulting in failure of the tank wall and/or rupture of a bladder if present. Normally, the greatest danger to an aircraft is fire. The complete loss of the fuel within a single fuel cell can be allowed if fire would not result and if the aircraft structure were not severely damaged; in fact, this has been suggested for limited usage where blowoff skin would act as a burst diaphragm. [2] However, this is an expedient; preferably the fuel should be saved to complete a mission. Several researchers have proposed or tested hydrodynamic ram resistant fuel cell constructions. [2,3,4]

The buffering concept herein reported is to provide an energy absorbing layer on the inside surfaces of the fuel tank. Two basic energy-absorbing materials were tested singly and in combination. One of these was "soft," the other "hard" -- varying greatly in their respective energy-absorbing capability. A bare configuration was tested to provide a baseline from which the relative efficacy of the different buffering concepts can be gauged.

Data are presented to show the relative damage resulting, the hydrodynamic ram pressure levels achieved, and other test details.

The order of presentation is:

a. a description of the test fixture, specimens, pressure instrumentation, and equipment;

b. a description of the conduct of the tests;

c. a presentation of the test results from physical inspection of the test specimens, hydrodynamic ram pressure data, and samples of high frame rate motion picture data;

d. an evaluation of the test results based upon the damage to the test specimens and a description of the two energy-absorbing materials used; and

e. a summary.

143

## 2. DESCRIPTION OF TEST PARAPHERNALIA

A rectangular fixture, Figure 1, having full-view windows on opposite sides, accommodated 45.72 cm by 45.72 cm (18 in by 18 in) test panels on the front, bottom, and rear sides, for a two-foot shotline configuration. This same fixture was used with steel side walls and front and rear test panels for the one-foot shotline configuration.

The test panels consisted of a structural assembly, Figure 2, with one of four combinations of buffering foam, Types A, B, C, and D shown on Figure 3, which, when mounted, were supported from internally generated pressure as shown in Figure 4. Each Z-stiffener, with a moment of inertia of 11.904 cm$^4$ (0.286 in$^4$) around the riveted flange, was supported at both ends by the steel frame when the pressure load was outward. The stiffeners for the panels in the front and rear apertures were always mounted vertically and those of the bottom panel parallel to the projectile trajectory. The rivets used were not truly representative of aircraft fasteners, being too light; however, they were useful in providing a relative measure of loading.

The buffering materials used were the white, reticulated 14.57 pores per centimeter (37 pores per inch-ppi), polyurethane Scott foam and the AVCO Thermarest 0.036 kg/m$^3$ (2.8 lb/cu ft) rigid foam, the properties of which are discussed in Section 5.2. To assure that the buffering material was not wetted prior to the test, a neoprene-coated nylon cloth was placed over the foam and bonded to the aluminum panel around the clamping edges (Figure 3), serving also as a gasket. To assure that this elastomer-coated cloth sealed the foam from the liquid, each assembly was leak checked by immersion in water prior to being installed in the test fixture. Ignoring the upper surface within the fixture, the total wetted area, total buffered area, and their ratios are shown in Table 1. Three Kistler piezoelectric

pressure transducers were installed for two-foot shotline tests to measure the hydrodynamic ram pressures. (See Figure 5.) Only the front two transducers were used for one-foot shotline tests. The test fixture was back-lighted to provide the necessary illumination for the high-speed camera coverage of the hydrodynamic ram events. A chronograph and a pair of photoelectric screens were used to determine the projectile velocity. (See Figure 6)

The rifled 14.5 mm Mann gun was located 10.97 meters (36 feet) from the test fixture. The barrel was modified to accept a muzzle-mounted attachment to provide the necessary projectile tumble. The exact tumble used during the program was determined for each test from the signature in the front panel. The projectile travel condition at impact may be more properly described as a "severe yaw" rather than a "tumble". This device was "calibrated" prior to hydrodynamic ram tests using the setup shown in Figure 7 with the results shown in Figure 8.

## 3. CONDUCT OF TESTS

The appropriate number of test panels were installed in the test fixture. An impact switch was mounted at the desired point of impact. The test fixture was filled with water. The tape recorder was started, then the automatic sequencing circuit initiated which fired the weapon after the high-frame-rate motion picture camera reached a desired speed. After the impact the tape recorder was stopped and the test fixture and panels inspected. The test panels were removed and photographed and the remnants of the projectile recovered.

For each shotline configuration, there was one baseline test with bare aluminum panels (there was a liquid seal consisting of a 2.54 cm [one-inch] wide border of neoprene-coated nylon around the perimeter), and three tests each of panels in the A, B, C, or D configuration. After the tests were concluded,

TABLE 1. WETTED/BUFFERED AREAS

| Shotline Configuration (ft) | Total Wetted Area m$^2$(sq.in.) | Total Buffered Area m$^2$(sq. in.) | Ratio Buffered/ Wetted Area (%) |
|---|---|---|---|
| 2 | 3.345 (5184) | .627 (972) | 18.75 |
| 1 | 2.508 (3888) | .418 (648) | 16.67 |

FRONT VIEW                    SIDE VIEW
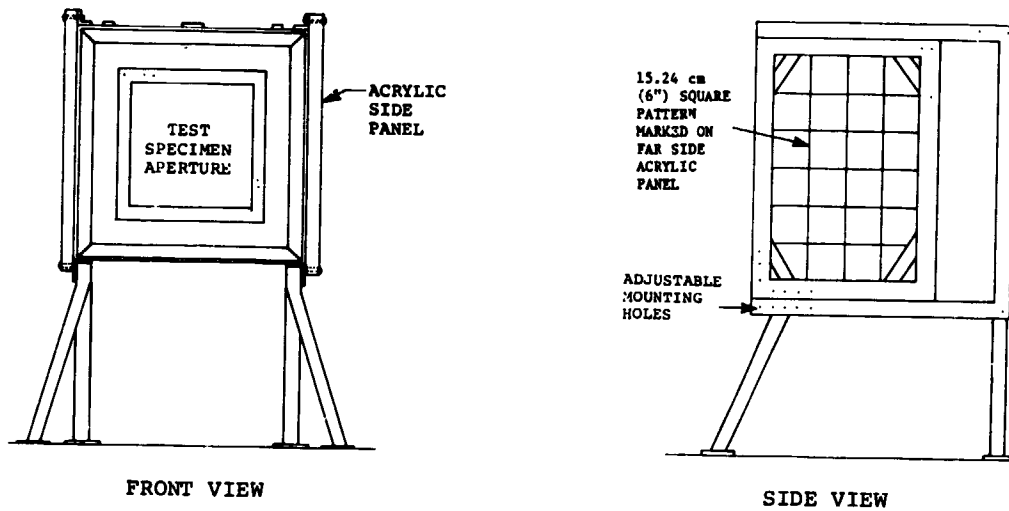
FIGURE 1.    HYDRODYNAMIC RAM TEST FIXTURE
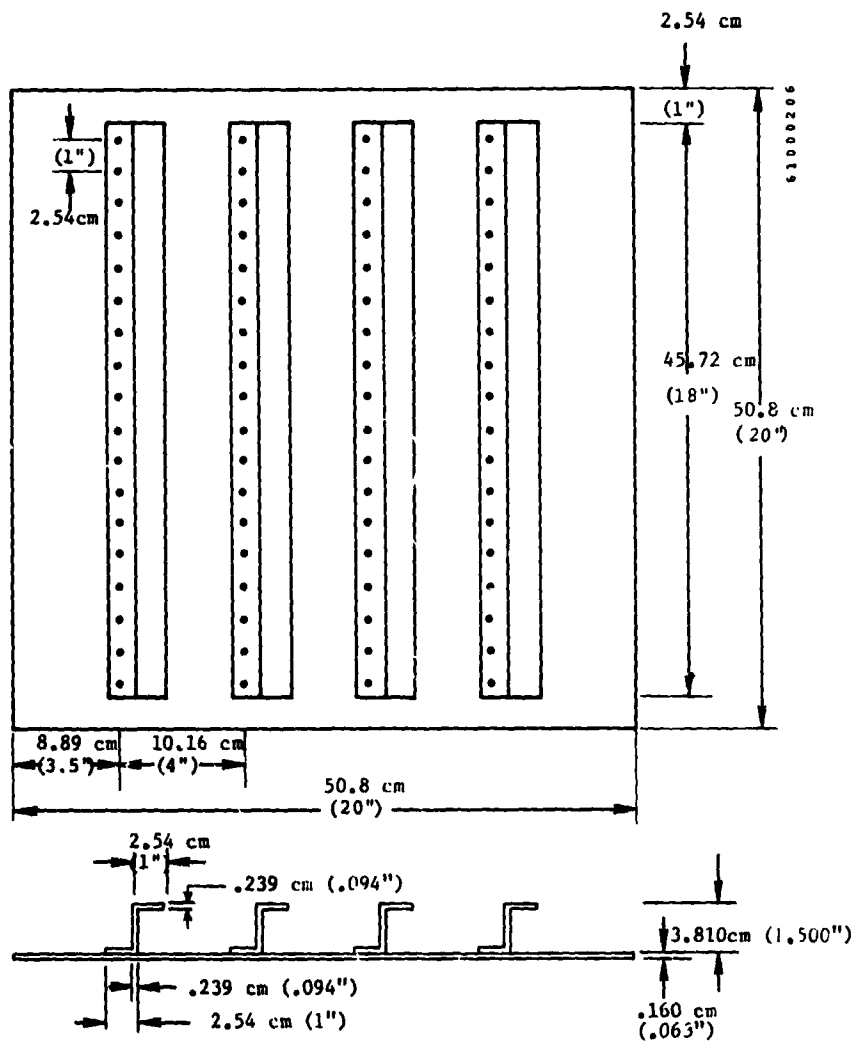
MATERIAL: PLATE AND STIFFENERS: 7075 T6 AL (STIFFENERS EXTRUDED)
RIVETS: ALUMINUM, 0.238 cm (3/32") PER MS20470 (BJ-3)

FIGURE 2. METALLIC STRUCTURES OF TARGET PANELS

146

NEOPRENE-COATED NYLON, COOLEY STYLE AT66,
141.8 GM (5-OZ) NYLON, 453.6 GM (16-OZ) NEOPRENE

FOAM, WHITE RETICULATED (PANEL TYPE A)
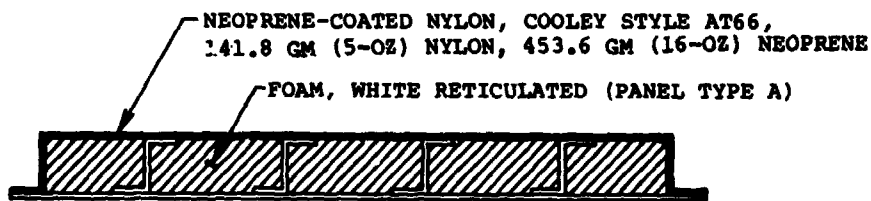
a.  CROSS-SECTION OF 3.810 CM (1-1/2-INCH) THICK FOAM PANEL

NEOPRENE-COATED NYLON, COOLEY STYLE AT66,
141.8 GM (5-OZ) NYLON, 453.6 GM (16-OZ) NEOPRENE

| PANEL TYPE | B | C | D | |
|---|---|---|---|---|
| | RIGID | RETICULATED | RIGID | FOAM |
| | RETICULATED | RETICULATED | RIGID | FOAM |
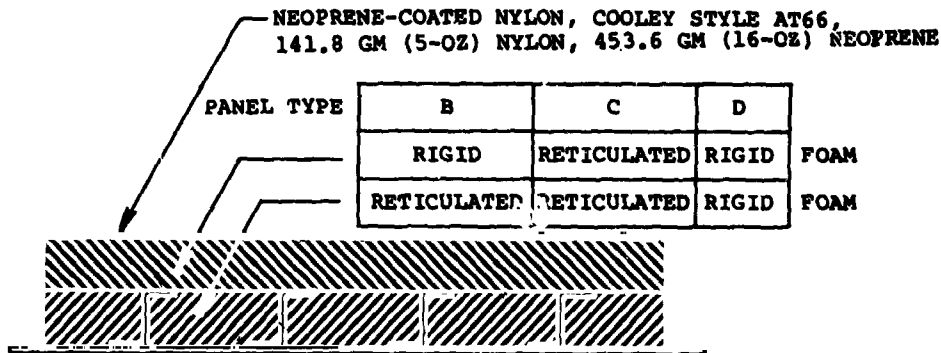
b.  CROSS-SECTION OF 7.62 CM (3-INCH) THICK FOAM PANEL

NOTE:  NEOPRENE-COATED NYLON FABRIC SECURED TO FOAM AND
PLATE WITH BOSTICK ADHESIVE NO. 1177.  THIS FABRIC
HAS A TENSILE STRENGTH OF 86.184 KG (190 LB) (WARP)
68.040 KG (150 LB) (WOOF) PER LINEAR INCH AND A TEAR
STRENGTH OF 3.629 KG (8 LB) (WARP) 3.175 KG (7 LB)
(WOOF).

FIGURE 3.  CROSS-SECTIONS OF TARGET PANELS
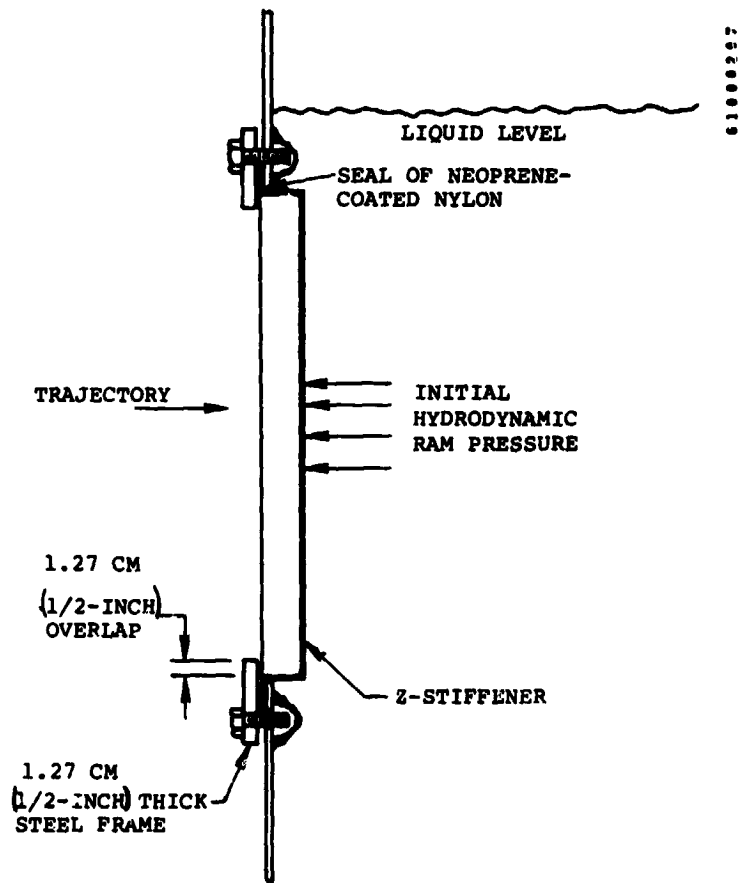
FIGURE 4. TEST PANEL MOUNTING ARRANGEMENT
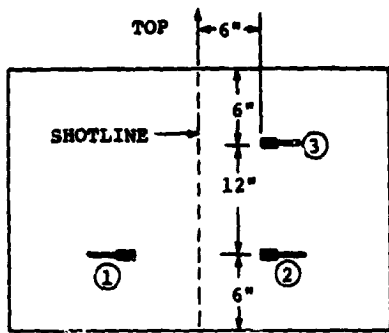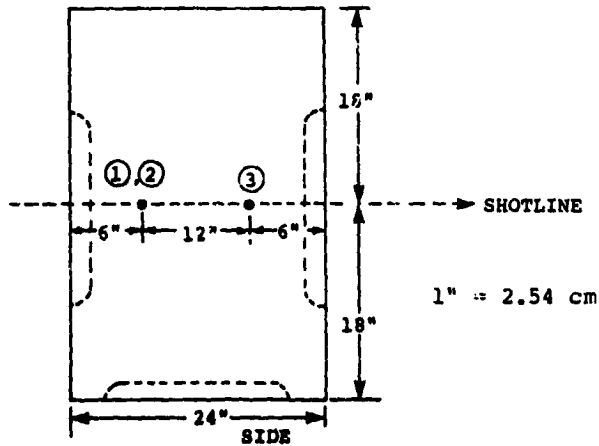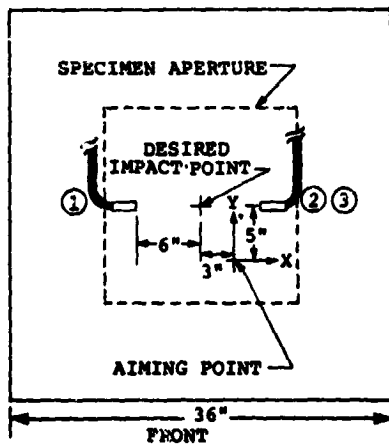
FIGURE 5.   PRESSURE TRANSDUCER LOCATIONS, TWO-FOOT SHOTLINE CONFIGURATION

149
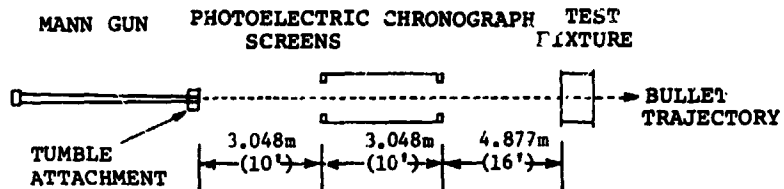
FIGURE 6. TEST SETUP SCHEMATIC



MANN GUN   PHOTOELECTRIC  CHRONOGRAPH  MANILA PAPER   TEST
WITH TUMBLE SCREENS WITH MANILA PAPER WITNESS ARRAY    FIXTURE
ATTACHMENT  WITNESS SHEETS ON EACH
            SCREEN AND IN MID-FRAME
            POSITIONS.
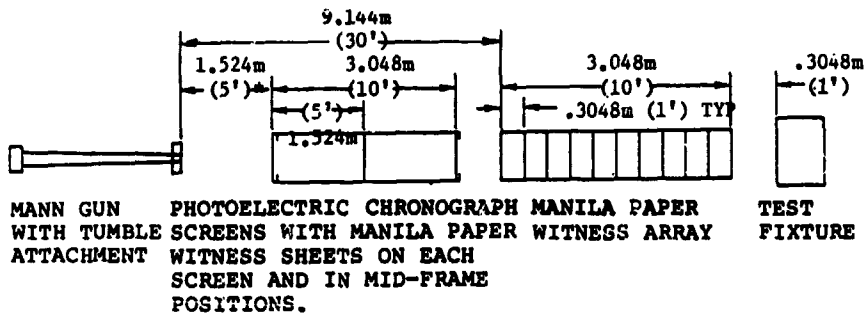
*These dimensions will vary for subsequent shots dependent upon the results of the pre-
ceding shot.

FIGURE 7. SETUP FOR INITIAL TUMBLE TEST SHOT

12.497m (41 FT)

2.54cm
(1 IN.)
SCALE

9.144m
(30 FT.)

NOTE: HOLES ARE THOSE MADE
BY TWO BULLETS FIRED
CONSECUTIVELY WITHOUT
MOVING WITNESS SHEETS

| RANGE | | HOLE LENGTH | | YAW | TUMBLE |
| M | FT | CM | IN | (DEG) | % |
|---|---|---|---|---|---|
| 9.144 | 30 | 2.39 | 0.94 | 15.1 | 33.4 |
| 9.449 | 31 | 3.00 | 1.18 | 21.0 | 43.2 |
| 9.754 | 32 | 3.56 | 1.40 | 24.7 | 51.0 |
| 10.058 | 33 | 3.94 | 1.55 | 28.5 | 57.0 |
| 10.363 | 34 | 4.22 | 1.66 | 32.3 | 61.4 |
| 10.668 | 35 | 4.37 | 1.72 | 34.4 | 63.8 |
| 10.973 | 36 | 4.47 | 1.76 | 35.8 | 65.4 |
| 11.278 | 37 | 4.32 | 1.70 | 33.6 | 63.0 |
| 11.582 | 38 | 4.06 | 1.60 | 30.2 | 59.0 |
| 11.887 | 39 | 3.76 | 1.48 | 26.5 | 54.2 |
| 12.192 | 40 | 3.25 | 1.28 | 22.2 | 47.2 |
| 12.497 | 41 | 2.64 | 1.04 | 17.0 | 37.6 |

AIMING
POINT

FIGURE 8. CALIBRATION OF TUMBLE ATTACHMENT

the panels were examined and the damage assessed. More complete tabulations of these are available. [5]

## 4. RESULTS OF THE BUFFERING TESTS

The test results are covered from three aspects. First, observations are tabulated which include an estimate of the damage suffered by the test panels, the functioning of the tracer and incendiary, the projectile velocity, the impact location, and the yaw attitude. Second, the pressure data are described. Third, observations are made from the high frame rate motion pictures.

### 4.1 Results from Physical Inspection of Test Panels and Projectiles

The basic test results are presented in Table 2. Typical damage is shown in Figures 9 through 13 for the two-foot (0.610 cm) shotline tests in the order of baseline (B.L.), Types A, B, C, and D panel assemblies, respectively, and on Figures 14 through 18 for the one-foot (0.305 m) shotline tests. The damage indices were determined by assigning numeric values to the damage descriptors:

| | |
|---|---|
| Nil | 1 |
| Minor | 2 |
| Moderate | 3 |
| Major | 4 |
| Severe | 5 |
| Destroyed | 6 |

The damage index for each panel was determined by adding the descriptor values and dividing the number of panels. The type damage indices for each shotline are the average of those of the panels. The type damage indices for the overall tests are:

| Type of Panel | Overall Index |
|---|---|
| Baseline | 4.00 |
| A | 3.13 |
| B | 2.73 |
| C | 2.53 |
| D | 2.87* |

*Probable value 2.67

The excessive damage to the front panel in Shot 15, Figure 19a was due to impact on one of the stiffeners. Had that projectile impacted on the skin between the stiffeners, the more probable overall damage index for Type D could have been 2.67. The rear panel is shown still in the fixture to illustrate how the steel frame limited damage to the panels, Figure 19b.

The mean projectile velocity for the twenty determinations was 1030 m/sec (3378.3 fps). The standard deviation of the population was 12 m/sec (38.45 fps). This is excellent considering that the projectiles were yawing severely as they passed through the photoelectric chronograph screens resulting in effective interscreen distance differences.

The impact accuracy and the tracer and incendiary functioning data are in Table 3. Part of the reason for the relatively poor impact accuracy is the precession which may be seen in Figure 9.

### 4.2 Pressure Data

The Kistler piezoelectric system showed pressures such as those in Figure 20. For this particular test, Shot No. 2, the left front pressure transducer was actually 2.36 cm (0.93 in) behind the right front transducer and the right front transducer 31.50 cm (12.40 in) in front of the right rear transducer which is borne by the difference in time of initiation of pressure change. Representative pressure traces for the test configurations and shotline distances are shown on the figures indicated in Table 4. Figures 21 through 29 show typical pressure versus time traces.
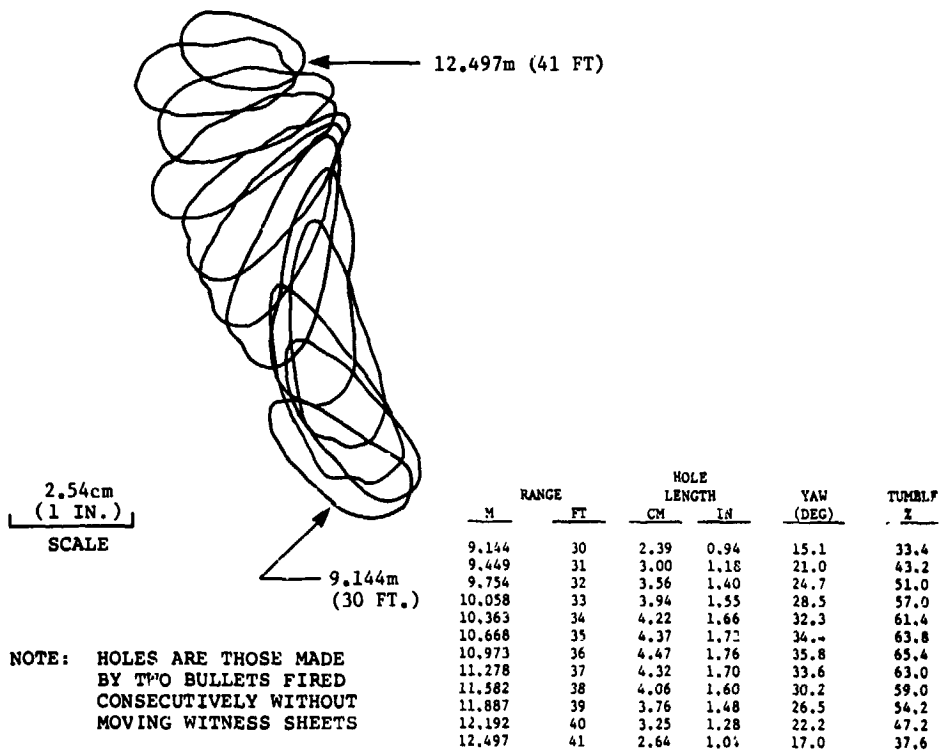
### 4.3 High Frame Rate Motion Picture Data

The impact, pressure expansion, buffering action, and cavitation actions are illustrated in Figures 30 and 31 for the Type C and D panel two-foot shotline tests, respectively. The motion pictures of the tests show:

a. That the incendiary was well initiated by the time the projectile penetrated the rubberized cloth protecting the front panel or the baseline bare panel.

b. That the projectiles were all well tumbled (traveling almost sideways) when passing between the two forward Kistler piezoelectric pressure transducers.

c. That the front panel buffering material compressed, then expanded as the hydrodynamic pressure first reached, then reflected from that panel. (The neoprene-coated fabric probably tore on this reflection.)

152

TABLE 2. IMPACT AND TEST PANEL DAMAGE SUMMARY

| Panel Type | Shot | Wetted Shotline cm | in | Tumble (Percent) | Yaw (Degree) | Impact Velocity m/sec | fps | Damage to Panel Front | Lower | Rear | Damage Index Panel | Type |
|---|---|---|---|---|---|---|---|---|---|---|---|---|
| B.L. | 1 | 61 | 24 | 65 | 35½ | 1043 | 3422 | Severe | Nil | Major | 3.33 | 3.33 |
| A | 5 | 53 | 21 | 56 | 27 | 1034 | 3394 | Minor | Nil | Major | 2.33 | |
|  | 12 | 53 | 21 | 65 | 35 | - | - | Minor | Nil | Major | 2.33 | 2.56 |
|  | 13 | 53 | 21 | 64 | 34 | - | - | Major | Nil | Major | 3.00 | |
| B | 4 | 46 | 18 | 50 | 23 | - | - | Minor | Nil | Severe | 2.67 | |
|  | 8 | 46 | 18 | 62 | 33 | 1028 | 3372 | Minor | Nil | Major | 2.33 | 2.44 |
|  | 11 | 46 | 16 | 50 | 23 | - | - | Minor | Nil | Major | 2.33 | |
| C | 2 | 46 | 18 | 65 | 35 | 1043 | 3425 | Nil | Nil | Moderate | 1.67 | |
|  | 6 | 46 | 18 | 63 | 63 | - | - | Minor | Nil | Major | 2.33 | 2.11 |
|  | 9 | 46 | 18 | 63 | 33 | 1042 | 3418 | Minor | Minor | Moderate | 2.33 | |
| D | 3 | 46 | 18 | 63 | 34 | 1026 | 3367 | Nil | Nil | Major | 2.00 | |
|  | 7 | 46 | 18 | 56 | 28 | 1023 | 3357 | Minor | Nil | Severe | 2.67 | 2.22 |
|  | 10 | 46 | 18 | 48 | 22 | - | - | Minor | Nil | Moderate | 2.00 | |
| B.L. | 26 | 30 | 12 | 48 | 22½ | 1030 | 3380 | Major | N/A | Destroyed | 5.00 | 5.00 |
| A | 17 | 23 | 9 | 52 | 24½ | 1024 | 3359 | Minor | N/A | Destroyed | 4.00 | |
|  | 21 | 23 | 9 | 51 | 23½ | 1027 | 3369 | Minor | N/A | Destroyed | 4.00 | 4.00 |
|  | 25 | 23 | 9 | 45 | 20½ | 1029 | 3376 | Minor | N/A | Destroyed | 4.00 | |
| B | 16 | 15 | 6 | 53 | 25 | 1017 | 3338 | Nil | N/A | Severe | 3.00 | |
|  | 20 | 15 | 6 | 53 | 25½ | 997 | 3271 | Nil | N/A | Severe | 3.00 | 3.17 |
|  | 24 | 15 | 6 | 59 | 23 | 1026 | 3365 | Nil | N/A | Major | 3.50 | |
| C | 14 | 15 | 6 | 53 | 2 | 1050 | 3446 | Nil | N/A | Severe | 3.00 | |
|  | 18 | 15 | 6 | 52 | 24½ | 1041 | 3416 | Nil | N/A | Severe | 3.00 | 3.17 |
|  | 22 | 15 | 6 | 44 | 20 | 1038 | 3407 | Nil | N/A | Destroyed | 3.50 | |
| D | 15 | 15 | 6 | 51 | 29 | 1023 | 3357 | Major* | N/A | Destroyed | 5.00 | |
|  | 19 | 15 | 6 | 49 | 23 | 1024 | 3358 | Nil | N/A | Destroyed | 3.50 | 3.83 |
|  | 23 | 15 | 6 | 45 | 20½ | 1027 | 3369 | Nil | N/A | Severe | 3.00 | |

*Excessive damage due to impact on a stiffener

Mean 1030 3378.3
Standard Dev. 12 38.45

153

FRONT REAR BOTTOM

a. EXTERIOR FACES

FRONT REAR BOTTOM

b. INTERIOR FACES
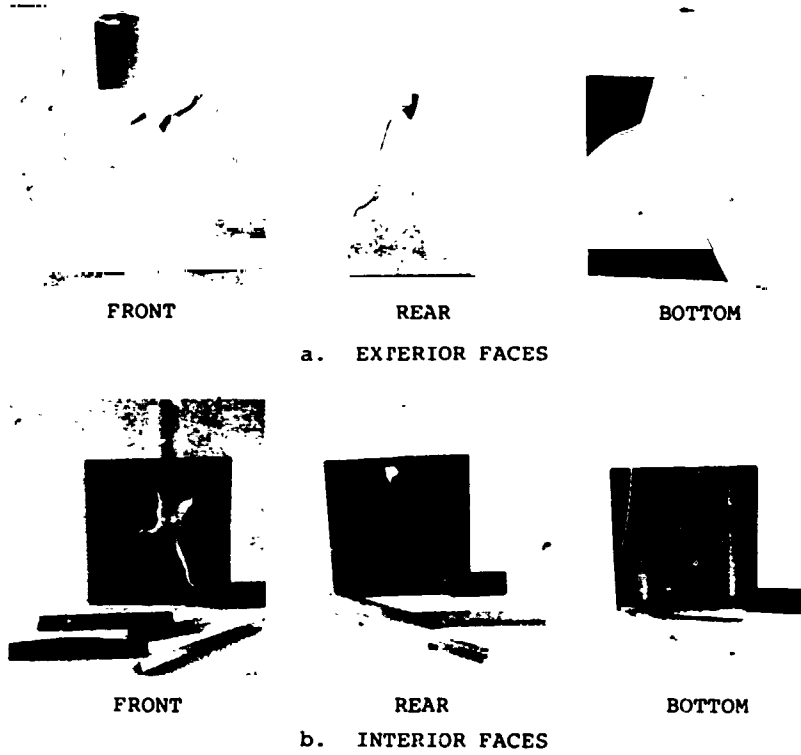
FIGURE 9. SHOT NO. 1, BASELINE PANELS, 2-FOOT SHOTLINE

a. EXTERIOR FACES

b. INTERIOR FACES
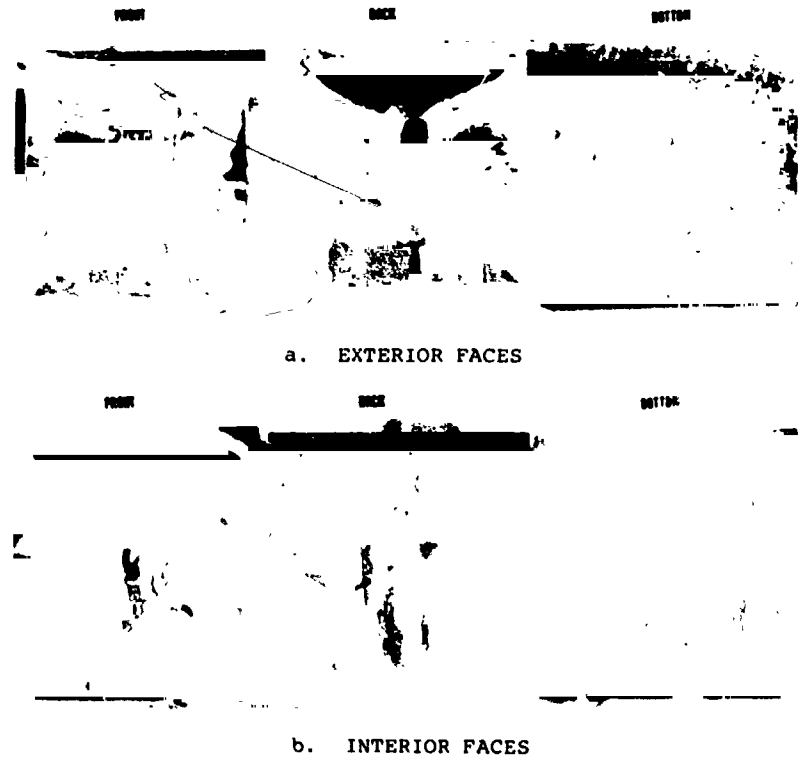
FIGURE 10. SHOT NO. 5, TYPE A PANELS, 2-FOOT SHOTLINE

154
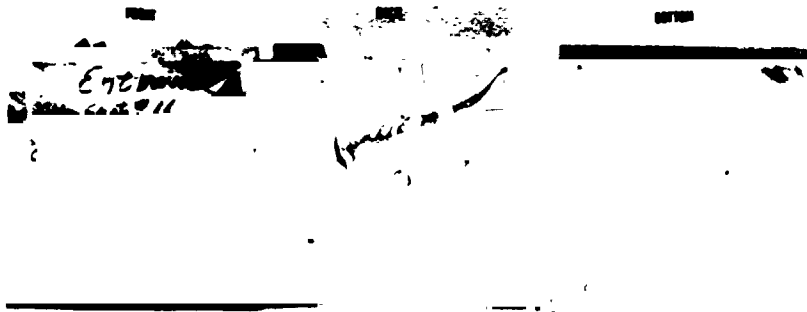
FIGURE 11.   SHOT NO. 11, TYPE B PANELS, 2-FOOT SHOTLINE
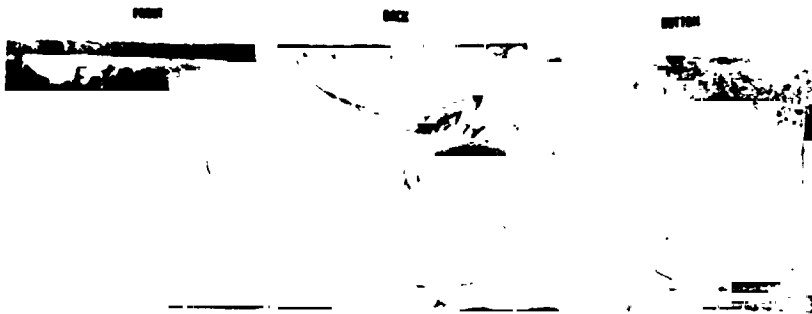


FIGURE 12.   SHOT NO. 9, TYPE C PANELS, 2-FOOT SHOTLINE



FIGURE 13.   SHOT NO. 7, . .C D PANELS, 2-FOOT SHOTLINE

155

FRONT PANEL                                    REAR PANEL

FIGURE 14.   SHOT NO. 26, BASELINE PANELS, 1-FOOT SHOTLINE



FRONT PANEL                                    REAR PANEL

FIGURE 15.   SHOT NO. 21, TYPE A PANELS, 1-FOOT SHOTLINE

FRONT PANEL                                    REAR PANEL

FIGURE 16.  SHOT NO. 24, TYPE B PANELS, 1-FOOT SHOTLINE
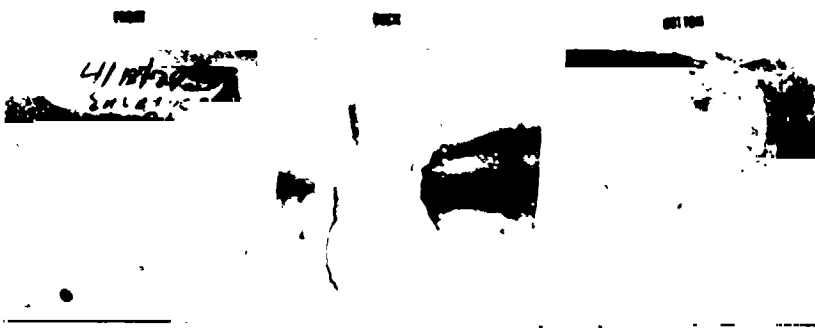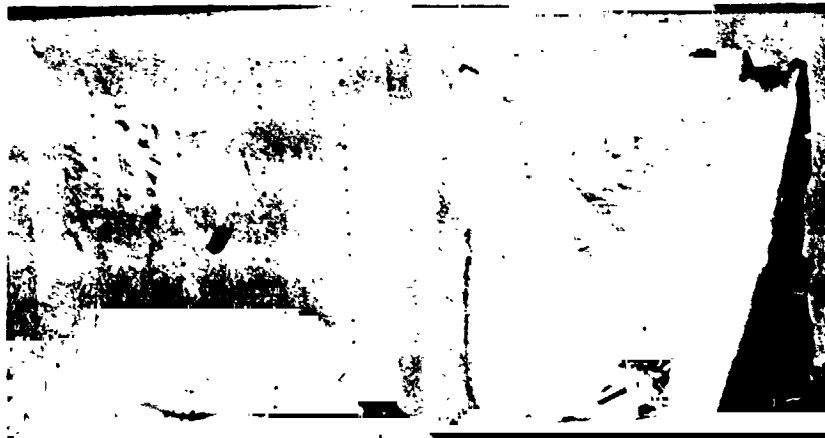


FRONT PANEL                                    REAR PANEL

FIGURE 17.  SHOT NO. 22, TYPE C PANELS, 1-FOOT SHOTLINE

FRONT PANEL                                    REAR PANEL

a.   EXTERIOR FACES



FRONT PANEL                                    REAR PANEL

b.   INTERIOR FACES

FIGURE 18.   SHOT NO. 19, TYPE D PANELS, 1-FOOT SHOTLINE

TABLE 3.  IMPACT ACCURACY, TRACER AND INCENDIARY FUNCTION DATA

| Panel Type | Shot | Distance of Impact Point From Desired cm (in.) Horizontal cm | in | Vertical cm | in | Tracer Found | Ignited | Quenched | Incendiary Jacket Tip Ignited | Found | Quenched | Remarks |
|---|---|---|---|---|---|---|---|---|---|---|---|---|
| Aluminum Sheet | Check-out | 0 | 0 | 0 | 0 | Y | Y | Y | Y | Y | Y | |
| B.L. | 1 | 0 | 0 | 0 | 0 | N | | | Y | Y | Y | Two Tracer cups found from 2 ft. shotline tests. Both were ignited and quenched. |
| A | 5 | .279 | 0.11 | -3.175 | -1.25 | N | | | Y | Y | Y | |
| | 12 | 2.438 | -0.96 | -2.108 | -0.83 | N | | | Y | Y | Y | |
| | 13 | 3.023 | -1.19 | 1.016 | 0.40 | Y | Y | Y | Y | Y | Y | |
| B | 4 | 2.159 | 0.85 | .864 | 0.34 | Y | Y | N | Y | N | - | |
| | 8 | 1.194 | -0.47 | .025 | 0.01 | N | | | Y | Y | Y | |
| | 11 | 1.829 | -0.72 | .305 | 0.12 | N | | | Y | Y | Y | |
| C | 2 | 2.286 | -0.90 | 5.080 | 2.00 | N | | | Y | Y | Y | |
| | 6 | 1.397 | -0.55 | -1.422 | -0.56 | N | | | Y | Y | Y | |
| | 9 | .762 | -0.30 | -3.226 | -1.27 | N | | | Y | Y | Y | |
| D | 3 | .686 | 0.27 | -2.540 | -1.00 | Y | Y | Y | Y | Y | Y | |
| | 7 | -.965 | -0.38 | -2.489 | -0.98 | N | | | Y | Y | Y | |
| | 10 | -2.184 | -0.86 | 1.804 | 0.71 | N | | | Y | Y | Y | |
| B.L. | 26 | -3.048 | -1.20 | 1.016 | 0.40 | N | | | ? | N | - | Two tracer cups were found from the 1 foot shotline tests. Both were ignited; one had been quenched, but the other had not been. |
| A | 17 | -2.692 | -1.06 | 1.270 | 0.50 | Y | Y | Y | Y | Y | Y | |
| | 21 | -2.134 | -0.84 | 1.143 | 0.45 | Y | Y | N | Y | Y | Y | |
| | 25 | -4.369 | -1.72 | -.660 | -0.26 | N | | | Y | Y | Y | |
| B | 16 | -3.505 | -1.38 | -4.064 | -1.60 | Y | Y | Y | Y | Y | Y | |
| | 20 | -3.556 | -1.40 | 0 | 0 | Y | Y | N | Y | Y | Y | |
| | 24 | -3.353 | -1.32 | -3.785 | -1.49 | N | | | ? | N | - | |
| C | 14 | -2.743 | -1.08 | -3.302 | -1.30 | N | | | Y | Y | Y | |
| | 18 | -3.099 | -1.22 | 1.219 | 0.48 | N | | | Y | Y | Y | |
| | 22 | -.864 | -0.34 | -1.067 | -0.42 | N | | | ? | N | - | |
| D | 15 | -2.134 | -0.84 | -2.998 | -1.18 | N | | | ? | N | - | |
| | 19 | -.203 | -0.08 | -1.016 | -0.40 | Y | Y | N | ? | N | - | |
| | 23 | -4.572 | -1.80 | -5.080 | -2.00 | Y | Y | N | Y | Y | Y | |
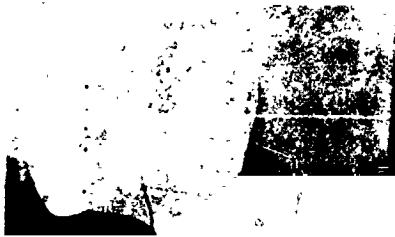
a. FRONT PANEL      b. REAR PANEL IN FIXTURE

FIGURE 19. SHOT NO. 15, TYPE D PANELS, 1-FOOT SHOTLINE

5. EVALUATION OF TEST RESULTS

5.1 Damage to Panels

The damage to all bottom panels in the two-foot shotline tests was quite minor (Table 2 and Figures 9 through 13). Damage to the rear panel was always greater than that to the front panel. This damage pattern indicates that:

1. The hydrodynamic ram energy is directed primarily along the projectile trajectory and secondarily to the rear; only a minor amount is directed perpendicular to the trajectory (see also Figures 30 and 31).

2. The relatively minor damage to the lower panel in the two-foot baseline test can be explained by the burst diaphragm action of the rear and front panels which quickly relieved any hydrodynamic pressure.

3. The Type A panels did not prove to have sufficient buffering. Compare the results of these tests with those of the Type C panels which had twice the buffering material thickness.

4. There was little difference in the damage suffered by the Type B and Type D panels.

5. There was slightly less damage suffered by the Type C panels than the Types B and D. This indicates that the flexible foam has a slight advantage over the rigid foam in absorbing the hydrodynamic ram energy with this type structure.

6. The results of all the one-foot shotline tests indicate that on the shorter shotlines the hydrodynamic ram energy has less distance in which to expand, hence is more concentrated when encountering the rear panel, and that once the rear panel failed, the pressures on the front panel were much less.

5.2 Energy-Absorbing Materials

The energy-absorbing materials deserve a more complete description. The two buffering materials used in this test program are:

1. Scott, flexible, reticulated polyurethane foam

160
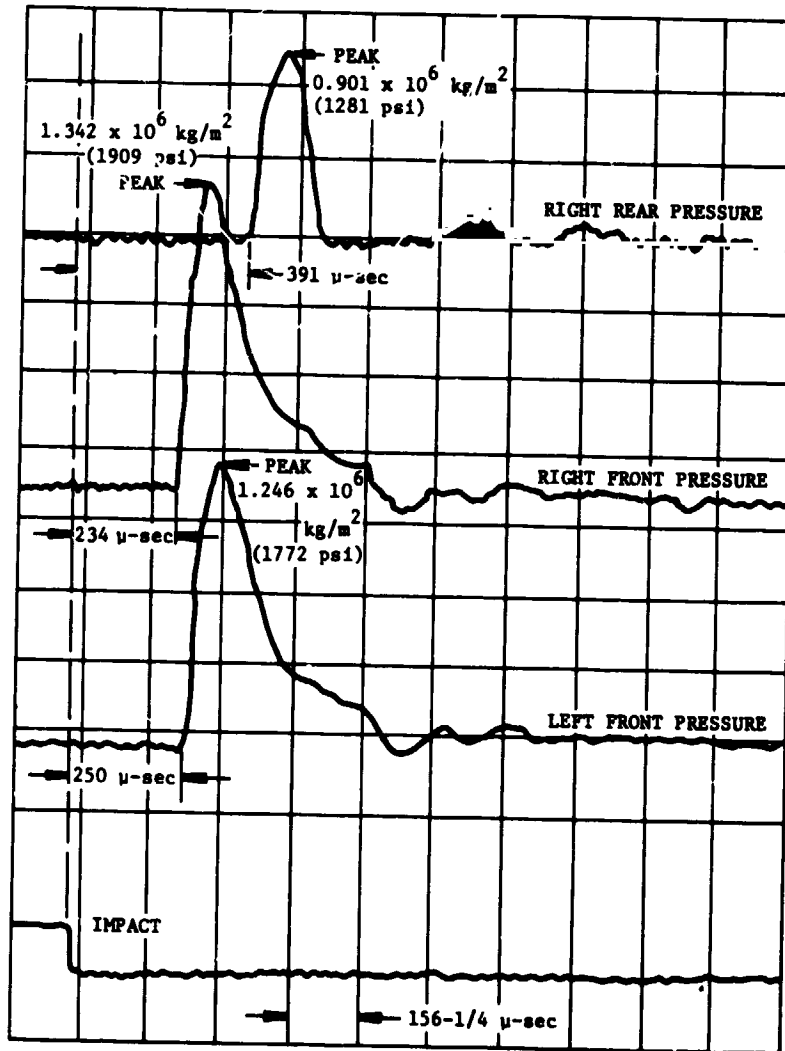
FIGURE 20.   PRESSURE VERSUS TIME, SHOT NO. 2, TYPE C PANELS
2-FOOT SHOTLINE

161

TABLE 4. PRESSURE VERSUS TIME DATA SUMMARY

| Configuration | Test Specimen Shotline Distance | Test | Figure | Peak Pressures Transducer | | | | | |
| | | | | KG/M² x 10⁻⁶ | | | PSI | | |
| | | | | No. 1 | No. 2 | No. 3 | No. 1 | No. 2 | No. 3 |
| Baseline | 2 feet | 1 | 21 | 1.623 | 0.958 | 0.873 | 2308 | 1363 | 1242 |
| A | 2 feet | 12 | 22 | 1.566 | 1.678 | 0.853 | 2227 | 2386 | 1213 |
| B | 2 feet | 11 | 23 | 1.374 | 2.093 | 1.398 | 1954 | 2977 | 1989 |
| C | 2 feet | 2 | 20 | 1.246 | 1.342 | 0.901 | 1772 | 1909 | 1281 |
| D | 2 feet | 10 | 24 | 0.911 | 1.566 | 1.279 | 1295 | 2227 | 1819 |
| Baseline | 1 foot | 26 | 25 | 1.810 | 1.808 | -- | 2575 | 1536 | -- |
| A | 1 foot | 17 | 26 | 2.024 | 1.095 | -- | 2878 | 1558 | -- |
| B | 1 foot | 24 | 27 | 1.719 | 0.715 | -- | 2445 | 1.17 | -- |
| C | 1 foot | 18 | 28 | 1.735 | 0.654 | -- | 2467 | 930 | -- |
| D | 1 foot | 19 | 29 | 1.643 | 0.319 | -- | 2337 | 454 | -- |
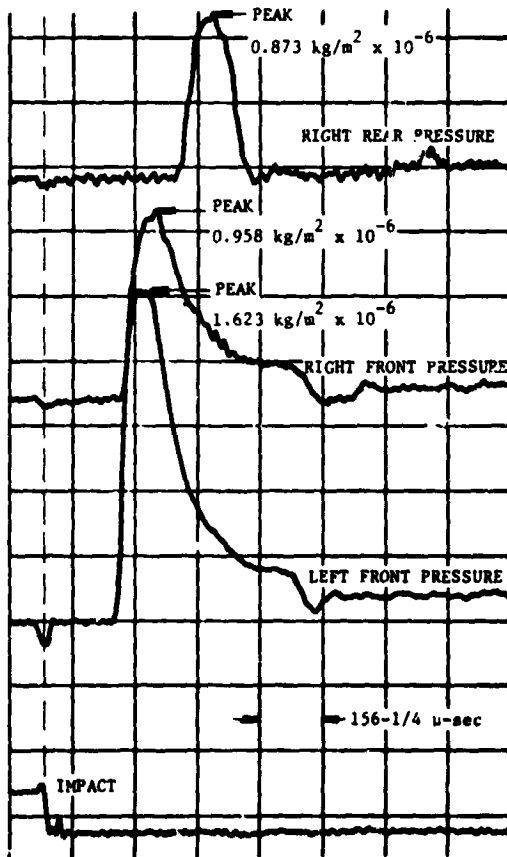


FIGURE 21. PRESSURE VS TIME, SHOT NO. 1 BASELINE CONFIGURATION, 2-FOOT SHOTLINE
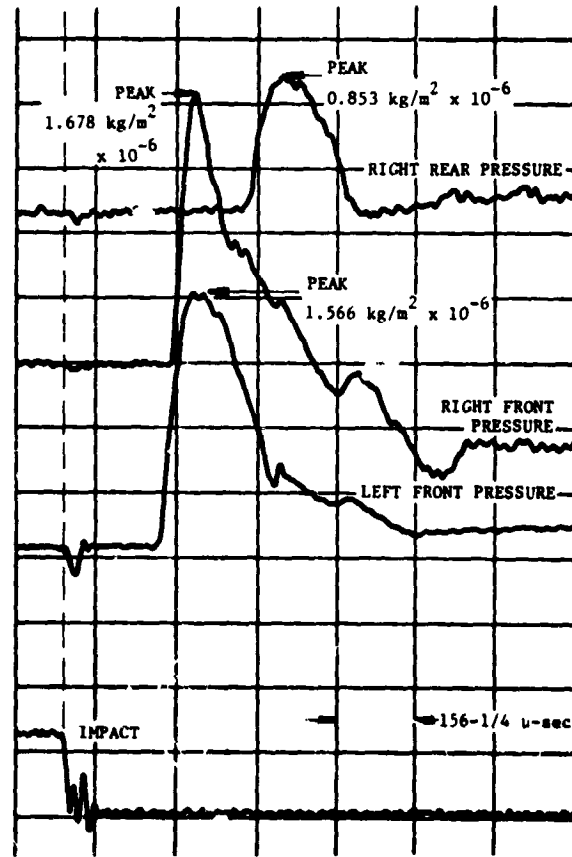
FIGURE 22. PRESSURE VS TIME, SHOT NO. 12, TYPE A PANELS, 2-FOOT SHOTLINE
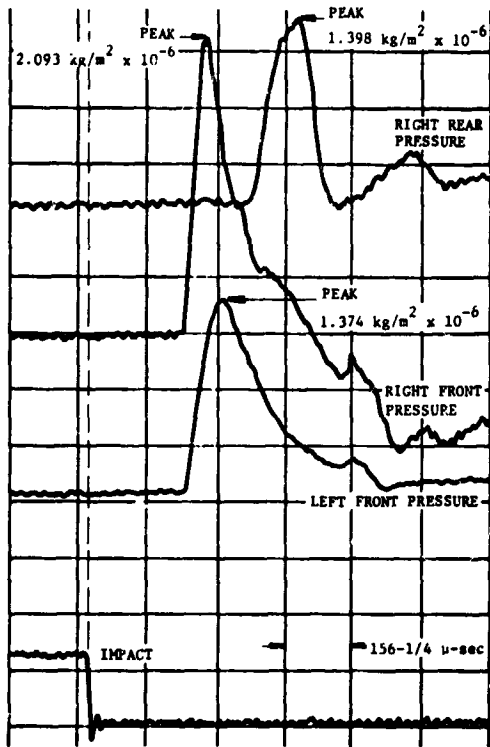
FIGURE 23. PRESSURE VS TIME, SHOT NO. 11, PANELS TYPE B, 2-FOOT SHOTLINE
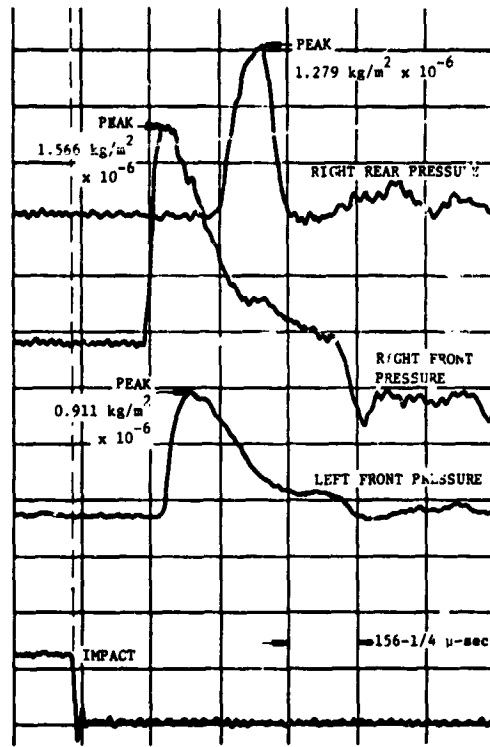


FIGURE 24. PRESSURE VS TIME, SHOT NO. 10, PANELS TYPE D, 2-FOOT SHOTLINE
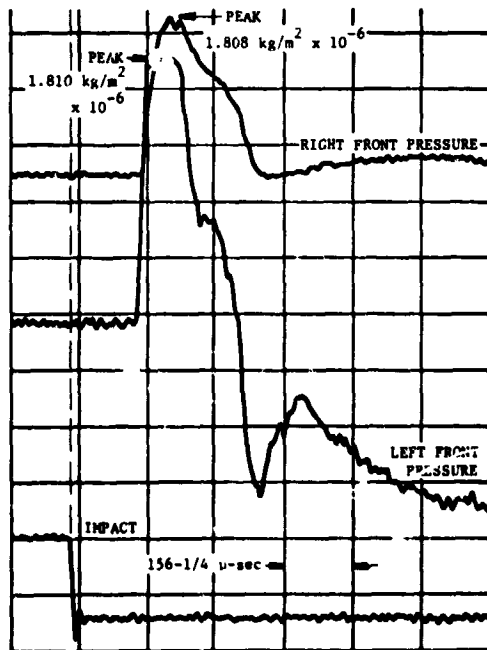


FIGURE 25. PRESSURE VS TIME, SHOT NO. 26, BASELINE CONFIGURATION, 1-FOOT SHOTLINE
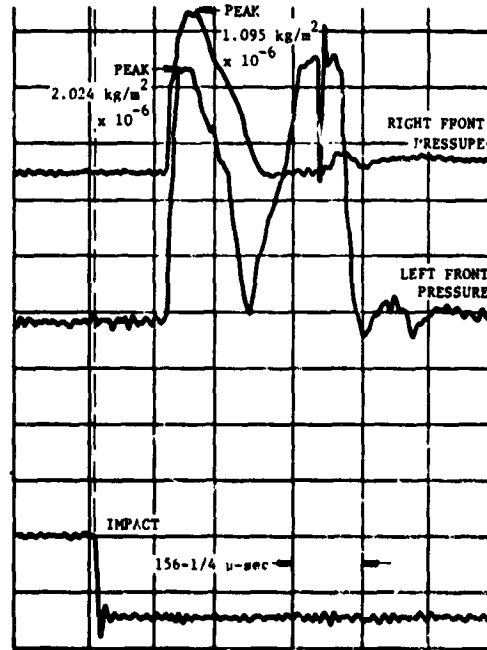


FIGURE 26. PRESSURE VS TIME, SHOT NO. 17, TYPE A PANELS, 1-FOOT SHOTLINE

163
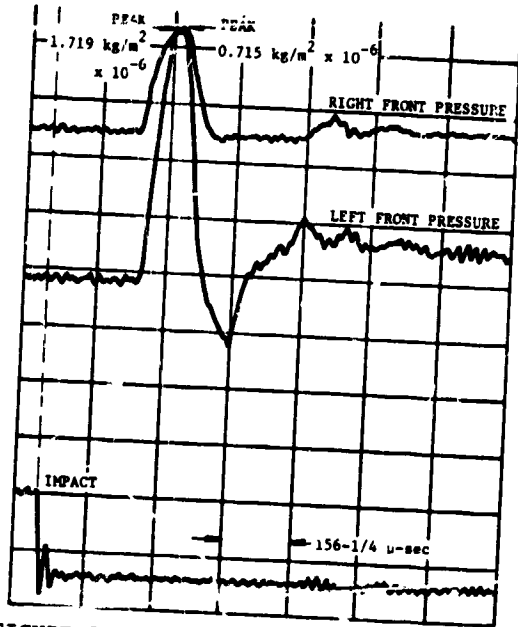
FIGURE 27. PRESSURE VS TIME, SHOT NO. 24, TYPE B PANELS, 1-FOOT SHOTLINE
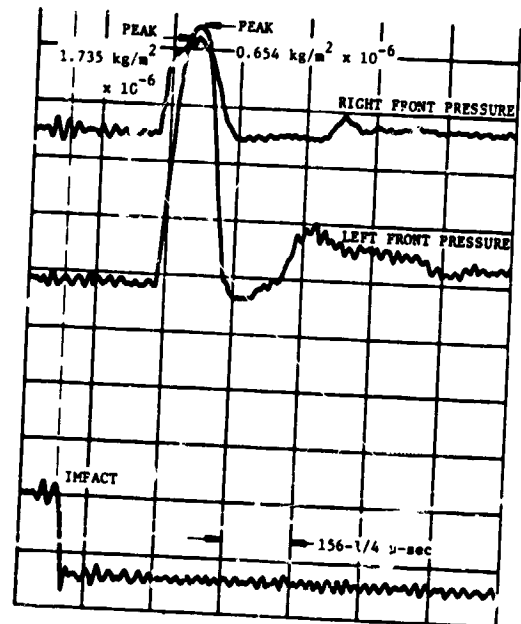


FIGURE 28. PRESSURE VS TIME, SHOT NO. 18, TYPE C PANELS, 1-FOOT SHOTLINE
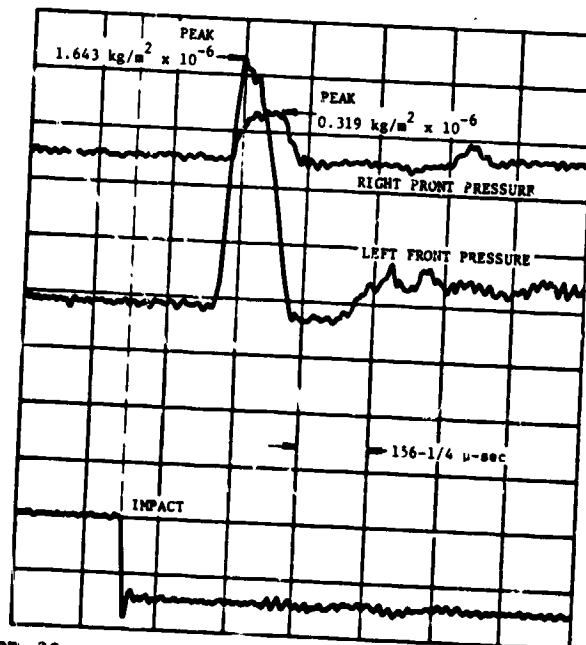


FIGURE 29. PRESSURE VS TIME, SHOT NO. 19, TYPE D PANELS, 1-FOOT SHOTLINE

164

FR. 1-0 MSEC  FR. 9-1.85 MSEC  FR. 43-9.69 MSEC

FR. 2-0.23 MSEC  FR. 14-3.00 MSEC  FR. 63-14.31 MSEC

FR. 3-0.46 MSEC  FR. 19.  FR. 100-22.85 MSEC

FR. 4-0.69 MSEC  FR. 25-5.54 MSEC  FR. 137-21.39 MSEC
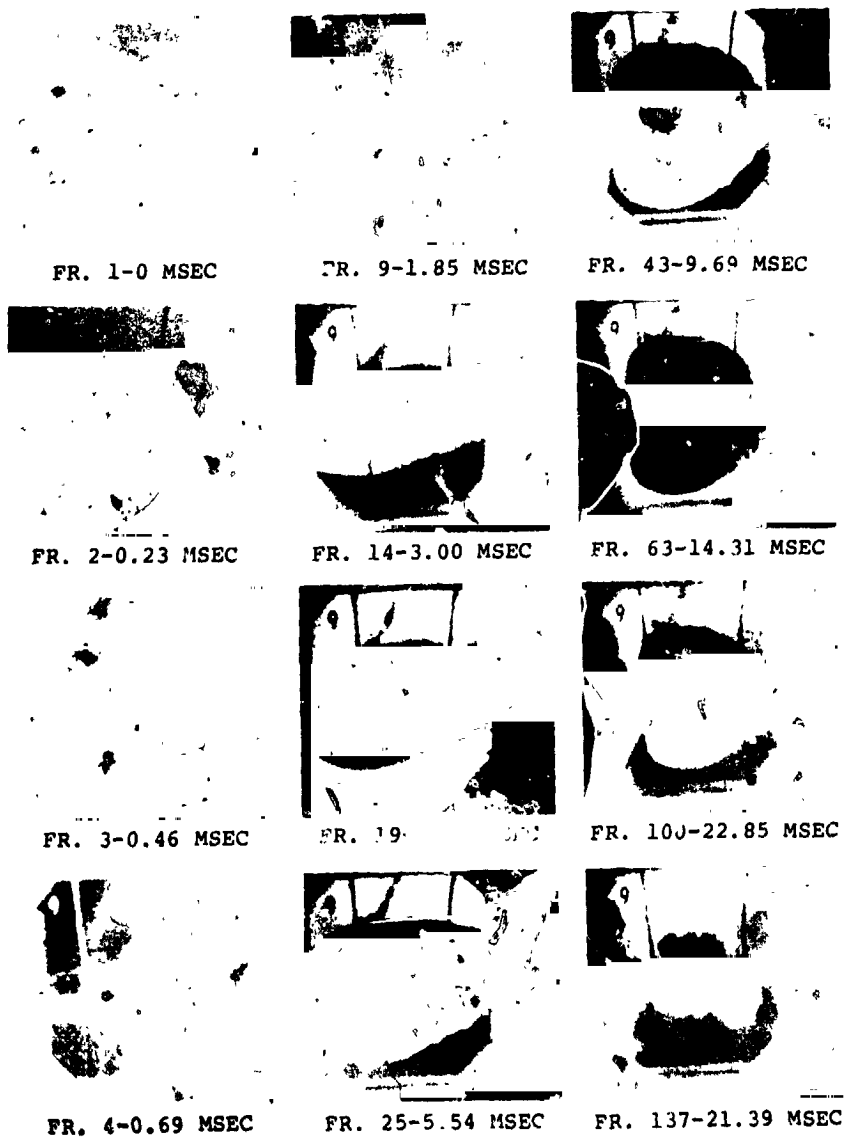
FIGURE 30.  SHOT NO. 9, TYPE C PANELS (3-IN. FLEXIBLE FOAM)
(TIME IN MILLISECONDS), FRAME RATE 4333 FT/SEC

FR. 2-0 MSEC     FR. 29-4.03 MSEC     FR. 63-0.19 MSEC

FR. 4-0.30 MSEC     FR. 36-5.07 MSEC     FR. 100-14.6? MSEC

FR. 6-0.60 MSEC     FR. 43-6.12 MSEC     FR. .37-20.15 MSEC

FR. 17-22.4 MSEC     FR. 53-213 MSEC     FR. 191-28.21 MSEC

FIGURE 31.    SHOT NO. 7, TYPE D PANELS (3-IN. RIGID FOAM)
(TIME IN MILLISECONDS), FRAME RATE 6700 FT/SEC

## 2. AVCO Thermarest AX 5052 rigid foam

The Scott flexible, reticulated polyurethane foam had a porosity of 14.57 pp cm (37 ppi). The most pertinent property, compression deflection versus pressure, is shown in Figure 32. The data shown thereon were derived by having an Instron tester move a platen at a constant rate of displacement of 5.08 cm per minute (2 in. per minute) toward a stationary platen compressing a 5.08 cm x 5.08 cm x 2.54 cm (2 in. x 2 in. x 1 in.) sample between. The test machine plotted the force required to maintain the rate of displacement versus the displacement. The foam compresses with very little outward bulging until it becomes a solid mass, presumably short of the 97% void space, hence 97% compression, advertised. This material has the unusual property of "stress-relieving" when the rate of application of the load stops even though the load remains. This is illustrated in Figure 32. The load was applied at a constant rate of displacement from points a through c. Note that there is an abrupt inflection in the curve at point b in which further displacement results in a lesser force on the platen. When 25% deflection was achieved (point c), the platen was stopped and remained at that deflection for one minute. During this minute, the resistance of the foam to platen displacement actually decreased from 1.043 kg (2.3 lb) to 0.771 kg (1.7 lb). The foam was in effect stress-relieving. The foam had reached an effective equilibrium at point d. Further dwell there would not have resulted in a further lessening of the force required to maintain the set displacement. After the one minute elapsed, the tester was restarted at the same rate of displacement with the result shown from point d to point g. Note that the first inflection point, e, is at what probably would have been the original curve had there been no pause at point c. At point f, approximately 42% compression deflection, the curve again inflects beginning another section in which force increases with displacement. When the tester reached the deflection at point g, further displacement was stopped with the same effective stress-relieving action as occurred between points c and d. The compression deflection data normally published is that for points d (25%) and h (65%). This curve show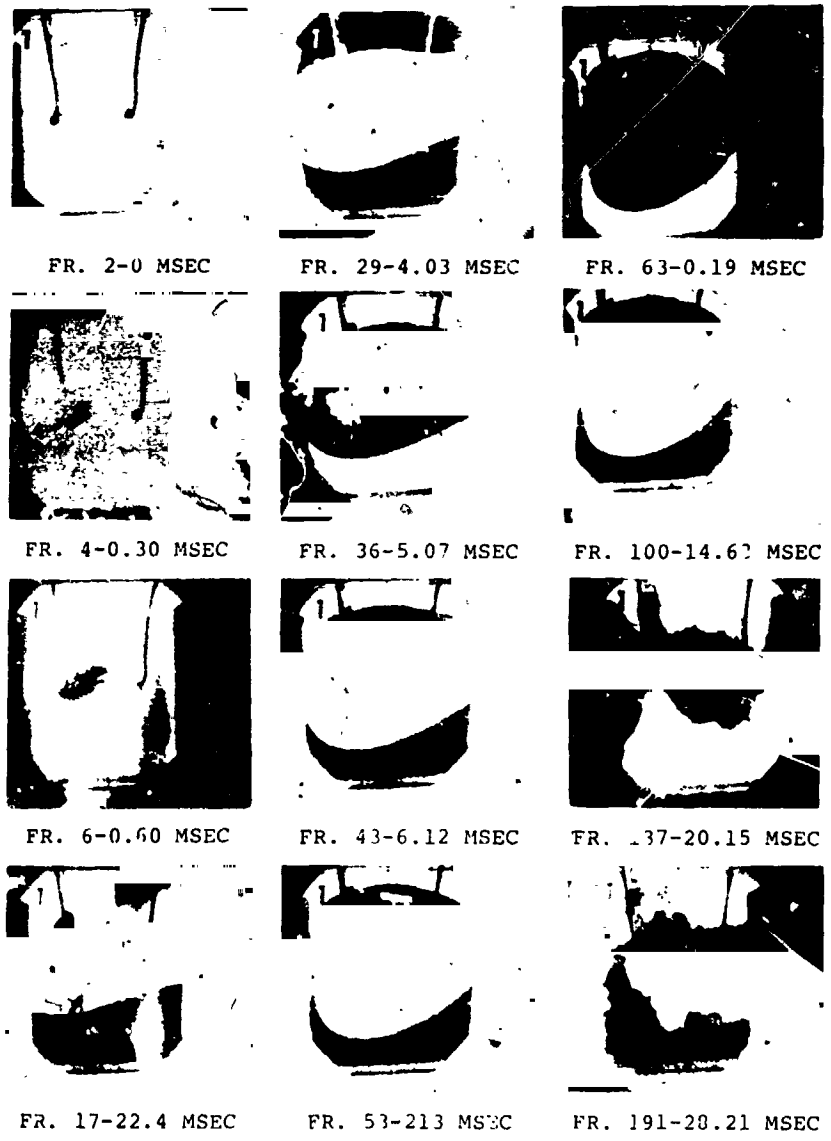s that even at the very slow rate of displacement, the foam can absorb much more energy than would a material which does not possess the effective stress

relief characteristic. This characteristic is very important in the installation of a fuel cell where any external energy-absorbing layer of material would very probably be partially precompressed. Additional data at higher crosshead speeds were essentially the same.

Similar compression, deflection data for the AVCO rigid foam, Figure 33, show that surprisingly little pressure is necessary to compress this material the first 10%. After the first 10%, very little additional pressure will result in a total of 60 to 70% deflection. These data were obtained in the same type of tests, using the same size of sample as those of the reticulated foam. A series of tests was performed by AVCO using samples 1, 2, 3, 4, and 5 inches thick and with the force applied in two relations to the direction of foam rise. The foam used in the buffering tests was compressed by the hydrodynamic ram pressures parallel to the direction of foam rise.

One piece of rigid foam from one of the tests exhibited little compression set. This indicates that the stress experienced by the foam was probably within the initial linear deflection region below 5%. The foam did not exhibit the crush which would be characteristic over 75% deflection.

The AVCO rigid foam does represent an increase in energy absorption capability of approximately one and a half orders of magnitude over the Scott flexible foam.

## 6. SUMMARY AND CONCLUSION

### 6.1 Summary

This paper covers a program in which hydrodynamic ram buffering concepts were tested. These buffering concepts, as well as other concepts, were utilized to demonstrate successful survival of a fuel cell impacted by a 23 mm HEI-T projectile in a later program described in Reference 6.

This was a test program in which a Z-reinforced skin panel was tested bare and with four variations of flexible foam and/or rigid foam buffering. These panels were assembled into a 91.44 cm x 91.44 cm (3-ft x 3-ft) fixture with shotline lengths of 60.96 cm (2 ft) or 30.48 cm (1 ft). Thirteen tests were made at each shotline length in which Soviet 14.5 mm API-T projectiles impacted one test panel while yawing severely at the normal-propellant

PRESSURE - KG/M² (PSI)

562 (0.8)

492 (0.7)

422 (0.6)

352 (0.5)

281 (0.4)

0.3

0.2

70 (0.1)

0 (0)

0    10    20    30    40    50    60    70

DEFLECTION - (PERCENT OF ORIGINAL THICKNESS)

COMPRESSION TEST OF 2" X 2" X 1" SAMPLE
COMPRESSION IN 1 IN. DIRECTION
INSTRON CROSSHEAD SPEED:   2 IN./MIN
RESULTS OF SIMILAR TESTS

| CROSSHEAD SPEED (IN. MIN) | PRESSURE IN PSI AT POINTS | | | |
|---|---|---|---|---|
| | c | d | g | h |
| 2 | 0.575 | 0.425 | 0.788 | 0.598 |
| 10 | 0.550 | 0.350 | 0.813 | 0.525 |
| 20 | 0.575 | 0.343 | 0.935 | 0.598 |

Data courtesy of Scott Paper Company,
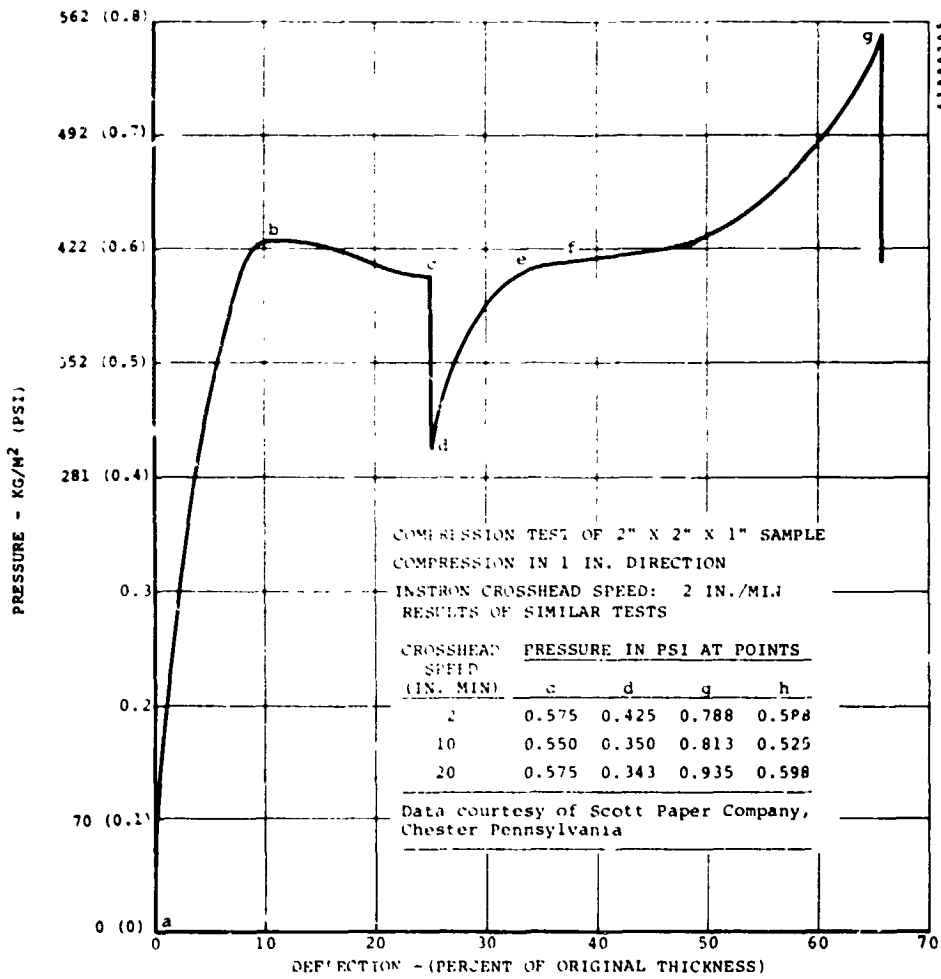Chester Pennsylvania

FIGURE 32.   COMPRESSION DEFLECTION VERSUS PRESSURE,
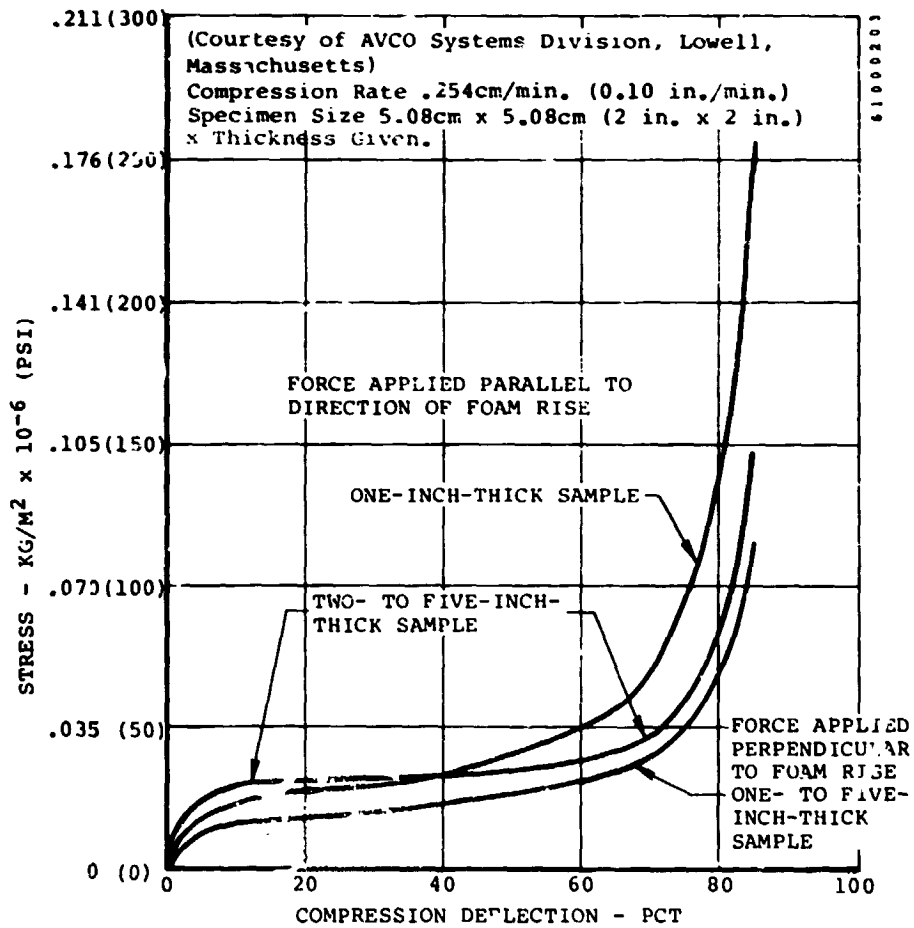SCOTT RETICULATED FOAM, 13.78 PPCM
(35 PPI)

168

FIGURE 33. COMPRESSION DEFLECTION VS STRESS, AVCO
THERMAREST AX5052-2.5 RIGID REINFORCED
POLYURETHANE FOAM

load, near-muzzle velocity. The projectiles achieved an energetic incendiary activation, released energy to the water within the fixture, and their penetrators generally exited through a second panel on the rear of the fixture. For the two-foot shotline tests, there was a third test panel on the bottom of the fixture, high frame rate motion pictures were taken through the transparent sides of the fixture, and three piezoelectric pressure transducer recordings were made. For the one-foot shotline tests, there was no third panel nor high frame rate motion pictures, but two pressures were recorded. After each test the panels were removed from the fixture, and the damage evaluated.

The evaluation of the damage indicates that the flexible foam provided a slightly better buffering than did rigid foam for the particular structure involved which had relatively rigid stiffeners. The tests also demonstrated that for very short shotlines there was extremely severe damage to the rear panels; much more damage than found with a mere 30.48 cm (12-in) increase in the wetted shotline length

## 6.2 Conclusions

These conclusions are based upon both this program and the one described in Reference 6. These conclusions are:

a. Buffering must be adapted to the structure - the rigid foam did not serve the more rigid Z-stiffeners of this test program as well as it did the less rigid ones of the program of Reference 6. In that second program, the rigid foam and the stiffeners appeared to distort together, supplementing one another. In more rigid shoring situations, the stiffer energy-absorbing material seemed to perform better. This is not to be interpreted, however, that a rigid structure will withstand hydrodynamic ram as witness severe distortions in heavy steel structures in this program and rupture of honeycomb structure in the second.

b. The size of the fuel cell is important - the hydrodynamic ram energy is exerted on the surfaces of the cell as a pressure. The magnitude of this pres-

sure is inversely proportional to the cube of the distance from the place of liberation of the energy (both kinetic and chemical) to the place the pressure is exerted. The fuel cell resisted this pressure by hoop-like tension. Where the liberation to exertion distance was short, the cell fabric failed in tension in a region closest to the center of liberation.

c. The overall fuel tank protective concepts given have been proven in practice even though many specific details remain to be defined.

## REFERENCES

1. Patrick H. Zabel, "Containment of Hydrodynamic Ram from 23 mm HEI-T Impact in a Fuel Cell," 15 Oct 1976, Cleared for open publication, Directorate for Freedom of Information and Security Review (OASD-PA), Department of Defense, 6 June 1977, Unclassified.

2. Robert J Bristow, "Design of Hydraulic Ram Resistance Structure," The Boeing Company, AMMRC MS 73-2, Proceedings of the Army Symposium on Solid Mechanics, 1972 - The Role of Mechanics in Design - The Ballistic Problems, Sept. 1973, Unclassified.

3. Charles M Pedriani, "Ballistic Investigation of Various Self-Sealing Fuel Cell Installation Concepts," Eustis Directorate, U. S. Army Air Mobility R & D Laboratories, USAAMRDL-TM-4, April 1974, Unclassified.

4. Andre J. Holten, "Ax Fuel Tank Vulnerability Evaluation Report," Air Force Flight Dynamics Laboratory, AFFDL-TR-74-55, July 1974, Unclassified.

5. Richard J. Dewitt and Patrick H. Zabel, "Tests of Hydraulic Ram Buffering Materials," Ultrasystems Dynamic Science Report 1560-74-43, for Naval Weapons Center, Sponsored by JTCG/AS, May 1974, Unclassified.

6. Patrick H. Zabel, "Reduction of Army Helicopter Fuel Tank Vulnerability to 23 mm HEI-T Projectiles," USAAMRDL TR-75-32, August 1975, Unclassified.

N80 16210

# PREDICTION OF FRAGMENT VELOCITIES AND TRAJECTORIES

J. J. Kulesz, L. M. Vargas & P. K. Moseley
Southwest Research Institute
San Antonio, Texas

This paper describes analytical techniques to predict
(1) the velocities of two unequal fragments from bursting
cylindrical pressure vessels, (2) the velocity and range of
portions of vessels containing a fluid which, when the ves-
sel ruptures, causes the fragment to accelerate as the fluid
changes from the liquid to the gaseous phase, and (3) the
ranges of fragments subjected to drag and lift forces during
flight.

To predict the velocity of two unequal fragments from
bursting cylindrical pressure vessels, the energy of the
confined gas is partitioned between the kinetic energy of
the fragment, the energy of the gas escaping through the
cracks between the fragments as they are formed, and the
energy of the expansion of the internal gas.  The amount of
energy expended to burst the containment vessel is con-
sidered small compared to the total amount of energy avail-
able.  Using similitude theory, the results are plotted in
nondimensional terms and consolidate numerically-generated
velocity data for two unequal fragments from bursting cylin-
crical vessels containing five different gases.  Using a
similar computational technique, plots are also included
for spherical and cylindrical pressure vessels containing
the same five gases which burst into two or more equal
fragments.

In many accidents involving propane storage vessels,
large fragments from the vessel have been known to exhibit
a rocketing behavior.  A technique is described which exa-
mines the changes in state of the fluid from a liquid to a
gas and subsequent exit of the gas out of the open end of
the fragmented vessel.  The thrust acting on the large
fragment is determined and fragment ra  es are calculated.
The outputs of computer runs are compa _d with actual post
accident results and, in most cases, are in good agreement.

Finally, the paper discusses a technique for deter-
mining the range of fragments once one knows the initial
flight conditions.  Combined drag and lift forces, plus
gravity forces, are assumed to act on the fragment during
flight.  Numerous computer runs were made with various ini-
tial conditions in an effort to generalize the results
for maximum range in plots of dimensionless range versus
dimensionless velocity for constant values of dimensionless
lift to drag ratios.

## I. INTRODUCTION

Under certain accident conditions, vessels containing compressed,gases or liquid fuels can rupture. Fragments from these bursting pressure vessels often acquire large velocities and can travel great distances resulting in considerable damage. A large fragment from a vessel containing a liquid fuel which vaporizes after fracture can be propelled like a rocket, and fire damage from burning fuel emitted along its trajectory as well as severe impact damage can occur. This paper describes techniques for determining the velocities of fragments from bursting gas pressure vessels, the ranges of rocketing fragments, and the ranges of fragments which do not exhibit rocketing behavior.

## II. PRESSURE VESSELS

### A. Fragment Velocities

The method developed by Taylor and Price (1971) and modified by Baker, et al (1975), Bessey (1974), and Bessey and Kulesz (1975) for calculating velocities of fragments from bursting spherical and cylindrical gas reservoirs was further adapted (Baker, et al 1978) to provide velocity calculations for unequal fragments from cylindrical gas vessels with hemispherical endcaps (Figure 1). To compute the velocity of fragments from bursting cylinders which contain gas under pressure, the following assumptions were made:

(1) The vessel with gas under pressure breaks into two unequal fragments along a plane perpendicular to the cylindrical axis, and the two container fragments are driven in opposite directions.

(2) Gas within the vessel obeys the ideal gas law.

(3) Originally contained gas escapes from the vessel through the opening between the fragments into a surrounding vacuum. The escaping gas travels perpendicular to the direction of motion of the fragments with local sonic velocity.

(4) Energy necessary to break the vessel walls is negligible compared to the total energy of the system.

(5) Drag and lift forces are ignored since the distance the fragment travels before it attains its maximum velocity is too short for these forces to have a significant effect.

A schematic depicting the essential characteristics of the modified solution for bursting cylinders is shown in Figure 2. Before accelerating into an exterior vacuum, the cylinder has internal volume $V_{oo}$ and contains a perfect gas of adiabatic exponent (ratio of specific heats) $\gamma$ and gas constant $R$ with initial pressure $P_{oo}$ and temperature $T_{oo}$ (Figure 2a). At a time $\tau = 0$, rupture occurs along a perimeter $\Pi$, and the two fragments are propelled in opposite directions due to forces applied against the area $F$ which is perpendicular to the axis of motion of the fragments (Figure 2b). The masses of the fragments, $M_1$ and $M_2$, are considered large relative to the mass of the remaining gas at elevated pressure (Figure 2c).

The equations of motion and initial conditions of the two fragments are:
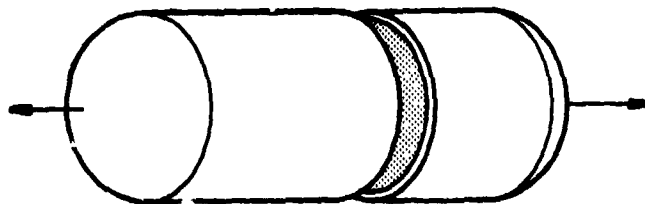


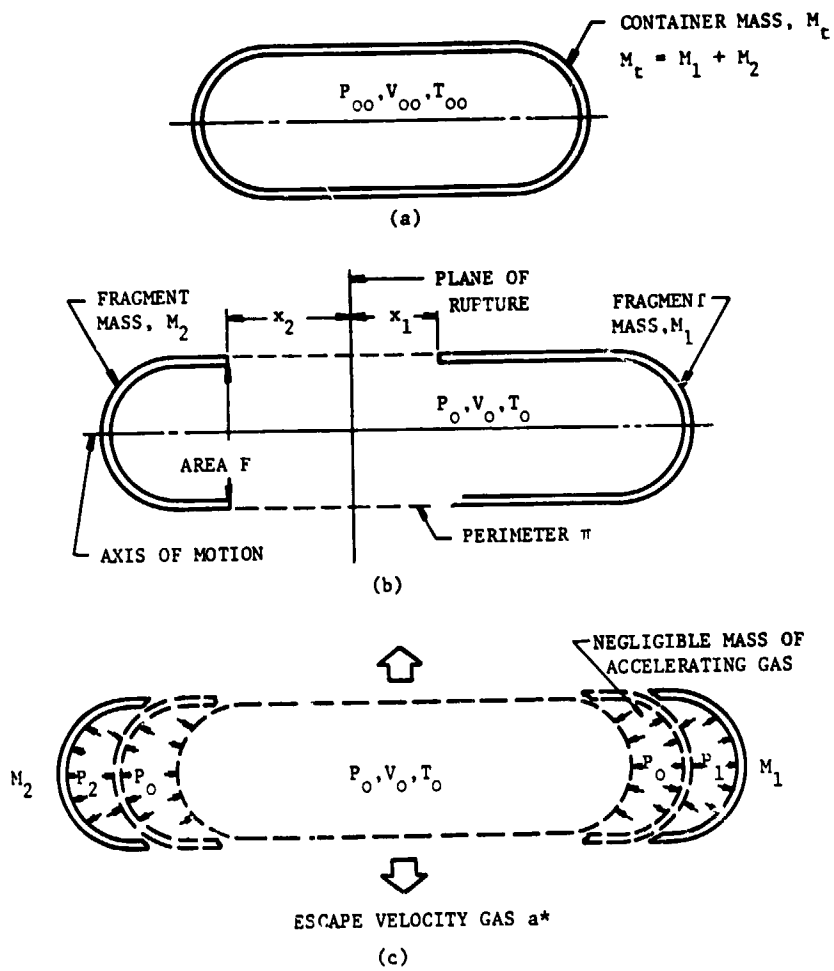FIGURE 1. ASSUMED BREAKUP INTO TWO UNEQUAL FRAGMENTS

FIGURE 2.   PARAMETERS FOR CYLINDER BURSTING INTO
TWO UNEQUAL PARTS

$$M_1 \frac{d^2 x_1(\tau)}{d\tau^2} = FP_1(\tau), \text{ with } x_1(0) = 0, \frac{dx_1(0)}{d\tau} = 0 \qquad (1)$$

$$M_2 \frac{d^2 x_2(\tau)}{d\tau^2} = FP_2(\tau), \text{ with } x_2(0) = 0, \frac{dx_2(0)}{d\tau} = 0 \qquad (2)$$

where subscripts refer to each fragment and $x$ is a displacement distance taken along the axis of motion. To allow for cylindrical containment vessels, the cross-sectional area F over which the force is applied becomes

$$F = \pi (r-C_t)^2 \qquad (3)$$

where $C_t$ is the thickness of the cylinder.

The equation of state for the un-accelerated gas remaining within the confinement of the container fragments is

$$P_o(\tau) V_o(\tau) = C(\tau) RT_o(\tau) \qquad (4)$$

where subscript "o" denotes reservoir conditions immediately after failure, R is the gas constant, P is pressure, V is volume, T is temperature and $C(\tau)$ is the mass of gas confined at high pressure as a function of time. The rate of change of the confined mass is

$$\frac{dC(\tau)}{d(\tau)} = k \Pi x \rho_* a_* \qquad (5)$$

where $x = x_1 + x_2$, $\qquad (6)$

k is the coefficient of discharge in the area between the fragments, and $\rho_*$ is the gas density at critical gas velocity $a_*$. The expression for perimeter $\Pi$ is

$$\Pi = 2\pi r \qquad (7)$$

Gas density $\rho_*$ and $a_*$ are standard expressions

$$\rho_* = \rho_o(\tau) \left( \frac{2}{\gamma + 1} \right)^{1/(\gamma-1)}$$

$$a_* = a_o(\tau) \left( \frac{2}{\gamma + 1} \right)^{1/2} \qquad (8)$$

where $\gamma$ is the adiabatic exponent (ratio of specific heats) for an ideal gas. The volume is assumed to be variable and can be described by

$$V_o(\tau) = V_{oo} + Fx \qquad (9)$$

Nearly all of the gas is assumed to be accelerated with the fragments, with gas immediately adjacent to the fragments being accelerated to the velocity of the fragments. From simple one-dimensional flow relationships,

$$P_1(\tau) = P_o(\tau) \left( 1 - \left\{ \frac{\gamma - 1}{2[a_o(\tau)]^2} \right\} \left[ \frac{dx_1(\tau)}{d\tau} \right]^2 \right)^{\gamma/(\gamma-1)}$$

$$P_2(\tau) = P_o(\tau) \left( 1 - \left\{ \frac{\gamma - 1}{2[a_o(\tau)]^2} \right\} \left[ \frac{dx_2(\tau)}{d\tau} \right]^2 \right)^{\gamma/(\gamma-1)} \qquad (10)$$

To generalize the solution, one can use the following nondimensional forms of the variables:

Dimension: $y(\tau) = Xg(\zeta)$, $x_1(\tau) = Xg_1(\zeta)$,

$\qquad\qquad x_2(\tau) = Xg_2(\zeta)$

Time: $\tau = \theta \zeta$ $\qquad (11)$

Pressure: $P_o(\tau) = P_{oo}P_*(\tau)$

The relationships between the derivatives are

174

$$\frac{dx_1(\tau)}{d(\tau)} = \frac{X}{\theta} g_1'(\zeta), \quad \frac{dx_2(\tau)}{d\tau} = \frac{X}{\theta} g_2'(\zeta)$$

$$\frac{d^2 x_1(\tau)}{d\tau^2} = \frac{X}{\theta^2} g_1''(\zeta),$$

$$\frac{d^2 x_2(\tau)}{d\tau^2} = \frac{X}{\theta^2} g_2''(\zeta) \tag{12}$$

$$\frac{dP_o(\tau)}{d\tau^2} = \frac{P_{oo}}{\theta} P_*'$$

Initial conditions are:

$$x_1(0) = x_2(0) = \frac{dx_1(0)}{d\tau} = \frac{dx_2(0)}{d\tau} =$$

$$g_1(0) = g_2(0) = g_1'(0) = g_2'(0) = 0 \tag{13}$$

and $P_*(0) = 1$

where primes denote differentiation with respect to $\tau$. The pair of characteristic values for dimension X and time $\theta$ chosen by Taylor and Price are:

$$X = \frac{M_t a_{oo}^2}{F P_{co}} \left(\frac{2}{\gamma - 1}\right)$$

$$\theta = \frac{M_t a_{oo}}{F P_{oo}} \left(\frac{2}{\gamma - 1}\right)^{1/2} \tag{14}$$

The final derived equations contain two dimensionless groups which define the nature of the solutions, these are

$$\alpha = \frac{P_{oo} V_{oo}}{M_t a_{oo}^2}$$

$$\beta = k \left(\frac{2}{\gamma + 1}\right)^{\frac{\gamma+1}{2(\gamma-1)}}$$

$$\left(\frac{2}{\gamma - 1}\right)^{1/2} \frac{\Pi V_{oo}}{F^2} \tag{15}$$

Differences between the Taylor and Price solution for spheres and our solution for cylinders, with spherical caps being a special case of cylinder, occur in the determination of area given by Equation (3) and perimeter given in Equation (7) where $r$ is cylindrical radius instead of spherical radius. A difference also exists in the calculation of initial volume of the gas which, for the cylindrical case with spherical segment endcaps with one base, becomes

$$V_{oo} = \pi \left\{ \left(r - C_t\right)^2 C_\ell + \left(E_\ell - E_t\right) \right.$$

$$\left. \left[\left(r - E_t\right)^2 + \frac{\left(E_\ell - E_t\right)^2}{3}\right] \right\} \tag{16}$$

where $r$ is the cylindrical radius, $C_\ell$ is the length of the cylinder excluding the endcaps, $E_\ell$ is the endcap length, and $E_t$ is the endcap thickness.

For the adiabatic case,

$$\frac{P_o(\tau)}{P_{oo}} = \left[\frac{\rho_o(\tau)}{\rho_{oo}}\right]^\gamma = \left[\frac{T_o(\tau)}{T_{oo}}\right]^{\frac{\gamma}{\gamma-1}}$$

$$= \left[\frac{a_o(\tau)}{a_{oo}}\right]^{\frac{2\gamma}{\gamma-1}} \tag{17}$$

Substitution of Equations (10), (12) through (15), and (17) into Equations (1) and (2) gives

$$\frac{M_1}{M_t} g_1'' = P_* \left[1 - \left(\frac{g_1'^2}{P_*^{(\gamma-1)/\gamma}}\right)\right]^{\gamma/(\gamma-1)} \tag{18a}$$

175

by analogy,

$$\frac{M_2}{M_t} \, g_2^{\prime\prime} = P_* \left[ 1 - \left( \frac{g_2^{\prime 2}}{P_*^{(\gamma-1)/\gamma}} \right) \right]^{\gamma/(\gamma-1)} \quad (18b)$$

Differentiation of Equation (4) and substitution of Equations (5) through (9), (11) and (12) yields

$$\left[ \left( \frac{\gamma-1}{2} \right) \alpha + g \right] \frac{P_*^\prime}{P_*} = - \frac{\beta\gamma}{\alpha} \, gP_*^{(\gamma-1)/2\gamma} -\gamma g^\prime \quad (19)$$

In the solution for equal fragments, the fragment masses are equal, and the equations for the motion of the two fragments become identical. However, since the fragment masses in the new solution are unequal, the equations of motion become

$$g_1^{\prime\prime} = \frac{M_t}{M_1} \, P_* \left[ 1 - \left( \frac{g_1^{\prime 2}}{P_*^{(\gamma-1)/\gamma}} \right) \right]^{\gamma/(\gamma-1)} \quad (20)$$

$$g_2^{\prime\prime} = \frac{M_t}{M_2} \, P_* \left[ 1 - \left( \frac{g_2^{\prime 2}}{P_*^{(\gamma-1)/\gamma}} \right) \right]^{\gamma/(\gamma-1)}$$

Rearranging terms in Equation (19) produced

$$P_*^\prime = \frac{\frac{\beta\gamma}{\alpha}(g_1+g_2)P_*^{(3\gamma-1)/2\gamma} -\gamma(g_1^\prime+g_2^\prime)P_*}{\left[ \left( \frac{\gamma-1}{2} \right) \alpha + \left( g_1 + g_2 \right) \right]} \quad (21)$$

For initial conditions, $g_1(0) = 0$, $g_2(0) = 0$, $g_1^\prime(0) = 0$, $g_2^\prime(0) = 0$, and $P_*(0) = 1$, nondimensional values of distance, velocity, acceleration and pressure as a function of time can be calculated by solving Equations (20) and (21) simultaneously using the Runge-Kutta method of numerical iteration. Dimensional values can then be calculated from

$$\tau = \theta \, \zeta, \; x_1(\tau) = Xg_1(\zeta), \; x_2(\tau)$$

$$= Xg_2(\zeta), \; x_1^\prime(\tau) = \frac{X}{\theta} \, g_1^\prime(\zeta), \; x_2^\prime(\tau)$$

$$= \frac{X}{\theta} \, g_2^\prime(\tau), \; x_1^{\prime\prime}(\tau) = \frac{X}{\theta^2} \, g_1^{\prime\prime}(\zeta), \quad (22)$$

$$x_2^{\prime\prime}(\tau) = \frac{X}{\theta^2} \, g_2^{\prime\prime}(\zeta), \; P_o(\tau) = P_{oo}P_*(\zeta)$$

A computer program was written to solve the equations, and several computer runs were made for various initial conditions. Computer runs were also made for gas pressure vessels bursting into two or more equal fragments (Baker, et al, 1975 and Baker et al, 1978). When the computer program was run for cylinders bursting into two pieces and with large length-to-diameter ratios, it was found that the exit area, when the velocity stabilized, was greater than the combined cross-sectional open area of the two fragments. Thus, as the distance between fragments increased beyond a certain point (the radius of the cylinder, in this case), the computer program predicted larger losses in gas mass and pressure than possible. The final result was prediction of lower velocities than possible. To remedy the situation, the computer code was stopped when the exit area calculated in the program equaled the combined cross-sectional open area of the two fragments. Final velocity of each fragment was then determined by developing and exercising a computer code based on ideal gas law isentropic expansion through the open cross-section (exit area) of each fragment. Input to this "rocketing" computer code were the initial velocity from the computer code above, the state variables of the gas at the start of the calculations, the mass of the fragment, and geometrical aspects of the fragment. The results from all of the computer runs coalesced into convenient graphical form after performing the model analysis described below.

B.  Model Analysis

The model analysis was patterned after the techniques described by Baker, Westine, and Dodge (1972). The physical parameters which are indigenous to the problem are listed in Table 1 and include vessel characteristics, gas properties, and a response term. Since only spheres and cylinders with hemispherical endcaps and with an L/D ratio of 10.0 (includes the endcaps) are being considered, one needs to include the vessel's diameter d, thickness h, length $\ell$, volume V, mass $M_c$, the yield strength, $\sigma_y$ of the material of the vessel's walls, and the number of fragments n that the vessel breaks into. It is assumed that the vessel breaks into n equal fragments. Cylinders break into either two equal fragments along a plane perpendicular to the axis of symmetry or n equal strip fragments along the cylindrical wall (endcaps are ignored). The special case involving cylinders breaking into

176

TABLE 1

PERTINENT PARAMETERS FOR BURSTING SPHERICAL AND
CYLINDRICAL CONTAINMENT VESSELS

| SYMBOL | DESCRIPTION | DIMENSIONS* |
|---|---|---|
| d | diameter | L |
| h | thickness | L |
| $\ell$ | length | L |
| V | volume | $L^3$ |
| $M_c$ | mass of container | $FT^2/L$ |
| $\sigma_y$ | yield strength of material | $F/L^2$ |
| n | number of fragments | -- |
| $\gamma$ | ratio of specific heats | -- |
| $R_M$ | ideal gas constant (adjusted for molecular weight) | $L^2/T^2\theta$ |
| $a_o$ | speed of sound in gas | L/T |
| $P_o$ | burst pressure | $F/L^2$ |
| $T_o$ | initial temperature of gas | $\theta$ |
| E | energy of gas | FL |
| $P_a$ | atmospheric pressure | $F/L^2$ |
| u | velocity of fragments | L/T |

* L = length
  F = force
  T = time
  $\theta$ = temperature

two unequal fragments will be included at the end of the model analysis. The relevant gas parameters are the ratio of specific heats $\gamma$, the ideal gas constant $R_M$ which is adjusted for molecular weight, the speed of sound $a_o$ of the gas, the pressure $P_o$ of the gas at burst, the temperature $T_o$ of the contained gas at burst, the energy E of the gas, and atmospheric pressure $p_a$. The response term is the velocity u of the fragment.

There are 11 pi terms or nondimensional ratios which can be created from the above 15 parameters using Buckingham pi term theory as explained by Baker, Westine, and Dodge (1973). Table 2 presents one possible list of these 11 pi terms. This list of 11 pi terms can be reduced to a smaller number of pi terms by examining some interrelationships among variables. There are only two values for $\ell/d(\pi_2)$ being considered, spheres with an $\ell/d$ of 1.0 and

cylinders with hemispherical endcaps and an $\ell/d$ of 10.0. Since there are so few values of $\ell/d$, one might consider putting several curves on one graph. Pi terms $\pi_7$ and $\pi_8$ are directly related through the relationship

$$a_o = \sqrt{\gamma R_m T_o} \qquad (23)$$

For the sake of simplicity, pi term $\pi_8$ will be eliminated.

The thickness of the vessel is related to its diameter and the yield strength of the vessel material. Consider a sphere as shown in Figure 3a. For the simplest design where the design thickness is much smaller than the diameter of the vessel, the vessel will burst when the force exerted on the vessel walls by the internal pressure equals the force required to break the vessel. If one considers that the vessel (sphere) bursts in half, one has

177

TABLE 2

LIST OF Pi TERMS FOR BURSTING
CONTAINMENT VESSELS

| | | |
|---|---|---|
| $\pi_1$ | $\dfrac{h}{d}$ | proportional to $(P_o - P_a)\sigma_y$ |
| $\pi_2$ | $\dfrac{\ell}{d}$ | constant (equals 1.0 or 10.0) |
| $\pi_3$ | $\dfrac{V_o}{d^3}$ | |
| $\pi_4$ | $\dfrac{M_c a_o^2}{P_a d^3}$ | |
| $\pi_5$ | $\dfrac{\sigma_y}{P_a}$ | constant |
| $\pi_6$ | $\mu$ | |
| $\pi_7$ | $\gamma$ | $a_o = \sqrt{\gamma R_M T_o}$ (see $\pi_4$ and $\pi_{11}$) |
| $\pi_8$ | $\dfrac{R_M T_o}{a_o^2}$ | |
| $\pi_9$ | $\dfrac{P_o}{P_a}$ | |
| $\pi_{10}$ | $\dfrac{E}{P_a h d^2}$ | $E = \dfrac{(P_o - P_a)V_o}{(\gamma - 1)}$ (see $\pi_3$, $\pi_7$ and $\pi_9$) |
| $\pi_{11}$ | $\dfrac{u}{a_o}$ | |

$$(P_o - P_a)\,\frac{\pi d^2}{4} = \sigma_y \pi d h \qquad (24)$$

or

$$\frac{h}{d} = \frac{P_o - P_a}{4\sigma_y} \qquad (25)$$

$$(P_o - P_a)d\ell = \sigma_y 2 \ell h \qquad (26)$$

or

$$\frac{h}{d} = \frac{(P_o - P_a)}{2\sigma_y} \qquad (27)$$

The most likely plane of fracture of a cylinder made of a homogeneous material is along the longitudinal axis as shown in Figure 3b. For vessels whose thickness is much smaller than its diameter, the vessel will burst when the force exerted on the vessel walls by the internal pressure equals the force required to break the vessel. Thus,

Equations (25) and (26) indicate that $(h/d)$ is proportional to $(P_o - P_a)/\sigma_y$ and thus pi term $\pi_1$ can be eliminated. If one assumes that only one material with one yield strength will be used in constructing the vessel, then pi term $\pi_5$ can also be eliminated.
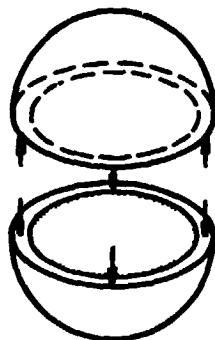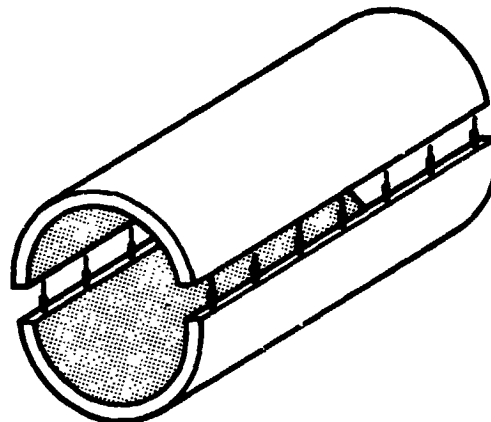
(a) Sphere                    (b) Cylinder

FIGURE 3. DETERMINATION OF VESSEL THICKNESS

Energy E in the gas is defined as

$$E = \frac{(P_o - P_a)V_o}{(\gamma - 1)} \qquad (28)$$

Pi term $\pi_9$ contains $P_o$ and $P_a$, $\pi_3$ contains $V_o$ and $\pi_7$ contains $\gamma$. Therefore, the energy of the gas is completely defined by these other pi terms and pi term $\pi_{10}$ can be eliminated.

Variables in $\pi_7$ and $\pi_8$ appear in $\pi_4$ and $\pi_{11}$. It seems logical that the problem has been overdefined and that $\pi_7$ and $\pi_8$ can be excluded from the analysis.

Since $\pi_3$, $\pi_4$ and $\pi_9$ have some terms in common, it is beneficial to combine them. Thus, one has

$$\pi_9' = \frac{(\pi_9)(\pi_3)}{(\pi_4)} = \frac{P_o V_o}{M_c \gamma R_m T_o} \qquad (29)$$

Substituting $(P_o - P_a)$ for $P_o$ in order to emphasize the importance of the differential in pressure between the inside and outside of the vessel walls, one obtains the abscissa of Figure 4. Plotting $\pi_{11}$ with Equation (23) substituted for $a_o$, versus the term in Equation (29) yields the desired result. Figure 4

consolidates the presentation of the analysis of allowing one to plot several curves for different L/D ratios and numbers of fragments n on one curve and still maintain accurate estimation of fragment velocity u. Several computer checks have shown that the curves presented in Figure 4 can be used for materials of different densities and yield strengths, provided that the thickness of the vessel is less than 1/3 of the diameter of the vessel. For cylinders bursting into three or more "strip" fragments as explained in Baker, Kulesz, et al (1975), the hemispherical endcaps were ignored. The dashed lines shown in Figure 4 demonstrate the variance in the results from the computer runs using many different input condition combinations.

Some cases were run for cylinders with hemispherical endcaps and an L/D ratio of 10.0 which burst into two unequal segments perpendicular to the cylindrical axis of symmetry. It seemed reasonable that the velocity of each fragment would be related to the velocity of the fragments from cylinders bursting in half by some constant k which depends on the unequal fragment's fraction of the total mass of the container. Figure 5 was plotted from an average of several computer runs for unequal fragments and the results show amazing consistency. Note that for equal fragments k equals 1.0. For unequal fragments from bursting cylinders (two fragments total), one must determine the fragment's fraction of the total mass and find k in Figure 5. The dashed lines in Figure 5 demonstrate

179

$$\frac{u}{k\sqrt{\gamma R_m T_o}}$$

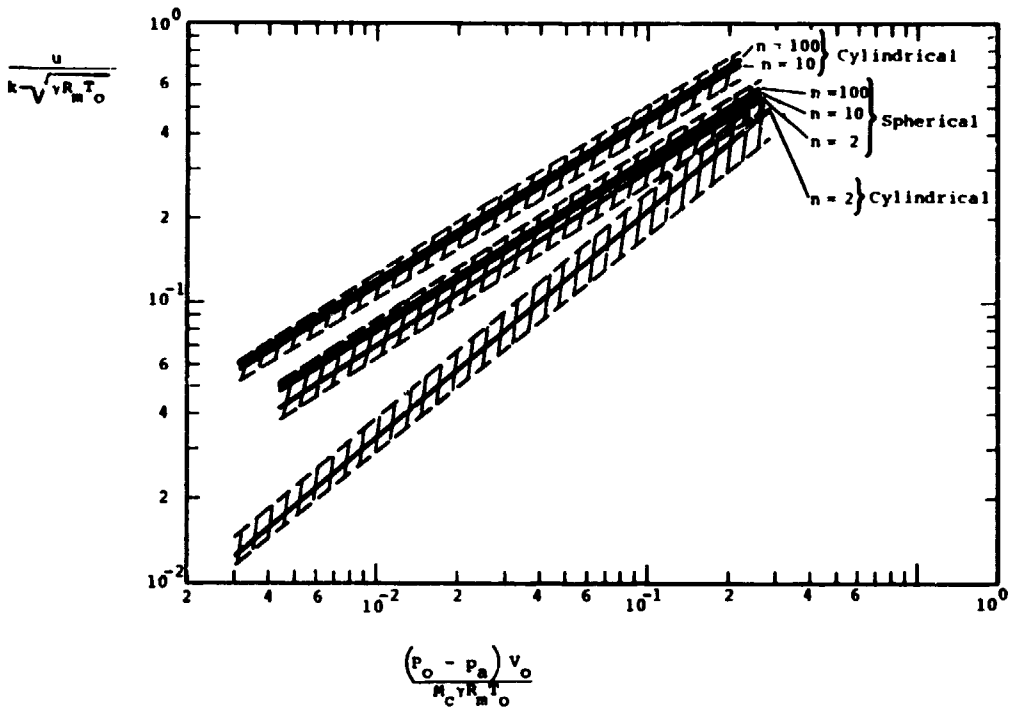$$\frac{\left(P_o - p_a\right) V_o}{M_c \gamma R_m T_o}$$

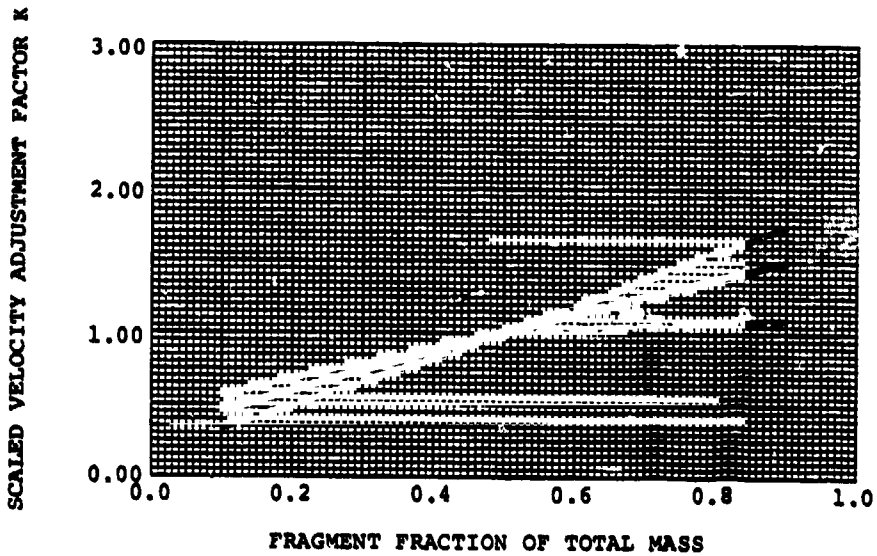FIGURE 4.    SCALED FRAGMENT VELOCITY VS SCALED PRESSURE



FIGURE 5.    ADJUSTMENT FACTOR FOR UNEQUAL MASS FRAGMENTS

the variance in the results from the computer runs using many different input condition combinations. Once k is known, Figure 4 can be used to calculate the velocity of the fragment. This figure can be used for hydrogen, air, argon, helium and carbon dioxide gases. The accuracy of predictions decreases when burst pressures are greater than 68.9 MPa (10,000 psi) because of phase changes in the gases.

## III. ROCKETING FRAGMENT

In an accident involving propellant (propane, butane, etc.) storage systems, fragments are often generated and propelled by the force of an explosion. The fragments generated in an explosion which travel large distances typically are of much smaller mass than that of the storage vessel. However, in some instances, a large portion or portions of the vessel (greater than one-fourth) will break free intact and will travel larger distances than would be possible solely from the force of the explosion. These large fragments exhibit a rocketing behavior which results from the changing of the liquid propellant into a gas when the external pressure is released during the fracturing of the vessel. The gas escapes from the opening in the vessel in a manner similar to gas exiting a rocket motor and propels the fragment to great distances.

Figure 6 schematically demonstrates the fragment rocketing process. After a portion of the vessel breaks off, the remaining portion of the tank emits gas out of its open end as the fluid in the tank vaporizes. This mass flows out of the aft end of the tank and produces a force F(t) in the direction opposite to the mass flow which varies as a function of time t, and the tank accelerates along a trajectory angle $\theta$ with respect to the horizontal axis (ground). The force of gravity Mg also acts on the vessel inhibiting its vertical ascent. Vertical and horizontal inertial forces $M\ddot{y}$ and $M\ddot{x}$, respectively, complete the simplified free-body diagram in Figure 6. Drag and lift forces are assumed to be much smaller than the thrust and gravitational forces and are ignored. It is also assumed that the "rocket" never changes its angle of attack $\theta$ during its flight.

The equations of motion for this simplified rocketing problem are then

$$M(t)g + M(t)\ddot{y} - F(t)\sin\theta = 0 \qquad (30)$$

and

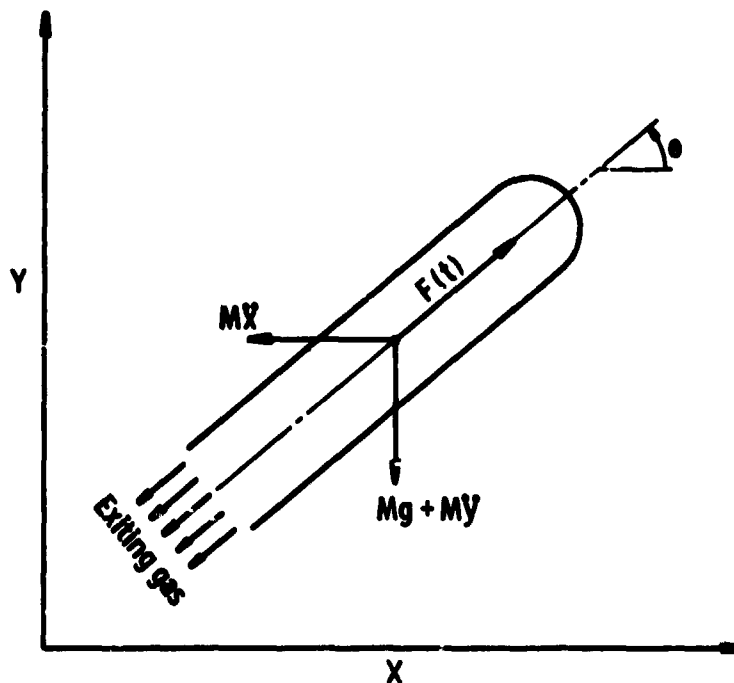$$M(t)\ddot{x} - F(t)\cos\theta = 0 \qquad (31)$$



FIGURE 6.  ROCKETING FRAGMENT

Note that the mass (mass of the fragment and its contents) as well as the force, changes with time. From basic rocketry, the thrust F is

$$F = A_e \left( \frac{U_e^2}{v_e g} + p_e - p_o \right) \tag{32}$$

where

$A_e$ = exit area

$U_e$ = exit velocity

$v_e$ = specific volume of the gas

$g$ = gravity constant

$p_e$ = exit pressure

$p_o$ = atmospheric pressure

Balancing the energy in the system, one has

$$h_i + q = h_e + \frac{U_e^2}{2g} \tag{33}$$

where

$h_i$ = enthalpy of the gas at time $t_i$

$q$ = energy expended in heating the gas

$h_e$ = enthalpy of the gas at the nozzle (exit)

If the gas expansion is isentropic, $q = 0$, and Equation (33) reduces to

$$\frac{U_e^2}{2g} = h_i - h_e \tag{34}$$

Flow continuity gives

$$\dot{w}v = AU \tag{35}$$

where $\dot{w}$ is the mass flow rate.

To determine the fragment's trajectory, one starts with a wet vapor in a tank having known initial state conditions of pressure $p_i$, specific volume $v_i$, entropy $s_i$, and enthalpy $h_i$ which can be determined from tables of thermodynamic properties. One next assumes isentropic expansion through the nozzle, that is

$$s_{i+1} = s_e = s_i \tag{36}$$

where $s_e$ is the entropy of the gas at the nozzle (exit) and $s_{i+1}$ is the entropy at time $t_{i+1}$.

When the backpressure $p_o$ is less than the critical pressure $p_c$ given by

$$p_c = 0.58\, p_i^* \tag{37}$$

the flow will be sonic and $p_e$ in Equation (32) equals $p_c$. When the backpressure $p_o$ is greater than the critical pressure $p_c$, then $p_e$ equals $p_o$ in Equation (32). Also, the pressure in the vessel at time $t_{i+1}$ is given by

$$p_{i+1} = p_e \tag{38}$$

Equations (36) and (38) allow one to obtain the value for $h_2$, the enthalpy at time $t_{i+1}$, from the table of thermodynamic properties once one knows the values of $s_e$ and $p_e$. Equation (34) gives $U_e$, and the thrust obtained by substitution into Equation (32). At the exit, Equation (35) gives

$$\dot{w}v_e = A_e U_e \tag{39}$$

where $v_e$ is also obtained from the thermodynamic tables. In reality, the state variables of the gas within the tank change continuously, but, for computational purposes, we will assume quasi-steady flow. From Equation (39), one can obtain the mass flow rate $\dot{w}$ and calculate a new total mass of the fluid after a small time $\Delta t$ from

---

* Equation (37) can be found in Smallwood and Potter (1946) p. 101. The coefficient 0.58 is an approximation and is equal to the critical gas flow constant for initially saturated steam. For a perfect gas, the coefficient is $\left( \frac{2}{\gamma+1} \right)^{\left( \frac{\gamma}{\gamma-1} \right)}$. For this to be 0.58, $\gamma$ would have to be 1.1.

$$M_{i+1} = M_i - \frac{\dot{w}}{g} \Delta t \qquad (40)$$

After this time, a new specific volume can be determined from

$$v_{i+1} = \frac{V}{g M_{i+1}} \qquad (41)$$

where V is the total volume of the fragment. Knowing $v_{i+1}$ one can then obtain $p_{i+1}$ from the table of thermodynamic properties of the gas and start a second iteration.

The above iteration process continues until backpressure $p_o$ is greater than the critical pressure in Equation (31). Then the flow becomes subsonic and Equation (32) reduces to

$$F = A_e \frac{U_e^2}{v_o g} \qquad (42)$$

Some thrusting will continue until the internal pressure $p_n$ equals $p_o$, and the state of the gas in the vessel after n iterations lies on the $p_o$ isobar.

To complete the process of calculating tank acceleration, velocity, and position one must solve Equations (30) and (31) during each iteration. The accelerations in the y and x directions are given by

$$\ddot{y}_i = \frac{F_i \sin\theta}{M_i} - g \qquad (43)$$

and

$$\ddot{x}_i = \frac{F_i \cos\theta}{M_i} \qquad (44)$$

Assuming the thrust $F_i$ and mass of the vessel and enclosed substance $M_i$ to be constant during the time step $\Delta t$, one can obtain velocity for time $t_{i+1}$ by integrating Equations (43) and (44) obtaining

$$\dot{y}_{i+1} = \Delta t \left( \frac{F_i \sin\theta}{M_i} - g \right) + \dot{y}_i \qquad (45)$$

and

$$\dot{x}_{i+1} = \Delta t \left( \frac{F_i \cos\theta}{M_i} \right) + \dot{x}_i \qquad (46)$$

where

$$\dot{y}(o) = \dot{x}(o) = 0$$

Integrating Equations (45) and (46), one can obtain displacement from

$$y_{i+1} = \frac{\Delta t^2}{2} \left( \frac{F_i \sin\theta}{M_i} - g \right) + \dot{y}_i \Delta t + y_i \qquad (47)$$

and

$$x_{i+1} = \frac{\Delta t^2}{2} \left( \frac{F_i \cos\theta}{M_i} \right) + \dot{x}_i \Delta t + x_i \qquad (48)$$

where $y(o) = x(o) = 0$

The thermodynamic processes followed by the expanding fluids are shown on the pressure-volume (p - v) plane and temperature entropy (T - s) plane in Figures 7 and 8, respectively.

A computer program was written to perform computations for determining acceleration, velocity, and position of a thrusting fragment as a function of time. The program was exercised using the state properties of propane gas to compare with measurements made after propane/butane accidents. The results of the computations shown in Table 3 are in good agreement with the accident statistics, especially when one takes the uncertainty of the initial conditions into account. Unfortunately, we were unable to find any further information for comparison.

## IV. RANGE

The analysis for calculating the range of a fragment once it has acquired an initial velocity is presented in detail in Baker, et al (1975). Allowing for the effect of drag and lift forces, one can calculate the
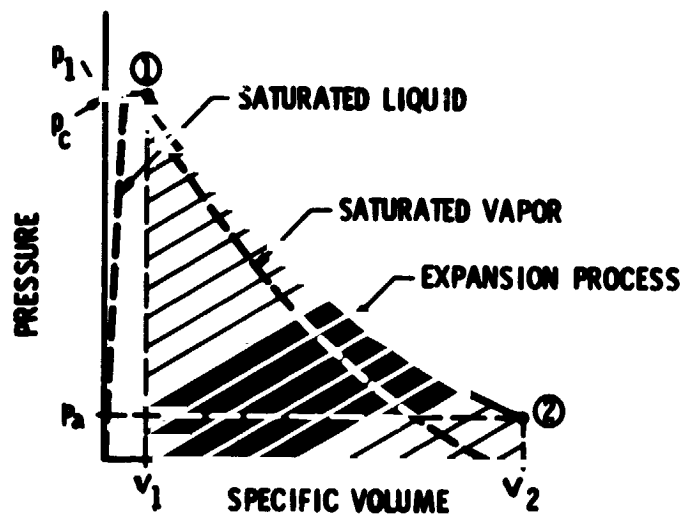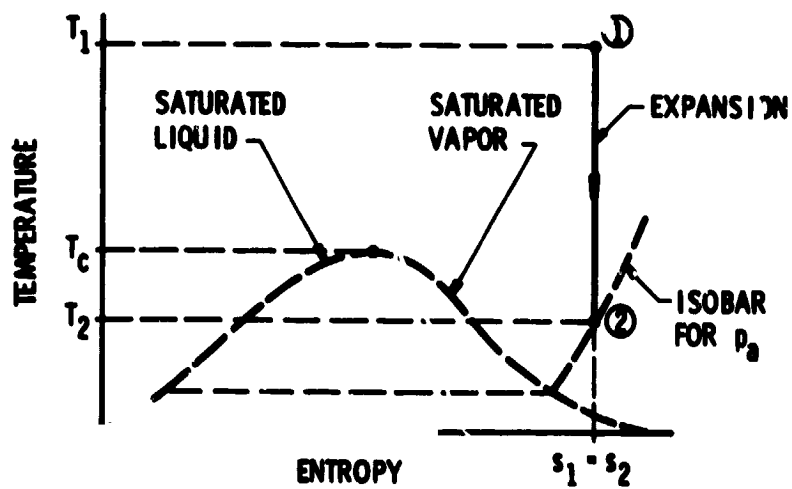
FIGURE 7. PRESSURE-VOLUME PLANE



FIGURE 8. TEMPERATURE-ENTROPY PLANE

## TABLE 3.

### COMPARISON OF COMPUTER PREDICTED RANGES AND REPORTED
### RANGES FOR ACCIDENTS INVOLVING ROCKETING FRAGMENTS
#### (From Baker, et al., 1978)

| EXAMPLE NUMBER | SOURCE OF ACTUAL DATA | INITIAL PRESSURE $(P_o)$ | VOLUME OF CONTAINER $(m^3)$ | VOLUME OF FRAGMENT ENCLOSURE $(m^3)$ | VOLUME OF LIQUID BE- FORE RUPTURE $(m^3)$ | VOLUME OF VAPOR BE- FORE RUPTURE $(m^3)$ | EXIT AREA $(m^2)$ | MASS OF FRAGMENT (kg) | LAUNCH ANGLE (degrees) | CALCULATED IMPACT VELOCITY (m/s) | CALCU- LATED RANGE (m) | ACTUAL RANGE (m) | PERCENT DIFFER- ENCE IN RANGE (%) | BEST ESTI- MATE FOR CD (WITH AP- PROX. VALUES) |
|---|---|---|---|---|---|---|---|---|---|---|---|---|---|---|
| 1 | NTSB- RAR- 76-4 4/29/75 | 701.197 | 38.02 | 28.23 | 33.10 | 4.916 | 3.75 | 3085 | 5 | 196 | 426 | 314 | 36 | 5 |
| 2 | NTSB- RAR- 73-4 9/21/72 | 1,034.214 | 37.85 | 50.32 | 27.29 | 10.56 | 3.41 | 5003 | 5 | 189 | 471 | 300 | 18 | 5 |
| 3 | NTSB- RAR- 73-4 9/21/72 | 1,034.214 | 37.85 | 1.28 | 27.29 | 10.56 | 3.41 | 652 | 5 | 94 | 156 | 165 | -6.7 | 5 |
| 4a | Propane Tank Explosion in San Antonio | 1,378.951 | 1.0927 | 0.5513 | 1.586 | 0.3067 | 2.336 | 171 | 5 | 159 | 450 | 123 | 266 | 5-10 |
| 4b | Propane Tank Explosion in San Antonio | 1,378.951 | 1.0927 | 0.5513 | 1.586 | 0.3067 | 2.336 | 171 | 10 | 154 | 446 | 123 | 288 | 5-10 |
| 4c | Propane Tank Explosion in San Antonio | 1,378.951 | 1.0927 | 0.2002 | 1.586 | 0.3067 | 0.6567 | 171 | 5 | 72 | 90 | 123 | -27 | 5-10 |
| 4d | Propane Tank Explosion in San Antonio | 1,378.951 | 1.0927 | 0.2002 | 1.586 | 0.3067 | 0.6567 | 171 | 10 | 71 | 179 | 123 | 46 | 5-10 |

horizontal and vertical accelerations of a fragment from

$$\ddot{X} = \frac{-A_D C_D \rho_o (\dot{X}^2 + \dot{Y}^2) \cos \alpha}{2M}$$

$$- \frac{A_L C_L \rho_o (\dot{X}^2 + \dot{Y}^2) \sin \alpha}{2M} \quad (49)$$

and

$$\ddot{Y} = -g - \frac{A_D C_D \rho_o (\dot{X}^2 + \dot{Y}^2) \sin \alpha}{2M}$$

$$+ \frac{A_L C_L \rho_o (\dot{X}^2 + \dot{Y}^2) \cos \alpha}{2M} \quad (50)$$

where

X = range, m

Y = altitude, m

$\dot{X}$ = horizontal velocity

$\dot{Y}$ = vertical velocity

$\ddot{X}$ = horizontal acceleration

$\ddot{Y}$ = vertical acceleration

$C_D$ = drag coefficient

$A_D$ = drag area

$C_L$ = lift coefficient

$A_L$ = lift area

$\rho_o$ = density of air, $kg/m^3$

M = mass, kg

$\alpha$ = trajectory angle, radians

$\alpha_i$ = initial trajectory angle, radians

g = acceleration of gravity

at t = 0

$$\dot{X} = V_i \cos \alpha_i \quad (51)$$

185

$$\dot{Y} = V_i \sin \alpha_i \qquad (52)$$

By solving the two second-order differential equations simultaneously, one can obtain velocity, and by numerically integrating the velocities, one can obtain the displacement, i.e., fragment range.

In crder to generalize the analysis for determining the range of a flying fragment from a bursting spherical or cylindrical container, a model analysis was performed. The pertinent physical parameters in the analysis, i.e., drag coefficient, drag area, lift coefficient, lift area, mass, etc., together with their fundamental dimensions, in a mass, length, and time (M, L, T) system are listed in Table 4.

### TABLE 4

### LIST OF DIMENSIONAL PARAMETERS FOR FRAGMENT TRAJECTORIES

| Parameter | Dimension |
|---|---|
| $C_D A_D \rho_o$ | $M/L$ |
| $C_L A_L \rho_o$ | $M/L$ |
| $V$ | $L/T$ |
| $M$ | $M$ |
| $g$ | $L/T^2$ |
| $R$ | $L$ |
| $\alpha$ | $-$ |

The coefficient of lift, the lift area, and the density of air are interrelated as are the coefficient of drag, the drag area, and the density of air. These parameters are combined in the table. The dimensional analysis produced the dimensionless parameters contained in Table 5. With the aid of the model analysis, the results of a large number of computer runs, exercised to obtain the range of fragments which have various initial flight conditions, can be consolidated into simple graphical form (Figure 9). Procedure for their use are:

Step 1. Calculate the lift/drag ratio

$$= \frac{C_L A_L}{C_D A_D} \text{ for the fragment.}$$

Step 2. Calculate the velocity term

$$= \frac{\rho_o C_D A_D V^2}{Mg} \text{ for the fragment.}$$

Step 3. Select the curve on the graph for the appropriate lift/drag ratio, locate the velocity term on the horizontal axis; find the corresponding

range term, $\frac{\rho_o C_D A_D R}{M}$ and determine

the range, R.

### TABLE 5.

### DIMENSIONLESS PARAMETERS (PI TERMS) FOR FRAGMENT TRAJECTORIES

| $\pi_1$ | $\alpha$ |
|---|---|
| $\pi_2$ | $\dfrac{\rho_o C_D A_D V^2}{Mg}$ |
| $\pi_3$ | $\dfrac{\rho_o C_D A_D R}{M}$ |
| $\pi_4$ | $\dfrac{C_L A_L}{C_D A_D}$ |

For lift to drag ratios $\dfrac{C_L A_L}{C_D A_D}$ that are not on the curve, a linear interpolation procedure can be used to determine the range from the curve. Interpolation in the steep areas of the curve can cause considerable error and it is recommended that, for these cases, the computer code FRISB be exercised.

### V. CONCLUSIONS

This paper summarizes some useful techniques for determining the velocity of fragments from bursting pressure vessels, the velocity and range of large fragments containing an evaporating fluid, and the range of fragments subjected to drag and lift forces during flight. Results of computer analysis of the bursting gas pressure vessels and the range of flying fragments are summarized in convenient graphical form, over a broad range of applicability, using similitude theory.

### VI. ACKNOWLEDGEMENTS

$$\frac{P_0 C_D A_D R}{M}$$

$$\frac{C_L A_L}{C_D A_D}$$
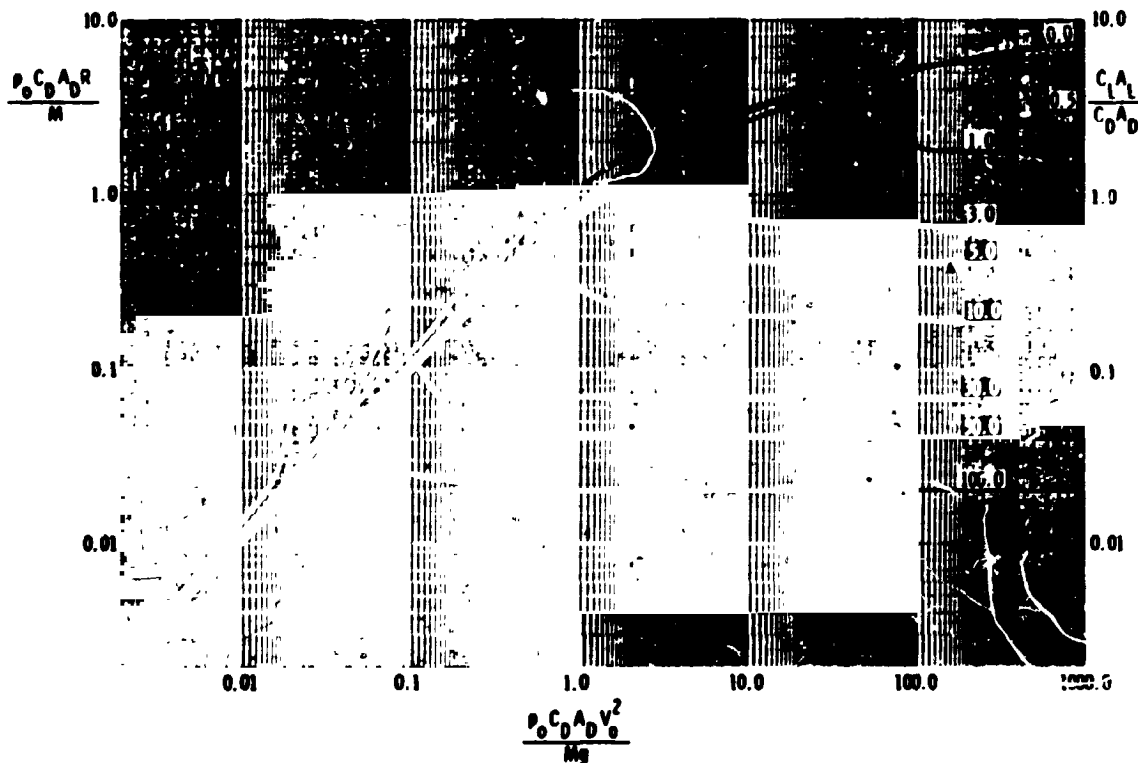
$$\frac{P_0 C_D A_D V_0^2}{Mg}$$

FIGURE 9. SCALED CURVES FOR PREDICTING RANGE OF FRAGMENTS
SUBJECTED TO DRAG AND LIFT FORCES

would like to express their sincere
gratitude to the late Mr. Robert Siewert
and Mr. Paul Ordin of NASA, Lewis Re-
search Center, Cleveland, Ohio, and
Dr. Wilfred E. Baker of Southwest
Research Institute, San Antonio, Texas
for their continued support and assis-
tance during the course of this work.

REFERENCES

1. Taylor, D. B. and Price, D. F.,
   (1971), "Velocities of Fragments
   from Bursting Gas Reservoirs,"
   ASME Transactions, Journal of
   Engineering for Industry,
   November, 1971.

2. Baker, W. E., Kulesz, J. J., Ricker,
   R. E., Bessey, R. L., Westine, P. S.,
   Parr, V. B., and Oldham, G. A.,
   (1975), "Workbook for Predicting
   Pressure Wave and Fragment Effects
   of Exploding Propellant Tanks and
   Gas Storage Vessels," NASA CR-134906,
   Contract NAS3-19231, November 1975,
   (reprinted September 1977).

3. Bessey, R. L., "Fragment Velocities
   from Exploding Liquid Propellant
   Tanks," Shock and Vibration Bulletin

No. 44, August 1974, pp 133-139.

4. Bessey, R. L. and Kulesz, J. J.,
   "Fragment Velocities from Bursting
   Cylindrical and Spherical Pressure
   Vessels," presented at 46th
   Annual Shock and Vibration Sym-
   posium, December 1975.

5. Baker, W. E., Kulesz, J. J., Ricker,
   R. E., Westine, P. S., Parr, V. B.,
   Vargas, L. M. and Moseley, P. K.,
   (1978), "Workbook for Estimating
   Effects of Accidental Explosions
   in Propellant Ground Handling and
   Transport Systems," NASA CR-3023,
   Contract No. NAS3-20497.

6. Baker, W. E., Westine, P. S., and
   Dodge, F. T., (1973), Similarity
   Methods in Engineering Dynamics,"
   Hayden Book Co., Rochelle Park, NJ.

7. Smallwood, J. C. and Potter, J. S.,
   (1946), Thermodynamics for Engin-
   eers, Edwards Brothers, Inc., Ann
   Arbor, Michigan.